
Constraining the formation and evolution of cluster galaxies at $z \sim 1.5$ using sizes and colour gradients

Chi Chung Chan



München 2016

Constraining the formation and evolution of cluster galaxies at $z \sim 1.5$ using sizes and colour gradients

Chi Chung Chan

Dissertation
an der Fakultät für Physik
der Ludwig–Maximilians–Universität
München

vorgelegt von
Chi Chung Chan
aus Hong Kong

München, den 23. September 2016

Erstgutachter: Priv.-Doz. Dr. Roberto Saglia

Zweitgutachter: Prof. Dr. Hans Böhringer

Tag der mündlichen Prüfung: 28. Oktober 2016

Zusammenfassung

Im vergangenen Jahrzehnt wurden die Eigenschaften von Galaxien bei hohen Rotverschiebungen, $z \approx 2$, mit zunehmender Genauigkeit erforscht. Dies ermöglicht die Vorgänger unsere lokalen Galaxie-Population zu untersuchen und Modelle zu ihrer Entstehung und Entwicklung zu überprüfen. Die Eigenschaften von Galaxien ändern sich stark in dem Rotverschiebungsbereich $1 < z < 2$. Insbesondere hat sich herausgestellt, dass die Mehrzahl der passiven Galaxien mit der Zeit räumlich wachsen. Trotz gewaltiger Fortschritte sind viele Fragen noch offen, wie zum Beispiel welche Rolle die Umgebung in der Entwicklung passiver Galaxien spielt.

Wir präsentieren in dieser Dissertation Ergebnisse zu den strukturellen Eigenschaften und den Farbgradienten für passive Galaxien in drei Galaxienhaufen, mit Rotverschiebung $1.39 < z < 1.61$. Die Galaxien sind Teil des KMOS Cluster Survey (KCS) und wurden mit der Red Sequence Methode ausgewählt. Wir benutzen Aufnahmen des *Hubble-Weltraumteleskops* (*HST*) in mehreren Bändern des optischen und nahen infraroten Spektrum. Wir bestimmen die leuchtkraftgewichtete Größe mit der Sérsic-Methode und berechnen damit räumlich aufgelöste stellare Massenkarten. Wir benutzen dafür eine empirische Beziehung zwischen dem Masse-Leuchtkraft-Verhältnis ($M_*/L_{H_{160}}$) und der beobachteten Farbe ($z_{850} - H_{160}$). Diese räumlich aufgelösten Karten werden dazu benutzt, um die massengewichteten Größen der passiven Galaxien in unserem Datensatz zu messen.

Wir zeigen, dass die leuchtkraftgewichteten Größen dieser Haufengalaxien im Mittel um einen Faktor $\simeq 2$ kleiner sind als die passiven Galaxien im lokalen Universum. Der Median der Größe sinkt um 20% vom U zum R -Band im Ruhesystem als Folge der Farbgradienten. Die Steigung der Abhängigkeit zwischen stellare Masse und leuchtkraftgewichteter Größe stimmt mit Ergebnissen neuerer Studien von Feldgalaxien überein. Die Untersuchungen ergeben auch, dass die massengewichteten Größen kleiner sind als die entsprechenden Größen im Ruhesystem R -Band. Der Unterschied schwankt um 20% – 55% zwischen verschiedenen Galaxienhaufen, verglichen mit einem Mittelwert von $\approx 12\%$ bei einer Rotverschiebung von $z \approx 0$.

Jüngere Studien ergeben, trotz immer noch laufender Debatten, dass Haufengalaxien eine andere Größenverteilung haben als in Regionen mit durchschnittliche Galaxiendichte ("Feld"). Das ist vermutlich auf zusätzliche oder stärkere Umgebungsprozesse in sehr dichten Umgebungen zurückzuführen. Der Vergleich mit einem Datensatz von Feldgalaxien zeigt, dass der Median von leuchtkraftgewichteten Größen in den zwei weiter entwickelten Galaxienhaufen größer ist als für Feldgalaxien. Der Unterschied ist kleiner, wenn die

massengewichteten Werte benutzt werden. Zusätzlich haben diese zwei Galaxienhaufen ein kleineres Verhältnis von massen- zu leuchtkraftgewichteter Größe im Vergleich zu den Feldgalaxien, mit einer logarithmischen Verschiebung von jeweils ≈ -0.07 dex und ≈ -0.16 dex.

Wir erklären die Entwicklung der Größenverhältnisse mit der Entwicklung der Masse-Leuchtkraft-Verhältnisse und der Farbgradienten. Wie erwartet ist das Verhältnis von massen- zu leuchtkraftgewichteten Größen mit dem M_*/L -Gradienten korreliert, zeigt jedoch keine weiteren Korrelationen mit anderen Galaxieneigenschaften. Wir beobachten, dass die Farbgradienten in unserem Datensatz meistens negativ sind, mit einem Median von ≈ -0.4 mag dex $^{-1}$, der zweimal größer ist als der lokale Wert. Durch detaillierte Modellierung von Farbgradienten unter der Benutzung von Sternpopulation-Modellen zeigen wir, dass diese Entwicklung am besten mit einer Entwicklung der Altersgradienten entlang der großen Halbachse a , $\nabla_{\text{age}} = d \log(\text{age})/d \log(a) \approx -0.3$, erklärt werden kann. Das Bestehenbleiben von schwächeren Farbgradienten in alten, lokalen Galaxien bedeutet, dass der Metallizitätsgradient ebenfalls von Bedeutung ist, mit $\nabla_Z = d \log(Z)/d \log(a) \approx -0.2$. Dieses Verhalten stimmt mit neueren Beobachtungen überein, die Hinweise dafür liefern, dass passive Galaxien bei hoher Rotverschiebung von innen nach außen wachsen und deutet auf eine graduelle Massenzunahme hin, wie zum Beispiel bei Verschmelzungen mit gasarmen, masse-armen Galaxien (“dry, minor mergers”). Außerdem zeigt das Vorhandensein von auf Umgebungsprozessen bei hoher Rotverschiebung, dass es einen Zusammenhang mit dem dynamischen Zustand der Galaxienhaufen gibt. Wir schlagen vor, dass diese “minor mergers”, solange diese nicht durch das Potential des Galaxienhaufens unterdrückt werden, den Unterschied zwischen Galaxienhaufen und Feldgalaxien erklären können.

Abstract

Over the last decade, galaxy properties have been explored in increasing detail to redshift $z \sim 2$, allowing us to study the progenitors of the local galaxy population and constrain their formation and evolution. The properties of the galaxy population changed rapidly from $1 < z < 2$. In particular, it has recently been established that the majority of passive galaxies have undergone a significant growth in size over time. Despite the tremendous progress, many questions remain open, such as the role of environment in the evolution of passive galaxies.

In this thesis, we present results on the structural properties and colour gradients for a sample of red-sequence selected passive galaxies in three galaxy clusters in the redshift range $1.39 < z < 1.61$, as part of the ongoing KMOS Cluster Survey (KCS). We make use of the multiband optical and near-infrared imaging from the *Hubble Space Telescope* (*HST*); we derive light-weighted sizes from Sérsic fits and generate spatially resolved stellar mass maps, using empirical relationships between the stellar mass-to-light ratio (M_*/L_{H160}) and the observed ($z_{850} - H_{160}$) colour. These resolved mass maps are used to measure mass-weighted sizes of our sample of passive galaxies.

We demonstrate that the light-weighted sizes of these cluster galaxies are on average a factor of ~ 2 smaller than the sizes of passive galaxies in the local universe. The median size decreases by $\sim 20\%$ going from rest-frame U to R band due to colour gradients. The slope of the relation between the stellar mass and the light-weighted size is consistent with recent studies in the field. Furthermore, we find that the mass-weighted sizes are smaller than their rest-frame R -band counterparts: the degree varies between $\sim 20 - 55\%$ between different clusters, compared with an average of $\sim 12\%$ at $z \sim 0$.

While the debate is still ongoing, recent studies indicate that cluster galaxies have a different size distribution compared to the field population at high redshift, presumably due to additional or stronger environmental processes present in high density environments. Comparing with a sample of field galaxies at similar redshifts, our structural analysis indicates that the median light-weighted sizes in the two more evolved clusters are larger compared to the field. The difference is reduced if mass-weighted sizes are used. In addition, these two clusters show a smaller ratio of mass-weighted to light-weighted size compared to the field, with a logarithmic offset of ~ -0.07 dex and ~ -0.16 dex, respectively.

We attribute the evolution of the size ratio discussed above to the evolution in the M_*/L_{H160} and colour gradients. Indeed, as expected, the ratio of mass-weighted to light-weighted size is correlated with the M_*/L gradient, but it shows no obvious correlations

with other galaxy properties. We find that the colour gradients in our sample are mostly negative, with a median value of ~ -0.4 mag dex $^{-1}$, twice the local value. Through detailed modelling of the colour gradients using stellar population models, we find that this evolution is best reproduced by an evolution in age gradients along the semi-major axis (a), with $\nabla_{age} = d\log(\text{age})/d\log(a) \sim -0.3$, while the survival of weaker colour gradients in old, local galaxies implies that metallicity gradients are also required, with $\nabla_Z = d\log(Z)/d\log(a) \sim -0.2$. This is consistent with recent observational evidence for the inside-out growth of passive galaxies at high redshift, and favours a gradual mass growth mechanism, such as dry minor mergers. Moreover, the evidence discussed above for environmental processes in place at high redshift argues for a link to the dynamical state of the clusters. We propose that minor mergers, when not yet inhibited by the cluster potential, are able to explain the observed differences between clusters and the field.

Contents

Abstract	v
Abstract	vii
1 Introduction	1
1.1 Galaxy clusters and dense environments	1
1.1.1 Early studies of galaxy clusters	1
1.1.2 The cosmological model	2
1.1.3 Structure formation	4
1.1.4 Properties of galaxy clusters	6
1.1.5 Detecting galaxy clusters	9
1.1.6 Protoclusters and large structure at high redshift	13
1.2 Properties of galaxies	14
1.2.1 Galaxy classification	15
1.2.2 The colour bimodality in galaxies	15
1.2.3 Galaxy population in clusters or high density environments	20
1.3 Structural properties of passive galaxies	23
1.3.1 Parametric methods	24
1.3.2 Non-parametric methods	26
1.3.3 Scaling relations and the fundamental plane	26
1.4 Size evolution in passive galaxies	28
1.4.1 Does environment play a role?	29
1.4.2 Physical processes resulting in size evolution	31
1.5 Colour gradients in passive galaxies	32
1.5.1 From light-weighted to mass-weighted structural parameters	33
1.6 Outline of this thesis	34
2 The KMOS Cluster Survey	35
2.1 Outline of the KMOS Cluster Survey	35
2.2 The KMOS Cluster Sample	37
2.2.1 XMMU J2235-2257	37
2.2.2 XMMXCS J2215-1738	38
2.2.3 Cl 0332-2742	39

2.2.4	JKCS 041	40
2.2.5	Backup cluster - RCS 2345-3632	41
2.3	<i>HST</i> Data and Data Reduction	41
2.3.1	Summary of the <i>HST</i> data sets	41
2.3.2	<i>HST</i> data reduction	42
2.3.3	Absolute WCS calibration	46
2.3.4	PSF derivation and matching	50
2.4	Construction of photometric catalogues	51
2.5	The Red Sequence Sample	55
2.6	KMOS Observations and Spectroscopic Data	57
2.6.1	Sample selection	57
2.6.2	Observations and summary of spectroscopic data	63
2.7	Local Comparison Sample	64
3	Methods and Analysis	69
3.1	Light-weighted structural parameters	69
3.1.1	Quality control of the fitted structural parameters	72
3.2	Elliptical aperture photometry and color gradients	74
3.3	Stellar mass-to-light ratio – colour relation	76
3.3.1	The calibration sample	79
3.3.2	Methods	79
3.4	Integrated stellar masses	81
3.4.1	Comparison of masses derived using M_*/L - colour relation with previous literature using SED fitting	83
3.5	Resolved stellar mass surface density maps	85
3.5.1	From colour to stellar mass surface density	85
3.5.2	Construction of stellar mass surface density maps	87
3.6	Mass-weighted structural parameters	87
3.6.1	Deviation of mass-weighted parameters - 1D vs. 2D	88
3.6.2	Comparison of our mass-weighted sizes with previous literature using resolved SED fitting	89
3.7	Error analysis with simulated galaxies	89
3.7.1	Outline of the simulations	90
3.7.2	Construction of the set of simulated galaxies	91
3.7.3	Quantifying the uncertainties on the photometry	93
3.7.4	Quantifying the uncertainties in light-weighted parameters	94
3.7.5	Quantifying the uncertainties in mass-weighted parameters	98
4	Structural parameters and Mass-size relations	111
4.1	Distribution of the light-weighted parameters	111
4.2	Wavelength dependence of light-weighted galaxy sizes	113
4.3	Stellar mass – light-weighted size relations	119
4.4	Comparison of light-weighted to mass-weighted structural parameters	124

4.5	Stellar mass – mass-weighted size relations	126
4.6	Dependence of ratio of mass-weighted to light-weighted sizes on galaxy properties	127
4.7	Evolution of the ratio of mass-weighted to light-weighted sizes to $z \sim 0$	130
4.7.1	Mass-weighted structural parameters at $z \sim 0$	130
4.7.2	Comparison between KCS clusters and SPIDER	134
5	The origin of the colour gradients and the effect of environment	137
5.1	Colour gradients in the red sequence galaxies	137
5.2	The origin and evolution of colour gradients with redshift	140
5.2.1	Methodology	140
5.2.2	Case I – Pure age-driven gradient evolution	143
5.2.3	Case II – Pure metallicity-driven gradient evolution	143
5.2.4	Case III – Age-driven gradient evolution with assumed metallicity gradient	145
5.2.5	Implications and limitations	145
5.2.6	Effect of assuming exponentially declining SFRs	150
5.2.7	Effect of using $(g-r)$ colour gradients and their evolution with redshift	153
5.2.8	Effect of dust obscuration	154
5.3	Physical processes responsible for the evolution of size and colour gradient	158
5.4	Formation histories of passive galaxies in KCS	159
5.4.1	Is Monolithic collapse still viable?	161
5.5	Environmental dependence of photometric properties of massive passive galaxies at high redshift	162
5.5.1	Size distributions in different environment	162
5.5.2	Environmental dependence of the ratio of mass-weighted to light-weighted sizes	165
5.5.3	Effect of environment on the evolution of passive galaxies	174
6	Conclusions and future work	177
6.1	Summary of this thesis	178
6.1.1	Structural parameters and Mass-size relations	178
6.1.2	The origin and evolution of the colour gradients	179
6.1.3	The role of the environment in the evolution	181
6.2	Future work	182
6.2.1	The stellar mass fundamental plane	183
6.2.2	Colour gradients and mass distributions of RCS 2345-3632 and JKCS 041183	
6.2.3	Size evolution in different environment with mass-weighted sizes	184
	Acknowledgements	209

List of Figures

1.1	The Cosmic microwave background anisotropies as seen by Planck	3
1.2	X-ray and optical view of the core of the nearby Perseus cluster	7
1.3	$Rz'3.6\mu m$ composite of the cluster SpARCS J163435+402151 at $z = 1.18$	12
1.4	A schematic view of the Hubble sequence	16
1.5	The $u - r$ colour-mass diagram for the SDSS galaxies	18
1.6	The UVJ classification of galaxies in different redshift	19
1.7	The morphology-density relation	22
1.8	The Sérsic profile with different values of n	25
1.9	The stellar mass – size relation for early-type and late-type galaxies	30
2.1	Example of a hot stripe in a ACS F850LP exposure and the masking	47
2.2	Example of the IVM and ERR RMS maps	49
2.3	Examples of the derived characteristic PSFs	52
2.4	Fractional encircled energy of the z_{850} and H_{160} PSFs	53
2.5	Colour-magnitude diagram of the three KCS clusters used in this thesis	58
2.6	Colour-Colour selection for the three KCS clusters	59
2.7	Spatial distribution of red sequence galaxies in XMMU J2235-2557	60
2.8	Spatial distribution of red sequence galaxies in XMMXCS J2215-1738	61
2.9	Spatial distribution of red sequence galaxies in Cl 0332-2742	62
3.1	Examples of surface brightness profile fitting of four passive galaxies in the three KCS clusters	73
3.2	Examples of the stability and quality checks on the fitted structural parameters	75
3.3	Examples of colour profile fitting of four passive galaxies in XMMU J2235-2557	77
3.4	The effect of applying different S/N thresholds on colour profile fitting in XMMU J2235-2557	78
3.5	Relations between stellar mass-to-light ratio and $z_{850} - H_{160}$ colour at redshifts of the three KCS clusters	82
3.6	Colour-mass relations of the three KCS clusters	84
3.7	Comparison of masses derived using M_*/L - colour relation with SED fitting from previous literature	86
3.8	Examples of resolved stellar mass map derivation of two passive galaxies in XMMU J2235-2557	88

3.9	Comparison of mass-weighted sizes derived using M_*/L - colour relation with resolved SED fitting from Lang et al. (2014)	90
3.10	Example of the parameter file for the simulation of XMMXCS J2215-1738 .	92
3.11	Differences between recovered and input aperture colour as a function of input H_{160} magnitude	95
3.12	Differences between recovered MAG_AUTO and input magnitudes as a function of input mean surface brightness	96
3.13	Differences between recovered and input structural parameters by GALFIT as a function of input mean H_{160} surface brightness in the simulation of XMMU J2235-2557	99
3.14	Differences between recovered and input structural parameters by GALFIT as a function of input mean H_{160} surface brightness in the simulation of XMMXCS J2215-1738	100
3.15	Differences between recovered and input structural parameters by GALFIT as a function of input mean H_{160} surface brightness in the simulation of Cl 0332-2742	101
3.16	Differences between recovered and input effective semi-major axes by GALFIT of XMMU J2235-2557 as a function of input mean H_{160} surface brightness	102
3.17	Differences between recovered and input mass-weighted structural parameters by GALFIT as a function of input mean H_{160} surface brightness in the simulation of XMMU J2235-2557	104
3.18	Differences between recovered and input mass-weighted structural parameters by GALFIT as a function of input mean H_{160} surface brightness in the simulation of XMMXCS J2215-1738	105
3.19	Differences between recovered and input mass-weighted structural parameters by GALFIT as a function of input mean H_{160} surface brightness in the simulation of Cl 0332-2742	106
3.20	Differences between recovered and input mass-weighted effective semi-major axes by GALFIT of XMMU J2235-2557 as a function of input mean H_{160} surface brightness	107
4.1	Distribution of the H_{160} light-weighted semi-major axis a_e against the Sérsic index n of the red sequence galaxies in the KCS clusters.	114
4.2	Distribution of the H_{160} light-weighted Sérsic index n against the axis ratio q of the red sequence galaxies in the KCS clusters.	115
4.3	Size-wavelength relation of the red sequence galaxies in the KCS clusters .	118
4.4	Stellar mass – light-weighted size relations of the red sequence galaxies in the KCS clusters	123
4.5	Comparison between mass-weighted size $R_{e-circ,mass}$ and light-weighted size R_{e-circ} of the red sequence galaxies in the KCS clusters	125
4.6	Stellar mass – mass-weighted size relations of the red sequence galaxies in the KCS clusters	128

4.7	Dependence of ratio of mass-weighted to light-weighted sizes on different galaxy parameters of XMMU J2235-2557	131
4.8	Dependence of ratio of mass-weighted to light-weighted sizes on different galaxy parameters of XMMXCS J2215-1738	132
4.9	Dependence of ratio of mass-weighted to light-weighted sizes on different galaxy parameters of Cl 0332-2742.	133
4.10	Comparison of the ratio of mass-weighted to light-weighted sizes vs. stellar mass at different redshift	136
5.1	Colour and M_*/L gradients in the KCS clusters	139
5.2	Rest-frame $U - R$ colour of stellar populations with different ages and metallicities	141
5.3	Evolution of colour gradient over redshift in case I (Pure age-driven gradient evolution) for the KCS clusters	144
5.4	Evolution of colour gradient over redshift in case II (Pure metallicity-driven gradient evolution) for the KCS clusters	146
5.5	Evolution of colour gradient over redshift in case III (Age-driven gradient evolution with assumed metallicity gradient) for the KCS clusters	147
5.6	Evolution of colour gradient over redshift in case III (Age-driven gradient evolution with assumed metallicity gradient) for XMMU J2235-2557 with assumed solar metallicity $Z = 0.02$	149
5.7	Rest-frame $U - R$ colour of stellar populations with different ages and metallicities with different values of τ	151
5.8	Evolution of colour gradient over redshift in case III (age and assumed metallicity gradient $\nabla_Z = -0.2$) for XMMU J2235-2557 using SSP and tau models with $\tau = 0.2, 0.4, 0.6$ with assumed solar metallicity $Z = 0.02$	152
5.9	$Y_{105} - H_{160}$ colour gradients in XMMU J2235-2557	154
5.10	Evolution of $(g - r)$ colour gradient over redshift in case III (age and metallicity gradient) for XMMU J2235-2557 with assumed solar metallicity $Z = 0.02$	155
5.11	Mass-normalised size distributions of the KCS clusters	163
5.12	Comparison of the mass-normalised size distributions of XMMU J2235-2557 and XMMXCS J2215-1738 with the field	166
5.13	Comparison of the mass-normalised size distributions of Cl 0332-2742 with the field	167
5.14	Comparison of the mass-normalised size distributions of the three KCS clusters with the field	168
5.15	Comparison of the size ratio of the three KCS clusters with the field	172
5.16	Comparison of the structural properties of the intersecting population of the Szomoru et al. (2013) and Lang et al. (2014) sample	173

List of Tables

2.1	Summary of the <i>HST</i> imaging of the KCS clusters used in this study. . . .	43
2.2	Summary of the Astrodrizzle parameters used for the HST data reduction.	48
2.3	Photometry of the red sequence galaxies in XMMU J2235-2557	66
2.4	Photometry of the red sequence galaxies in XMMXCS J2215-1738	67
2.5	Photometry of the red sequence galaxies in Cl 0332-2742	68
3.1	Structural parameters and colour gradients of the red sequence galaxies in XMMU J2235-2557	108
3.2	Structural parameters and colour gradients of the red sequence galaxies in XMMXCS J2215-1738	109
3.3	Structural parameters and colour gradients of the red sequence galaxies in Cl 0332-2742	110
4.1	Summary of the wavelength dependence parameter γ of the three KCS clusters.	117
4.2	Best-fit parameters of the stellar mass – light-weighted size relations of the three KCS clusters	122
4.3	Best-fit parameters of the stellar mass – mass-weighted size relations of the three KCS clusters	127
5.1	The derived median age gradient (Case III) of the KCS clusters at the cluster redshift and $z = 0$	150
5.2	The derived median age gradient (Case III) of XMMU J2235-2557 at $z = 1.39$ and $z = 0$ with exponentially declining τ -models	151
5.3	The derived median age gradient (Case III) of Cl 0332-2742 at $z = 1.61$ and $z = 0$ with different values of $\langle A_V \rangle$	157
5.4	The mean (of the best-fit skew normal distributions) and the median of the mass-normalised size distributions of the KCS clusters and the L14 field sample	169
5.5	The results of the Kolmogorov-Smirnov test on the mass-normalised size distributions of the KCS clusters and the L14 field sample	170

Chapter 1

Introduction

1.1 Galaxy clusters and dense environments

Galaxy clusters are the largest known gravitationally collapsed configurations in our universe that are close to and evolving towards a dynamical equilibrium. With a typical mass of $10^{14} - 10^{15} M_{\odot}$, galaxy clusters in the present day universe are also the most massive structure to have formed and bounded by gravity. With much theoretical and observational effort dedicated on galaxy clusters, we now know that they are not merely a dense environment of ~ 5 Mpc where several hundred to thousands of galaxies reside. A galaxy cluster can be separated into three main components: a massive dark matter halo that makes up 80 – 90% of the total cluster mass, hot, diffuse X-ray emitting gas, namely the intracluster medium (ICM), that fills the cluster and contributes ~ 10 to 15% of mass, and lastly, galaxies themselves. Galaxies hence contribute only to around $\sim 5\%$ of the cluster mass. Although they represent a small fraction of the total mass of galaxy clusters, galaxies in clusters have attracted much scientific interest and study over time. The massive dark matter haloes and ICM provide an unique environment for the formation and evolution of cluster galaxies. In the haloes and ICM, cluster galaxies experience astrophysical processes that are distinct from, or in addition to, those experienced by the general field galaxy population.

1.1.1 Early studies of galaxy clusters

The beginning of scientific studies on galaxy clusters dates back to the 18th century, when Charles Messier compiled the first catalogue of ‘nebulae’ in 1784, containing a total of 103 extended objects that are bright and diffuse on the sky. He noticed an exceptional concentration of thirteen nebulae in the Virgo constellation (Messier, 1784), which we know today are members of the Virgo cluster. Continuation of the search by William Herschel, John Herschel, and John Dreyer led to the discovery of order of magnitudes more of these ‘nebulae’ as reported in the New General Catalogue published in 1888, which we still widely used today. At that time they are unsure whether some of these nebulae are indeed galaxies or related to galaxy clusters. Not until Edwin Hubble’s discovery in 1925 from distance

measurements using Cepheid variables did they realize that some of these nebulae are indeed extragalactic objects (Hubble, 1925). Edwin Hubble also showed that the recession velocities of the galaxies are related to the distance linearly (Hubble, 1929; Hubble & Humason, 1931), demonstrating that the Universe is indeed expanding. The first evidence for the existence of dark matter (DM) in the Universe is also provided using some of these measurements of galaxy velocities: from the dynamics of cluster galaxies, it is revealed that the total gravitating mass in the clusters are much larger than the total mass of the stars (for Coma, Zwicky, 1933, 1937 ; and for Virgo, Smith, 1936).

1.1.2 The cosmological model

The remarkable discovery of the expanding universe by Hubble (1929) also sparked the development of the ‘Big Bang’ model by George Gamow, which then developed gradually and eventually gave rise to the standard model of cosmology (or the ‘concordance model’) we widely accept today. According to this model, the universe began with an extremely hot and dense state to synthesise (light) chemical elements, a process known as primordial nucleosynthesis. As the universe expanded it gradually cooled down. The strongest evidence for the model comes from its prediction of the observed cosmic microwave background (CMB). The CMB, detected in 1965 (Penzias & Wilson, 1965), is a background of thermal radiation with a temperature of few kelvin.

In 1992, we had, for the first time, an all-sky view of the cosmic microwave background from the Cosmic Background Explorer (COBE), followed by its more sensitive successors, the Wilkinson Microwave Anisotropy Probe (WMAP) (Bennett et al., 2003) and Planck (Planck Collaboration I, 2011). Subtracting the dipole pattern due to motion of the Earth relative to the radiation (Smoot et al., 1977), the observed CMB is almost isotropic with a temperature of ~ 2.73 K (Smoot et al., 1992), with extremely small temperature fluctuations (i.e. anisotropies) of the order of $\sim 10^{-5}$ K across the sky. Figure 1.1 shows an all sky CMB anisotropy map from Planck after both the monopole and dipole are subtracted. The distribution of these temperature fluctuations is highly Gaussian: so far there is no evidence for significant non-Gaussianity from large ($\sim 10^\circ$) to small angular scales ($\sim 10'$) (e.g. Kogut et al., 1996; Komatsu et al., 2003; Planck Collaboration XXIII, 2014). The CMB is the image of the Universe further back in time we can ‘see’ with light, i.e. when the Universe first became optically thin to photons. This epoch, known as the epoch of recombination, happened at ~ 380000 years after the Big Bang ($z \sim 1100$). At that time, the temperature of the primordial baryon-photon plasma cooled to a temperature (~ 3000 K) where protons could start capturing free electrons in the plasma. This reduces the rate of Thomson scattering and eventually the plasma became optically thin.

The recombination era, or more accurately the decoupling of radiation and baryonic matter, is an important milestone of structure formation in the Universe. The anisotropies in the CMB we see in Figure 1.1, are an effect of the primordial density fluctuations in the density field of the baryonic matter, which are considered as the ‘seeds’ of the large-scale structures we observe in the Universe today. These fluctuations are thought to arise from a period of rapid exponential expansion, known as the inflationary epoch (Guth, 1981),

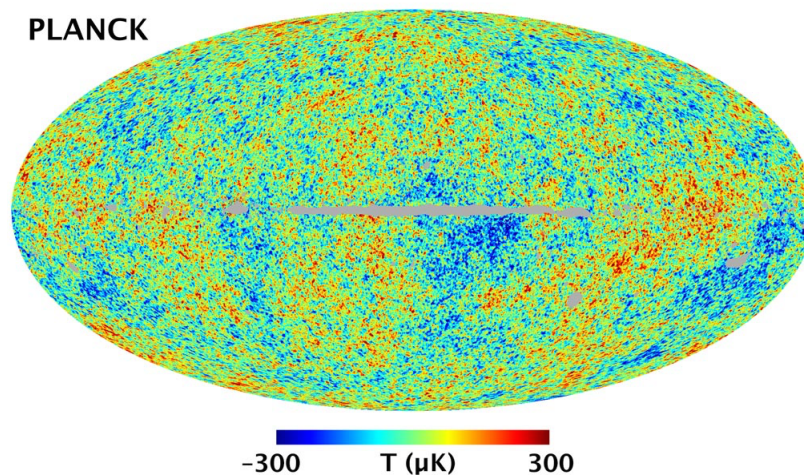


Figure 1.1: The Cosmic microwave background as seen by Planck. Planck SMICA CMB map with dipole and monopole subtracted. The colour bar below indicates the level of amplitude fluctuations in the maps. Image credits: NASA/GSFC.

happened at very early times. This inflationary epoch increased the volume of the early universe by a factor of $\sim 10^{78}$ and generated the primordial density fluctuations, which were quantum fluctuations in the inflationary field (Hawking, 1982; Starobinsky, 1982) and set the initial conditions for structure formation. The fact that the anisotropies in the CMB are Gaussian and with extremely small amplitudes is consistent with the simple inflation model.

One thing to note about the anisotropies in the CMB is that although they mark the decoupling of radiation and baryonic matter and the beginning of the growth of the baryon density fluctuations, the baryons did not actually form the fluctuations themselves autonomously when recombination happened. As the coupling of radiation and baryonic matter is not perfect, the photons can diffuse through the baryon-photon plasma driven by photon pressure, which results in the damping of the small-scale fluctuations known as ‘Silk damping’ (Silk, 1968). The Silk damping is able to erase all small-scale fluctuations at the time of recombination and only large perturbations can be retained. This is not consistent with the observed anisotropies in the CMB. To circumvent this problem, it is now believed that before the recombination era the density perturbations of the dark matter have already started to grow and amplify as they were not coupled with the baryon-photon plasma and experienced only gravitational effects. After recombination the baryons traced dark matter and collapsed quickly into the potential wells of dark matter that already existed at that time. If there were no dark matter, the baryons would have collapsed at a much slower pace as there would be much smaller effect of gravity, and the small-scale fluctuation would not have the chance to grow. The large-scale structure we see in the Universe today would have never been formed.

The model that gives rise to the above picture is currently the most popular cosmological

model, known as the ‘Lambda–cold dark matter’ (Λ CDM) model. The ‘cold’ in CDM refers to the slow speed of the DM particles relative to the speed of light (see e.g. Blumenthal et al., 1984, for a review and explanation of why cold DM dominates ‘warm’ or ‘hot’ DM). The Λ CDM model is described with a set of cosmological parameters, including the density parameter for baryon Ω_b , radiation (including photon and neutrino) Ω_r , dark matter Ω_m , and dark energy Ω_Λ , as one can define using the Friedmann equations:

$$\Omega_b = \frac{\rho_b}{\rho_{\text{crit}}} = \frac{8\pi G\rho_b}{3H_0^2}, \quad \Omega_c = \frac{8\pi G\rho_c}{3H_0^2}, \quad \Omega_\Lambda = \frac{c^2\Lambda}{3H_0^2}, \quad \Omega_r = \frac{8\pi G\rho_r}{3H_0^2} \quad (1.1)$$

where ρ_X is the density of the species at present day, $\rho_{\text{crit}} = 3H_0^2/8\pi G$ is the critical density and H_0 is the Hubble constant, the speed of the cosmic expansion at the present epoch. The Λ CDM model became the favoured model after the discovery of the accelerating expansion of the Universe using Type Ia supernovae (SNe Ia) as standard candles (Riess et al., 1998; Perlmutter et al., 1999), which placed constraints on the cosmological parameters, most importantly on the dark energy density parameter Ω_Λ , and demonstrated the need of a positive cosmological constant Λ . As a result, this discovery indicated the presence of dark energy. The current revision of the model suggests that our universe is flat (e.g. de Bernardis et al., 2000; Planck Collaboration XIII, 2015), with $\sim 70\%$ of the energy density due to dark energy, while the cold dark matter contributes to $\sim 27\%$, and the baryons only contributes to $\sim 3\%$ of the Universe.

1.1.3 Structure formation

With the initial conditions specified by the anisotropies of CMB and cosmological model specified by the Λ CDM model, one can derive the growth of these small density fluctuations over time. It is useful to define the density contrast of the matter density fluctuations at a given position \vec{x} and time t as:

$$\delta(\vec{x}, t) = \frac{\rho_m(\vec{x}, t) - \overline{\rho_m(t)}}{\overline{\rho_m(t)}} \quad (1.2)$$

where $\rho_m(\vec{x}, t)$ is the matter density of the fluctuations at a certain position and $\overline{\rho_m(t)}$ is the mean density of the matter at time t . According to the Λ CDM model, the main component of $\rho_m(\vec{x}, t)$ is cold dark matter, as it is the main driver of the evolution of the density perturbations. At early times when the perturbations are small ($\delta(\vec{x}) \ll 1$, i.e. the linear regime), one can describe the dark matter as an ideal pressure-less fluid of particles and derive the growth of the perturbations with a linearised set of fluid equations, the continuity equations, Eulers equation and the Poisson equation, which give the resultant equation:

$$\frac{\partial^2 \delta}{\partial t^2} = -2H(t) \frac{\partial \delta}{\partial t} + 4\pi G \overline{\rho_m} \delta \quad (1.3)$$

where the $H(t)$ is the Hubble parameter and is related to the scale factor a and the Hubble constant H_0 as

$$H(t) = \frac{\dot{a}}{a} = H_0 \sqrt{(\Omega_b + \Omega_c)a^{-3} + \Omega_r a^{-4} + \Omega_\Lambda} \quad (1.4)$$

One of the two linearly independent solutions in Equation 1.3, i.e. the ‘growing mode’ $\delta_+(z)$, dominates the evolution at later times and describes the amplitude of the growing perturbation. The exact amplitude of δ at different times can be solved numerically. Below we quote an analytic approximation discussed in Carroll et al. (1992), which has the following form in terms of redshift z :

$$\delta_+(z) \propto \frac{\Omega_m(z)}{(1+z)} \left[\Omega_m^2(z) - \Omega_\Lambda(z) + \left(1 + \frac{1}{2}\Omega_m(z)\right) \left(1 + \frac{1}{70}\Omega_\Lambda(z)\right) \right]^{-1} \quad (1.5)$$

where $\Omega_m(z) = (H_0/H(z)^2)(\Omega_b + \Omega_c)(1+z)^3$ and $\Omega_\Lambda(z) = (H_0/H(z)^2)\Omega_\Lambda$.

Conceptually, Equation 1.3 describes the relative effects of gravity and the cosmological expansion. In regions of positive density contrast (overdense regions), the perturbations start accreting surrounding (dark) matter due to their stronger gravitational effect compared to the average. At the same time this accretion is damped by the ‘stretching’ due to the cosmological expansion. The small density fluctuation hence grows in mass and size by accreting surrounding matter, and evolves continually by merging with other neighbouring denser-than-average regions. The massive dark matter haloes we see in galaxy and galaxy clusters today were hence formed ‘bottom-up’, such a formation process is termed as the hierarchical formation scenario.

As the perturbation grows, the density contrast gradually reaches $\delta(\vec{x}) \sim 1$. The growth of the perturbations is now beyond the linear regime and enters the non-linear regime. At this point, in order to follow the evolution and subsequently the gravitational collapse of these objects, one needs to start taking into account gravitational effects from the mass distributions. The evolution of the perturbations can be solved analytically only if assumptions about the symmetry of the mass distributions are made (see, e.g. Mo et al., 2010, for examples of the analytical models of spherical collapse).

Due to these complexities, numerical simulations are performed to understand the non-linear evolution of these structures in detail. For example, the Millennium Simulations (Springel et al., 2005), the Millennium-II (Boylan-Kolchin et al., 2009) and the Millennium-XXL (Angulo et al., 2012) are some of the state-of-the-art N-body simulations to follow the growth of dark matter structures. The simulations successfully demonstrate that the perturbations evolve in a hierarchical manner. In general, the gravitational collapse of the dark matter perturbations results in a quasi-equilibrium state of the object, via a process known as violent relaxation. This quasi-equilibrium state is the dark matter halo we observed today. Small structures can be seen to develop early in the simulations, and merge into larger and larger haloes, forming a filament-like structure known as the Cosmic web. It is shown that more massive haloes are more strongly clustered (e.g. Efstathiou et al., 1988; Sheth & Tormen, 1999). Besides halo mass the clustering also depends on the assembly history, in the sense that haloes that assembled their mass earlier are more strongly clustered than haloes that formed later, even having the same mass (e.g. Sheth & Tormen, 2004). This effect, termed as ‘assembly bias’, can also be applied to galaxy formation by extension, which suggests galaxies that formed earlier would be more strongly clustered today than galaxies of like mass and younger stellar populations (e.g. Cen &

Ostriker, 1993; Cooper et al., 2010). A commonly used analytical formation to describe the mass function of the haloes formed via spherical collapse and hierarchical clustering, is the Press-Schechter formalism (Press & Schechter, 1974). The simulations allow us to study the dark matter halo abundance with the entire complexity of halo formation (e.g. Jenkins et al., 2001; Tinker et al., 2008) and compare with results from analytic models (Press & Schechter, 1974; Sheth & Tormen, 1999). It is shown that the Press-Schechter formalism underpredicts the high-mass end of the mass function by up to an order of magnitude (Springel et al., 2005).

In summary, according to the current hierarchical structure formation paradigm, the dark matter haloes we see today are formed via gravitational collapse of the peaks in the primordial density field and hierarchical clustering. Being the most massive gravitational bounded structures in the Universe, galaxy clusters are hence signatures of the primordial density fluctuations that have collapsed early and grown all the way via hierarchical accretion and clustering since the epoch of recombination. Their growth and development directly trace the process of structure formation, which is sensitive to the cosmological parameters. As a result, the galaxy cluster population as a function of redshift can also be used as cosmological probe (e.g. Borgani et al., 2001; Vikhlinin et al., 2009; Mantz et al., 2014; de Haan et al., 2016).

1.1.4 Properties of galaxy clusters

Being the most massive virialized structure in the Universe, different components of a galaxy cluster host important and unique properties. In this section, we summarise briefly some of the properties of the intracluster medium and dark matter halo. The properties of galaxies in clusters will be described in detail in the next section.

The intracluster medium

The intracluster medium hosts the majority of the baryons of a galaxy cluster and contributes to ~ 10 to 15% of the cluster mass. The existence of the massive ICM basically indicates galaxy formation is an inefficient process. The ICM is a reservoir of fully ionized gas with a temperature of $10^7 - 10^8$ K, presumably shock heated by the potential well of the galaxy cluster during infall (Sarazin, 1988).

Much of the knowledge of the ICM is based on X-ray observations. The Uhuru X-ray satellite first revealed that the X-ray emission in Perseus and Coma cluster are spatially extended (e.g. Forman et al., 1972). Subsequent observations by ROSAT mapped the extended emission in local clusters to much larger radii and even detected substructures (e.g. Briel et al., 1992; Böhringer et al., 1993, 1994). We now know that galaxy clusters are bright extended X-ray sources with a luminosity L_X of $\sim 10^{43} - 10^{45}$ erg s^{-1} . Figure 1.2 shows a matching image of the Perseus cluster in X-ray and optical as an example.

Due to its high temperature, the ICM emits in X-rays mainly via thermal bremsstrahlung radiation (free-free emission). The bremsstrahlung radiation is caused by the deflection of electrons at close passage to an ion (hence, mainly ionized hydrogen for ICM). The specific

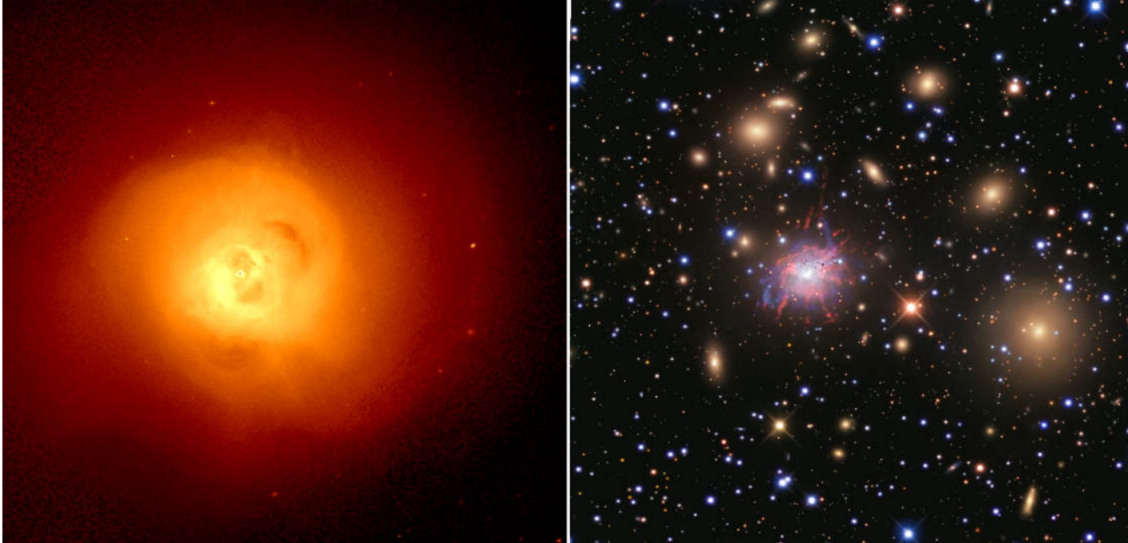


Figure 1.2: X-ray and optical view of the core of the nearby Perseus cluster. Left: Chandra X-ray ACIS-I composite from 0.5 – 7 keV. Right: Optical multicolour composite, taken with broadband RGB and narrowband filters from Blackbird observatory. The images are 11.8 arcmin across from north to south, corresponds to ~ 270 kpc across. Image taken from Fabian et al. (2011).

emissivity of the bremsstrahlung radiation is given by

$$\epsilon_\nu \propto n_e n_i T_X^{-1/2} Z^2 g_{ff}(\nu, T) \exp\left(\frac{-h\nu}{k_B T_X}\right) \quad (1.6)$$

where n_e and n_i are the electron and ion number density, respectively. Z is the charge of the ion and $g_{ff}(\nu, T)$ is the Gaunt factor that takes into account the quantum mechanical effects. Hence the shape of the spectrum can provide information on the temperature T_X of the ICM. Since the emissivity is $\epsilon_\nu \propto n_e n_i = n^2$, the X-ray surface brightness is the highest at the densest core of the cluster. The observed ICM has an electron density n_e in the range of $10^{-4} - 10^{-1} \text{ cm}^{-3}$ from the cluster outskirts to the core.

Besides the bremsstrahlung continuum, line emissions (e.g. Fe, O, Si, S) can also be observed in X-ray spectra of the ICM. The line emissions are produced by collisional excitation of K - and L -shell transitions of highly ionized metals (bound-bound emission). The line strengths and ratios provide a measure of the temperature and metal abundance. The presence of heavy elements implies that the ICM is not pristine, but has been enriched with metals presumably ejected from supernovae explosions in the cluster galaxies (see Böhringer & Werner, 2009, for a review on X-ray spectroscopy and chemical enrichment of ICM in clusters).

In the core of the cluster where the ICM is the densest, the X-ray emission can have a significant cooling effect on the ICM and drive an inflow of gas towards the cluster centre, known as a cooling flow. The central cooling times are known to be short compared to

the Hubble time. Observations show that a type of clusters, namely the cool-core clusters, exhibits a centrally peaked X-ray surface brightness profile (and Fe abundance profile) and a gradual drop in the ICM temperature towards the centre, consistent with the cooling flow picture. Nevertheless, Peterson et al. (2001) found that the central ICM is not cooling at rates predicted by the cooling flow model (see also, e.g. Peterson et al., 2003; Hudson et al., 2010), which led to the famous cooling flow problem. Various heating mechanisms that can quench the central cooling have been proposed, among those the most discussed one is heating by the active galactic nucleus (AGN) in the central galaxy of galaxy clusters (see Fabian, 1994, for a review). Although AGN outflow is clearly energetically favourable, it is unclear how its energy can distribute homogeneously in the ICM. One likely explanation is that the AGN jet inflates a ‘bubble’ of relativistic plasma that displaces the ambient ICM, which then rises buoyantly subsequently. This interaction between the bubble and the surrounding ICM drives turbulence, which then offsets the radiative cooling (Zhuravleva et al., 2014, 2016). Observationally, this picture is supported by the X-ray cavities found near the centre of clusters (e.g. Fabian et al., 2000; Sanders & Fabian, 2002; Dunn et al., 2005; Fabian et al., 2011), which one can also see at the centre of the X-ray image of the Perseus cluster in Figure 1.2. Recent studies of cool-core clusters have extended to high redshift $z > 1$ (e.g. Santos et al., 2008; De Grandi et al., 2014), although the number of high-redshift clusters is still scarce.

The density and temperature profile of the X-ray emitting ICM also allow us to measure the total cluster mass. Assuming the ICM is in hydrostatic equilibrium and spherically symmetric, one can compute the mass profile of the cluster, the mass enclosed within radius r ($M(r)$) is given by (Böhringer & Werner, 2009; Allen et al., 2011):

$$M(r) = -\frac{rkT(r)}{G\mu m_p} \left(\frac{d \ln n}{d \ln r} + \frac{d \ln T}{d \ln r} \right) \quad (1.7)$$

where $T(r)$ is the temperature of the ICM, $n(r)$ is the particle density, k is the Boltzmann constant, G is the Newton’s constant, μ is the mean molecular weight and m_p is the mass of proton. While the assumption of hydrostatic equilibrium is more or less valid for virialized (dynamically relaxed) clusters, it might not hold for merging clusters, or clusters that are young and not yet virialized. For the same reason, it cannot be applied to the central regions of cool-core clusters where the gas might be highly turbulent and hence have large non-thermal pressure support.

The dark matter halo

As mentioned above, 80 – 90% of the total cluster mass is in the form of dark matter. From N-body simulations of structure formation, Navarro et al. (1996, 1997) found that the density profile of the simulated cold dark matter haloes can be described by the following analytical form, which is now commonly referred to as the Navarro, Frenk & White (NFW) profile:

$$\rho_{\text{NFW}}(r) = \frac{\delta_c \rho_{\text{crit}}}{(r/r_s)(1 + r/r_s)^2} \quad (1.8)$$

where r_s is the scale radius, δ_c is a characteristic dimensionless density, and ρ_{crit} is the critical density defined in Equation 1.1. To describe the size and mass of a galaxy cluster, density contrasts with respect to ρ_{crit} are commonly used as a benchmark to ‘bound’ the halo. For example, the cluster radius r_{200} corresponds to the radius where the mean density within $r \leq r_{200}$ is 200 times the critical density. The mass M_{200} is then the total mass enclosed within r_{200} . Another parameter that characterises the shape of the NFW profile is the concentration c , defined as $c_{200} = r_{200}/r_s$ for the case of r_{200} . The concentration parameter c (more accurately c_{200}) is related to δ_c in Equation 1.8 by the following:

$$\delta_c = \frac{200}{3} \frac{c^3}{\ln(1+c) - c/(1+c)} \quad (1.9)$$

Simulations have shown that the concentration parameter c is inversely correlated with halo mass (e.g. Bullock et al., 2001; Gao et al., 2008). Although initially formulated for dark matter haloes, the NFW profile is often used to parametrise the gas density (for computing X-ray masses) and total mass profile of galaxy clusters (e.g. Voigt & Fabian, 2006; Sharma et al., 2012).

Although the NFW profile provides a good description of the density profiles of the dark matter halo in most cases, recently there has been reports from high resolution simulations demonstrating systematic deviations of the density profiles of the simulated haloes from the corresponding NFW fits. Other formulations have been suggested to provide better description of the DM profiles; one of the seemingly better candidates is the Einasto profile (Einasto, 1965), which has one extra free parameter (three in total) compared to the NFW (e.g. Navarro et al., 2004; Reed et al., 2011; Dutton & Macciò, 2014).

1.1.5 Detecting galaxy clusters

Traditionally galaxy clusters are identified by looking for areas on the sky with a concentrated distribution of galaxies against the general field on photographic plates. An example is the famous Abell catalogue (Abell, 1958), which consists of 2712 clusters found on the Palomar Sky Survey plates. Some of the criteria employed in the Abell catalogue to distinguish whether a concentration is a cluster are still widely used to describe a cluster. For example, the ‘richness’ of a cluster is often used to refer to the number of galaxies that are member of the cluster. Nowadays, we have a plethora of detection methods in different wavelengths to search for galaxy clusters at different redshifts. Different methods utilise different physical properties of the components of a galaxy cluster. In this section we give a brief overview on the detection methods, with a particular focus on high-redshift clusters.

The Sunyaev-Zel’dovich effect

One of the recently flourishing methods of cluster detection is via the Sunyaev-Zel’dovich (SZ) effect. While CMB photons pass through a galaxy cluster, some of them get distorted by the electrons in the ICM via inverse Compton scattering. The photons receive an energy

boost and this results in a distortion in the CMB spectrum. As a result, one will see a (small) decrement in intensity of the CMB in the millimeter wavelength range and an increase at lower wavelengths in the region where a galaxy cluster resides. This process is known as the thermal Sunyaev-Zel'dovich effect (Sunyaev & Zeldovich, 1972). There is also an additional effect caused by the motion of the cluster, which results in a small shift in the brightness temperature, known as the kinematic Sunyaev-Zel'dovich effect (Sunyaev & Zeldovich, 1972). For clusters, the kinematic Sunyaev-Zel'dovich effect is typically a magnitude smaller compared to the thermal Sunyaev-Zel'dovich effect. As the magnitude of the thermal SZ effect is proportional to the line-of-sight integral of the product of the electron density and temperature, SZ observations are in general difficult due to various contamination, as well as sources of confusion (e.g. radio sources and anisotropy of the CMB, see Carlstrom et al., 2002, for a review).

On the other hand, an advantage of the SZ effect is that its magnitude is independent of redshift. Hence the SZ effect can do equally well in detecting high-redshift clusters compared to those at low redshift. Measurements of the SZ effect have recently improved dramatically with the CMB data from the Atacama Cosmology Telescope (Marriage et al., 2011), the South Pole Telescope (Carlstrom et al., 2011) and the Planck satellite (Planck Collaboration XXIII, 2014), which have detected and confirmed (subsequently by spectroscopic redshift) galaxy clusters up to $z \sim 1 - 1.5$ (e.g. Bayliss et al., 2014; Rettura et al., 2014; Ruel et al., 2014; Sifón et al., 2016).

Extended X-ray sources

As we mentioned in Section 1.1.4, clusters appear as bright, extended X-ray sources on the sky due to their hot ICM. The bright and centrally concentrated X-ray surface brightness profiles of clusters make the search of galaxy cluster in X-ray surveys very effective. Moreover, extended X-ray detection is often regarded as a direct confirmation whether an overdensity of galaxy is a gravitationally bounded structure. The limitations on X-ray surveys, similar to those in optical, are on the area coverage and flux limits, which make the detection of high-redshift clusters more difficult due to surface brightness dimming. An advantage is that this method is relatively uninfluenced by projection effects. A projection of mass along the same line of sight would simply have low X-ray surface brightness, as the intensity of the bremsstrahlung radiation is proportional to n_e^2 .

There have been numerous X-ray surveys that successfully detected galaxy clusters at $z > 1$, for example the ROSAT Deep Cluster Survey (RDACS, e.g. Rosati et al., 1998; Stanford et al., 2001; Rosati et al., 2004), the XMM Large-Scale Structure Survey (XMM-LSS, e.g. Valtchanov et al., 2004; Willis et al., 2013), the XMM-Newton Distant Cluster Project (XDCCP, e.g. Böhringer et al., 2005; Nastasi et al., 2011; Fassbender et al., 2011), and the XMM Cluster Survey (Lloyd-Davies et al., 2011). Two of the clusters we focus on in this thesis are also first detected in X-rays, XMMU J2235-2557 at $z = 1.39$ (Mullis et al., 2005; Rosati et al., 2009) and XMMXCS J2215-1738 at $z = 1.46$ (Stanford et al., 2006). Pushing to the detection limits of current instruments, X-ray detection has successfully found clusters at even higher redshifts $z > 1.5$ (e.g. Henry et al., 2010; Tanaka et al., 2010;

Gobat et al., 2011; Santos et al., 2011; Fassbender et al., 2014).

Optical and infrared selection

Complementary to the SZ and X-ray detection method, another way to identify clusters is to make use of their galaxy populations, mainly in optical and infrared (IR) wavelength. There are many ways to identify clusters in the optical and IR data, but the idea is basically the same: the goal is to look for overdense regions with galaxies that are presumably belonged to the same cluster. Early optical cluster surveys, for example the Palomar Distant Cluster Survey (PDCS, Postman et al., 1996), the Postman et al. (1998) KPNO survey and the Las Campanas Distant Cluster Survey (Gonzalez et al., 2001), utilised a matched-filter method to detect galaxy clusters, in which they used a single ‘optimal’ filter that tries to enhance the contrast between the galaxy population in clusters and those in the field. Although these surveys are successful in detecting $z < 1$ clusters, searches with a single filter are subject to strong projection effects, which can result in spurious detections.

Another approach is to use two filters that are separated in wavelength, namely the Cluster Red-Sequence (CRS) technique (Gladders & Yee, 2000). The CRS technique exploits the fact that many galaxy clusters host a population of old, red galaxies, which forms a very tight colour-magnitude relation (the red sequence, e.g. Kodama et al., 1998) (see Section 1.2.3 for a description). The two filters are preferentially selected to bracket the 4000\AA break, an age-sensitive spectral feature due to absorption by heavy elements in old stars. Hence with a suitable pair of filters one can construct a colour distribution of galaxies that provides high contrast from the field population. The Red-sequence Cluster Surveys (RCS-1 and 2 Gladders & Yee, 2005; Yee et al., 2007) implemented this method using the R and z' band filters. With the CRS technique, the RCS surveys effectively detected numerous clusters up to $z = 1.4$. One of the downsides of this method is that it is only effective for clusters in a certain redshift range. Since the z' band becomes bluer than the 4000\AA break at $z \sim 1.2$, the R and z' combination no longer brackets the 4000\AA break and starts to fail to detect high(er) redshift clusters.

One can extend this method to higher redshifts by using a filter combination at redder wavelengths. The Spitzer Adaption of the Red-sequence Cluster Survey (SpARCS, Muzzin et al., 2009; Wilson et al., 2009), as the name implied, used IRAC IR imaging data from Spitzer Space Telescope to extend the CRS technique. Instead of using the R and z' band, SpARCS uses z' as the ‘blue’ filter and the $3.6 \mu\text{m}$ channel from Spitzer as the ‘red’ filter. Figure 1.3 shows one of the clusters, SpARCS J163435+402151 at $z = 1.18$, detected using this method. This method has been shown to be highly successful in detecting clusters in the redshift range $1 < z < 1.5$. With other variants of the red sequence method, recent works have reported detection of cluster at $z > 1.5$. For example, Andreon et al. (2014) identified the cluster JKCS 041 (which we adopted in the KMOS cluster sample, see Section 2.2) at $z = 1.8$ using $J - K$ colour. Other rest-frame wavelength ranges have also been used for cluster detection, Papovich et al. (2010) identified a cluster at $z = 1.62$ using the $3.6 \mu\text{m} - 4.5 \mu\text{m}$ ($[3.6] - [4.5]$) colour. Muzzin et al. (2013a) identified a cluster at $z = 1.63$ using the ‘stellar bump sequence’ method, which uses a combination of the

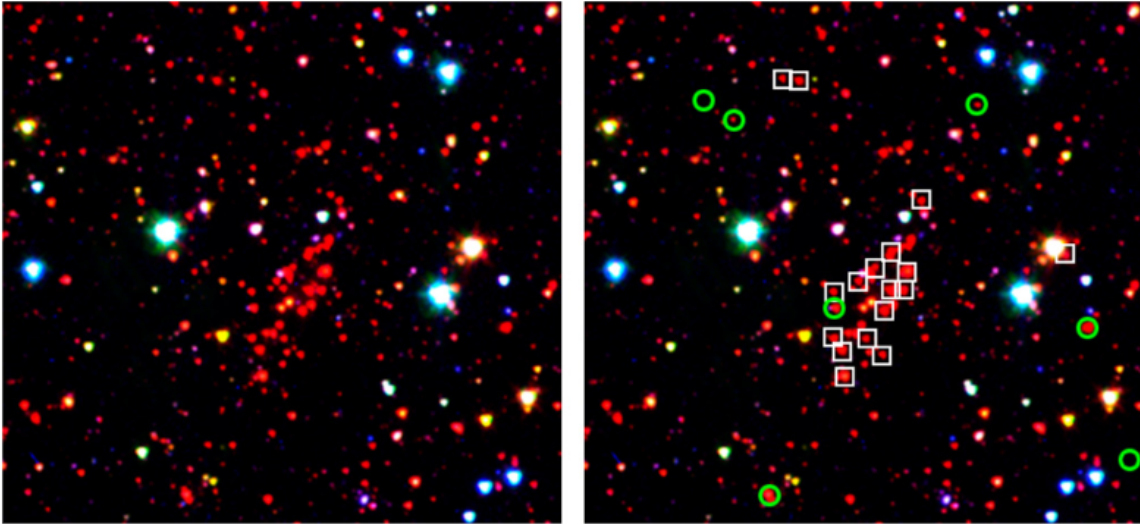


Figure 1.3: $Rz'3.6\mu m$ composite of the cluster SpARCS J163435+402151 at $z = 1.18$, detected using the red sequence method. On the right panel, the spectroscopically confirmed cluster members marked as white squares and spectroscopically confirmed foreground or background galaxies are marked as green circles. The images are ~ 3.5 arcsec across. Image taken from Muzzin et al. (2009).

$z' - 3.6 \mu m$ colour and the $[3.6] - [4.5]$ colour to trace the rest-frame $1.6 \mu m$ stellar bump feature instead of the 4000\AA break (see also, e.g. Kodama et al., 2007; Wilson et al., 2008, for other selection methods).

Besides using the assumption of the presence of a red sequence, another way is to use the redshift information of a galaxy. Galaxy clusters show up as a spatial overdensity in the three-dimensional density map of galaxy distributions. Nevertheless, it is observationally expensive to obtain spectroscopic redshifts for high-redshift galaxies (as they are faint due to surface brightness dimming), hence this technique has been mostly used with photometric redshifts. The photometric redshift of a galaxy is derived by matching the observed multi-band photometries to a set of SED templates. This has the advantage of providing redshifts for a large sample of galaxies with a relatively modest amount of time. The accuracy of the photometric redshifts depends mainly on the sampling of the galaxy SED (i.e. number of bands used) and the range covered in wavelength. To detect clusters at high redshift, IR data are required to well-sample the SED for accurate photometric redshifts. The Spitzer IRAC Shallow Cluster Survey (ISCS, Eisenhardt et al., 2008), as well as the IRAC Distant Cluster Survey (IDCS) employed this technique (together with overdensity in IR) and successfully confirmed tens of clusters at $1 < z < 1.5$ (e.g. Stanford et al., 2005; Brodwin et al., 2006, 2011), and even at $z > 1.5$ (e.g. Stanford et al., 2012; Zeimann et al., 2012; Brodwin et al., 2016). This technique can also be applied to galaxy surveys, for example, Castellano et al. (2007) identified the cluster Cl 0332-2742 at $z = 1.61$ (one of the clusters we focus on in this thesis, see Section 2.2) based on the three-dimensional

galaxy density computed using photometric redshifts from the Great Observatories Origins Deep Survey Multiwavelength Southern Infrared Catalog (GOODS-MUSIC) (Grazian et al., 2006).

Besides using the density and temperature profile of the X-ray emitting ICM (see Section 1.1.4), one can also use the galaxy population to estimate cluster mass. One way to do this is to rely on the kinematics of the galaxy population in the cluster as they trace the gravitational potential of the cluster. Assuming the cluster is relaxed to a static dynamical state, according to the virial theorem, the dynamical mass enclosed within the cluster radius R ($M(R)$) is given by:

$$M(R) = A \frac{\sigma^2 R}{G} \quad (1.10)$$

where A is a factor of order unity that depends on the density profile and definition of the cluster radius, and σ is the observed velocity dispersions of the cluster galaxies. This technique is suitable for rich clusters given that large galaxy population. Nevertheless, it has been shown that a number of possible systematics can bias the estimation of dynamical mass, for example, the effect of interlopers, radially dependent incompleteness and uncertainties on the redshift of the cluster galaxies (e.g Biviano et al., 2006; Saro et al., 2013).

Besides using cluster members, another way to measure cluster mass is to use the background galaxies, via an effect known as gravitational lensing. Due to the massive potential of the cluster, the geodesics along which photons propagate are affected, which results in a distortion of the image of the background sources. There are two types of lensing phenomena: strong and weak lensing. The former happens with the most massive objects with suitable spatial distribution of background galaxies, features such as arcs and multiple images of the background galaxies can be seen. Weak lensing manifests itself instead as the deformation of the shape (i.e. magnification and shear) of the background galaxies. These signals can then be used to estimate mass profile of the ‘lenses’. One advantage of gravitational lensing is that it does not rely on any assumption on the dynamical state of the cluster. As a result, it is highly complementary to the mass derived by X-ray observations. This advantage makes lensing a good technique for high-redshift clusters where the assumption of virialisation (or hydrostatic equilibrium) may not hold. Nevertheless, observing lensing signals for $z > 1$ clusters is challenging, in part due to the difficulties in quantifying the deformation in the faint background sources, which are located at very high redshift. Hence, both high-resolution and deep imaging are required to perform a lensing analysis. For example, Jee et al. (2011) successfully performed weak gravitational lensing analysis for 22 high-redshift $z > 1$ clusters using *HST* images, and studied the lensing mass – temperature relation at $z > 1$.

1.1.6 Protoclusters and large structure at high redshift

Moving to higher redshift, the definition of a galaxy cluster starts becoming a little bit vague. Most galaxy clusters at $z > 1.5$ we now confirmed are not the massive virialized

haloes like the Coma cluster we see in the local universe. Instead the haloes are just merged or even shown as groups of small haloes that are eventually going to merge into a single cluster. The term ‘protocluster’ is often used to describe these structures, but different definitions are used in the literature. According to Muldrew et al. (2015), protoclusters are diffuse collections of haloes, which are linked by filaments and will merge to become the clusters we see at low redshift.

These protoclusters exist in a range of evolutionary states, many of them do not even show up as a main halo that can be identified similar to a galaxy cluster. As a result, identifying protoclusters is very difficult, as most the abovementioned detection methods for galaxy clusters fail at some point. Due to their low halo masses and non-virialized nature, the SZ and X-ray detection are not effective. The young (mean) ages of the faint galaxy population in these objects also render the red sequence method ineffective. One of the techniques that can be used is the photometric redshifts, similar to what we describe in the last section. Nevertheless, since protoclusters have low number density of galaxies, very precise photometric redshifts are required. Despite the difficulties, applying a variant of this method Chiang et al. (2013, 2014) successfully detected 36 potential cluster and protocluster candidates from the COSMOS/UltraVISTA Survey (Muzzin et al., 2013b).

Another method that is successful in identifying protoclusters relies on the fact that a lot of protoclusters host high redshift radio galaxies (HzRGs). These HzRGs are AGNs with radio-loud jets and are preferentially formed in high density environments presumably because of the high merger rate (Hatch et al., 2014). A number of studies have used HzRGs as a tracer population to locate protoclusters or large scale structure at high redshifts (e.g. Le Fevre et al., 1996; Galametz et al., 2010, 2013; Husband et al., 2016).

1.2 Properties of galaxies

After introducing the most massive gravitationally bounded structure in the Universe, galaxy clusters, we then move to the smaller building blocks, galaxies. Since Edwin Hubble discovered that some of the early observed ‘nebulae’ are indeed galaxies (Hubble, 1925), the formation and evolution of galaxies have attracted a lot of attention in astronomy. In recent decades, different high sensitivity wide field instruments provide much larger (in area) and more complete (down to fainter magnitude) samples of local galaxies than before and hence allow us to perform statistical studies on galaxies. With high resolution instruments, it is now possible to probe the high redshift galaxy population, and study in detail their structural and kinematics properties. In this section, we give a brief general review on the galaxy population, before we focus on the structural properties and colour gradients of passively evolving galaxies which are the main focuses of this thesis.

Passive galaxies can be broadly characterised by their evolved stellar population, red colours, low star formation rates, and lack of spiral arms, although these characteristics are often correlated but not equivalent (e.g. Renzini, 2006a; Cappellari, 2016), especially at high redshift. This gives rise to various nomenclature: for example, the term ‘early-type galaxies’ stems from morphological classification of galaxies (see Section 1.2.1), ‘red

galaxies’ refers to a selection on colour (Section 1.2.2), ‘passively evolving galaxies’ refers to the evolutionary state of their stellar populations and ‘quiescent galaxies’ refers to those with low (specific) star formation rates (SFR). Even in the local universe where these definitions are generally compatible, selecting the sample with different criteria often has an impact on the derived properties or scaling relations (e.g. Conselice, 2006; Renzini, 2006a; Bernardi et al., 2010; Lange et al., 2015) and selection effects have to be taken into account. At high redshift, one has to be careful as these definitions may not refer to the same population.

1.2.1 Galaxy classification

One of the traditional classifications of galaxies that we still use today is the Hubble sequence, or the Hubble tuning-fork diagram (Hubble, 1926, 1936). Figure 1.4 shows a slightly modified version of the original Hubble sequence. The Hubble sequence classifies galaxies into four classes based on their visual morphology.

The leftmost class E in Figure 1.4, or commonly called early-types, corresponds to elliptical galaxies which have no spiral arm structure and have smooth, elliptical isophotes. The subclasses 1 to 7, refer to the ratio between semi-major a and semi-minor axes b of the galaxy multiplied by 10 ($10(1 - b/a)$). Moving to the right, the second class is the lenticular or commonly called S0 galaxies, which have a more prominent disk compared to the ellipticals, and is thought to be a transition between elliptical galaxies and the next class, spiral galaxies. Spiral galaxies (late-type, denoted with S) are thin disks with spiral arms. They are divided into two branches (S and SB) depending on whether there is a bar-like structure at the centre of the galaxy. They are further divided into subclasses (a,b,c) according to the fraction of the light in the bulge and the tightness of the spiral arms. The last class, which is originally not included in the Hubble sequence, is the category of Irregular galaxies (Im, IBm) that lack symmetry and have neither an obvious disk or bulge.

Since the Hubble sequence is motivated by the variations in morphology in galaxies, the sequence from early to late-type has no temporal or physical basis and is not related to the evolutionary state of a galaxy. Another limitation is that it suggests the S0 galaxies always have bulge fractions intermediate between elliptical galaxies and Sa galaxies, which is not supported by observations (e.g. Sandage et al., 1970; Poggianti et al., 1999; Cappellari et al., 2011). Since the Hubble sequence is established, there have been numerous attempts to incorporate intrinsic galaxy properties to improve the classification (e.g van den Bergh, 1976; Kormendy & Bender, 1996; Cappellari et al., 2011; Kormendy & Bender, 2012).

1.2.2 The colour bimodality in galaxies

Besides the morphology, another way to characterise a galaxy is to use its colour. The colour of a galaxy refers to the difference between the observed magnitude in two different bands. We now know that the colour between bands in UV to IR wavelength is directly related to the stellar population properties of the galaxy, such as age, metallicity

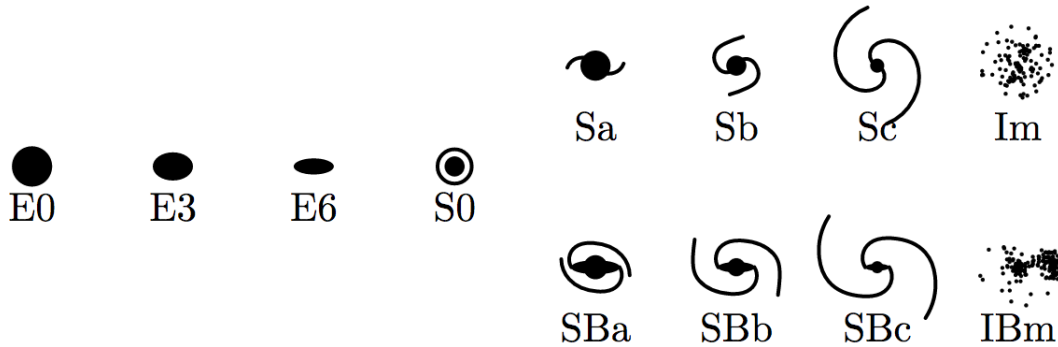


Figure 1.4: A schematic view of the Hubble sequence. Image taken from Abraham (1998).

of the population and the dust content. Hence the colour distribution of a galaxy provides information on the evolutionary pathways of galaxies.

The advent of large scale galaxy surveys, such as the Sloan Digital Sky survey (SDSS) (York et al., 2000), allowed us to study the global population of galaxy colours. The SDSS revealed the bimodality in galaxy colour in the galaxy colour-magnitude and colour-mass space with large statistics (Strateva et al., 2001; Blanton et al., 2003; Baldry et al., 2004, 2006). In Figure 1.5 we show an example of the rest-frame $u - r$ colour-mass diagram of a large sample of local galaxies, in a redshift range of $0.02 < z < 0.05$ from SDSS (Schawinski et al., 2014). A rest-frame colour of an object at redshift z is the colour measurement converted to an equivalent measurement in the rest-frame of the object. This is usually done by applying a magnitude correction (the ‘k-correction’) computed using spectral templates (see, Hogg et al., 2002, for a review on the k-correction).

It is clear from Figure 1.5 that the two types of galaxies reside at different regions of the colour mass-diagram. Several important properties of early-type galaxies can be seen: a) Early-type galaxies mainly have a red $u - r$ colour, although they also span a large range in colour. b) At high stellar masses, one preferentially find galaxies in early-types rather than late-types, i.e. the passive fraction increases with mass (Kauffmann et al., 2003b). c) The colour distribution is correlated with stellar masses. Most early-type galaxies ($\sim 90\%$) lie on a narrow relation between colour and masses (the ‘red sequence’), with only a small fraction having blue $u - r$ colours. High mass early-type galaxies tend to have a redder colour. On the other hand, the late-type galaxies do not show a clear sequence (the diffuse ‘blue cloud’) and have a continuous population ranging from blue to red colours (Renzini, 2006b).

The bimodality in colour indicates that early-type and late-type galaxies have different stellar populations. Today with the help of evolutionary syntheses techniques (e.g. Tinsley, 1978; Bruzual A., 1983; Bruzual & Charlot, 2003; Maraston, 2005; Vázquez & Leitherer, 2005; Conroy et al., 2009; Maraston & Strömbäck, 2011; Vazdekis et al., 2012), stellar population models can be constructed to model the colour (and other spectrophotometric properties) of an observed galaxies and relate the observed colour to their underlying stellar

population properties. In general, the stellar population in a galaxy can be characterised by its star formation history (SFH), its history of chemical enrichment (the metallicity distribution) and initial mass function (IMF) (the number of stars per mass interval when the stars were born) (see e.g. Maraston, 2005; Mo et al., 2010; Peletier, 2013, for a review on the principle of stellar population synthesis).

Nevertheless, a fundamental limitation of applying stellar population models to galaxy colours is the degeneracy between different stellar population properties, which hinders accurate estimation of individual properties. One example is the age-metallicity degeneracy. For example, an old stellar population with low metallicity can have identical colours with the one with younger ages and higher metallicity. To break this degeneracy, the strength of various features on the galaxy spectra (i.e. spectral indices) can be used (Burstein et al., 1984). In the case of early-type galaxies, absorption line indices, such as the Lick indices (Worthey et al., 1994), are particularly successful in breaking the age-metallicity degeneracy; some indices, like the Balmer lines H_β , H_δ and the strength of the 4000 Å break (D_n4000) are more sensitive to the age of the population, while indices with magnesium and iron lines like Mgb and $\langle \text{Fe} \rangle$ ($= 0.5(\text{Fe}5270 + \text{Fe}5335)$) are sensitive to metallicities. Another important indicator that can be used to constrain the formation epoch of the galaxy is the alpha element abundance ratio (i.e. α/Fe element ratio). α elements are the group of elements that are produced in stars via the triple- α process from helium as well as subsequent capturing of α particles to its products, which includes C, O, Ne, Mg, Si, S, Ar, Ca etc. These heavy elements are delivered mainly by Type II supernova explosions of massive stars. On the other hand, iron (and the other iron-peak elements) comes from delayed Type Ia supernovae. The α/Fe ratio ($[\alpha/\text{Fe}]$) hence carries information on the relative importance of chemical enrichment from Type II and Type Ia supernovae, and can be used to quantify the timescale over which star formation occurs (Thomas et al., 2005, 2010).

With the abovementioned tools, it is now established that local passive early-type galaxies have typically older ages and higher metallicities compared to late-type galaxies (e.g. Kauffmann et al., 2003a; Gallazzi et al., 2005). In addition, there has been studies suggesting that passive galaxies with higher mass are also older and have higher metallicities and $[\alpha/\text{Fe}]$ ratio (e.g. Thomas et al., 2005; Gallazzi et al., 2006; Clemens et al., 2009; Cooper et al., 2010; Thomas et al., 2010). The emerging picture is that of a local population of massive, quiescent red sequence galaxies. These are distinct from typically less massive, late-type blue clouds that are still forming stars.

The colour bimodality at high redshift and the colour selection

Interestingly, the colour bimodality appears to persist out to high redshift. Recent galaxy surveys have extended the colour studies to $z \sim 3$ and found that there is a separation of a red sequence and blue cloud in colour, although the contrast is lower as one moves to higher redshift (e.g. Bell et al., 2004; Kriek et al., 2008; Taylor et al., 2009b; Brammer et al., 2009; Whitaker et al., 2011; Muzzin et al., 2013b; Marchesini et al., 2014). In recent years, the colour bimodality have become a very useful properties to classify high-redshift

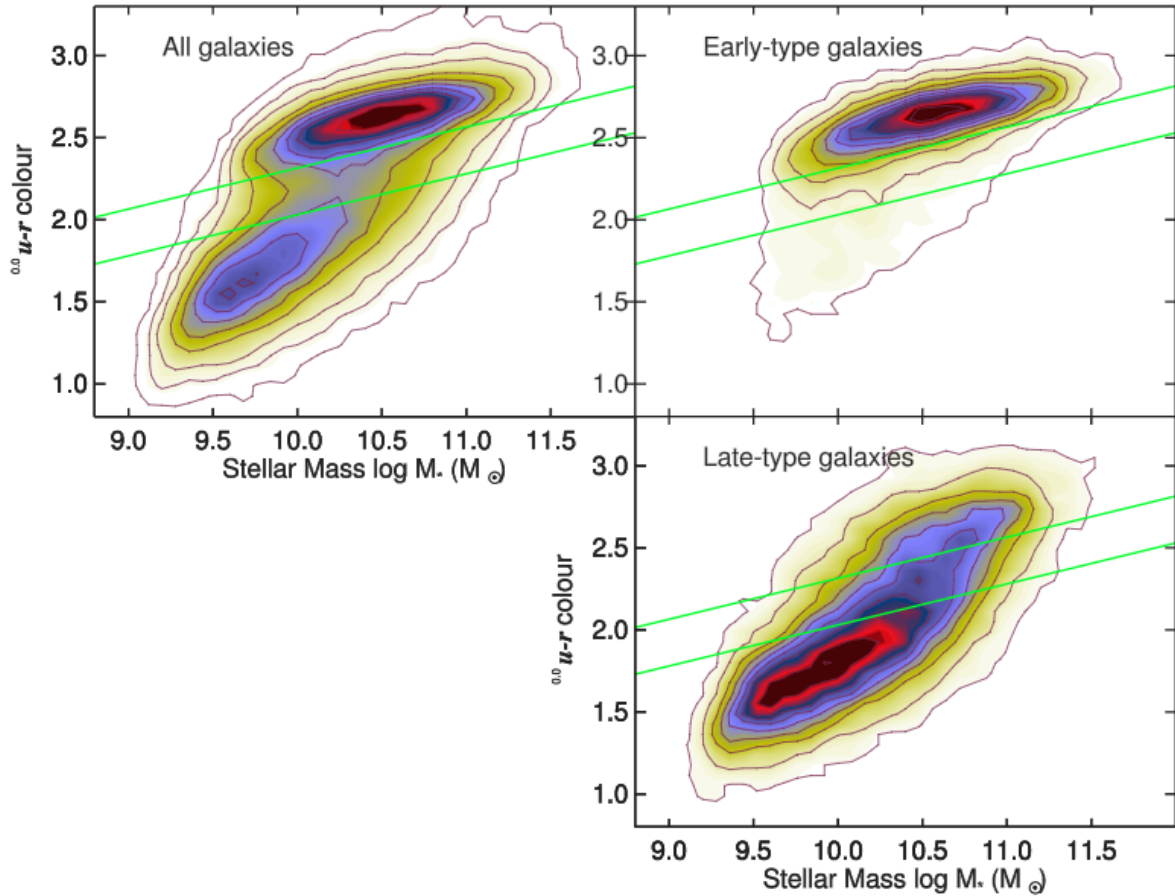


Figure 1.5: The $u-r$ colour-mass diagram for the SDSS galaxies. Top left: all galaxies are shown. Top right: Only early-type galaxies in the sample are included. Bottom right: Only late-type galaxies are included. Contours in the panels show the linear density of galaxies. The green lines show the ‘green valley’, a transition population between the two clouds, as defined by Schawinski et al. (2014). The morphological classification is from Galaxy Zoo project (Lintott et al., 2008, 2011). Image taken from Schawinski et al. (2014).

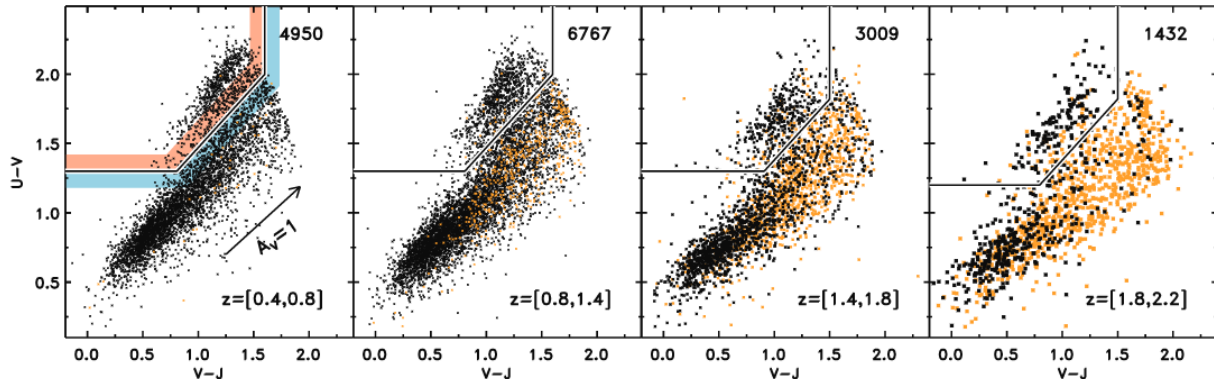


Figure 1.6: The UVJ classification of galaxies in different redshift. The solid line and coloured bands indicate the red / blue or quiescent/ dusty+star-forming selection. The reddening vector for one magnitude of extinction in the V-band is indicated, assuming a Calzetti et al. (2000) dust extinction law. Galaxies that have star formation rate $> 40M_{\odot} \text{ yr}^{-1}$ are shown in orange. Image taken from Brammer et al. (2011).

galaxies into the passive or star forming categories, so one can trace a particular type of galaxies and study the evolution of their properties, such as the number density and mass density (e.g. Brammer et al., 2011).

One of the currently popular colour selection technique is the UVJ classification, which galaxies are classified using the rest-frame $U - V$ and $V - J$ colours (e.g. Labbé et al., 2005; Wuyts et al., 2007; Williams et al., 2009; Whitaker et al., 2011; Muzzin et al., 2013b; Marchesini et al., 2014). Passive and star forming galaxies occupy different regions on the $U - V$ versus $V - J$ colour space (the UVJ diagram). Figure 1.6 shows an example of the UVJ digram of the galaxy population from the NEWFIRM Medium-Band Survey (NMBS) (Brammer et al., 2011), which spans a large redshift range of $0.4 < z < 2.2$. The passive galaxies appear as a clump on the top of the UVJ diagram, distinct from the area occupied by the star forming galaxies. One of the advantage of the UVJ classification is that it utilises information from optical to near-IR, which makes it able to distinguish between star forming galaxies that are dusty and ‘genuine’ passive galaxies. Dusty star forming galaxies will reside on the right side of the UVJ quiescent region, due to their higher dust reemission (larger $V - J$ colour). This classification has been tested and compared with for example, dust observations and selections using star formation rates, and consistent results have been found (e.g. Wuyts et al., 2007; Williams et al., 2010; Brammer et al., 2011).

Note that while the UVJ classification can effectively and consistently classify galaxies into passive or star forming up to $z \sim 3$, it does not correspond to a morphological selection at high redshift as in the local universe. In fact, high-redshift passive galaxies do not correlate exclusively with early-type morphologies as they do in the local universe (e.g. Buitrago et al., 2013). A number of studies have found that a substantial population of these galaxies appear to be dominated by massive exponential disks, and in general more

‘disky’ (McGrath et al., 2008; van der Wel et al., 2011; Wuyts et al., 2011; Chang et al., 2013).

Though we now know from observations that the colour bimodality exists out to high redshift, the underlying reason why this exists is not fully understood. Number density and mass function studies of the two populations have revealed that the total stellar mass in red passive galaxies has grown by roughly a factor of two since $z \sim 1$, whereas blue galaxies have kept constant or only changed a little over redshift (e.g. Bell et al., 2004; Faber et al., 2007; Ilbert et al., 2010; Marchesini et al., 2010). This mass growth is shown to be coming from addition of low mass galaxies to the red sequence at late times, while the most massive red-sequence galaxies are already in place since high redshift (e.g. Cimatti et al., 2006; Brown et al., 2007). This points to the existence of a morphological transformation from late-type star forming galaxies to early-type ellipticals, as well as a colour transition from blue to red galaxies.

As the colour is reflected by the underlying population, the colour transition from blue to red is manifested by the shut off of star formation in galaxies, known as ‘quenching’. Various physical mechanism that can suppress star formation in a galaxy have been proposed, and can be classified in two main categories, as suggested by Peng et al. (2010b): internal processes that happen within the galaxies (‘mass quenching’) versus external processes that are related to the environment where the galaxy resides (‘environmental quenching’).

The nature of these internal and external physical processes is still under debate. The mass function of global and star-forming galaxies shows a mass-dependent evolution, with the low-mass end of the mass functions evolving more rapidly than the high-mass end (Ilbert et al., 2013; Whitaker et al., 2014), suggesting massive galaxies evolve more rapidly at high redshift. Various studies have agreed on the significant importance of internal processes on massive galaxies (over environmental processes), in which the star formation is shut off (and is kept suppressed) in a short period of time (Peng et al., 2010b, 2012; Kovač et al., 2014). Possible candidates for mass quenching include AGN feedback (e.g. Bower et al., 2006; Croton et al., 2006; Hopkins et al., 2007; Bundy et al., 2008) and the formation of bulges due to disk instabilities, which then stabilises the gas disk and suppresses star formation (e.g. Elmegreen et al., 2008; Dekel et al., 2009; Martig et al., 2009; Lang et al., 2014).

1.2.3 Galaxy population in clusters or high density environments

It is well known that the environment in which a galaxy resides has an effect on its properties. Hubble & Humason (1931) have noticed that the densest regions are largely composed of early-type galaxies, while late-type galaxies mainly populate in the low density field. Early studies on galaxy clusters found the same result (e.g. Abell, 1965). The first quantitative measurements on the effect of the environment come from Dressler (1980), which he studied the relationship between the morphologies of galaxies and the local galaxy density in 55 rich clusters. This is known as the morphology-density relation, shown in Figure 1.7. It is clear that the fraction of early-types galaxies increases from $\sim 10\%$ in the lowest density regions (field) to around $\sim 40\%$ in the highest density region, while the late-type and

irregular galaxies show the opposite. S0 galaxies show a similar behaviour as the early-type galaxies, although the increase is not as prominent.

Recent large galaxy surveys allow for a more detailed study of the environmental dependence of galaxy properties with larger statistics. Studies from the SDSS have confirmed that red early-types preferentially reside in dense environments. They further demonstrated that early-types in dense environments are more massive, redder and with less gas (e.g. Kauffmann et al., 2004; Hogg et al., 2004; Balogh et al., 2004; Baldry et al., 2006; Weinmann et al., 2006). There has been claims that early-type galaxies that locate in dense environment are also on average ~ 2 Gyr older (e.g. Thomas et al., 2005; Cooper et al., 2010), although some other works suggests the difference is smaller (e.g. Clemens et al., 2009), or simply does not exist (Trager et al., 2008; Thomas et al., 2010).

Galaxy clusters, being the densest environment, are the ideal place to study as one would expect galaxies experience the strongest environmental effect. With observations and simulations, various environmental physical processes responsible for the dependence have been proposed (see e.g. Boselli & Gavazzi, 2006, 2014, for a review), including but not limited to: a) the gravitational interactions between galaxies in the clusters or with the potential of the halo, known as ‘galaxy harassment’ (e.g. Moore et al., 1998), b) merging of cluster galaxies mainly near the central region of the cluster as they slowly migrate towards the centre due to dynamical friction, a process called ‘galactic cannibalism’ (e.g. Merritt, 1985), c) the rapid stripping of the cold gas in galaxies due to ram pressure as they pass through the hot ICM (Gunn & Gott, 1972), known as ‘ram-pressure stripping’ and d) the suppression of ongoing accretion of cold gas onto galaxies due to the dark matter halo and the ICM, which leads to a gradual suppression of star formation as they run out of ‘fuel’, termed as ‘strangulation’ or ‘starvation’ (e.g. Larson et al., 1980). Note that the relative importance of these process is different on different types of galaxies, as well as on galaxies with different mass, for example galaxy harassment and ram pressure stripping have a much stronger impact on late-type galaxies compared to early-types (Moore et al., 1999). For example, detailed studies of a spiral galaxy in the local Norma cluster have revealed evidence for shock heating due to ram pressure stripping (ESO137-001, Fumagalli et al., 2014; Fossati et al., 2016).

Recently, the study of the role of environment has extended to high redshift. Various works have demonstrated that the fraction of quiescent / red galaxies increases with the density of environment up to $z \sim 1$ (e.g. Quadri et al., 2012; Kovač et al., 2014; Darvish et al., 2015). The abovementioned physical processes, although shown to be in effect in the local universe, might have different relative importance at high redshift (e.g. Balogh et al., 2016). In addition, the environmental processes usually require a relatively long time scale to quench the galaxy ($\sim 2 - 5$ Gyr at $z \sim 0.7 - 1.5$) compared to internal processes (e.g. AGN), hence environmental quenching of galaxies may not be the dominant process at high redshift (Fossati et al. 2016, in prep.).

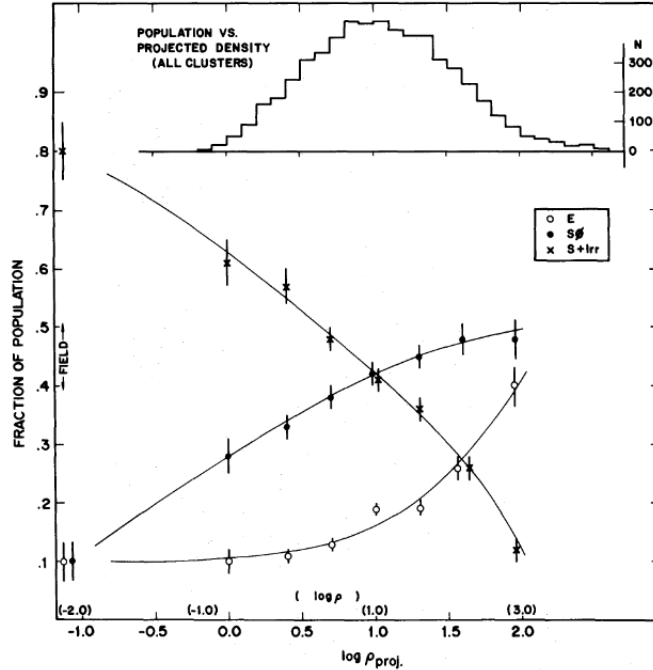


Figure 1.7: The morphology-density relation. Top: the number histogram of the total galaxy sample from 55 clusters. Bottom: The fraction of early-type, S0 and late-type+irregular galaxies as a function of the projected galaxy density (number of galaxy per Mpc^{-2}). Image taken from Dressler (1980).

The red sequence in clusters

In the last section, we show that early-type (passive) galaxies have predominately red colours. Combining with the fact that one can preferentially find these early-type galaxies in high density environment (partly) due to various environmental effect, it seems intuitive that most galaxy clusters show an overdensity of red galaxies or the ‘red sequence’. The red sequence of local galaxy clusters, such as Virgo and Coma, were known to exist for decades (e.g. de Vaucouleurs, 1961; Visvanathan & Sandage, 1977). Moreover, the red sequence appears to be a tight linear relation in the colour-magnitude space (or on the colour-magnitude diagram).

The red sequence is typically characterised by the slope, scatter and zero point of the relation. The scatter of the red sequence in local clusters shows a very small scatter (~ 0.1 mag) (e.g. Bower et al., 1992). Theoretical models have been proposed to explain the red sequence (e.g. Arimoto & Yoshii, 1987; Kodama & Arimoto, 1997). The scatter of the red sequence is thought to be reflecting the scatter in age of the red sequence galaxies (e.g. Bower et al., 1992, 1998), although dust could play a role (Lidman et al., 2008), while the slope of the red sequence is driven by the difference in metallicity in galaxies with different mass (the mass-metallicity relation) (Kodama & Arimoto, 1997; Kodama et al., 1998).

Discovery of high-redshift clusters allows us to extend the studies of red sequence galax-

ies and look at the build up of the red sequence. The red sequence is seen in clusters up to redshift $z \sim 2$ (e.g. Stanford et al., 1998; Tanaka et al., 2005; Gobat et al., 2011; Tanaka et al., 2013; Strazzullo et al., 2013; Andreon et al., 2014). Moving to higher-redshift clusters, various studies have found an evolution on the faint end of the luminosity function of the red sequence, which indicates a significant build up of the faint end of the red sequence towards lower redshift (e.g. Kodama et al., 2004; De Lucia et al., 2007; Stott et al., 2007; Rudnick et al., 2009; Bildfell et al., 2012; Rudnick et al., 2012; Cerulo et al., 2016). There is also little or no evolution in the slope of the red sequence in clusters, up to redshift $z \sim 1.5$ (Stanford et al., 1998; Mei et al., 2009; Stott et al., 2009; Snyder et al., 2012). In addition, Demarco et al. (2010) have demonstrated that the galaxies on the high mass end of the red sequence are on average older than the low mass end in a cluster at $z \sim 0.8$ (see also Smith et al., 2012). All the evidence seems to suggest that the high mass end of the red sequence was already in place at high redshifts ($z \sim 2$), while the low-mass galaxies joined the red sequence later at lower redshifts. This is consistent with the above-mentioned rapid suppression of star formation via internal processes for massive galaxies, followed by a slow(er) suppression in primarily low mass galaxies due to the environmental effect. This can also be reconciled with the fact that in high-redshift clusters ($z \gtrsim 1.5$), a substantial massive population is found to be still actively forming stars (e.g. Hilton et al., 2010; Hayashi et al., 2011; Gobat et al., 2013; Strazzullo et al., 2013; Bayliss et al., 2014; Ma et al., 2015). This implies that the star-forming galaxies are being transformed onto the passive red sequence over time.

One thing to note for the above picture is that, while it is true for the cluster population as a whole, for individual clusters one may find different properties in the red sequence. There have been reports of high-redshift clusters showing no evidence for a deficit of galaxies at the faint end of the red sequence (e.g. Lidman et al., 2008; Strazzullo et al., 2010; Andreon et al., 2014). This suggests the variation of the properties in clusters, such as halo masses, may play an important role in setting the time-scales for the build-up of the red sequence (see e.g. Lemaux et al., 2012; Tanaka et al., 2013).

1.3 Structural properties of passive galaxies

In the last section, we intentionally left out one of the fundamental properties of a galaxy, the measurement of its structure. The structural properties of galaxies are of great importance as they are direct measurable quantities, and their evolution provides important clues about the assembly history of the galaxies. In recent years, thanks to large galaxy surveys and advancement in computing power, the structural properties of a large sample of galaxy can be quantified in a consistent manner. This allows comparison of structural properties of galaxies across redshift and environment. As with the main focus of this thesis, in the section we focus on the structural properties of passive galaxies and the methods that have been used to quantify these properties. Note that most of the techniques we discussed are generally applicable to the global galaxy population.

1.3.1 Parametric methods

Traditionally, the structural parameters are measured via one-dimensional surface brightness profile of the galaxy. This profile can be obtained in various ways: the most straightforward technique is to take the annular average of the observed intensity of the galaxy as each radius and trace how this intensity varies as a function of radius. This surface brightness profile is then compared to a parametric model, in which one can derive useful quantities like effective radius and concentration of the profile. Early as the 1910s, numerous parametrisation of galaxy profiles have been proposed (e.g. Reynolds, 1913; Hubble, 1930; King, 1962, 1966).

One of the most used parametrisation is the de Vaucouleurs (1948) $R^{1/4}$ profile, proposed by de Vaucouleurs (1948) to describe the surface brightness profile of a sample of local elliptical galaxies.

Later work by Caon et al. (1993) showed the deviation from the de Vaucouleurs profile and demonstrated the need of a more general parametrisation, the Sérsic profile, proposed by Sérsic (1968), which has the following form:

$$I(R) = I_e \exp \left[-b_n \left(\left(\frac{R}{R_e} \right)^{1/n} - 1 \right) \right] \quad (1.11)$$

where R_e is the effective radius, the radius that encloses half of the total luminosity from the model, I_e being the intensity at R_e , n is the Sérsic index which describe the shape of the light profile. The parameter b_n is a function of the Sérsic index ($\Gamma(2n) = 2\gamma(2n, b_n)$, which γ is the incomplete gamma function), where the exact values can only be solved numerically (Ciotti, 1991). Various approximations exist for b_n , one of such given by Capaccioli (1989) has $b_n \approx 1.9992n - 0.327$, is applicable for $0.5 < n < 10$.

The de Vaucouleurs (1948) $R^{1/4}$ profile is a special case of the Sérsic profile with $n = 4$. In fact, the exponential and Gaussian functions are also special cases of the Sérsic function when $n = 1$ and $n = 0.5$, respectively. Figure 1.8 shows the behaviour of the Sérsic profile with different n . In principle, the Sérsic index n is a measure of concentration of the profile. A profile with a larger n shows a more cuspy profile at the centre, although at the same time it also have a broader wing at the outskirt.

The Sérsic profile is able to describe the surface brightness profile of most elliptical galaxies reasonably well (e.g. Kormendy & Bender, 2009). The arrival of high resolution data from *HST* first demonstrated that a single Sérsic profile is often not able to properly describe the inner part of the elliptical galaxies, especially in massive elliptical galaxies. Most massive galaxies exhibit surface brightness profile that shows a clear break at $R \sim 50 - 500$ pc (the core radius), with a steeper outer Sérsic-like profile followed by a significantly flatter inner profile (core). To well describe this type of profile, the double power-law (or known as the Nuker law) (e.g. Lauer et al., 1995; Faber et al., 1997) or the ‘Core-Sérsic’ parametrisation is used instead (e.g. Graham et al., 2003; Trujillo et al., 2004; Côté et al., 2007; Kormendy & Bender, 2009).

One can also quantify the structure of the profile of an early-type galaxy using the shape of the isophote. Isophotes are basically contours joining points of equal surface brightness

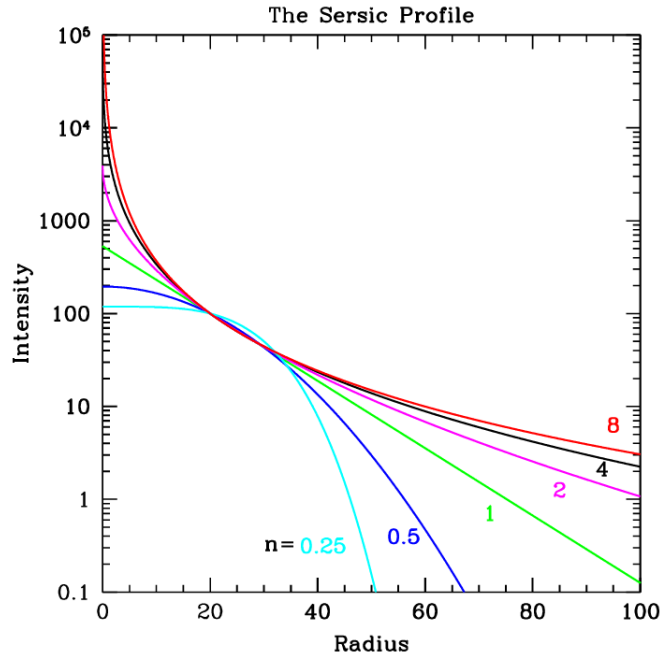


Figure 1.8: The Sérsic profile with different values of n . The effective radius R_e are fixed at 20 and I_e are fixed at 100 for the different profiles. Image taken from Peng et al. (2010a).

on a surface. The procedure starts by first finding the best-fitting ellipse, which provides a good first-order approximation to the isophotes. Then the deviations from that ellipse are measured using the truncated Fourier expansion (Bender et al., 1988; Peletier et al., 1990a). Studies of isophote fitting have led to the classification of whether the isophote is ‘boxy’ or ‘disky’ and the connection with their kinematics (Bender et al., 1988; Kormendy & Bender, 1996). The best-fitting ellipse is also often used as a reference to construct one-dimensional profile for the abovementioned surface brightness profile fitting.

At high redshift, the angular scale (the ratio of the physical size of an object compared to its angular size) is larger compared to the local universe. Combined with the fact that passive galaxies are physically smaller (see Section 1.4), the angular extent of high-redshift galaxies is much smaller than local ellipticals. They are often comparable to the size of the point spread function (PSF) of the telescope, which makes the consideration of the effect of PSF smearing essential.

For this reason, Sérsic profile fitting directly with two-dimensional images has been used extensively in measurements of structural properties of high-redshift galaxies. The crucial advantages of two-dimensional fitting are that it takes into account the effect of PSF using convolution techniques, and does not require the extraction of surface brightness profiles (see Section 3.1 for some technical discussions).

1.3.2 Non-parametric methods

Besides fitting of surface brightness profile or isophotes, the structural parameters of galaxies can also be described using non-parametric measurements. Non-parametric measurements do not assume the underlying form of the surface brightness profile, which in some case, is beneficial especially if one would like to compare measurements across galaxy types.

The basic way to measure galaxy size non-parametrically is by integrating the surface brightness profile out to a certain radius to estimate the total galaxy flux, then derive a radius where the fraction of the inner light reach a certain fraction of the total fluxes. For example, R_{50} refers to the radius that contains 50% of the total light (= effective radius), while R_{20} and R_{90} corresponds to 20% and 90%, respectively. This, of course, somehow depends on the surface brightness limit of the data and how far out one integrates.

One of the widely used way is the Petrosian radius (Petrosian, 1976) (r_P), which measure a fraction of light independent on the surface brightness limit. Various modifications exist but the basic idea is to look for a radius where the ratio between the surface brightness at that particular radius to the mean surface brightness within the radius drops to a defined value. 0.2 is commonly adopted to compute r_P . This defined r_P can then be varied or used to compute different size measurements (Shen et al., 2003; Conselice, 2003).

To measure the concentration (c) of the profile, a common estimation is to divide two radii that corresponds to different fraction of the total light. For example, R_{50} and R_{90} are commonly used to derive $c = R_{90}/R_{50}$. A higher value of the concentration means the profile is more concentrated at the centre. The concentration is found to be correlated with galaxy types (e.g. Strateva et al., 2001).

Another quantity that can be used to measure the concentration is the Gini and M_{20} coefficients (Lotz et al., 2004). The Gini coefficient G , widely used in economics to quantify the distribution of wealth, can be used to similarly describe the distribution of the light in a galaxy in pixelated images. A Gini of 1 suggests the light is all concentrated at a spot, while 0 means they are equally distributed. M_{20} is the second order moment of the brightest 20% flux of the galaxy divided by the total moment of the light in all pixels.

Other parameters, such as the asymmetry index A , smoothness S , or the multimode M , are invented to describe the asymmetry and clumsiness of the galaxy profiles. While they may not be very relevant for elliptical galaxies that have generally smooth profiles, these indices are very useful in assessing properties of late-type galaxies and galaxies undergoing mergers (Conselice, 2003; Freeman et al., 2013). The interested reader are refer to Conselice (2014) for a review.

1.3.3 Scaling relations and the fundamental plane

Passive galaxies exhibit a set of scaling relations with their properties such as luminosity L , size R_e and stellar velocity dispersion σ . The stellar velocity dispersion is the dispersion of the velocities of the stars in the galaxy about their mean velocity along the line of sight. Some of these scaling relations connect the photometric properties to the kinematic properties of passive galaxies, and were primarily used in the 80s as distance indicators to

infer distance of galaxy, given that luminosity and size are distance dependent (Dressler et al., 1987; Djorgovski & Davis, 1987). We now know that these scaling relations are useful tools to study the formation and evolution of passive galaxies, as different models predict very different evolution on these relations across redshift.

Faber & Jackson (1976) discovered a correlation between the luminosity L of passive galaxies and their stellar velocity dispersion σ , which can be expressed in the form $L \propto \sigma^4$. Kormendy (1977) subsequently pointed out a correlation between the galaxy surface brightness Σ and galaxy size R_e , known as the Kormendy relation. Note that this relation can be rearranged into a relation between L and R_e , as the mean surface brightness are currently often defined as $\Sigma = L/2\pi R_e^2$.

It was revealed later that the above two relations are two projections of a plane in three-dimensional space spanned by the surface brightness, size and velocity dispersion of passive galaxies, known as the fundamental plane (FP) (e.g. Dressler et al., 1987; Djorgovski & Davis, 1987). The FP has the following form:

$$\log(R_e) = a \log \sigma + b \log(\langle I_e \rangle) + c \quad (1.12)$$

where $\langle I_e \rangle$ is the mean surface brightness within R_e . The fact that passive galaxies lie on a tight plane was interpreted as evidence that they satisfy the virial equilibrium. At virial equilibrium, the virial theorem shows that the dynamical mass M follows $M/R_e \propto \sigma^2$, which predicts $a = 2$ and $b = -1$ for the FP.

Studies of large samples of passive galaxies in the field and clusters, however, found a significant deviation of a and b from the virial prediction (e.g. Jorgensen et al., 1996; Bernardi et al., 2003). This deviation, commonly refer to the ‘tilt’ of the plane, is thought to be mainly a result of variation in the mass-to-light ratio (M/L) of the stellar population with galaxy luminosity, potentially due to a variation in dark matter fraction with mass (see discussion in e.g. Forbes et al., 1998; Ciotti et al., 1996; Hyde & Bernardi, 2009), and/or a systematic variation of the stellar initial mass function (IMF). Additional contributions to the ‘tilt’ include rotational support and structural non-homology (e.g. Bender et al., 1994; Prugniel & Simien, 1997)

Aiming at including the effect of M/L , Hyde & Bernardi (2009) replaced the luminosity in the FP with stellar mass (known as the stellar mass fundamental plane) and the tilt from the virial prediction is reduced (see also Bolton et al., 2008). Cappellari et al. (2013) replaced the luminosity with dynamical mass (see also Scott et al., 2015) and found that the values derived in the mass-FP are consistent with virial predictions (see Cappellari, 2016, for a review).

At high redshift, while there are still ongoing debates on whether the FP is tilted compared to local passive galaxies (e.g Holden et al., 2010; Saglia et al., 2010), different studies agree on an evolution of the zero-point (c) of the plane with redshift, which is the result of the evolving (average) M/L of the galaxy population as the population is younger (e.g van Dokkum & van der Marel, 2007; Toft et al., 2012; Bezanson et al., 2013a; van de Sande et al., 2014). There has also been attempts to study the mass-FP (with stellar mass) at high redshift, although with small sample at $z > 1$, and they found minimal evolution compared to local passive galaxies (e.g. Bezanson et al., 2013a).

The study of the evolution of FP to higher redshift $z > 1$ is hindered by the fact that it is extremely difficult (and expensive in time) to obtain stellar velocity dispersion measurements for a large sample of high-redshift passive galaxies. One of the aim of our currently ongoing KMOS Cluster Survey (KCS) is to expand the sample at high redshift for FP studies and explore environmental dependencies (see Chapter 2 for a description). With a large sample of cluster galaxies at $z \sim 1.5$, the FP of the KCS clusters at $z \sim 1.5$ consistently shows an offset in the zero-point compared to those of the Coma cluster (e.g. Jørgensen et al., 2006) and enables a study of the mean M/L and formation age of the galaxy population at this redshift (Beifiori et al., 2016, in prep).

Another scaling relation that has become popular in recent years, especially for high redshift studies, is the stellar mass – size relation of passive galaxies (hereafter mass – size relations). The mass – size relation of local passive galaxies have been studied extensively in the local universe (e.g. Shen et al., 2003; Bernardi et al., 2011). Note that the mass – size relation is indeed a projection of the mass-FP. The study of the mass – size relation is often used to constrain galaxy evolution models, as it is directly related to the mass assembly of the passive galaxies. The mass – size relation is usually parametrised as a power law:

$$\log(R_e) = \alpha + \beta \log(M_*) \quad (1.13)$$

Shen et al. (2003) demonstrated that the mass – size relation of passive galaxies has a significant steeper slope ($\beta = 0.55$) than late-type galaxies ($\beta = 0.4$ for $\log(M_*/M_{sun}) > 10.6$, $\beta = 0.15$ for $\log(M_*/M_{sun}) < 10.6$). Bernardi et al. (2011, 2012) found that the mass – size relation shows curvature (also in other relations such as the colour – mass relation) at $\log(M_*/M_{sun}) \gtrsim 11.3$, but this curvature is not present if mass is replaced by σ . They interpreted this as an evidence of major dry mergers acting on these massive galaxies, which change the sizes and colour but leaving the velocity dispersion unchanged.

At high redshift, the study of the mass – size relation is usually limited to massive galaxies ($\log(M_*/M_{sun}) \geq 10.5$), partially due to surface brightness dimming, which corresponds to a mass completeness limit of the survey. Also note that at higher and higher redshift, the number density of low mass ($\log(M_*/M_{sun}) \leq 10.5$) passive galaxies is simply lower than at lower redshift, as we have discussed before. We left the discussion of the current findings from mass – size relation to the next section.

1.4 Size evolution in passive galaxies

One of the most important findings in galaxy evolution in recent years is the discovery of the remarkably small size of high-redshift passive galaxies. With *HST* imaging in rest-frame UV, it was first shown that massive passive galaxies with stellar masses $M_* \geq 10^{11} M_\odot$ at $z \sim 2$ have an effective radii R_e of only $\simeq 1$ kpc (e.g. Daddi et al., 2005; Trujillo et al., 2006a). Such massive yet compact objects are believed to be relatively rare in the local universe (e.g. Trujillo et al., 2009; Ferré-Mateu et al., 2012), yet the exact abundance is still under debate (Valentinuzzi et al., 2010b; Trujillo et al., 2012; Poggianti et al., 2013).

Many evidence point to the existence of a size evolution over cosmic time. Previous studies have attempted to quantify this evolution from different samples; most suggest that massive passive galaxies have grown by a factor of ~ 2 in size since $z \sim 1$ (e.g. Trujillo et al., 2006b; Longhetti et al., 2007; Cimatti et al., 2008; van der Wel et al., 2008; Saglia et al., 2010; Beifiori et al., 2014), and a factor of $\sim 3 - 4$ since $z \sim 2$ (e.g. Trujillo et al., 2007; Toft et al., 2007; Zirm et al., 2007; Buitrago et al., 2008; van Dokkum et al., 2008; Newman et al., 2012; Szomoru et al., 2012; Barro et al., 2013; van der Wel et al., 2014) through a comparison with local passive galaxies with comparable masses.

Initial possible biases regarding the observed evolution included a) overestimates of stellar masses in high redshift owing to uncertainties in the stellar population synthesis models and initial mass functions, b) underestimates of sizes due to surface brightness dimming and c) underestimates of sizes due to missing low-surface brightness components ascribed to the low throughput of near-IR detectors (e.g. Bezanson et al., 2009; Conroy et al., 2009; Muzzin et al., 2009; Mancini et al., 2010; Szomoru et al., 2011; Ryan et al., 2012). Nevertheless, subsequent dynamical mass measurements from spectroscopic data have independently demonstrated that the mass estimates are reliable (e.g. Cappellari et al., 2009; van de Sande et al., 2013; Belli et al., 2014a; Shetty & Cappellari, 2014). In addition, deep observation of a single galaxy by Szomoru et al. (2010) has confirmed the absence of the suggested low-surface brightness component. Recent size measurements with the *HST* infrared Wide Field Camera 3 (*HST*/WFC3) (e.g. Szomoru et al., 2011; van der Wel et al., 2012, 2014), which has superb near-IR sensitivity, have further established that the measured small sizes are genuine.

This progressive growth appears to happen mainly at the outer envelopes, as several works have shown that massive ($M_* \geq 10^{11} M_\odot$) passive galaxies at high redshift have comparable central densities to local ellipticals, suggesting that the mass assemble took place mainly at outer radii over cosmic time (i.e. the “inside-out” growth scenario, Bezanson et al., 2009; van Dokkum et al., 2010; Patel et al., 2013).

Currently the largest study on the evolution of mass – size relation for both passive and star-forming galaxies is from van der Wel et al. (2014), which utilizes data from the imaging and spectroscopic survey CANDELS (Grogin et al., 2011; Koekemoer et al., 2011) and 3D-HST (Brammer et al., 2012; Skelton et al., 2014). Figure 1.9 shows the mass – size relations of both passive and star-forming galaxies in the redshift range $0 < z < 3$ from van der Wel et al. (2014). They found that the slope of the mass – size relation for galaxies with $M_* \geq 3 \times 10^{11} M_\odot$ shows no evolution from $z \sim 3$ to 0 (with $\beta = 0.75$). The intercept of the relation (mean size at $M_* \geq 5 \times 10^{11} M_\odot$), on the other hand, show a very strong evolution with $R_e \propto (1 + z)^{-1.48}$, confirming the sizes evolve by a factor of ~ 3 from $z \sim 2$ to the local universe.

1.4.1 Does environment play a role?

In Section 1.2.3, we have described that in high density environments there are a lot of physical processes that can potentially quench and morphologically transform galaxies. A very important question, hence, is whether the environment have an effect on the sizes

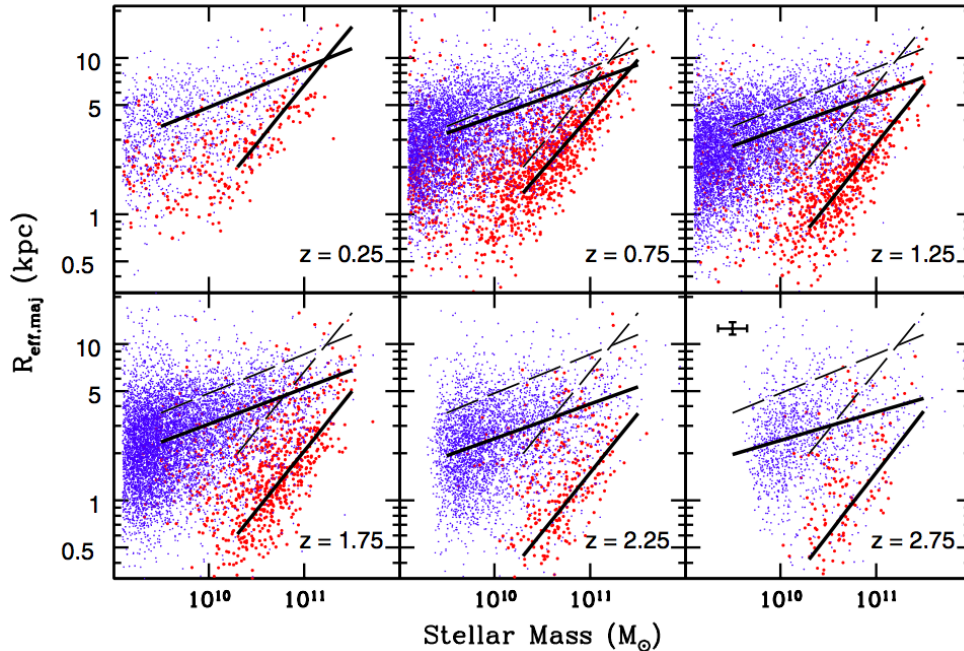


Figure 1.9: The stellar mass – size relation for early-type (red) and late-type galaxies (blue). The lines indicate model fits to the early- and late-type galaxies at each redshift. The dashed lines in each panel represent the model fits to the galaxies at redshifts $0 < z < 0.5$. Image taken from van der Wel et al. (2014).

(and size evolution) of passive galaxies.

Perhaps quite surprisingly, several studies have established that there is no obvious environmental dependence on passive galaxy sizes in the local universe by comparing the sizes in clusters, groups and the field (Guo et al., 2009; Weinmann et al., 2009; Taylor et al., 2010; Cappellari, 2013; Huertas-Company et al., 2013), although Valentinuzzi et al. (2010a) reported a significant number of massive compact galaxies in moderately massive (low σ) medium redshift clusters from the EDisCS survey and Poggianti et al. (2013) reported that galaxies (both passive and star-forming) in the field are generally larger than those in clusters.

On the other hand, at high redshift this is still under debate. Studies at high redshift show contrasting results, in part due to different definitions of environment and compactness, the use of different cluster / field samples for comparison or low number statistics. A number of works have found that sizes of passive galaxies are larger in clusters compared to the field, suggesting an accelerated size evolution in high density environments (e.g. Cooper et al., 2012; Zirm et al., 2012; Papovich et al., 2012; Lani et al., 2013; Strazzullo et al., 2013; Jørgensen & Chiboucas, 2013), although the magnitude of the effect is not yet clear and might depend on the cluster mass or richness (e.g. Jørgensen et al., 2014). Nevertheless, there were also reports at different redshifts showing cluster passive galaxies have no significant size difference with those in the field (e.g. Maltby et al., 2010; Rettura

et al., 2010; Newman et al., 2014), or even being smaller (e.g. Raichoor et al., 2012). A recent study from Delaye et al. (2014) analysed an ensemble of ~ 400 passive galaxies with $M_* \geq 3 \times 10^{11} M_\odot$ in nine clusters at $z \sim 1$. They found that although the median of the size distribution in cluster and the field shows no difference at different redshift, the shape of their size distributions are different; the size distribution in cluster shows an extended tail towards large sizes, which is not present in the field. Furthermore, they found that this difference is mainly driven by the galaxies in the mass range of $10.5 < \log(M_*/M_{sun}) < 11.0$ but not by the most massive population.

1.4.2 Physical processes resulting in size evolution

While the observational results start converging to the consensus that size evolution is genuine, the processes responsible for this evolution in sizes is not well understood. To explain the observed evolution, the physical processes invoked have to result in a large growth in size but not in stellar mass, nor drastic increase in the star formation rate.

The two most plausible candidates are mass-loss driven adiabatic expansion (“puffing-up”) (e.g. Fan et al., 2008, 2010; Ragone-Figueroa & Granato, 2011) and dry mergers scenarios (e.g. Bezanson et al., 2009; Naab et al., 2009; Trujillo et al., 2011).

In the former scenario, the AGN or supernovae feedback trigger galactic wind in the galaxy which drives a mass loss from the centre. This results in a change in the gravitational potential, which then leads to an expansion in size when the galaxy reaches a new equilibrium.

In the merger scenario, there are two types of mergers that are being considered: major mergers and minor mergers. Major mergers involve merging with another galaxy of comparable mass, while minor mergers involve accretion of low mass companions. Mergers can be further classified to ‘dry’ or ‘wet’ based on the gas content of the galaxy being merged, in the case of size evolution of passive galaxies, the proposed mergers (no matter major or minor) have to be dry (gas-poor) to keep the low star formation rate (Trujillo et al., 2011).

Nevertheless, major mergers are not compatible with the observed growth in mass function in clusters as well as the observed major merger rates since $z \sim 1$ (e.g. Nipoti et al., 2003; Bundy et al., 2009), as to produce the observed growth in size they need to also significantly increase the mass. On the other hand, minor mergers are able to produce an efficient size growth (see e.g. Trujillo et al., 2011; Shankar et al., 2013). The question is then whether the rate of minor mergers are enough to produce the observed growth. The rates of minor mergers are roughly enough to account for the size evolution only up to $z \lesssim 1$ (e.g. Kaviraj et al., 2009; Newman et al., 2012; Belli et al., 2014a), at $z \sim 2$ additional mechanisms are required (e.g. AGN feedback-driven star formation, Ishibashi et al., 2013).

One additional effect that further complicates the interpretation is the ‘progenitor bias’, which is the effect of continual quenching of galaxies onto the red sequence as well as morphological mixing (e.g van Dokkum & Franx, 2001). Several studies have examined the effect of ‘progenitor bias’ and show it has non-negligible effect on the size evolution (e.g. Saglia et al., 2010; Valentini et al., 2010a; Carollo et al., 2013; Poggianti et al.,

2013; Beifiori et al., 2014; Delaye et al., 2014; Shankar et al., 2015; Fagioli et al., 2016). It, however, cannot fully explain the size evolution (e.g. Belli et al., 2015). For clusters, abovementioned processes that are specific in high density environment such as harassment, strangulation and ram-pressure stripping (e.g. Treu et al., 2003; Moran et al., 2007) might play an important role in quenching and morphologically transforming galaxies, which increases the effect of ‘progenitor bias’ at low redshift.

1.5 Colour gradients in passive galaxies

In addition to size or structural parameter measurements, colour gradients also provide valuable information for disentangling the underlying physical processes involved in the evolution of passive galaxies, and have been used as tracers of stellar population properties and their radial variation.

The colour gradients in passive galaxies have been known for decades and are widely studied in the local universe (e.g. de Vaucouleurs, 1961; Peletier et al., 1990b). The colour gradient is generally defined as the logarithmic gradient in colour, hence the colour gradient measured with band A and B will have the following form:

$$\nabla_{A-B} = \frac{d(A-B)}{d \log(R)} \quad (1.14)$$

Studies of local passive galaxies show that they generally display negative colour gradients, which means that the outskirts of the galaxy has a bluer colour (e.g. Franx et al., 1989; Peletier et al., 1990b; Idiart et al., 2002). The colour gradient, similar to the global colour, is believed to be due to variations of the stellar population properties, such as age and metallicity. Similarly, the interpretation of the colour gradient is complicated by the age-metallicity degeneracy as well as dust (see Section 1.2.2).

Because of the degeneracy, the colour gradients in passive galaxies are mostly interpreted as either age gradients at fixed metallicity or metallicity gradients at fixed age, which is given as

$$\nabla_{age} = \frac{d \log(\text{age})}{d \log(R)}, \quad \nabla_Z = \frac{d \log(Z)}{d \log(R)} \quad (1.15)$$

Hence the values of the derived gradients depend strongly on the assumption one has made. For example, Peletier et al. (1990b) found a metallicity gradient of ~ -0.2 , assuming the age is uniform throughout the galaxies. With the help of stellar population models, Saglia et al. (2000) found that the colour gradients in a sample of cluster galaxies at $z \sim 0.4$ are more likely to be a result of metallicity gradients than age gradients, which is supported also by later works (e.g. La Barbera et al., 2005; Tortora et al., 2010). The average metallicity gradient is found to be of $\nabla_Z \approx -0.1$ to -0.3 , while the age gradients are consistent with 0 or slightly positive (e.g. Wu et al., 2005; La Barbera & de Carvalho, 2009). This is consistent with values derived by resolved absorption line indices analysis (e.g. Mehlert et al., 2003; Kuntschner et al., 2010; Greene et al., 2013; González Delgado et al., 2014; Oliva-Altamirano et al., 2015; Wilkinson et al., 2015).

Measuring the colour gradients in passive galaxies at high redshift is more challenging due to their compact sizes, as well as limitations on instrumental angular resolution. Limited number of works have shown that passive galaxies at high redshift also appear to have negative colour gradients (e.g. Wuyts et al., 2010; Guo et al., 2011; Szomoru et al., 2011; Chan et al., 2016). Nevertheless, the strength of the gradients and their evolution are still not clear. Guo et al. (2011) studied the colour gradients in $(U - V)$, $(U - B)$ and $(B - V)$ of six massive galaxies with $M_* > 10^{10} M_\odot$, and found a hint of steeper colour gradients at $z \sim 2$ compared to the local ones. By contrast, Szomoru et al. (2011) measured the $(u - g)$ colour gradients of 16 massive galaxies at redshift $z \sim 2$ and compared with a sample of ~ 100 galaxies in the redshift range $0 < z < 1$. They reported that the average colour gradients are constant with redshift within the uncertainties.

1.5.1 From light-weighted to mass-weighted structural parameters

Due to the abovementioned colour and M_*/L gradients within the galaxies, the size of the galaxies measured from surface brightness profiles (i.e. luminosity-weighted sizes) is not always a reliable proxy of the stellar mass distribution, and is dependent on the filter band of the image. If the colour gradient is steeper at high redshift (as suggested by Guo et al., 2011), this may bias the size measurements of passive galaxies and subsequently affects the derived size evolution, or comparison between different environment.

As a result, measuring characteristic sizes of the stellar mass distribution (i.e. mass-weighted sizes) is preferable over the wavelength dependent luminosity-weighted sizes. Recently a number of works attempted to reconstruct stellar mass profiles taking into account the M_*/L gradients. Two techniques have been primarily used: resolved spectral energy distribution (SED) fitting (e.g. Wuyts et al., 2012; Lang et al., 2014) and the use of a scaling M_*/L - colour relation (e.g. Bell & de Jong, 2001; Bell et al., 2003).

In the former, stellar population modeling is performed on resolved multi-band photometry to infer spatial variations in the stellar population in two-dimensions. A binning technique is first applied on the images in a single band, then the same binning is applied to images in all bands to obtain an SED in each bin. SED modelling is then performed on each bin to derive M_*/L (Wuyts et al., 2012). While this is a powerful way to derive resolved properties, deep and high-resolution multi-band imaging are required to well constrain the SED in each resolved region, which is not available for most datasets.

The latter method, demonstrated by Zibetti et al. (2009) and Szomoru et al. (2013), relies on an empirical relation between M_*/L and colour to determine the spatial variation of M_*/L . The existence of such a relation is due to the fact that the variation in stellar population properties (i.e., changes in stellar age, metallicity, and dust content) all produce roughly the same effects in the M_*/L - colour plane (Bell & de Jong, 2001). Nevertheless, it is important to pick a colour that is sensitive to changes in these stellar population properties to maximise the dynamic range of colour versus M_*/L , a common approach is to pick a colour that straddle the 4000\AA break. Since the M_*/L - colour relation is

degenerate between age, dust and metallicity, this method cannot provide information on these properties as in resolved SED modelling. Nevertheless, it provides a relatively inexpensive way to study the stellar mass distribution of galaxies.

1.6 Outline of this thesis

In this thesis, we analyse the structural and photometric properties of a sample of passive galaxies in clusters at $1.39 < z < 1.61$, as part of the ongoing KMOS Cluster Survey (KCS). The goal is to study the properties of high redshift cluster galaxies and compare them with the field population, to dissect the effect of environment and constraint the formation and evolution of this population.

This thesis is organised as follows. In Chapter 2, we describe the outline of the KMOS Cluster Survey, including the cluster sample, the data reduction of the *HST* imaging, as well as the selection of the galaxy sample. We also describe the local sample we used throughout this thesis to compare with the KCS cluster galaxies. At the end of the chapter, we provide a catalogue of the photometry of the cluster sample.

In Chapter 3, we focus on the methods we used to derive the photometric properties of the cluster galaxies from the images and the subsequent analysis. The procedure to derive structural parameters, resolved stellar mass surface density maps and colour gradients are described. In this chapter, we also examine the reliability of our derived parameters with simulated galaxies and present the findings. We also provide a catalogue of the photometric properties of the cluster sample.

We present the main results in Chapter 4 and Chapter 5. In Chapter 4 we focus on the structural parameters of the cluster galaxies and the mass–size relations, while Chapter 5 is mainly focused on the analysis of the colour gradients of the KCS cluster galaxies.

Finally, in Chapter 6, we summarise the results of this work and describe the future prospects and possible works on the KCS passive galaxies.

Throughout the thesis, we assume the standard flat Λ CDM cosmology with $\Omega_\Lambda = 0.7$, $\Omega_m = 0.3$ and $H_0 = 70 \text{ km s}^{-1} \text{ Mpc}^{-1}$. Magnitudes quoted are in the AB system (Oke & Gunn, 1983). The stellar masses in this paper are computed with a Chabrier (2003) initial mass function (Chabrier IMF). Quoted published values are transformed to Chabrier IMF when necessary.

Chapter 2

The KMOS Cluster Survey

In this chapter we introduce the background of the KMOS-Cluster GTO Survey. We start with an outline of the survey, followed by a description of the individual clusters in the KMOS cluster sample. The focus of this thesis is mainly on the photometry part of the program, from the reduction of the *Hubble Space Telescope* (*HST*) data and build up of the photometric catalogues for the KMOS observations, to the derivation of photometric properties. In Section 2.3 and 2.4 we describe the data reduction of both new and archival *HST* imaging¹ and the construction of photometric catalogues. We then introduce briefly the ongoing KMOS observations and spectroscopic data in Section 2.6.

2.1 Outline of the KMOS Cluster Survey

The KMOS Cluster Survey (KCS) is one of the ongoing guaranteed time observation (GTO) programs with the new generation IR integral field spectrograph, *K*-band Multi-Object Spectrograph (KMOS), at the Very Large Telescope (VLT) on the Cerro Paranal in Chile (Davies et al., 2015, Davies, Bender et al., 2016 in prep, Beifiori et al., 2016, in prep). The main goal of this program is to characterise the evolution of kinematics and stellar populations of galaxies in dense environments at high redshift ($z \sim 1.5$).

The KCS can be roughly divided into two main parts, spectroscopy and photometry. We derived (or are currently deriving) stellar velocity dispersions, structural parameters, colour gradients, resolved stellar masses and other measurements of a homogenous sample of passive galaxies residing in high density environment at redshift $1.4 < z < 1.8$. With these quantities, we are able to address science topics including but not limited to the following:

- The evolution of size and velocity dispersion in high density environment and the underlying physical processes from scaling relations.

¹This work is based on observations made with the NASA/ESA HST, which is operated by the Association of Universities for Research in Astronomy, Inc., under NASA contract NAS 5-26555. These observations are associated with program ID13687 as well as with the CANDELS Multi-Cycle Treasury Program.

- The evolution of colour gradients as a probe of the stellar populations over redshift (Chan et al., 2016, Chan et al., 2017, in prep).
- Stellar population properties from spectral fitting or indices on stacked spectrum of a population of passive galaxies.
- The fundamental plane (FP) and the evolution of age, metallicity and size along the FP, and the evolution of dynamical M/L (Beifiori et al., 2016, in prep).
- The formation history and evolutionary path of passive galaxies through comparison with existing evolutionary models.
- The effect of environment on the properties of passive galaxies through comparison with our complementary survey VIRIAL (Mendel et al., 2015) and other similar field surveys at high redshift.

One of the strength of KCS is the deep absorption line spectroscopic study enabled by KMOS, a multi-object spectrograph. Currently there is a lack of a large and complete samples of stellar velocity dispersions at $z > 1$ due to limitations of available facilities. The sample of stellar velocity dispersions in the redshift range $1.4 < z < 2$ are limited to 23 galaxies, including mostly bright and relatively blue galaxies in the field (e.g. Belli et al., 2014a,b; van de Sande et al., 2013, 2014). This is because an extremely long exposure time (of the order of ~ 10 hrs for $S/N > 10$) is required to obtain spectra of high redshift passive galaxies due to their low surface brightness and small sizes. This quickly escalates to an unfeasible amount of time to build up a statistical sample.

With its multiplexing capability, KMOS is perfect for conducting this kind of survey. As a 2D multi-object spectrograph, KMOS hosts 24 configurable arms linked to respective integral field units (IFU), which enable observers to target 24 objects within the field of view simultaneously. The size of the KMOS patrol field ($7.2'$ in diameter) can cover the extent of the core of high redshift clusters on the sky. These advantages can bring an order of magnitude increase in observing efficiency. Compared to traditional slit spectroscopy, the 2D IFU nature of KMOS eliminates spectroscopic slit losses. The extent of each IFU is $2.8'' \times 2.8''$, which is generally larger than the size of passive galaxies at $z \sim 1.5$ and hence allows us to collect most of their fluxes within the IFU. The high sensitivity of the NIR detectors in KMOS also boosts the observing efficiency and allows us to perform deep spectroscopic observation in a homogenous way for a relatively large sample of galaxies.

The deep KMOS observations for absorption line spectroscopy of KCS is almost complete. In current as well as coming semesters, we will additionally target star-forming galaxies in the KCS clusters to spatially map their emission lines (such as $H\alpha$ and [NII]), in order to trace the star formation, gas phase metallicity and map the kinematics of the galaxies. Together with the absorption line spectroscopy of passive galaxies in the clusters this will give us a holistic view of the KCS clusters at $1.4 < z < 2$.

We describe the KCS sample and data below. Since my focus is mainly on the photometry part of the program, we will describe in detail the methods of deriving photometric

properties and structural parameters in Chapter 3. On the other hand, brief descriptions of the KMOS observations, data reduction and summary are given in Section 2.6. The interested reader is referred to the quoted reference for further information.

2.2 The KMOS Cluster Sample

The sample of KCS comprises a total of ~ 75 galaxies, of which 56 are passive, in four main overdensities at $1.39 < z < 1.8$. The clusters are XMMU J2235-2557 at $z = 1.39$, XMMXCS J2215-1738 at $z = 1.46$, Cl 0332-2742 at $z = 1.61$ and JKCS 041 at $z = 1.80$, and a backup cluster at lower redshift, RCS 234526-3632.6, at $z = 1.04$.

These clusters are selected to have a significant amount of archival data, spanning from multi-band *HST* imaging to deep ground-based imaging, in order to derive structural parameter and multi-band photometry. They are also selected to have a large number of spectroscopically confirmed members, which helps to maximise the selection and observing efficiency by removing objects with strong contamination from sky emission or telluric absorption on desired spectral features.

2.2.1 XMMU J2235-2257

The cluster XMMU J2235-2257 was serendipitously detected in an X-ray observation of NGC 7314, a nearby galaxy by *XMM-Newton* and discovered by Mullis et al. (2005). They acquired images with VLT/FORS2 *R* and *z*-bands and ISAAC *K_s*-band and revealed a population of red galaxies spatially coincident with the peak of the extended X-ray observation. Using VLT/FORS2 spectroscopic data of 12 galaxies, Mullis et al. (2005) confirmed the redshift of the cluster to be $z \sim 1.39$ and derived the velocity dispersion of the cluster to be $762 \pm 265 \text{ km s}^{-1}$. Subsequent follow up VLT/FORS2 spectroscopy by Rosati et al. (2009) confirmed the cluster membership of 34 galaxies. Among them 16 within the central 1 Mpc are passive. Using Chandra data they inspected the X-ray surface brightness profile of this cluster out to 500 kpc and revealed an excess of X-ray emission in the centre, a common characteristic of cool core cluster (see Section 1.1.4 for a description of cool core clusters). The presence of cool core is commonly referred to a signature of being in a dynamically relaxed state (see the discussion in e.g. Santos et al., 2008). Assuming hydrostatic equilibrium, they measured an X-ray mass within $r < 1 \text{ Mpc}$ to be $(5.9 \pm 1.3) \times 10^{14} M_{\odot}$. On the other hand, Jee et al. (2009) performed a weak-lensing analysis on this cluster and reported a substantial lensing signal at $\gtrsim 8\sigma$ level. They estimated the projected mass of the cluster within $r < 1 \text{ Mpc}$ to be $(8.5 \pm 1.7) \times 10^{14} M_{\odot}$. A revised study of Jee et al. (2011) estimated the M_{200} to be $\sim 7.3 \times 10^{14} M_{\odot}$.

Being one of the most massive clusters seen at high redshift, XMMU J2235-2257 has attracted some attention in the community. Several studies attempt to study the stellar population in the galaxy population using optical colours and colour-magnitude relations and agreed on an early formation epoch of the high mass end of the galaxy population in this cluster (e.g. Lidman et al., 2008; Rosati et al., 2009; Strazzullo et al., 2010). The

presence of the high mass end in the stellar mass function of this cluster also indicates it is already at a very evolved mass assembly stage (Strazzullo et al., 2010).

Bauer et al. (2011) studied the star formation in this cluster and found a correlation between SFR and distance from the cluster centre, suggesting the star formation is shut off within $r < 200$ kpc. Grützbauch et al. (2012) extended the star formation study out to a projected radius of 1.5 Mpc and found that all massive galaxies have low specific star formation rates, and galaxies in the cluster centre have lower specific star formation rates than the rest of the cluster galaxies at fixed stellar mass.

For the galaxy structural properties, this cluster has been investigated by Strazzullo et al. (2010) and was also included in the cluster sample of Delaye et al. (2014), De Propris et al. (2015) and De Propris et al. (2016). They showed that the average galaxy size in XMMU J2235-2257 is smaller than expected from local stellar mass-size relation, we will study the structural properties of XMMU J2235-2257 in Chapter 4.

2.2.2 XMMXCS J2215-1738

The cluster XMMXCS J2215-1738 was discovered in the *XMM* Cluster Survey (Stanford et al., 2006). It was initially detected as an extended source in the X-ray observation of the quasar LBQS 2212-1759. Spectroscopic follow up with Keck DEIMOS revealed 6 galaxies at redshift $z \sim 1.45$, confirming the redshift of the cluster (Stanford et al., 2006). The cluster has an X-ray temperature of ~ 4.1 keV based on a joint analysis of Chandra and *XMM-Newton* data (Hilton et al., 2010), which corresponds to a X-ray mass of $M_{200} \sim 2.1 \times 10^{14} M_{\odot}$ (Stott et al., 2010). The weak lensing study by Jee et al. (2011) estimated the weak lensing mass of this cluster to be $M_{200} \sim 4.3 \times 10^{14} M_{\odot}$. With additional spectroscopy from DEIMOS, VLT/FORS2 (Hilton et al., 2007, 2009) and GMOS, Hilton et al. (2010) derived the velocity dispersion of the cluster to be 720 ± 110 km s⁻¹, they also observed a bimodality in the velocity distribution of the 44 confirmed members. This together with the fact that XMMXCS J2215-1738 is under-luminous in X-ray (i.e. with X-ray luminosity lower than expected by the local $L_X - T$ relation) suggests this cluster is probably not virialized (Hilton et al., 2007; Ma et al., 2015).

Contrary to XMMU J2235-2557 and most local clusters, XMMXCS J2215-1738 does not have a clear brightest cluster galaxy (BCG) and in general shows a lack of bright galaxies within the cluster. Hilton et al. (2009) studied the colour magnitude relation of the early type galaxies in this cluster and found that it has a huge intrinsic scatter, about three times greater than the scatter measured in the Coma cluster. They also studied the star formation in this cluster using mid-IR imaging from *Spitzer* and detected eight $24 \mu\text{m}$ sources in the core of the cluster, which three of them are within 2.3σ of the red sequence in the colour magnitude relation. With SED fitting they revealed that most of these objects have high star formation rates that are obscured by dust, which suggests that XMMXCS J2215-1738 has a significant amount of obscured star formation in the core (Hilton et al., 2010).

Similarly, using Subaru Suprime-Cam and Multi-object Infrared Camera and Spectrograph (MOIRCS) narrow-band and broad band imaging, Hayashi et al. (2010) identified

44 [O II] emitters in this cluster and derived their SFRs from the [O II] fluxes, which suggests substantial star formation activities even at the core of the cluster, although with the caveat that these derived SFRs can suffer from uncertainties due to dust obscuration. A subsequent wide-field imaging and spectroscopic survey of [O II] emitters of this cluster confirmed the cluster membership of some of these [O II] emitters, and the SEDs of those on the red sequence resemble passive galaxies with AGNs (Hayashi et al., 2011). They argued that the cluster has experienced high star-forming activity at rates comparable to the field at $z \sim 1.4$ and the contribution from AGN is not negligible. A recent search of dust-obscured ultra luminous infrared galaxies (ULIGS) with SCUBA-2 provides further evidence of star formation in the cluster core (Ma et al., 2015). They detected eight probable submillimeter galaxy candidates within the virial radius of the cluster ($\sim 0.8\text{Mpc}$) and computed SFR using dust thermal emission in the FIR and submillimeter bands. The existence of substantial star formation throughout XMMXCS J2215-1738 together with the hints that this cluster is not virialized may indicate that the cluster is dynamically disturbed (Hilton et al., 2010) and is not as mature as XMMU J2235-2257.

For the galaxy structural properties, this cluster was also included in the cluster sample of Delaye et al. (2014). We will study the structural properties in Chapter 4.

2.2.3 Cl 0332-2742

The cluster Cl 0332-2742 at $z = 1.61$ is particularly interesting as it is one of the few high redshift cluster detected by clustering in the redshift space, as opposed to extended X-ray emission (e.g. XMMU J2235-2557 and XMMXCS J2215-1738) or photometry of the red cluster members (e.g. RCS234526-3632.6 in Section 2.2.5). Cl 0332-2742 was discovered and spectroscopically confirmed from the Galaxy Mass Assembly ultra-deep Spectroscopic Survey (GMASS), a spectroscopic survey targeting photometric redshift selected galaxies ($z_{phot} > 1.4$) in the Great Observatories Origins Survey (GOODS) Southern field (hereafter GOODS-S, Giavalisco et al., 2004) using VLT/FORS2. Prior to GMASS, Castellano et al. (2007) reported the discovery of this structure as a localised density peak based on three-dimensional galaxy density computed using photometric redshifts from the GOODS-MUSIC catalogue (Grazian et al., 2006). From the GMASS sample and other existing sources, Kurk et al. (2009) found 42 galaxies lying in the redshift range $1.600 < z < 1.622$, which are plausibly members of the cluster. The velocity dispersion of the cluster is estimated to be $440 \pm 59 \text{ km s}^{-1}$. Assuming the structure is virialized, they derived the virial mass of the cluster to be $M_{vir} = 9 \times 10^{13} M_{\odot}$.

Nevertheless, the cluster members show a bimodal distribution in redshift space, it is possible that the structure is indeed two smaller groups, one at $z = 1.603$ and the other with redshift $z = 1.611$ (Kurk et al., 2009), albeit with no clear evidence of spatial separation. They suggested these groups represent a sheet-like structure in the cosmic web and hence not yet an evolved cluster. Kurk et al. (2009) also reported that this cluster has no clear bright extended X-ray source (with upper limit $3.5 \times 10^{43} \text{ erg s}^{-1}$) around the main region of the cluster. With deeper Chandra data, Tanaka et al. (2013) recently reported the discovery of extended X-ray emission in a region coinciding with one of the

substructure in Cl 0332-2742, off-centered from the Kurk et al. (2009) high-density peak. A concentration of red galaxies at $z \sim 1.61$ were found around this extended X-ray emission. Tanaka et al. (2013) confirmed this (sub)structure as a gravitationally bound X-ray group. They measured the X-ray mass of the group to be $(3.2 \pm 0.8) \times 10^{13} M_{\odot}$, making it the lowest mass group confirmed at $z > 1.5$. This strengthens the suggestion that Cl 0332-2742 is a (proto)cluster still in its age of assembly and comprises several interacting group structures.

Despite this, Cl 0332-2742 has a clear modality in the colour-magnitude relation and hence has a well defined red sequence (Kurk et al., 2009). The stacked spectrum of seven red galaxies in this cluster shows relatively young age (~ 1 Gyr), very low specific star formation rates ($< 3 \times 10^{-2} \text{ Gyr}^{-1}$) and very low dust extinction Cimatti et al. (2008). With *HST*/ACS z -band imaging, Cimatti et al. (2008) derived the sizes of these galaxies using GALFIT and found that they are systematically smaller compared to the local mass-size relation. Similarly, the members in the Tanaka et al. (2013) group have low star formation rates ($\ll 1 M_{\odot} \text{ yr}^{-1}$) and small sizes, but also a high fraction of AGNs: 3 out of 8 of the group members host AGNs.

2.2.4 JKCS 041

JKCS 041 at $z = 1.80$ is the highest redshift cluster included in our KCS sample. In this thesis, we only focus on the result of the cluster XMMU J2235-2557, XMMXCS J2215.9-1738 and Cl 0332-2742. We describe the possible future work on this cluster in Section 6.2.2. Hence, for completeness we describe also the properties of this cluster.

Initially detected in the UKIRT Infrared Deep Sky Survey (UKIDSS) as a population of sources of similar $J - K$ colour using a modified red-sequence method, JKCS 041 was detected as an extended X-ray source in the follow-up Chandra observations (Andreon et al., 2009). Andreon et al. (2014) derived the mass of this cluster using various methods (e.g. using the L_X -mass relation or the gas mass) and found consistent mass estimates of $M_{200} \sim 2 - 3 \times 10^{14} M_{\odot}$. With *HST*/WFC3 imaging and grism spectroscopy, Newman et al. (2014) confirmed the redshift of the cluster to be $z = 1.80$ and the cluster membership of 19 galaxies, of which 15 are quiescent galaxies.

This cluster has a very prominent red sequence down to $\log(M/M_{\odot}) = 9.8$. The red sequence galaxies are concentrated towards the cluster centre and coincide with the extended X-ray emission (Andreon et al., 2014). Newman et al. (2014) studied the stellar population of the quiescent members through SED fitting of the grism spectroscopy, the quiescent members have an average luminosity-weighted age of ~ 1 Gyr and span a very similar range of ages in the field at this redshift. They derived the sizes of these galaxies using GALFIT and found that the sizes are smaller compared to local passive galaxies. In addition, Newman et al. (2014) reported there is no significant difference in the sizes and mass density profiles of passive galaxies in JKCS 041 compared to the field. The axis ratio of the galaxies in JKCS 041, on the other hand, seems to be less disky than the field; JKCS 041 has a lower fraction of disk-like systems compared to the field galaxies at a similar redshift.

2.2.5 Backup cluster - RCS 2345-3632

Beside the four main clusters, there is an extra cluster, RCS 2345-3632, in the KCS sample acting as a observation backup when the observing conditions at the VLT become unfavourable for the other clusters. For example, strong northerly wind would prevent us from observing clusters at high declination at Paranal. Currently there is a lack of observation in the redshift range $0.9 < z < 1.2$. Being at redshift $z \sim 1.04$, this cluster allows us to bridge the observations to lower redshift studies.

As one of the cluster discovered in the red cluster survey (Gilbank et al., 2007, 2011), RCS 2345-3632 is an optically rich cluster with 34 spectroscopic confirmed members (combining catalogues from Gilbank et al., 2007; Meyers et al., 2010). It has a dynamical velocity dispersion of $670 \pm 190 \text{ km s}^{-1}$. Jee et al. (2011) estimated the weak lensing mass of the cluster to be $M_{200} = 2.4 \times 10^{14} M_{\odot}$. The cluster was also included in the cluster sample of Delaye et al. (2014).

2.3 *HST* Data and Data Reduction

In this section we provide a summary of the *HST* data of the KCS clusters used in this work and describe the procedure of the data reduction. As we explain in Section 1.3.1, the main difficulty of studying the structural parameter of galaxies at high redshift comes from their small sizes which are often unresolved in most seeing-limited ground-based images. *HST* data is therefore crucial to our study as we require high resolution imaging in two (or more) bands to reliably trace the structure and study the colour gradients of these cluster galaxies. The red IR WFC3 bands allow us to trace the stellar components at rest-frame optical wavelengths and the optical ACS bands provide information at rest-frame wavelengths bluer than the 4000Å break.

2.3.1 Summary of the *HST* data sets

We make use of both new and archival deep optical and near-infrared *HST* imaging of the clusters. The optical imaging are obtained with ACS Wide Field Camera (WFC). The ACS/WFC detector has two 4096×2048 charge-coupled devices (CCDs), chip 1 and 2, providing a total area of 4096×4096 pixels. It has a native pixel scale of $\sim 0.05'' \text{ pixel}^{-1}$ and covers a field of view of $202'' \times 202''$. On the other hand, the near-infrared imaging are obtained using the Wide Field Camera 3 IR imager (WFC3/IR). The IR detector is a 1024×1024 HgCdTe array, of which the central 1014×1014 pixels are useful for imaging. It covers a field of view of $136'' \times 123''$ with a native pixel scale of $\sim 0.128'' \text{ pixel}^{-1}$.

Table 2.1 summaries the *HST* data of the three clusters and the backup cluster in various bands. XMMU J2235-2557 was observed in June 2005 (GTO-10698), July 2006 (GO-10496) and April 2010 (GO/DD-12051). The archival ACS data are mostly from a program (GO-10496) designed to search for Type Ia supernovae in galaxy clusters (Dawson et al., 2009), while the archival WFC3/ data are from a calibration program (GO/DD-12051) aiming at cross-calibrating the zero point of WFC3 and the Near Infrared Camera

and Multi-object Spectrometer (NICMOS). The *HST*/ACS data consist of F775W and F850LP bands (hereafter i_{775} and z_{850}), while the WFC3 data comprise four IR bands, F105W, F110W, F125W and F160W (hereafter Y_{105} , YJ_{110} , J_{125} and H_{160}). The YJ_{110} data are not used in this study as they have a shorter exposure time. The WFC3 data have a smaller field of view than the ACS data, $145'' \times 126''$, correspond to a region of ~ 550 kpc from the cluster centre.

The ACS data of XMMXCS J2215-1738 are also from program GO-10496 and consist of F775W and F850LP bands, observed during the period of April to August 2006. The F775W data are not used due to its short exposure time. The IR data of this cluster come from our new Cycle 22 WFC3 observation (GO-13687) observed in June 2015, designed to study particularly the structural parameters and colour gradients of KCS cluster galaxies. Our new WFC3 data comprise three IR bands, F125W, F140W, F160W (hereafter J_{125} , JH_{140} and H_{160}), which are selected to study the properties at the same rest-frame wavelength as other clusters. Similar to XMMU J2235-2557, the WFC3 data provide the limiting field of view of $136'' \times 123''$.

Cl 0332-2742 is part of the WFC3 Early Release Science (ERS) field within the GOODS-S field (Windhorst et al., 2011). *HST* data is publicly available from the CANDELS (Grogin et al., 2011; Koekemoer et al., 2011)² and 3D-HST programs (Brammer et al., 2012; Skelton et al., 2014)³. We make use of the *HST*/ACS and WFC3 mosaics reduced by the 3D-HST team, which incorporates all the available *HST* observations in the GOODS-S field. Of all the available imaging we mainly use the ACS F850LP, WFC3 F125W and F160W for the structural parameter measurements, but we also use the photometry from the public released v1.0 CANDELS ACS F814W mosaics included in the 3D-HST photometry catalogue. Details of the mosaics and catalogues are described in Koekemoer et al. (2011) and Skelton et al. (2014).

For the backup cluster RCS 2345-3632, there are also ACS data from program GO-10496 and consist of F775W and F850LP bands, observed during the period of June to August 2006. Our Cycle 22 WFC3 observation (GO-13687) also comprises IR data for this cluster in F105W and F160W bands, obtained in November 2015. Although we will not discuss the backup cluster in this thesis, the data are reduced as the other WFC3 data in the two clusters. The future work on this cluster is described in Section 6.2.2.

2.3.2 *HST* data reduction

We reduce the *HST* data for the cluster XMMU J2235-2557 and XMMXCS J2215-1738, for Cl 0332-2742 we make use of the publicly available 3D-HST mosaics. We start with downloading the calibrated images (`_flt.fits`), association tables (`_asn.fits`) and calibration

²This work is based on observations taken by the CANDELS Multi-Cycle Treasury Program with the NASA/ESA HST, which is operated by the Association of Universities for Research in Astronomy, Inc., under NASA contract NAS5-26555.

³This work is based on observations taken by the 3D-HST Treasury Program (GO 12177 and 12328) with the NASA/ESA HST, which is operated by the Association of Universities for Research in Astronomy, Inc., under NASA contract NAS5-26555.

Table 2.1: Summary of the *HST* imaging of the KCS clusters used in this study.

Cluster	Name	Filter	Rest-frame pivot wavelength (\AA)	Exposure time (s)
XMMU J2235-2557	i_{775}	ACS F775W	3215.2	8150
	z_{850}	ACS F850LP	3776.1	14400
	Y_{105}	WFC3 F105W	4409.5	1212
	J_{125}	WFC3 F125W	5217.7	1212
	H_{160}	WFC3 F160W	6422.5	1212
XMMXCS J2215-1738	z_{850}	ACS F850LP	3673.2	16935
	J_{125}	WFC3 F125W	5075.6	2662
	JH_{140}	WFC3 F140W	5659.8	1212
	H_{160}	WFC3 F160W	6247.6	1312
Cl 0332-2742	z_{850}	ACS F850LP	3462.1	2837*
	J_{125}	WFC3 F125W	4783.9	1430*
	H_{160}	WFC3 F160W	5888.5	1518*
RCS 2345-3632 (KCS backup)	i_{775}	ACS F775W	3771.6	4890
	z_{850}	ACS F850LP	4429.5	10020
	Y_{105}	WFC3 F105W	5172.5	3923
	H_{160}	WFC3 F160W	7533.8	1362

* Average exposure time in the section of the GOODS-S field where Cl 0332-2742 resides, derived using the exposure maps in each band.

reference files of the two clusters from the Mikulski Archive for Space Telescopes (MAST) archive⁴. The fit images are data products of the `calacs` (for ACS data) or `calwfc3` (for WFC3 data) pipeline, which processes data on the fly and applies all the standard calibrations to the raw data, including dark current subtraction, a linearity correction and flat fielding, as well as an initial identification of cosmic rays. For the WFC3/IR data each fit image consists of five extensions: the science image (SCI), the error array (ERR), the data quality array (DQ), the number of samples array (SAMP) and the integration time array (TIME). For the ACS/WFC data, besides the science (SCI), error (ERR) and data quality array (DQ) for each chip, there are also several correction extensions that save the tabular data of the corrections applied. The details of the calibration steps applied by `calacs` and `calwfc3` are described in the ACS data handbook (Lucas, 2016) and WFC3 data handbook (Deustua, 2016). The calibration reference files include images (e.g. bias and dark) and reference tables used in `calacs` and `calwfc3`. They also include information that are occasionally required in combining the data, such as the image distortion coefficient table which provides a conversion from the (distorted) detector space to the undistorted space.

The *HST* observations are obtained with dithering, in order to alleviate the effects of bad pixels and hot pixels on the detector as well as to provide sub-pixel sampling. Each exposure within a single visit is spatially offset with a small shift (i.e. “dithered” between each other). The association tables provide information of this dithering between exposures and the used pattern. The WFC3 data we used here were obtained using the default WFC3/IR dither pattern `WFC3-IR-DITHERBOX-MIN`, a four-point dither pattern, designed to provide optimal sampling of the point spread function (PSF). For the ACS data, the data are obtained using a custom dither pattern similar to (but finer than) the default ACS/WFC dither `ACS-WFC-DITHER-LINE`, which spans across the gap between the two CCDs of the WFC and covers the missing FOV there.

Data in each band are combined using `Astrodrizzle` and `DrizzlePac` (version 1.1.8), an upgraded version of the `MultiDrizzle` pipeline in the `PyRAF` interface (Gonzaga et al., 2012). `Astrodrizzle` is a package specifically used for combining dithered *HST* images with the `Drizzle` algorithm (Fruchter & Hook, 2002). The `Drizzle` algorithm is an image reconstruction technique which maps the undersampled and dithered exposures to a linear subsampled output grid (a mosaic), at the same time taking into account the geometric distortion, rotation between exposures, and statistical significance of each pixel via weighting. Similar to stacking, artifacts present in individual images such as cosmic rays can also be removed. Prior to drizzling the images into a final mosaic, we applied a number of extra reduction steps to improve the data quality. Below we describe these reduction steps in details.

The extra reduction steps we applied have mainly two aims: a) improve the identification of cosmic rays and bad pixels by the pipelines `calacs` and `calwfc3` and b) optimize the alignment of the exposures. Within a single visit, the exposures are usually well-aligned given the extremely high pointing accuracy and stability of *HST* ($\sim 2 - 5$ milliarcsecond). For datasets taken in multiple visits this is not the case as the observations are

⁴<https://archive.stsci.edu/>

done in different telescope positions, roll angles and with different guide stars, resulting in an offset between exposures (up to $\sim 0.2 - 0.5$ arcsec). The quality of the final mosaic depends largely on how accurate one can align these exposures, as well as the rejection of cosmic rays. Drizzling images with inaccurate alignment can significantly broaden the PSF and compromise the spatial resolution of the data. On the other hand, insufficient or overextended cosmic ray rejection can affect the noise properties of the final mosaic. In practice, these two aspects are tangled together, the accuracies of the cosmic ray rejection often depends on how accurate one can register different exposures; on the other hand the existence of “blemishes” on the images can cause confusions while aligning images.

1. We first examine the data quality array (DQ) of all the fit files to check if the identification of cosmic rays or bad pixels by `calacs` and `calwfc3` is reasonable. Occasionally some fit images have huge hot stripes that span across the FOV (could be satellite trails, for example) which are not fully flagged. If left untreated these stripes will leave artifact on the drizzled mosaic. Figure 2.1 shows an example of these stripes on a ACS F850LP exposure. We mask these regions generously (to ensure most of these pixels are removed) by setting them to be 4096 in the DQ array.
2. We then run `Astrodrizzle` on the set of exposures during a single visit (those within a single association table) to do a first identification of the cosmic rays. For WFC3 data, this will be the final combination of the data as they are mostly obtained in a single visit. We will describe the `Astrodrizzle` parameter used for combination below.
3. The next step is to align the exposures taken in different visits. We use the task `tweakreg` in `DrizzlePac` to do the matching. First we generate a source coordinate file for each fit image as an input to `tweakreg`. We extract the science and error extensions (SCI and ERR) of the fit images and run `SExtractor` (Bertin & Arnouts, 1996) on them to produce coordinate files. The fit images are not used directly as an input as the used version of `tweakreg` does not take into account of the DQ array, hence the cosmic rays will heavily affect the source finding algorithm in `tweakreg`. Using our coordinate files as input to `tweakreg` we derive the shifts between exposures and apply them to the data to improve the alignment of the images.
4. With the aligned exposures we can combine them into final mosaics for each filter using `Astrodrizzle`. For XMMU J2235-2557 the ACS and WFC3 images have been drizzled to pixel scales of 0.05 and 0.09 arcsec pixel⁻¹ respectively. For the new Cycle 22 data (e.g. XMMXCS J2215-1738 and RCS 2345-3632) we adopt a pixel scale of 0.03 and 0.0642 arcsec pixel⁻¹ for the ACS and WFC3 images to better match the 3D-HST mosaics. We will update the reduction of XMMU J2235-2557 in the future to provide a homogenous set of images. Note that the choice of pixel scale (0.03 or 0.05) does not affect the result, as we have tested extensively with the data of XMMXCS J2215-1738. An important parameter in drizzling images is about how much you shrink the original pixels from individual exposures before mapping them to the final grid (hence, to subsample), known as the “drop size”. The drop size is

controlled by the `pixfrac` parameter in `Astrodrizzle`, which governs the ratio of the drops size to the original pixels linear size. We use `pixfrac = 0.8`, a square kernel, and produce weight maps using both inverse variance map (`IVM`) and error map (`ERR`) weighting for different purposes. The differences of the output weight maps from the `IVM` and `ERR` settings are discussed below. A list of the used `Astrodrizzle` parameters is given in Table 2.2, parameters that are not listed are kept as default values.

The `ERR` weight maps contain all sources of the noises including read noise, dark current, sky background as well as the Poisson noise of the observed sources. Since they are computed using the error extensions (`ERR`) of each exposure, they provide an accurate measurement of the variance in each drizzled pixel taking into account the dither pattern of the observations. On the other hand, the `IVM` weight maps contain all background noise sources except the Poisson noise of the sources. `IVM` maps are commonly used for object detection such as with `SExtractor` (as described in Section 2.4), while the `ERR` weight maps are used for structural analysis as the Poisson noise of the objects is included (see description in Section 3.1).

Due to the nature of the drizzle process, the resulting drizzled mosaics have correlated pixel-to-pixel noise. To correct for this we follow Casertano et al. (2000) to apply a scaling factor to the weight maps using the following formula:

$$\sqrt{F_A} = (s/p)(1 - (s/3p)), \text{ if } s < p \quad (2.1)$$

$$\sqrt{F_A} = 1 - p/(3s), \text{ if } s > p \quad (2.2)$$

where p is the `pixfrac` parameter used in drizzling and s is ratio between the output (drizzled) pixel to the original pixel scale. For example for the XMMXCS J2215-1738 ACS data, $s = 0.03/0.05 = 0.6$, $p = 0.8$ and hence $\sqrt{F_A} = 0.5625$. This factor is applied when we convert the drizzled weight maps (`IVM` / `ERR`) into root-mean-square (RMS) maps:

$$\text{MAP}_{RMS} = \frac{F_A}{\sqrt{\text{MAP}_{(IVM/ERR)}}} \quad (2.3)$$

Figure 2.2 shows the H_{160} `IVM` and `ERR` RMS maps of XMMU J2235-2557 as an example. To avoid confusion, below we will always use “images” to refer to the mosaics, and “RMS maps” to refer to the `IVM` or `ERR` RMS maps.

2.3.3 Absolute WCS calibration

Using `tweakreg` we correct for the relative offset between exposures before combining them to a final mosaic. Here we focus on the calibration of the “absolute” astronomical coordinate system, the world coordinate system (WCS), of the images. The WCS is a convention used in FITS files to map image coordinates (x,y) to astronomical coordinates (RA, DEC). To calibrate the WCS, one needs to use several known reference locations (usually stars) on the image to construct the mapping. We calibrate the WCS of the images using `GAIA` (Graphical Astronomy and Image analysis Tool) in the Starlink library

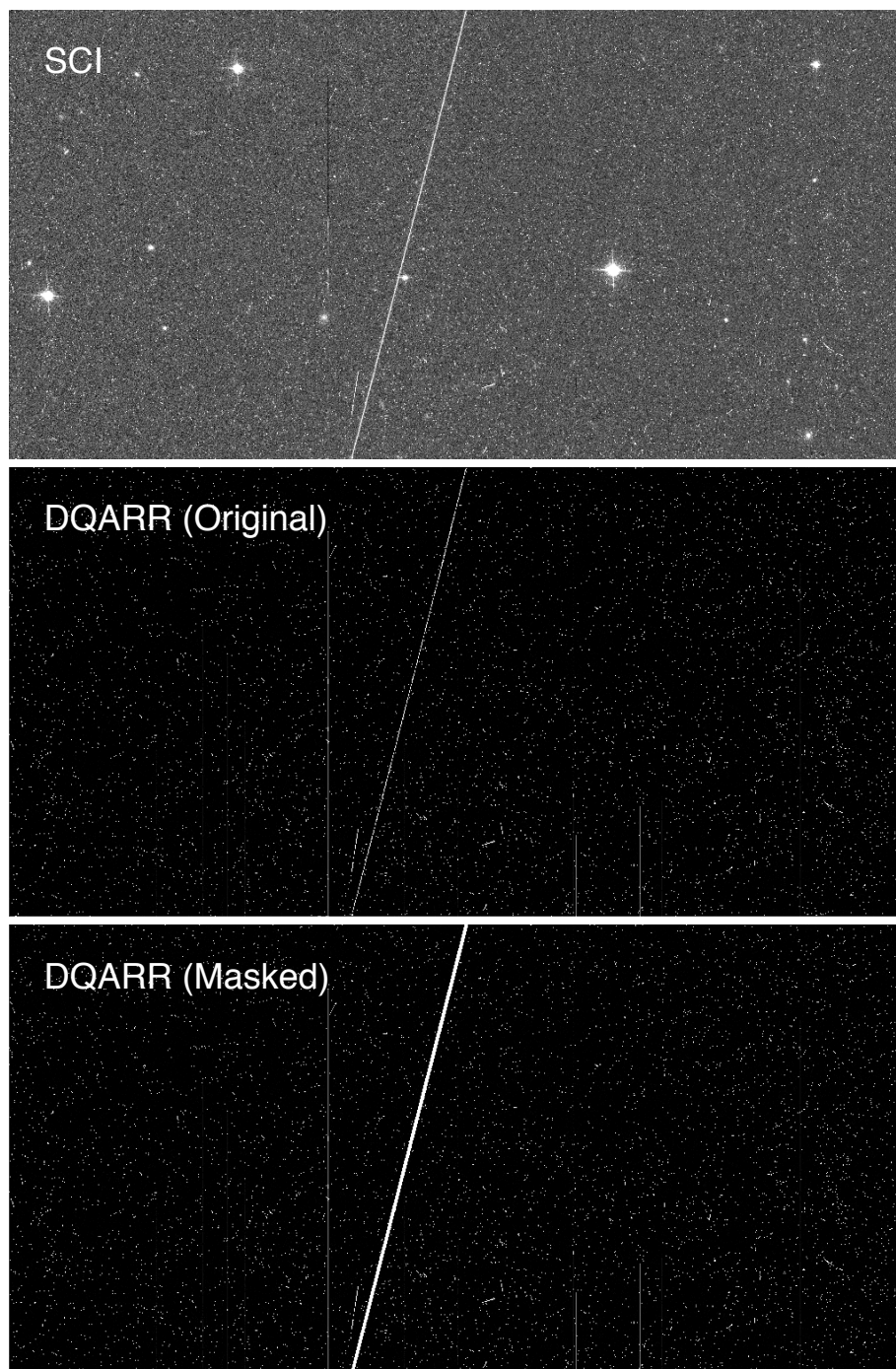


Figure 2.1: Example of a hot stripe in a ACS F850LP exposure and the masking. Top: Science extension (SCI) of the second detector (chip 2) of the exposure. Middle: The original data quality array (DQ) output by *calacs*. Bottom: DQ array with additional masking. The hot stripe goes across the entire chip and is not fully flagged in the original DQ array by *calacs*. The affected regions are generously masked to avoid artifacts on the drizzled mosaic.

Table 2.2: Summary of the Astrodrizzle parameters used for the HST data reduction.

Parameter	Value
crbit	4096
resetbits	0
skysub	Y
skywidth	0.1
driz_separate	Y
driz_sep_kernel	turbo
driz_pixfrac	0.8
driz_sep_wcs	Y
driz_sep_rot	0.0
driz_sep_scale	0.05*
median	Y
combine.type	minmed
blot	Y
blot_interp	poly5
driz_cr	Y
driz_cr_snr	5.0 4.0
driz_cr_scale	1.2 0.7
driz_combine	Y
final_wht_type	IVM/ERR
final_kernel	square
final_wt_scl	exptime
final_pixfrac	0.8
final_units	counts
final_wcs	Y
final_rot	0.0
final_scale	0.05*

* Choice of the final pixel scale depends on the instrument and cluster, see text for details.

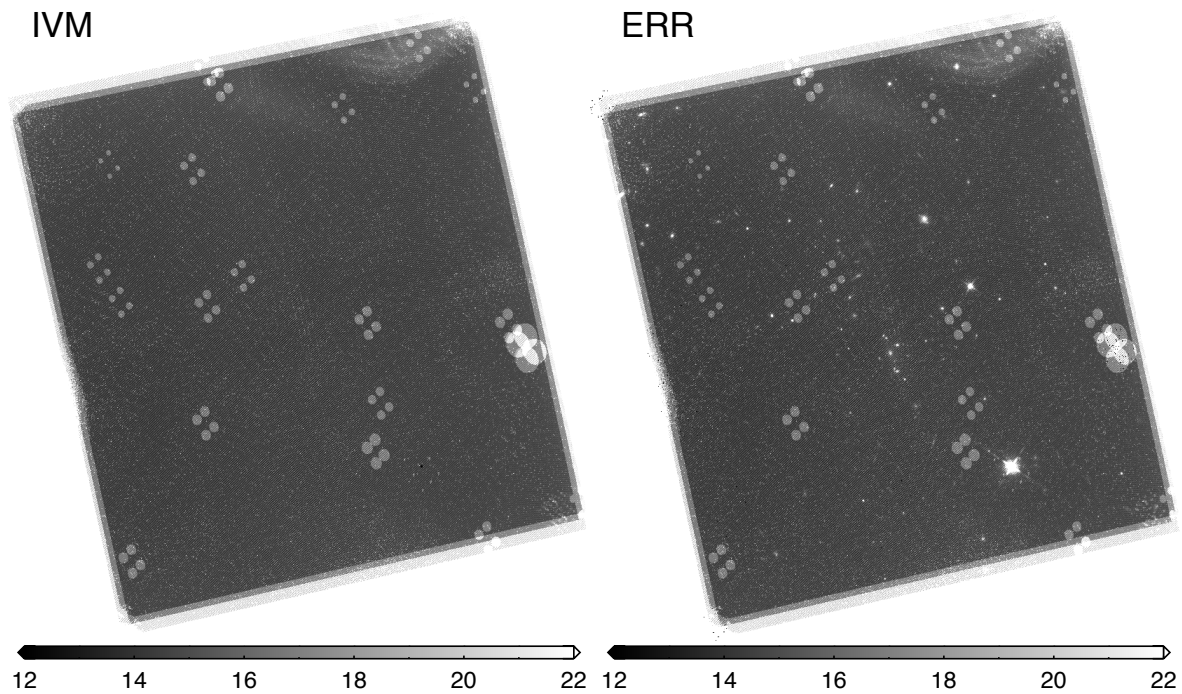


Figure 2.2: Example of the IVM and ERR RMS maps. Left: H_{160} RMS map of XMMU J2235-2557 derived with the IVM setting in Astrodrizzle (in ADU). Right: H_{160} RMS map derived with the ERR setting in Astrodrizzle. The ERR map contains all background noise sources while the IVM map does not include Poisson noise of the objects. One can also see the regions of dead pixels on the WFC3 detector, shown as bright circles (hence higher RMS) on the maps.

(Berry et al., 2013). GAIA provides an easy-to-use interface to assess the RA and DEC of astronomical objects from various on-line catalogues. We select reference star coordinates from Guide Star Catalog II (GSC-II) (Lasker et al., 2008).

For the ACS image we are able to select a sufficient number of unsaturated bright stars ($\sim 4 - 5$) from GSC-II within the FOV to perform the WCS calibration. Due to the smaller FOV this is not possible for the WFC3 data. For the WFC3 images, we derive the WCS using the ACS images as references and compare the coordinates of unsaturated stars on the WFC3 images to those on the WCS calibrated ACS z_{850} images. We select 12 stars from the WFC3 image of XMMU J2235-2557 and 13 stars from the image of XMMXCS J2215-1738 for the matching. With this amount of unresolved stars, we are able to match the WCS between the ACS and WFC3 images very well. We also apply the derived WCS to the images in each band to their corresponding RMS maps respectively.

The WCS of the public 3D-HST GOODS-S mosaics was calibrated using an astrometric reference catalog created from the CANDELS ACS i_{814} mosaic (Skelton et al., 2014). The CANDELS GOODS-S mosaics (Koekemoer et al., 2011) are calibrated using an external astrometric reference catalogue from an R -band mosaic of Chandra Deep Field South (CDF-S) from the ESO-MPI 2.2m /Wide Field Imager (WFI) obtained as part of the ESO Imaging Survey (EIS) (Arnouts et al., 2001), which is also registered to GSC-II.

2.3.4 PSF derivation and matching

Originated from different instruments and hence different optics, the PSFs of *HST*/ACS and *HST*/WFC3 in each band have different profiles. The diffraction spikes of the PSF depend also on the observing pattern and rotation of the telescope. Hence, before we start measuring photometry from the images and construct catalogues, we need to first match the PSFs between different images. PSF matching is crucial in photometry as well as our resolved stellar mass measurements (see Section 3.5), as the measured flux of the galaxy has to come from the same physical (projected) region. In this section we describe the PSF matching procedure of the ACS z_{850} and WFC3 H_{160} images of XMMU J2235-2557 and XMMXCS J2215-1738, which we used to derive photometry and resolved stellar mass measurements. For Cl 0332-2742, the 3D-HST releases have already provided PSF-matched images in multiple bands that are matched to the H_{160} band.

The characteristic PSFs of individual bands are constructed by median-stacking bright unsaturated stars in the images. We select around 12-15 stars for the ACS bands and 4-6 stars for the WFC3 bands due to smaller FOV. Neighbouring objects around the stars are first masked before stacking. The stacked PSFs are normalised to a total sum of one. Figure 2.3 shows the stacked z_{850} and H_{160} PSFs of XMMU J2235-2557 and XMMXCS J2215-1738 as an example. For each PSF two different stretches in the colour scale are presented to show the airy ring and the diffraction spikes more clearly. The full-width-half-maximum (FWHM) of the ACS z_{850} PSF is $\sim 0.11''$ and that for the WFC3 H_{160} is $\sim 0.18''$. Note that we did not take into account the slight variation of PSF profiles with detector position, but such differences are tiny and there are not enough stars to quantify this variation in our images. The multiple set of speckles of the ACS PSFs come

from multiple epoch observations.

Besides using stacking of unsaturated stars to obtain the PSF, we have also tried to derive a `TinyTim` PSF composite by adding PSF models using the `TinyTim` code (Krist, 1995) into the raw data and drizzling them as science images. Nevertheless, we notice that the `TinyTim` drizzled PSF does not match well the empirical PSF in the outer part: a much stronger outer envelope (as well as diffraction spikes) can be seen in the empirical PSF (see also, Appendix A in Bruce et al., 2012, for a similar description). On the other hand, van der Wel et al. (2012) produced hybrid PSF models by replacing the central pixels of the median-stacked star by the `TinyTim` PSF. We do not employ this correction as we find that the median-stacked star matches the `TinyTim` PSF reasonably well in the inner part.

The z_{850} images are then PSF-matched to the resolution of the H_{160} images, as the PSF of WFC3 H_{160} has larger FWHM than the one from ACS. We do not match the other WFC3 PSFs to the H_{160} PSF as they have similar FWHM. To match the PSFs we use the `psfmatch` task in IRAF to generate a matching kernel. Cosine bell tapering is applied to filter the high frequency component of the input z_{850} PSF, which is presumably induced by noise, to clean the output kernel. In the `psfmatch` task there are several free parameters that can be tuned (e.g. kernel sizes, highest cosine bell frequencies and apodize), a systematic search is performed to find the best parameters to match the PSFs. We then apply the matching kernel to the z_{850} image. The PSF matched z_{850} image is resampled to the same grid as the H_{160} image using the software SWarp (Bertin et al., 2002) with a `Lanczos3` kernel.

We assess the accuracy by comparing the fractional encircled energy of the z_{850} PSF before and after the procedure to the H_{160} PSF in XMMU J2235-2557 and XMMXCS J2215-1738. The convolved z_{850} PSF matches almost perfectly the H_{160} PSF with only tiny difference in the wing ($< 1\%$). We also re-constructed new z_{850} PSFs from the PSF matched z_{850} images to assess the result. Figure 2.4 shows the fractional encircled energy of the PSFs constructed from images before and after PSF matching for XMMU J2235-2557 and XMMXCS J2215-1738. For both clusters, the ratios of their growth curves deviate by $< 2.5\%$ from unity. For Cl 0332-2742, the resultant growth curves after PSF matching are consistent within 1% (Skelton et al., 2014).

2.4 Construction of photometric catalogues

To construct a multi-band photometric catalogue for individual cluster, the photometry in different bands needs to be measured through a consistent set of apertures. SExtractor (Bertin & Arnouts, 1996) is a software package specified for this purpose and is commonly used in object identification and catalogue construction. We make use of the dual image mode of SExtractor, the object detection is performed on the first input image, while the photometry of the defined objects is measured on the second separate input image. This allows us to use a consistent detection image for each cluster and measure photometry in different bands with an identical set of apertures respectively.

For each cluster we use the H_{160} image, the reddest available band, as the detection

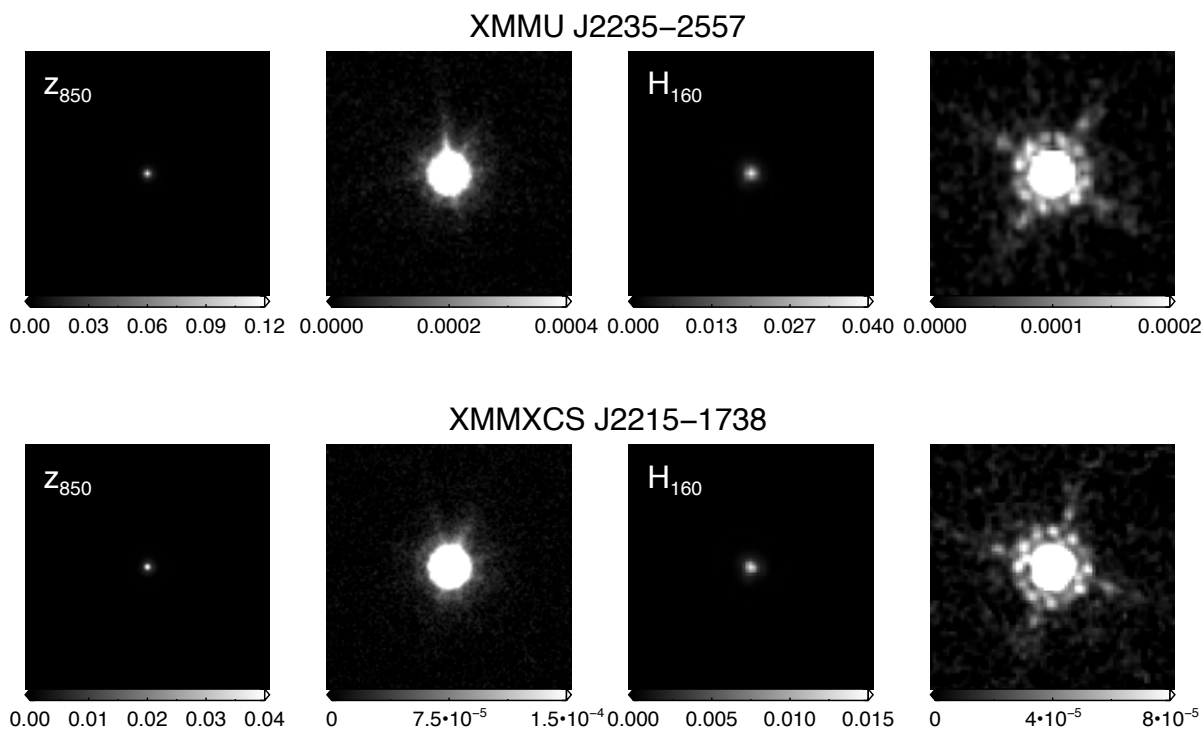


Figure 2.3: Examples of the derived characteristic PSFs. Top left panels: z_{850} PSF of XMMU J2235-2557 shown in two different stretches of the colour scale. Top right panels: H_{160} PSF of XMMU J2235-2557. Bottom left and right: z_{850} and H_{160} PSFs of XMMXCS J2215-1738. Two stretches in the colour scale are shown to show the airy ring and the diffraction spikes of the PSFs more clearly. The scales are different for the two clusters due to the normalisation and different pixel scale adopted in the drizzled images. Each panel corresponds to an area of $4.5'' \times 4.5''$.

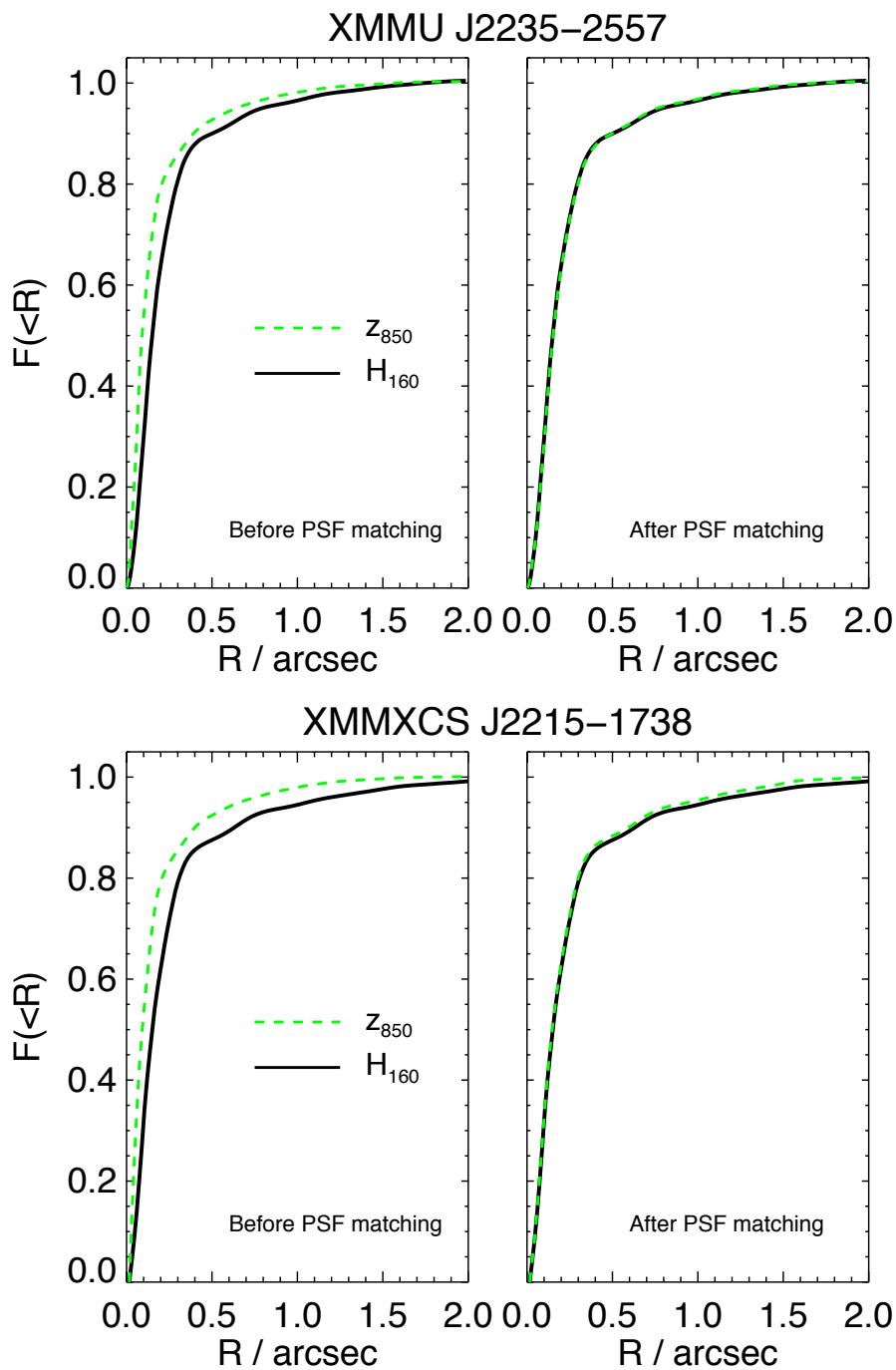


Figure 2.4: Fractional encircled energy of the z_{850} and H_{160} PSFs. Top left: XMMU J2235–2557 PSFs before PSF matching. Top right: XMMU J2235–2557 PSFs after matching. Bottom left: XMMXCS J2215–1738 PSFs before PSF matching. Bottom right: XMMXCS J2215–1738 PSFs after matching. The green dashed line corresponds to the z_{850} PSF while the black solid line corresponds to the H_{160} PSF.

image for SExtractor. The H_{160} IVM RMS map is used as the weight image for SExtractor as a reference of the background noise in individual pixels. We apply a detection threshold (DETECT_THRESH) of 3.0 and a minimum detection area (DETECT_MINAREA) of 9, hence a group of pixel that have nine adjacent pixels with signal three times higher than the background RMS noise will be identified as an object. Standard deblending and cleaning are applied to disentangle close neighbours as separate objects and remove spurious detections.

We derive MAG_AUTO magnitudes and aperture magnitudes for galaxy magnitudes and colour measurements for different bands (including the PSF-matched z_{850} band) respectively. A fixed circular aperture size of $1''$ in diameter is used for the aperture magnitude. Note that $1''$ corresponds to ~ 8.5 kpc at $z \sim 1.5$, the effective radii of most galaxies in the clusters are generally much smaller than the aperture size. Since the 3D-HST photometry catalogue (Skelton et al., 2014) does not provide aperture colour measurements for the ACS bands as well as they used a $0.7''$ aperture for the WFC3 bands, we run SExtractor also on Cl 0332-2742 to have consistent photometry measurements for all the KCS clusters. We will describe the cross-matching of our catalogue to the 3D-HST photometry catalogue below. Galactic extinction is corrected using the dust map of Schlegel et al. (1998) and the recalibration $E(B - V)$ value from Schlafly & Finkbeiner (2011). The extinction correction is tiny, for example for XMMU J2235-2557 it is 0.0249 mag for z_{850} and 0.0102 mag for H_{160} . The catalogues are then trimmed by removing point sources indicated by SExtractor (i.e. those with `class_star` ≥ 0.9).

As described in Section 2.2.1, Grützbauch et al. (2012) studied the star formation in the cluster out to a projected radius of 1.5 Mpc. We cross-match our SExtractor catalogue to theirs to identify spectroscopically confirmed cluster members from previous literature (mostly from Mullis et al., 2005; Lidman et al., 2008; Rosati et al., 2009). 12 out of 14 spectroscopically confirmed cluster members are within the WFC3 FOV and are identified.

Similarly, we cross-match our catalogue of XMMXCS J2215-1738 with the catalogue from Hilton et al. (2009, 2010). The Hilton et al. (2009) catalogue was built using a MOIRCS K_s image as the detection image and include objects with photometric redshifts $1.27 < z < 1.65$ and 24 spectroscopic confirmed members. We detected 52 objects out of 64 of the Hilton et al. (2009) catalogue, most of the undetected objects are out of the WFC3 FOV or are deblended to be multiple objects with our higher resolution *HST*/WFC3 imaging. The Hilton et al. (2010) catalogue comprises 44 spectroscopically confirmed members either by visually identified spectral features or cross-correlation of special templates. 26 out of the 44 objects are detected, again the undetected objects are mostly out of the WFC3 FOV.

For Cl 0332-2742, we cross-match our catalogue with the 3D-HST photometry catalogue (v4.1.5) of the GOODS-S field (Skelton et al., 2014; Momcheva et al., 2016). Since the GOODS-S field is large and contains objects at various redshifts, a cut was first applied to select objects that are plausibly cluster members in a targeted region for the KMOS observation. The 3D-HST catalogue comprises spectroscopic, grism and photometric redshifts of the objects hence we can perform a redshift cut. In some cases additional redshift information from KMOS was also used. We select objects with redshifts within ± 3000 km s $^{-1}$ of the cluster redshift and within a region of 10 arcmin in diameter, enclosing the

Tanaka et al. (2013) group and the upper main parts of Kurk et al. (2009) structures. This gives 594 objects and among them 37 are *UVJ* passive objects. Our catalogue detects all the *UVJ* passive objects and 543 out of 594 objects.

2.5 The Red Sequence Sample

With the photometric catalogues of the KCS clusters, here we select the definitive galaxy sample used in this work. As the goal of this work is to study the evolution of massive passive galaxies in high-density environments, we identify passive galaxies through the red sequence method. As we mentioned in Section 1.1.5, the red sequence method exploits the tight relationship of passive early-type galaxies in color-magnitude space, and has been commonly used for cluster detection (e.g. Gladders & Yee, 2005).

Figure 2.5 shows the colour-magnitude diagram of the detected sources in the three clusters within the *HST*/WFC3 field of view. We use the PSF-matched $1''$ aperture $z_{850} - H_{160}$ colours for the cluster XMMU J2235-2557 and XMMXCS J2215-1738, while for the Cl 0332-2742 we use the $i_{814} - J_{125}$ colours from the 3D-HST catalogue in GOODS-S (Momcheva et al., 2016), in order to match the selection of the galaxy sample for KMOS observations (see Section 2.6.1). The i_{814} and J_{125} magnitudes provided in the 3D-HST catalogue are measured within a PSF-matched $0.7''$ aperture and scaled to a ‘total’ magnitude using the SExtractor `MAG_AUTO` magnitude and the curve of growth in the H_{160} band (see Skelton et al., 2014, for details). Here only the objects in GOODS-S that pass the abovementioned selection with redshift and area are plotted (see Section 2.4 for details). Although the 3D-HST $i_{814} - J_{125}$ colours are measured within a $0.7''$ aperture instead of $1''$, the effective radii of most galaxies in Cl 0332-2742 are much smaller than this aperture size, using this will not have any effect on the selection. From Figure 2.5 it is clear that the three clusters harbour a distinct red sequence. The colour-magnitude relation is fitted from the colour-magnitude diagram, and the scatter is measured through first rectifying the colour with the relation, then marginalising over the magnitude to obtain a number density distribution of the galaxies. The dotted lines in each colour-magnitude diagram correspond to $\pm 2\sigma$ derived from a Gaussian fit to the distribution.

We generally select objects that are within 2σ from the fitted red-sequence in each cluster as the red sequence sample, with the exception that some red objects that are slightly above 2σ are also selected for completeness. We applied a magnitude cut for each cluster: $H_{160} < 22.5$ for the cluster XMMU J2235-2557 and XMMXCS J2215-1738, $J_{125} < 23.5$ for Cl 0332-2742. This magnitude cut corresponds to a completeness of $\sim 95\%$ (see Section 3.7.3). This red sequence selection results in a sample of 35 objects in the cluster XMMU J2235-2557, 45 objects in XMMXCS J2215-1738 and 17 objects in Cl 0332-2742.

One of the downside of the red sequence method is that it suffers from contamination from dusty star forming galaxies. As we describe in Section 1.2.2, the colour selection technique, such as the *UVJ* classification, is able to distinguish between star forming galaxies that are dusty and genuine passive galaxies. Hence, on top of the red sequence

selection, we perform an additional colour-colour selection to remove the contamination.

For Cl 0332-2742, the rest-frame ($U - V$) and ($V - J$) colour, derived from multi-band photometry, are available from the 3D-HST photometric catalogue (Skelton et al., 2014; Momcheva et al., 2016), hence a UVJ classification can be performed. The bottom right panel of Figure 2.6 shows the UVJ digram of the red sequence of this cluster. We remove the two objects that are not in the quiescent region.

For XMMU J2235-2557 and XMMXCS J2215-1738, since the rest-frame J -band magnitude is not available and the extrapolation of the J -band magnitude from SED is not preferable, we construct a similar colour-colour selection using the observed $1''$ aperture $z_{850} - J_{125}$ and the $J_{125} - H_{160}$ colour. These two colours correspond roughly to the rest-frame ($U - V$) and ($V - R$) colour (hereafter UVR selection). One caveat of the two used colour here is that they are not PSF matched, but given the small effective radii of most galaxies this will not have any effect on the selection.

To examine the feasibility of this UVR selection, we make use of the Bruzual & Charlot (2003) stellar population models and compute evolution tracks with different star formation histories and stellar properties for each cluster redshift, as shown on the top and bottom left panel of Figure 2.6. As one can see in Figure 2.6, while this combination of colour is not as effective of the UVJ classification, the evolution track of a constant star forming population (CSF, blue) is still clearly separated from the passively evolving populations (SSP with different metallicities and an exponentially declining τ model with $\tau = 1$ Gyr). We also examine the effect of dust on the colours of these different populations, as shown as the dust vector on Figure 2.6. This suggests that the UVR selection is able to distinguish between star forming and passive galaxy, in a way similar to the UVJ classification.

We define the star forming region on the UVR plane using the constant star forming population track. The star forming region, shaded in grey on Figure 2.6, is the region spanned by the constant star forming population track with various dust extinction values. The edge of the shaded star forming region is hence parallel to the dust vector. Objects that are within this region are presumably dusty-star forming objects or interlopers that are not at the cluster redshift. This is, indeed, a conservative estimate on the number of star formation objects. Additional information would be required to identify extra star forming objects that have lower SFR.

Also shown on the plot are the other properties of the red sequence objects from the literature. For XMMU J2235-2557, the $H\alpha$ excess emitters from Grützbauch et al. (2012) are shown. The $H\alpha$ excess emitters have a H narrow band flux that is a factor of 3 greater than the noise in the H broad band (continuum) image and an equivalent width $> 20\text{\AA}$ to remove foreground interlopers (Hayes et al., 2010). For XMMXCS J2215-1738, the $24\mu\text{m}$ sources from Hilton et al. (2010), submillimeter sources at 450 and $850\mu\text{m}$ from Ma et al. (2015) and [O II] sources from Hilton et al. (2010) and Hayashi (private communication) are shown. The $24\mu\text{m}$ and submillimeter emission come from the thermal emission of dust, which is powered by UV (and optical) photons from either star formation or AGN. Hence, these far-IR and submillimeter emissions are star formation tracers and can be used to derive the SFR of the galaxies. Using the template library of Chary & Elbaz (2001) and Dale & Helou (2002), Hilton et al. (2010) and Ma et al. (2015) found that these sources

are dusty-starburst galaxies with $\text{SFR} \gtrsim 100M_{\odot} \text{ yr}^{-1}$. We find that three $24 \mu\text{m}$ sources (among them one also detected in submillimeter) that have extremely high SFR as shown by Hilton et al. (2010) and Ma et al. (2015) are not within the star forming region on the *UVR* diagrams.

Combining these information, we exclude galaxies that have strong evidence of star formation in our red sequence sample, including objects that are within the star forming region and those with high derived SFR from the literature. As a result, 8 objects are removed from the red sequence sample of XMMU J2235-2557, and 16 objects are removed from the red sequence sample of XMMXCS J2215-1738. The excluded objects are marked with a black dot at the centre on Figure 2.6.

In summary, the red sequence and colour-colour selection result in a sample of **27** objects in the cluster XMMU J2235-2557, **29** objects in XMMXCS J2215-1738 and **15** objects in Cl 0332-2742, which we use in our analysis below. The photometric catalogues of the red sequence objects in XMMU J2235-2557, XMMXCS J2215-1738 and Cl 0332-2742 are provided in Table 2.3, Table 2.4 and Table 2.5, respectively, at the end of this chapter.

Figure 2.7, 2.8 and 2.9 show the spatial distribution of the selected red sequence galaxies in the three clusters. In XMMU J2235-2557 and XMMXCS J2215-1738, the red sequence galaxies are preferentially found near the core of the cluster. On the other hand, in Cl 0332-2742 the red sequence objects are more dispersed (see Section 2.2.3 for a description on the spatial distribution of Cl 0332-2742). As we described in Section 2.2.3, Cl 0332-2742 is plausibly a protocluster still in the assembly phase and comprises several interacting group structures. The Tanaka et al. (2013) group can be seen as a cluster of red sequence objects on the bottom right of Figure 2.9 (e.g. ID 13096). As a result, there is no clear BCG in Cl 0332-2742. XMMU J2235-2557 has a very clear BCG (ID 170) located at the cluster core, while the BCG in XMMXCS J2215-1738 is off-centered (ID 1182).

2.6 KMOS Observations and Spectroscopic Data

2.6.1 Sample selection

Besides the red sequence sample for deriving photometric properties, the photometric catalogues of the KCS clusters are also used to select the primary galaxy sample for the KMOS observations (hereafter the KMOS passive sample). Nevertheless, since the selection was done prior to the observation of the Cycle 22 WFC3 data of XMMXCS J2215-1738, the sample for this cluster is selected using an early version of the photometric catalogue built with the ACS z_{850} image as the detection image. The photometry in the catalogue is derived from the ACS z_{850} image and the MOIRCS J-band image (hereafter J_{MOIRCS}) (Hilton et al., 2009).

The KMOS passive sample is primarily selected using the red sequence method. For XMMU J2235-2557 the red sequence is derived from the z_{850} and H_{160} band, for XMMXCS J2215-1738 it is derived from the z_{850} and J_{MOIRCS} and for Cl 0332-2742 the $i_{814} - J_{125}$ colour from the 3D-HST catalogue in GOODS-S (Momcheva et al., 2016) is used. For

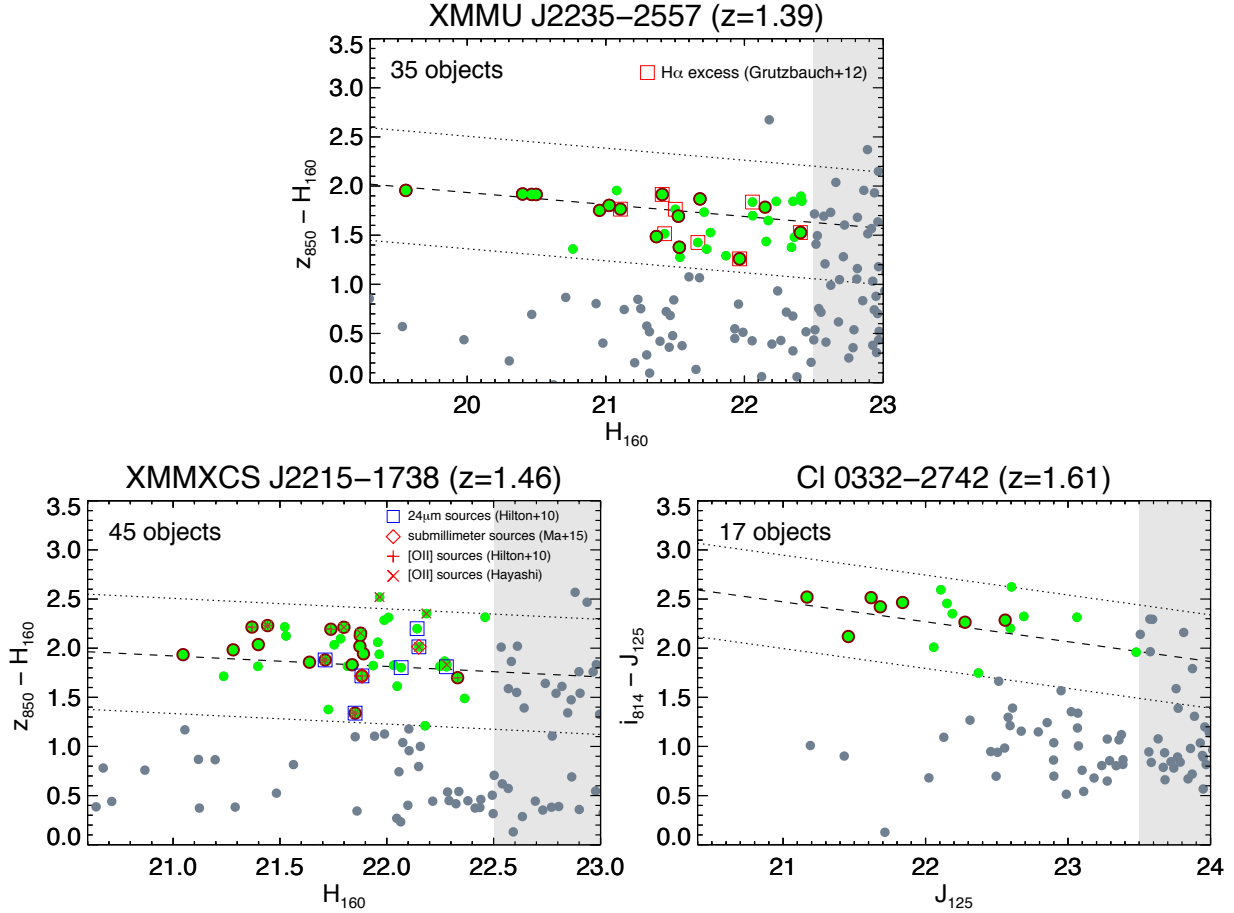


Figure 2.5: Colour-magnitude diagram of the three KCS clusters used in this thesis. For XMMU J2235-2557 and XMMXCS J2215-1738, the H_{160} magnitudes are *HST*/WFC3 MAG_AUTO magnitudes while the $z_{850} - H_{160}$ colours are from 1'' aperture magnitudes. For Cl 0332-2742, the J_{125} magnitudes and $i_{814} - J_{125}$ colours are from total magnitudes of the 3D-HST photometric catalogue (Momcheva et al., 2016). The dashed line in each panel corresponds to the fitted red sequence and the dotted lines are $\pm 2\sigma$. Green circles correspond to objects that are included in our sample, which are within the dotted line and are not in the shaded area (i.e. $H_{160} < 22.5$ for XMMU J2235-2557 and XMMXCS J2215-1738, $J_{125} < 23.5$ for Cl 0332-2742). Objects that are spectroscopically confirmed cluster members (combining KCS observations and previous literature) are circled in dark red. For XMMU J2235-2557 and XMMXCS J2215-1738, other properties of these galaxies from the literature are shown. See text for details.

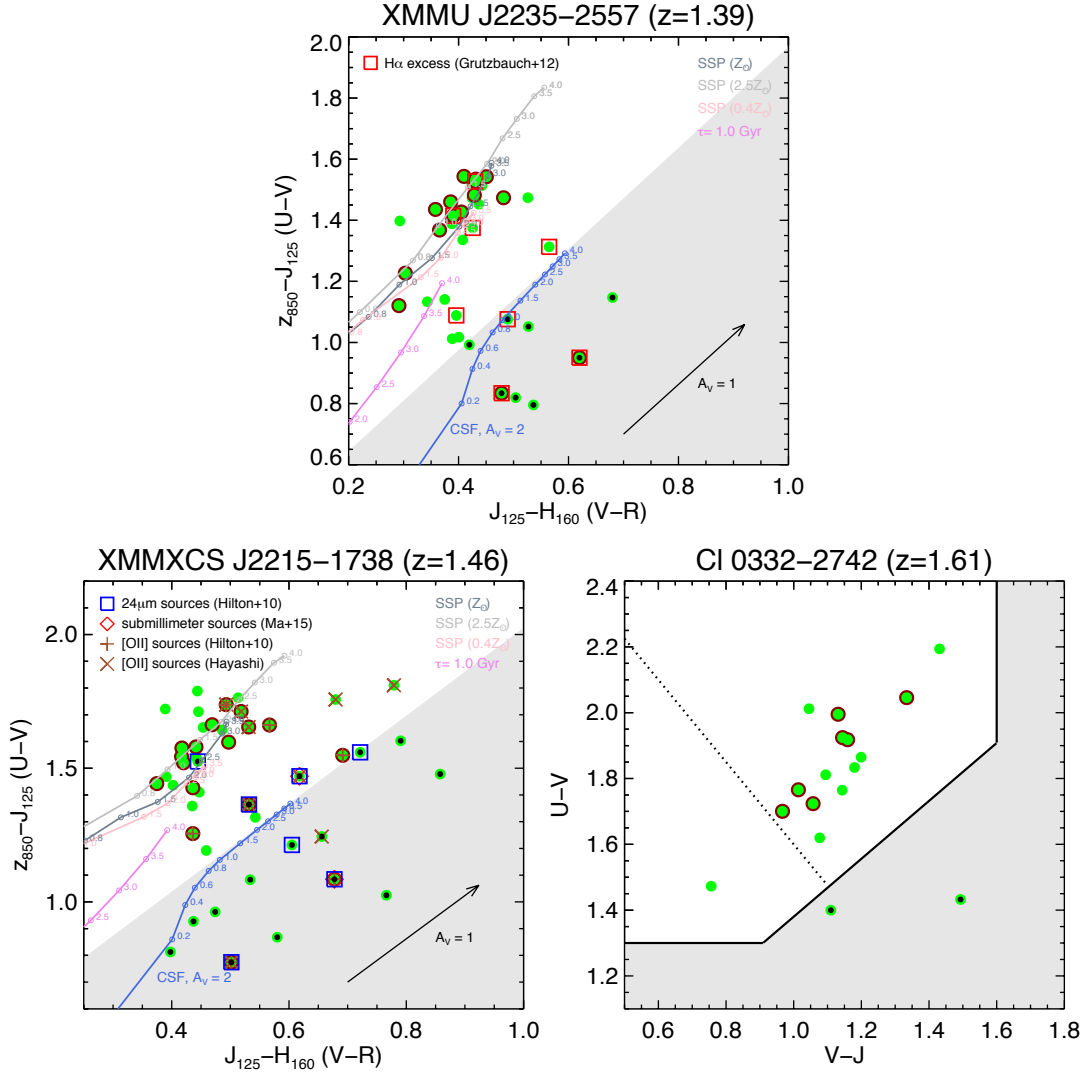


Figure 2.6: Colour-Colour selection for the three KCS clusters. Only red sequence selected galaxies are shown. Objects that are spectroscopically confirmed cluster members (combining KCS observations and previous literature) are circled in dark red. For XMMU J2235-2557 (top) and XMMXCS J2215-1738 (bottom left), the selection is performed using $z_{850} - J_{125}$ versus $J_{125} - H_{160}$ colour, which correspond to rest-frame $(U - V)$ and $(V - R)$. The colours are derived from $1''$ aperture magnitudes. Different coloured lines correspond to the evolution tracks of Bruzual & Charlot (2003) models with different properties: a constant SFH with $A_V = 2$ mag of extinction (CSF, blue), SSPs with sub-solar, solar and super-solar metallicities with no dust ($0.4Z_{\odot}$, Z_{\odot} , $2.5Z_{\odot}$ with pink, grey, dark grey, respectively), an exponentially declining SFH with no dust ($\tau = 1$ Gyr, violet). The empty circles represent the model colors at the specified ages (in Gyr). The dust vector indicates an extinction of $A_V = 1$ mag, assuming the Calzetti et al. (2000) extinction law. Different properties available from the literature (H α , 24 μ m, [O II] and submillimeter sources) are overplotted. For Cl 0332-2742 (bottom right), the UVJ colour selection is used. The rest-frame $(U - V)$ and $(V - J)$ colour are taken from the 3D-HST photometric catalogue (Skelton et al., 2014; Momcheva et al., 2016). The dashed line corresponds to the division between ‘young’ and ‘old’ passive galaxies based on their colours, adopted from Whitaker et al. (2013). The grey shaded region in each panel is where the ‘star-forming’ galaxies reside. Objects that are excluded are labeled with a black dot at the centre. See text for details.

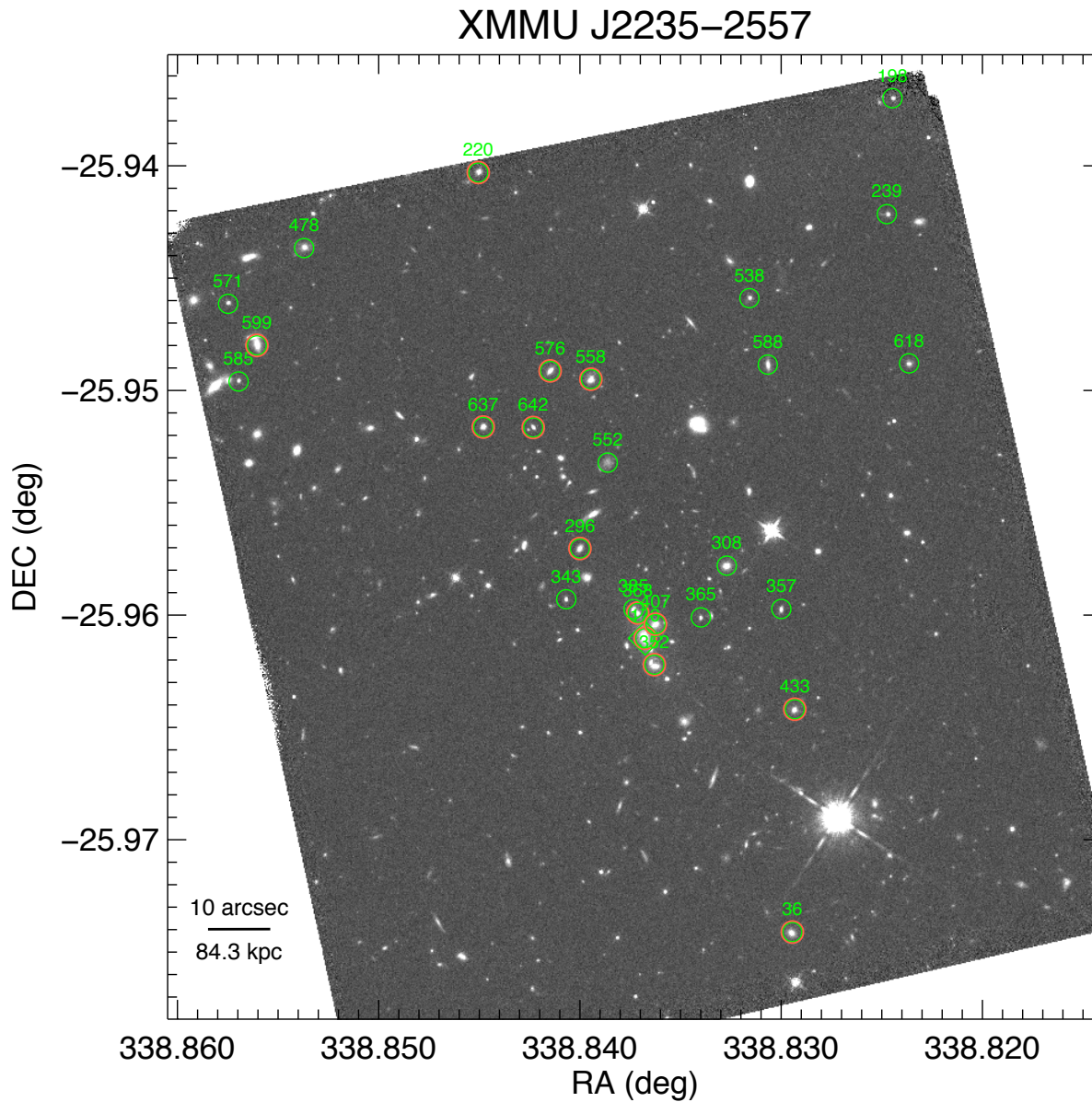


Figure 2.7: Spatial distribution of red sequence galaxies in XMMU J2235-2557. The background image is the *HST*/WFC3 image of XMMUJ2235-2557 in the H_{160} band showing the central region of the cluster. Selected red sequence objects are indicated by green circles. Red circles correspond to spectroscopic confirmed cluster members from KCS and Grützbauch et al. (2012). The BCG in this cluster (ID 170) is indicated by the green diamond.

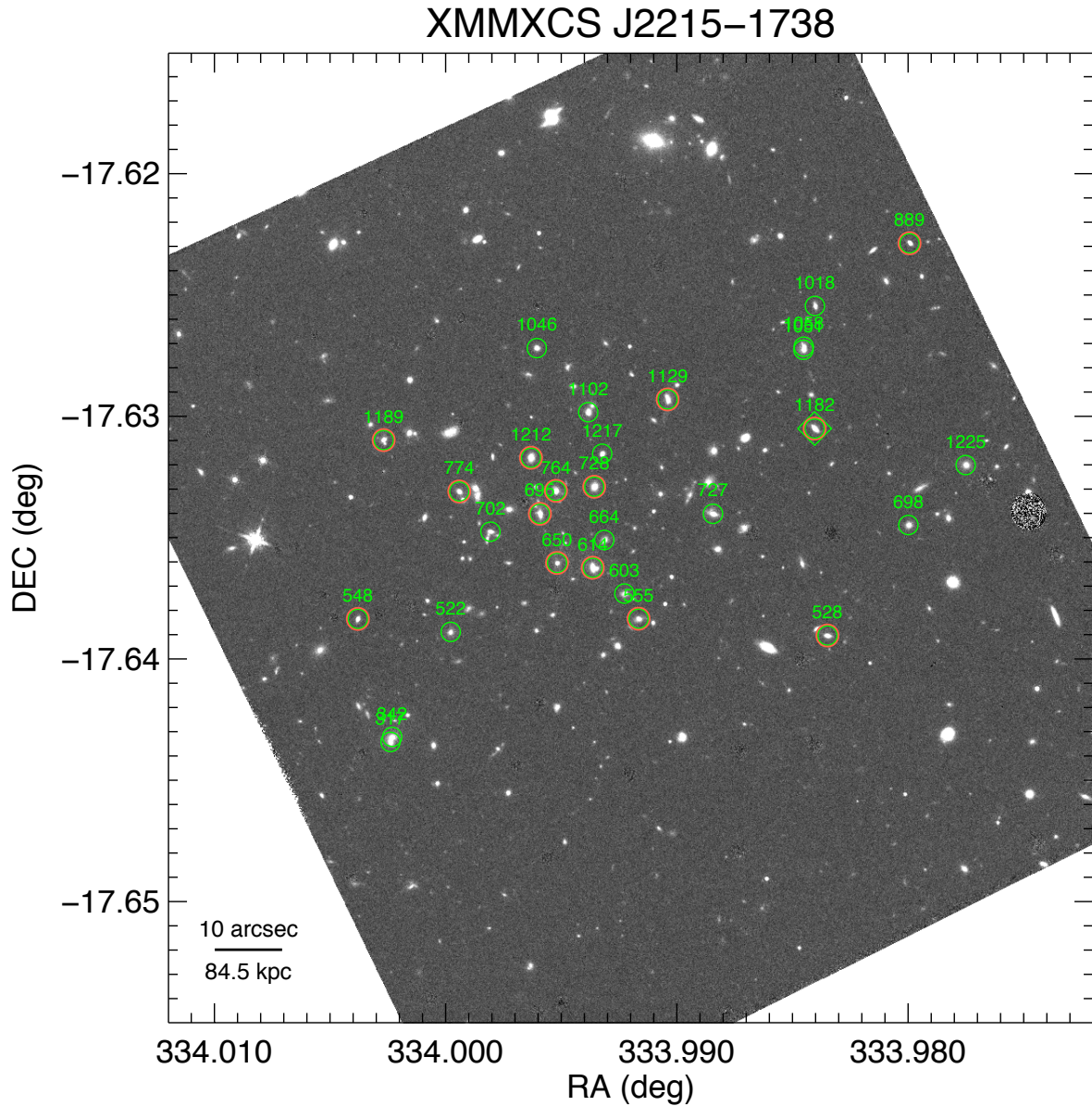


Figure 2.8: Spatial distribution of red sequence galaxies in XMMXCS J2215-1738. The background image is the *HST*/WFC3 image of XMMXCSJ2215-1738 in the H_{160} band showing the central region of the cluster. Selected red sequence objects are indicated by green circles. Red circles correspond to spectroscopically confirmed cluster members from KCS and Hilton et al. (2010). The BCG in this cluster (ID 1182) is indicated by the green diamond.

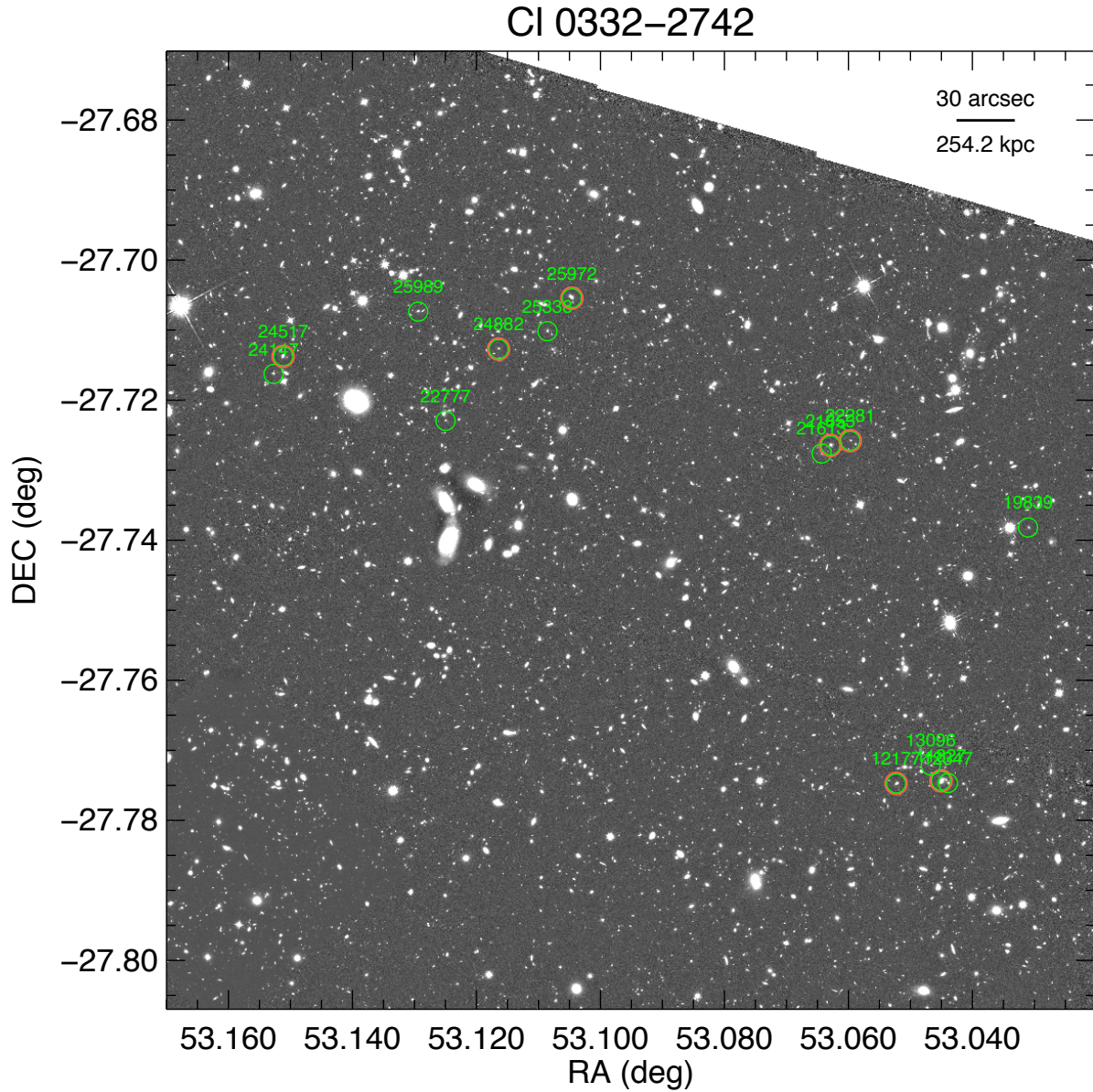


Figure 2.9: Spatial distribution of red sequence galaxies in CI 0332-2742. The background image is the 3D-HST *HST*/WFC3 image of CI 0332-2742 in the H_{160} band. Selected red sequence objects are indicated by green circles. Red circles correspond to spectroscopic confirmed cluster members from KCS and Momcheva et al. (2016).

JKCS 041 we use the photometric catalogue from Newman et al. (2014), which includes photometry from ACS z_{850} and J -band from WIRCam at the Canada-France-Hawaii Telescope (CFHT) for the red sequence selection. For the backup cluster RCS 2345-3632, we use the ACS $i_{775} - z_{850}$ colour to select the red sequence.

The objects are selected to have J_{140} brighter than 22.5 mag, rescaled to the band used to derive the red sequence (i.e. $H_{160} < 22.29$ for XMMU J2235-2557, $J_{\text{MOIRCS}} < 22.5$ for XMMXCS J2215-1738 and $J_{125} < 22.76$ for Cl 0332-2742, respectively to match the original J_{140} cut). The KMOS passive sample is almost entirely covered by the red sequence sample, except for one object that is not within the WFC3 imaging FOV of XMMXCS J2215-1738.

2.6.2 Observations and summary of spectroscopic data

The observations of KCS have been in progress since ESO period P92 (October to November 2013). The multiplexity of KMOS allows ~ 20 galaxies to be targeted simultaneously in each cluster. The sample in each cluster is prioritised to facilitate detection efficiency. Red sequence objects with known spectroscopic redshifts (i.e. confirmed red cluster members) are given the highest priority and are designated to be allocated first in the observations. Objects that are in the red sequence but are not confirmed members are ranked the second. Objects that are confirmed members but not in the red sequence (star forming galaxies) are occasionally allocated as filler targets.

Galaxies were observed in KMOS YJ band which covers a wavelength range of $1 - 1.36 \mu\text{m}$. At the redshift of clusters ($1.4 < z < 1.8$) this covers the known rest-frame optical features such as G -band, Mgb (for XMMU J2235-2557), $\text{H}\gamma$ and $\text{H}\beta$. As one of the primary goal of KCS is to perform deep absorption line spectroscopic study on these galaxies, a long exposure time is required for the spectra to reach a sufficient S/N. We aim at a total integration time of ~ 20 hours on-source for the selected galaxies in the KMOS passive sample.

Up to period P96 (October 2015), we have observed 75 galaxies that reach the targeted integration time. Of these galaxies, 20 belong to XMMU J2235-2557, of which 19 are passive; XMMXCS J2215-1738 has 19 galaxies, of which 15 are passive; we observed 20 galaxies in Cl 0332-2742, of which 10 are passive. The remaining 16 galaxies belong to JKCS 041 and 12 of them are passive. Hence in total there are 56 passive galaxies in the observed sample.

Data of XMMXCS J2215-1738, Cl 0332-2742 and JKCS 041 were taken with a standard object-sky object nodding pattern so each object frame has an adjacent sky frame. For XMMU J2235-2557, data were taken with a technique for crowded regions (which we named as ‘50-50’), in which a pair of IFUs are used for a single galaxy. During the observation, the two IFUs alternate between sky and object, hence 100% of the observation time is on-source. This reduces in half the number of targets that are observed simultaneously. Typical exposure times were 300s for XMMXCS J2215-1738, Cl 0332-2742 and JKCS 041 and 450s for XMMU J2235-2557. The exposures are dithered with $0.1 - 0.6''$ to improve bad pixel rejection and the extraction of spectra.

Data of the three KCS clusters (XMMU J2235-2557, XMMXCS J2215-1738 and Cl 0332-2742) are reduced using a combination of the Software package for Astronomical Reductions with KMOS pipeline tools (SPARK, Davies et al., 2013) and custom Python scripts (Mendel et al., 2015, Mendel et al 2016, in prep). 1D spectra of the galaxies are extracted from the data with optimal extraction (Horne, 1986) using the *HST* images described in this thesis as references of the spatial light distribution of the galaxies. Spectra are extracted to one half-light radius of individual galaxies. The details of the KMOS data reduction and spectra extraction will not be discussed here. The interested reader can refer to Mendel et al. (2015), Beifiori et al., (2016), in prep and Mendel et al., (2016), in prep. for details. With an exposure time of ~ 20 hours we derived spectra that have a typical S/N of 5 – 12.

The passive galaxies of the three KCS clusters (i.e. 44 out of 56) have been analysed. Redshifts are derived using either cross-correlation method or with the Penalized Pixel-fitting method (pPXF) (Cappellari & Emsellem, 2004). We update the redshifts in the cross-matched photometric catalogues with the derived KMOS redshifts whenever available. Stellar velocity dispersions are measured with pPXF using the Maraston & Strömbäck (2011) stellar population models based on the ELODIE v3.1 stellar library (Prugniel & Soubiran, 2001; Prugniel et al., 2007) as templates. The derive stellar velocity dispersions have typical error of about 20 – 30%. The interested reader can refer to Beifiori et al., (2016), in prep for details.

With the KMOS spectroscopic data we have derived, for the first time, stellar velocity dispersions for clusters at $z > 1.3$. From the three KCS clusters we have currently derived 18 stellar velocity dispersions. This sample represents one of the largest sample of passive galaxies in dense environment at $z > 1.3$ that are homogeneously observed and analysed. In Section 6.2 we discuss some of the current and future work with the KCS spectroscopic data, including the stellar mass fundamental plane (see Section 1.3.3) that combines the photometric properties described in this thesis with the KMOS absorption line analysis of Beifiori et al., (2016), in prep.

2.7 Local Comparison Sample

In order to study the evolution of galaxy properties over redshift, we compose a local sample of passive galaxies from the Spheroids Panchromatic Investigation in Different Environmental Regions (SPIDER) survey (La Barbera et al., 2010b) as a comparison sample for KCS.

The publicly available SPIDER primary sample includes 39993 early-type galaxies selected from the Sloan Digital Sky Survey (SDSS) Data Release 6 (DR6), among them 5080 are in the near-infrared UKIRT Infrared Deep Sky Survey-Large Area Survey Data release (UKIDSS-LAS DR4). The galaxies are magnitude selected to have $^{0.1}M_r < -20$, where $^{0.1}M_r < -20$ is the k-corrected SDSS Petrosian r -band magnitude, and a redshift range of $0.05 < z < 0.095$. To identify early-type galaxies, La Barbera et al. (2010b) selected galaxies with the SDSS spectroscopic parameter $eClass < 0$ and photometric parameter $fracDev_r > 0.8$, following the criteria adopted by Bernardi et al. (2005). The parameter

fracDev provides the weight of the de Vaucouleurs component in the best fit exponential+de Vaucouleurs models, hence a large fracDev suggests the galaxy is better fitted by a de Vaucouleurs model than an exponential (disk) model. The parameter eClass, on the other hand, specifies the spectral type of a galaxy from a principal component analysis of the SDSS spectrum. La Barbera et al. (2010b) applied an additional criterion on the velocity dispersion from SDSS to ensure that they are reliable; only galaxies with central velocity dispersion σ_0 in the range of 70 to 420 kms^{-1} and with no spectroscopic warning are selected. The structural parameters of the SPIDER primary sample are derived in all available bands (*grizYJHK*) with single Sérsic profile fitting with 2DPhot (La Barbera et al., 2008).

We select a subsample of galaxies from SPIDER to be our local comparison sample with KCS. We follow similar criteria as in the structural parameter analysis of La Barbera et al. (2010b): a magnitude cut at the 95% completeness magnitude ($M_r \leq -20.55$), a χ^2 cut from the Sérsic fit for both *g*-band and *r*-band ($\chi^2 < 2.0$), and a seeing cut of $\leq 1.5''$ are applied. This results in a sample of 4050 objects. We then compute aperture *g* – *r* colour for the sample from direct numeral integration of the *g*-band and *r*-band Sérsic profiles to 5 kpc instead of using GALFIT total magnitudes. With the *g* – *r* colour we derive and select red-sequence galaxies within 2σ following the same method discussed in Section 2.5; we end up with a sample of 3634 objects (hereafter the SPIDER sample).

On top of that we use the group catalogue from La Barbera et al. (2010c) to select a subsample of galaxies residing in high density environments. The group catalogue is based on the updated friends-of-friends group catalogue from SDSS (Berlind et al., 2006), from which La Barbera et al. (2010c) re-derived the central redshift of the groups and obtained a list of the group members. Virial analyses are then performed to obtain the velocity dispersion, halo masses M_{200} , M_{500} and radius R_{200} , R_{500} of the groups (for details, see e.g. Lopes et al., 2009; La Barbera et al., 2010c). Applying a halo mass cut of $\log(M_{200}/M_\odot) \geq 14$ to the SPIDER sample, we end up with a subsample of 627 objects (hereafter the SPIDER cluster sample), which we will use as the main comparison sample for our high-redshift cluster galaxies.

Table 2.3: Photometry of the red sequence galaxies in XMMU J2235-2557

ID	R.A. (J2000)	Decl. (J2000)	H_{160}^a (MAG_AUTO)	$z_{850} - H_{160}^b$ (AB mag)	$z_{850} - J_{125}^c$ (AB mag)	$J_{125} - H_{160}^c$ (AB mag)	UVR^d passive	Spec- z^e
36	338.829482	-25.974178	21.105 ± 0.004	1.765 ± 0.010	1.414 ± 0.009	0.390 ± 0.005	1	1
61	338.815837	-25.971949	21.727 ± 0.008	1.359 ± 0.018	0.993 ± 0.017	0.419 ± 0.011	0	0
77	338.818075	-25.972015	22.351 ± 0.013	1.844 ± 0.037	1.147 ± 0.035	0.680 ± 0.019	0	0
148	338.833366	-25.967277	21.755 ± 0.008	1.527 ± 0.024	1.052 ± 0.023	0.527 ± 0.014	0	0
159	338.825351	-25.968396	21.965 ± 0.011	1.259 ± 0.015	0.834 ± 0.015	0.478 ± 0.010	0	1
170	338.836760	-25.961046	19.558 ± 0.003	1.956 ± 0.009	1.542 ± 0.008	0.451 ± 0.004	1	1
198	338.824435	-25.936956	22.339 ± 0.024	1.377 ± 0.025	1.017 ± 0.026	0.401 ± 0.032	1	0
220	338.845004	-25.940239	21.523 ± 0.014	1.694 ± 0.013	1.368 ± 0.012	0.365 ± 0.008	1	1
239	338.824725	-25.942130	22.059 ± 0.008	1.699 ± 0.018	1.336 ± 0.017	0.407 ± 0.008	1	0
296	338.839994	-25.957034	21.530 ± 0.005	1.377 ± 0.011	1.121 ± 0.009	0.291 ± 0.006	1	1
308	338.832707	-25.957812	20.763 ± 0.003	1.360 ± 0.006	1.012 ± 0.005	0.388 ± 0.003	1	0
343	338.840679	-25.959298	22.229 ± 0.006	1.844 ± 0.022	1.473 ± 0.021	0.425 ± 0.008	1	0
352	338.836309	-25.962228	20.400 ± 0.004	1.919 ± 0.009	1.535 ± 0.008	0.431 ± 0.004	1	1
357	338.830000	-25.959751	22.157 ± 0.007	1.436 ± 0.014	1.133 ± 0.013	0.343 ± 0.008	1	0
365	338.833995	-25.960121	22.414 ± 0.007	1.847 ± 0.021	1.453 ± 0.020	0.437 ± 0.010	1	0
368	338.837132	-25.959916	21.679 ± 0.005	1.869 ± 0.013	1.482 ± 0.012	0.429 ± 0.006	1	1
385	338.837337	-25.959744	21.709 ± 0.006	1.735 ± 0.013	1.388 ± 0.012	0.388 ± 0.006	1	0
407	338.836249	-25.960420	20.465 ± 0.003	1.915 ± 0.008	1.544 ± 0.006	0.410 ± 0.003	1	1
433	338.829341	-25.964228	21.407 ± 0.005	1.915 ± 0.013	1.527 ± 0.012	0.430 ± 0.006	1	1
478	338.853658	-25.943596	21.078 ± 0.005	1.955 ± 0.013	1.474 ± 0.012	0.526 ± 0.005	1	0
516	338.840945	-25.952995	21.867 ± 0.006	1.292 ± 0.011	0.795 ± 0.010	0.536 ± 0.007	0	0
534	338.840824	-25.953826	22.404 ± 0.012	1.527 ± 0.021	0.950 ± 0.021	0.620 ± 0.013	0	1
538	338.831556	-25.945870	22.172 ± 0.009	1.649 ± 0.018	1.398 ± 0.017	0.293 ± 0.009	1	0
552	338.838607	-25.953202	21.664 ± 0.010	1.426 ± 0.026	1.089 ± 0.026	0.396 ± 0.017	1	0
558	338.839434	-25.949475	20.955 ± 0.004	1.753 ± 0.009	1.435 ± 0.008	0.358 ± 0.004	1	1
571	338.857439	-25.946078	22.360 ± 0.007	1.480 ± 0.016	1.141 ± 0.015	0.375 ± 0.009	1	0
576	338.841456	-25.949101	21.024 ± 0.003	1.803 ± 0.008	1.460 ± 0.007	0.386 ± 0.004	1	1
585	338.856925	-25.949546	22.408 ± 0.008	1.896 ± 0.023	1.514 ± 0.022	0.442 ± 0.010	1	0
588	338.830650	-25.948840	21.502 ± 0.006	1.764 ± 0.015	1.375 ± 0.014	0.426 ± 0.007	1	0
599	338.856012	-25.947936	20.497 ± 0.003	1.915 ± 0.008	1.474 ± 0.007	0.482 ± 0.004	1	1
611	338.857465	-25.949521	21.535 ± 0.007	1.276 ± 0.012	0.820 ± 0.012	0.504 ± 0.009	0	0
617	338.858363	-25.948902	21.424 ± 0.009	1.515 ± 0.016	1.076 ± 0.015	0.489 ± 0.011	0	0
618	338.823636	-25.948795	22.058 ± 0.009	1.837 ± 0.023	1.313 ± 0.022	0.565 ± 0.011	1	0
637	338.844783	-25.951602	21.365 ± 0.004	1.486 ± 0.008	1.227 ± 0.007	0.303 ± 0.004	1	1
642	338.842302	-25.951626	22.149 ± 0.007	1.785 ± 0.019	1.427 ± 0.018	0.405 ± 0.008	1	1

^a MAG_AUTO magnitude from SExtractor.

^b $z_{850} - H_{160}$ colours are derived using PSF-matched 1'' aperture magnitudes from SExtractor.

^c Derived using 1'' aperture magnitudes from SExtractor. The quantities are not PSF matched and are only used for the UVR selection.

^d '1' indicates that the object is passive according to our UVR selection criteria.

^e '1' indicates that the object is spectroscopically confirmed.

Table 2.4: Photometry of the red sequence galaxies in XMMXCS J2215-1738

ID	R.A. (J2000)	Decl. (J2000)	H_{160}^a (MAG_AUTO)	$z_{850} - H_{160}^b$ (AB mag)	$z_{850} - J_{125}^c$ (AB mag)	$J_{125} - H_{160}^c$ (AB mag)	UVR^d passive	Spec- z^e
121	333.977575	-17.648633	22.142 ± 0.005	2.199 ± 0.016	1.560 ± 0.015	0.721 ± 0.005	0	0
317	334.002392	-17.643430	21.816 ± 0.003	1.817 ± 0.010	1.436 ± 0.008	0.402 ± 0.003	1	0
321	334.000533	-17.643555	22.249 ± 0.004	1.815 ± 0.013	1.025 ± 0.010	0.766 ± 0.005	0	0
342	334.002320	-17.643223	21.523 ± 0.003	2.216 ± 0.011	1.789 ± 0.009	0.444 ± 0.003	1	0
498	333.992567	-17.639461	22.067 ± 0.004	1.802 ± 0.011	1.213 ± 0.009	0.605 ± 0.004	0	0
500	333.984598	-17.636046	22.364 ± 0.006	1.489 ± 0.013	0.868 ± 0.010	0.580 ± 0.006	0	0
522	333.999785	-17.638891	22.460 ± 0.006	2.315 ± 0.026	1.764 ± 0.023	0.513 ± 0.006	1	0
528	333.983477	-17.639039	21.874 ± 0.003	2.020 ± 0.010	1.580 ± 0.008	0.441 ± 0.003	1	1
548	334.003804	-17.638355	21.891 ± 0.003	1.943 ± 0.009	1.543 ± 0.007	0.417 ± 0.003	1	1
555	333.991651	-17.638347	21.877 ± 0.004	2.152 ± 0.013	1.654 ± 0.011	0.531 ± 0.004	1	1
603	333.992265	-17.637311	22.186 ± 0.005	2.352 ± 0.018	1.757 ± 0.018	0.679 ± 0.005	1	0
614	333.993634	-17.636243	21.399 ± 0.003	2.037 ± 0.008	1.597 ± 0.007	0.497 ± 0.003	1	1
650	333.995179	-17.636047	22.331 ± 0.004	1.700 ± 0.011	1.256 ± 0.009	0.436 ± 0.004	1	1
664	333.993134	-17.635098	21.784 ± 0.003	2.096 ± 0.010	1.653 ± 0.008	0.454 ± 0.003	1	0
691	333.987102	-17.634603	21.852 ± 0.011	1.339 ± 0.010	0.774 ± 0.008	0.502 ± 0.006	0	1
695	333.995923	-17.634019	21.442 ± 0.003	2.230 ± 0.010	1.738 ± 0.008	0.493 ± 0.003	1	1
697	333.989467	-17.633262	22.281 ± 0.007	1.833 ± 0.021	1.244 ± 0.020	0.656 ± 0.008	0	0
698	333.979975	-17.634479	22.049 ± 0.005	1.613 ± 0.010	1.192 ± 0.009	0.459 ± 0.004	1	0
702	333.998064	-17.634756	21.965 ± 0.003	1.938 ± 0.013	1.540 ± 0.012	0.442 ± 0.003	1	0
709	333.999781	-17.630649	21.237 ± 0.031	1.714 ± 0.009	1.083 ± 0.007	0.534 ± 0.004	0	0
717	333.998622	-17.633249	22.150 ± 0.005	2.014 ± 0.017	1.470 ± 0.016	0.618 ± 0.005	0	0
727	333.988433	-17.634018	21.397 ± 0.003	1.815 ± 0.007	1.468 ± 0.005	0.391 ± 0.002	1	0
728	333.993570	-17.632903	21.281 ± 0.003	1.983 ± 0.007	1.576 ± 0.005	0.417 ± 0.002	1	1
743	333.997259	-17.633831	21.727 ± 0.003	1.376 ± 0.008	0.927 ± 0.006	0.437 ± 0.003	0	0
764	333.995228	-17.633072	21.638 ± 0.003	1.857 ± 0.008	1.427 ± 0.006	0.436 ± 0.003	1	1
768	333.998707	-17.632975	21.988 ± 0.004	2.285 ± 0.017	1.478 ± 0.016	0.858 ± 0.005	0	0
771	333.988630	-17.632683	22.008 ± 0.005	2.313 ± 0.020	1.603 ± 0.019	0.790 ± 0.006	0	0
774	333.999416	-17.633098	21.838 ± 0.003	1.832 ± 0.008	1.442 ± 0.006	0.374 ± 0.003	1	1
870	333.986653	-17.622715	22.279 ± 0.007	1.811 ± 0.019	1.525 ± 0.019	0.445 ± 0.007	0	0
889	333.979925	-17.622857	21.876 ± 0.003	2.129 ± 0.010	1.663 ± 0.008	0.469 ± 0.003	1	1
1018	333.984021	-17.625445	22.271 ± 0.004	1.868 ± 0.012	1.316 ± 0.010	0.543 ± 0.005	1	0
1046	333.996057	-17.627185	22.032 ± 0.004	1.827 ± 0.011	1.411 ± 0.009	0.447 ± 0.004	1	0
1051	333.984515	-17.627253	21.754 ± 0.003	2.035 ± 0.010	1.643 ± 0.009	0.486 ± 0.003	1	0
1058	333.984504	-17.627123	21.958 ± 0.004	2.060 ± 0.012	1.722 ± 0.010	0.389 ± 0.004	1	0
1102	333.993831	-17.629828	21.966 ± 0.004	2.519 ± 0.018	1.810 ± 0.017	0.779 ± 0.005	1	0
1125	334.001558	-17.628495	22.179 ± 0.004	1.211 ± 0.008	0.813 ± 0.006	0.398 ± 0.004	0	0
1129	333.990396	-17.629299	21.738 ± 0.004	2.193 ± 0.012	1.548 ± 0.011	0.692 ± 0.004	1	1
1182	333.984031	-17.630501	21.047 ± 0.002	1.934 ± 0.005	1.520 ± 0.004	0.420 ± 0.002	1	1
1189	334.002686	-17.630979	21.799 ± 0.004	2.213 ± 0.012	1.712 ± 0.010	0.518 ± 0.003	1	1
1200	334.001576	-17.630686	21.712 ± 0.003	1.880 ± 0.008	1.364 ± 0.006	0.532 ± 0.003	0	1
1202	333.988429	-17.631413	21.884 ± 0.005	1.718 ± 0.011	1.085 ± 0.009	0.677 ± 0.005	0	1
1212	333.996308	-17.631707	21.369 ± 0.003	2.215 ± 0.010	1.662 ± 0.009	0.567 ± 0.003	1	1
1217	333.993226	-17.631543	21.936 ± 0.003	1.823 ± 0.009	1.359 ± 0.007	0.435 ± 0.003	1	0
1225	333.977494	-17.632007	21.529 ± 0.003	2.125 ± 0.009	1.712 ± 0.008	0.446 ± 0.003	1	0
1335	334.004870	-17.622908	20.385 ± 0.001	1.430 ± 0.003	0.963 ± 0.002	0.474 ± 0.001	0	0

^a MAG_AUTO magnitude from SExtractor.

^b $z_{850} - H_{160}$ colours are derived using PSF-matched 1'' aperture magnitudes from SExtractor.

^c Derived using 1'' aperture magnitudes from SExtractor. The quantities are not PSF matched and are only used for the UVR selection.

^d '1' indicates that the object is passive according to our UVR selection criteria.

^e '1' indicates that the object is spectroscopically confirmed.

Table 2.5: Photometry of the red sequence galaxies in Cl 0332-2742

ID	R.A. (J2000)	Decl. (J2000)	i_{814} ^a (total)	$i_{814} - J_{125}$ ^a (AB mag)	$z_{850} - H_{160}$ ^b (AB mag)	$U - V$ ^c (AB mag)	$V - J$ ^c (AB mag)	UVJ ^d passive	Spec- z ^e
11827	53.044943	-27.774395	21.168 ± 0.007	2.520 ± 0.017	2.418 ± 0.017	2.046	1.334	1	1
12177	53.052200	-27.774770	21.682 ± 0.005	2.422 ± 0.011	2.173 ± 0.014	1.924	1.145	1	1
12347	53.043829	-27.774707	22.188 ± 0.007	2.351 ± 0.015	2.059 ± 0.015	1.764	1.143	1	0
12412	53.049043	-27.774496	23.478 ± 0.018	1.960 ± 0.032	1.689 ± 0.031	1.432	1.493	0	0
13096	53.046607	-27.772185	23.063 ± 0.013	2.315 ± 0.030	2.045 ± 0.025	1.811	1.095	1	0
19839	53.030910	-27.738183	22.595 ± 0.009	2.203 ± 0.026	1.980 ± 0.020	1.620	1.077	1	0
21613	53.064240	-27.727622	22.603 ± 0.012	2.624 ± 0.051	2.496 ± 0.028	2.194	1.431	1	0
21853	53.062822	-27.726461	21.458 ± 0.004	2.119 ± 0.010	1.978 ± 0.011	1.724	1.057	1	1
22281	53.059632	-27.725791	22.559 ± 0.008	2.285 ± 0.023	2.029 ± 0.019	1.700	0.967	1	1
22701	53.122820	-27.722807	22.371 ± 0.006	1.748 ± 0.021	1.654 ± 0.015	1.400	1.110	0	0
22777	53.124958	-27.722957	22.690 ± 0.008	2.323 ± 0.039	2.150 ± 0.019	1.833	1.180	1	0
24147	53.152727	-27.716252	22.150 ± 0.006	2.455 ± 0.057	2.160 ± 0.017	1.865	1.199	1	0
24517	53.151174	-27.713724	21.618 ± 0.004	2.514 ± 0.043	2.287 ± 0.015	1.995	1.131	1	1
24882	53.116399	-27.712702	22.277 ± 0.006	2.264 ± 0.023	2.073 ± 0.017	1.766	1.014	1	1
25338	53.108524	-27.710147	22.107 ± 0.006	2.595 ± 0.026	2.343 ± 0.018	2.012	1.045	1	0
25972	53.104571	-27.705422	21.839 ± 0.006	2.465 ± 0.021	2.241 ± 0.016	1.918	1.159	1	1
25989	53.129375	-27.707345	22.058 ± 0.006	2.009 ± 0.020	1.712 ± 0.012	1.473	0.756	1	0

^a Total magnitudes in i_{814} and J_{125} band, adopted from the 3D-HST catalogue (Skelton et al., 2014).

^b $z_{850} - H_{160}$ colours are derived using PSF-matched 1'' aperture magnitudes from SExtractor.

^c Rest frame PSF-matched ($U - V$) and ($V - J$) magnitudes, adopted from the 3D-HST catalogue (Skelton et al., 2014).

^d '1' indicates that the object is passive according to the UVJ selection criteria.

^e '1' indicates that the object is spectroscopically confirmed.

Chapter 3

Methods and Analysis

In this chapter, we focus on the methods we used to derive the photometric properties of the cluster galaxies from the images and the subsequent analysis. We first describe in detail the procedure we used to derive light-weighted structural parameters and colour gradients in Section 3.1 and 3.2. We then move to mass-related quantities such as the stellar mass-to-light ratio – colour relation, resolved mass maps and mass-weighted structural parameters in Section 3.3, 3.5 and 3.6. To ensure the reliability of our derived parameters, we examine the parameters with various tests and estimate the uncertainties with simulated galaxies. We present the setup and results of these simulations in Section 3.7. In addition, we compare our derived parameters with literature whenever available. Part of this chapter is discussed in Chan et al. (2016).

3.1 Light-weighted structural parameters

We first measure the light-weighted structural parameters of the passive galaxies, such as their half-light sizes and axial ratios. Galaxy sizes are commonly derived through parametric fitting, either through one-dimensional (1D) fitting of the surface brightness profiles or two-dimensional (2D) fitting of the images. In theory, fitting in 1D and in 2D should give identical results, as statistically fitting an averaged smaller group of points and fitting all the points without averaging are equivalent (see, Peng, 2015, for a detailed discussion). In practice, the complication is on proper extraction of the 1D surface brightness profiles. A common practice is to use isophote fitting, which extracts light from elliptical annuli on the images. This works reasonably well if the galaxy is well-resolved, isolated in the image and has high S/N ratio. Nevertheless, if a galaxy have very close neighbour or in a field with very high object density (such as in galaxy clusters), it is not straightforward how one can deal with neighbour contamination. Masking the neighbouring object could be an option, however galaxies can have very extended halos and in close pairs, there is almost no way to completely deblend these contaminations. In addition, it is often difficult to propagate this ambiguity in extracting 1D profiles to the fitting process, which in some cases can introduce systematic errors to the derived structural parameters (see the discussion in, e.g.

Byun & Freeman, 1995).

Fitting in 2D, on the other hand, does not require the extraction of surface brightness profiles and can easily take into account the light contribution of the neighbouring objects by fitting them simultaneously. An additional crucial advantage of 2D fitting is that it takes into account the effect of the point spread function (PSF) using convolution techniques. This is very important for high redshift galaxies due to their small intrinsic sizes (often with order of magnitude that are comparable to the FWHM of the PSF) and low S/N data. 2D fitting is hence preferred for our work, since we are studying passive galaxies in distant high redshift clusters which are faint, small galaxies in crowded regions.

Numerous software has been developed specifically for fitting galaxy images in 2D, such as GIM2D (Simard et al., 2002), GALFIT (Peng et al., 2002), GASP2D (Méndez-Abreu et al., 2008) and 2DPHOT (La Barbera et al., 2008). Even with these sophisticated tools, results can suffer from systematics if one takes inadequate consideration in any of the pre-fitting processing steps, including determining background sky levels, deriving PSF, providing reasonable initial guesses of the parameters, and treatment of neighbouring objects. Häussler et al. (2007) showed that the performance GALFIT is substantially better than that of GIM2D for fainter galaxies. Recently a number of packages have been developed as wrappers of these fitting codes to homogenise the processing procedures, including GALAPAGOS (Barden et al., 2012) and PyMorph (Meert et al., 2013).

We measure the light-weighted structural parameters of the passive galaxies in various *HST* bands for the three KCS clusters, i_{775} , z_{850} , Y_{105} , J_{125} and H_{160} for XMMU J2235-2557, z_{850} , J_{125} , JH_{140} and H_{160} for XMMXCS J2215-1738 and z_{850} , J_{125} , H_{160} for Cl 0332-2742 (see Table 2.1 for a summary on the *HST* imaging).

The structural parameters are derived using a self-modified version of GALAPAGOS (Barden et al., 2012) with GALFIT (v.3.0.5). GALAPAGOS combines source detection with SExtractor and 2D galaxy fitting with GALFIT, as well as other IDL routines that perform some of the abovementioned pre-fitting processing steps. GALAPAGOS first runs SExtractor to detect sources in the image. For each detected object, it generates a postage stamp and measures the local sky level around the object using an elliptical annulus flux growth routine. The routine iteratively calculates the average background level in elliptical annuli centred on the object as a function of radius, and stops once the slope of the background level over the last few annuli flattens. The local sky value is then determined from the last few annuli. We examine different settings of this sky estimation routine, such as the width and spacing of the annulus, to ensure the robustness of the sky value estimation. GALAPAGOS then identifies adjacent sources from the SExtractor segmentation map and determines the number of neighbours inside the postage stamp. It outputs an object file including information of the sky level and locations of neighbouring objects. This object file is used by GALFIT, in order to model the galaxy surface brightness profile. Neighbouring objects are either masked out or fitted simultaneously if their light profiles have a non-negligible influence to the central object.

We have modified GALAPAGOS for two main purposes to facilitate the fitting:

1. As our ACS and WFC3 images have a different spatial resolution (see Section 2.3.2

for details), we modify GALAPAGOS to allow the use of a single detection catalogue (in our case, the H_{160} band) in all bands. This allows us to use the same photometric detection catalogue as input, and at the same time retain the high(er) spatial resolution in the ACS images for fitting.

2. The code is adjusted to generate postage stamp of each galaxy from the RMS maps derived from ERR weight maps output by Astrodrizzle (see Section 2.3.2 for details) and use them for fitting with GALFIT. The original GALAPAGOS code does not allow these maps as input and rely on the internal error estimation in GALFIT to perform χ^2 fitting. The RMS maps that we generate from ERR weight maps are a more realistic representation of the noise than the internal error estimation in GALFIT, as they include pixel-to-pixel exposure time differences originated from image drizzling and dithering patterns in observations, as well as a more accurate estimation of shot noise.

We fit a two-dimensional Sérsic profile (Sersic, 1968) to each galaxy (see Section 1.3.1 and Equation 1.11 for a description), which can be written as

$$I(a) = I_e \exp \left[-b_n \left(\left(\frac{a}{a_e} \right)^{1/n} - 1 \right) \right] \quad (3.1)$$

along the semi-major axis a , where the effective intensity I_e can be described by

$$I_e = \frac{L_{tot}}{2\pi n q a_e^2 b_n^{-2n} \Gamma(2n)} \quad (3.2)$$

where $\Gamma(2n)$ is the complete gamma function.

The Sérsic profile of a galaxy can be characterised by five independent parameters: the total luminosity L_{tot} , the Sérsic index n , the effective semi-major axis a_e , the axis ratio q ($= b/a$, where a and b is the major and minor axis respectively) and the position angle $P.A.$. The parameter b_n is a function of the Sérsic index ($\Gamma(2n) = 2\gamma(2n, b_n)$, where γ is the incomplete gamma function) and can only be solved numerically (Ciotti, 1991).

All five parameters as well as the centroid (x, y) of the galaxy are left to be free parameters in our fitting process with GALFIT. The constraints of each parameter for GALFIT are set to be: $0.2 < n < 8$, $0.3 < a_e < 500$ (pix), $0 < mag < 40$, $0.0001 < q < 1$, $-180^\circ < P.A. < 180^\circ$. The sky level is fixed to the value determined by GALAPAGOS. The Sérsic model is convolved with the PSF constructed from stacking bright unsaturated stars in the images (see Section 2.3.4 for details about the PSF derivation). We provide the light-weighted structural parameters of the three clusters in Table 3.1, Table 3.2 and Table 3.3, respectively.

Four galaxies from our sample and their best-fit Sérsic H_{160} models and residuals are shown in Figure 3.1 for illustrative purposes. These objects have been selected to show the impact of clustering of sources in dense regions, and the effect of very close neighbours. Galaxy 170, the BCG of XMMU J2235-2557, is located in the central region of the cluster with high object density. Galaxy 642 is located in a more outer region of the cluster, yet is

still affected by an extremely close neighbour. Galaxy 317 is a close pair (with object 342) in the outer region of XMMXCS J2215-1738. Galaxy 11827 locates at a crowded region of the Tanaka et al. (2013) group in Cl 0332-2742. As seen in Figure 3.1, even in the cluster centre where there are multiple neighbouring objects, GALFIT with GALAPAGOS can accurately minimise the residual of individual objects simultaneously. Below we discuss the reliability and uncertainties in these light-weighted structural parameters.

3.1.1 Quality control of the fitted structural parameters

GALAPAGOS coupled with GALFIT performs very well in most cases. However in some exceptions, it is rather tricky to obtain a good-quality fit due to various issues. In this section we investigate and discuss the stability and quality control of the fits. The global systematics and uncertainties will be addressed in Section 3.7.

We find that using an inadequate number of fitting components for the neighbouring sources (due to inadequate deblending in the SExtractor catalogue or appearance of extra structures / sources in bluer bands, e.g. z_{850} band, compare to our H_{160} detection catalogue) can lead to significant residuals that adversely affect the fit of the primary object. Similarly, since GALAPAGOS fits sources with a single Sérsic profile by default, GALFIT will likely give unphysical outputs for unresolved sources / stars in the field (with a_e hitting the lower boundary of the constraint $a_e = 0.3$ pix, or Sérsic index hitting the upper boundary $n = 8$) or even not converging in these cases, which again affects the result of the object of primary interest. Moreover, the best-fit output can vary if we use a different treatment for neighbouring sources. We notice that in a few cases the results can be very different depending upon whether neighbouring sources are masked or are fitted simultaneously.

To ensure high reliability, we perform three additional checks for each galaxy in our sample, Figure 3.2 illustrates the difference before and after these checks:

1. We visually inspect the fits as well as the segmentation maps (output by SExtractor) in each band to ensure adjacent sources are well-fitted. Extra Sérsic components are added to missing or poorly fitted neighbouring objects iteratively if necessary. In the top row of Figure 3.2, the neighbouring object above galaxy 599 in cluster XMMU J2235-2557 was initially poorly fitted and this affected the fit of our primary object. It is clear from the image and residual that an extra Sérsic component is needed. Note the significant improvement in the residuals afterwards, as well as the change in Sérsic index and size.
2. For neighbours for which GALFIT gives ill-constrained results (i.e. hitting the boundaries of the constraints), we replace the Sérsic model with a PSF model and rerun the fit, which often improves the convergence and the quality of the best-fit model. Regarding this, Barden et al. (2012) explained the need of fitting Sérsic profiles to saturated stars instead of PSF model in GALAPAGOS, since the PSF often lacks the dynamic range to capture the diffraction spikes of the bright saturated stars. In our case this is not necessary since there are only a few bright saturated stars in the

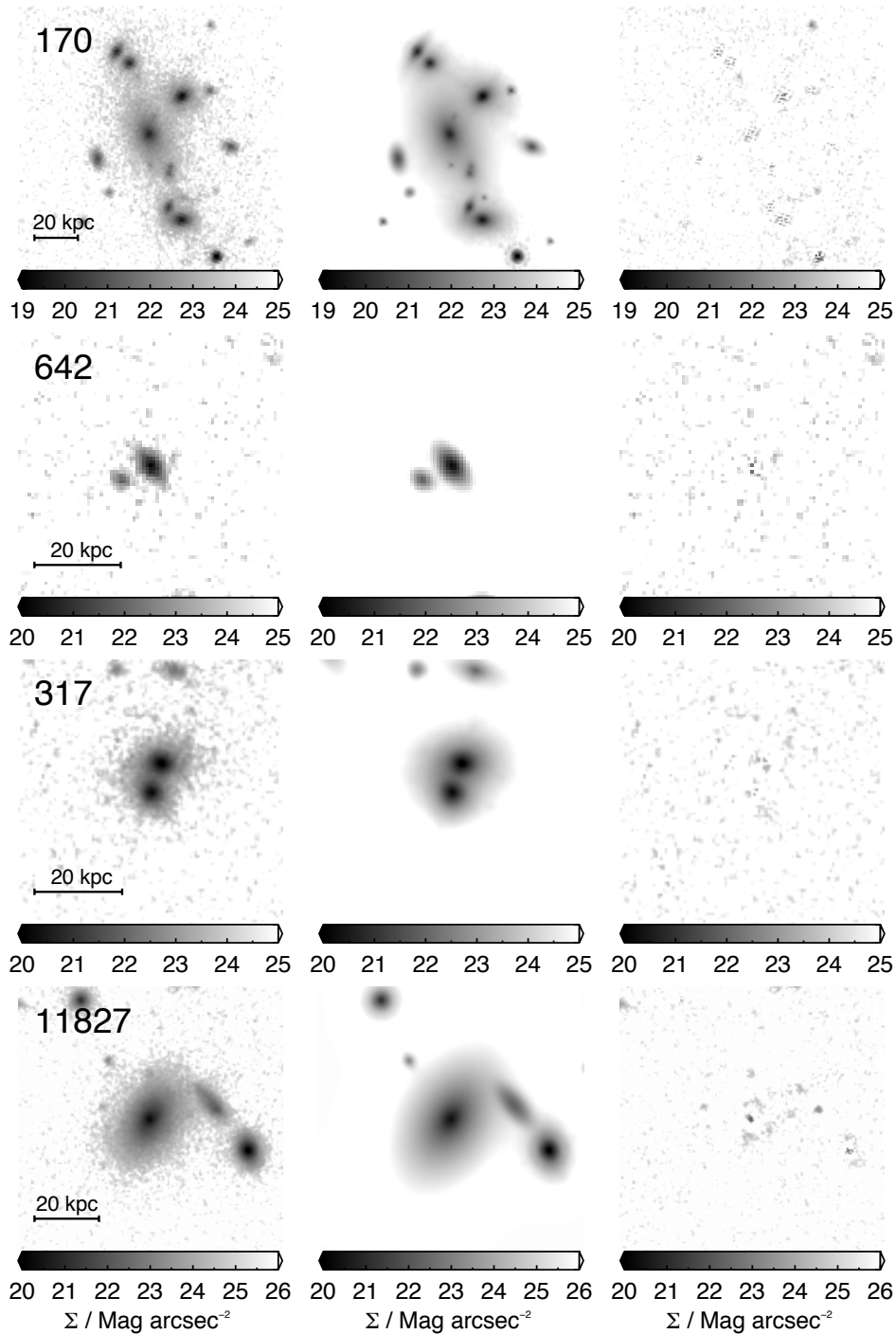


Figure 3.1: Examples of surface brightness profile fitting of four passive galaxies in the three KCS clusters. From left to right: H_{160} galaxy image cut-out centered on the primary object, GALFIT best-fit models and residuals. The colour scale is inverted to enhance contrast. The examples are selected to demonstrate the clustering of sources and we refer to the text for their descriptions. Multiple objects are fitted simultaneously as described in Section 3.1.

field, for which we can safely mask their diffraction spikes. These stars are also far away from most of our objects of interest. Galaxy 77 in cluster XMMU J2235-2557 in the middle row of Figure 3.2 demonstrates the result of this check, the neighbour at the top right corner is a star which was poorly fitted by a Sérsic model (second panel from the left). The residual is much lower after we replaced it with a PSF and this leads to better convergence in the primary object.

3. We compare the results of masking and simultaneously fitting neighbouring objects. In most cases the two methods give results that are within 1σ . The galaxy in the bottom row (ID 1355 in cluster XMMXCS J2215-1738) shows the differences in the output structural parameters in different treatment of neighbours. For galaxies with close neighbours (e.g. within $5 a_e$) we prefer to fit them simultaneously as any inadequate or over-masking can result in problematic fits, judging by examining the residual map output by GALFIT. On the other hand, masking is more suitable when the neighbouring objects are not axisymmetric or show certain substructures, which causes the single Sérsic fit to not reach convergence.

3.2 Elliptical aperture photometry and color gradients

In addition to structural parameters, we derive $z_{850} - H_{160}$ colour profiles and colour gradients for the passive sample with PSF-matched elliptical annular photometry.

Previous literature derive colour profiles with annular photometry (i.e. with sets of concentric apertures, e.g. Guo et al., 2011). While this may be reasonable for round objects, azimuthally averaging does not make physical sense for objects with low axis ratio and may lead to inaccurate results. Morishita et al. (2015) demonstrates that deriving colour profiles with elliptical apertures has certain advantages over circular apertures. Using circular apertures can bias the profiles at the outer radius where the effect of the axis ratio is more severe. This would worsen the S/N of the profile as the scatter in each annuli is larger, and artificially bias the profile to be more centrally concentrated.

To derive the colour profiles, we convert the 2D postage stamps of each galaxy in both z_{850} and H_{160} bands into 1D radial surface brightness profiles along the major axis. The sky levels obtained by GALAPAGOS are subtracted from the PSF-matched z_{850} and H_{160} images. We then perform elliptical annular photometry on the images in both bands at the galaxy centroid derived from GALFIT. The GALFIT best-fit axis ratios and position angles of individual galaxies (in H_{160} band) are used to derive a set of elliptical apertures for each galaxy.

Due to the proximity of objects in the cluster, it is necessary to take into account (as in 2D fitting) the effect of the neighbouring objects. Since now we already have the best-fit Sérsic models for the neighbouring objects in the images (if not masked), we can remove their light contribution by subtracting the best Sérsic fit (or PSF fit in some cases) in both

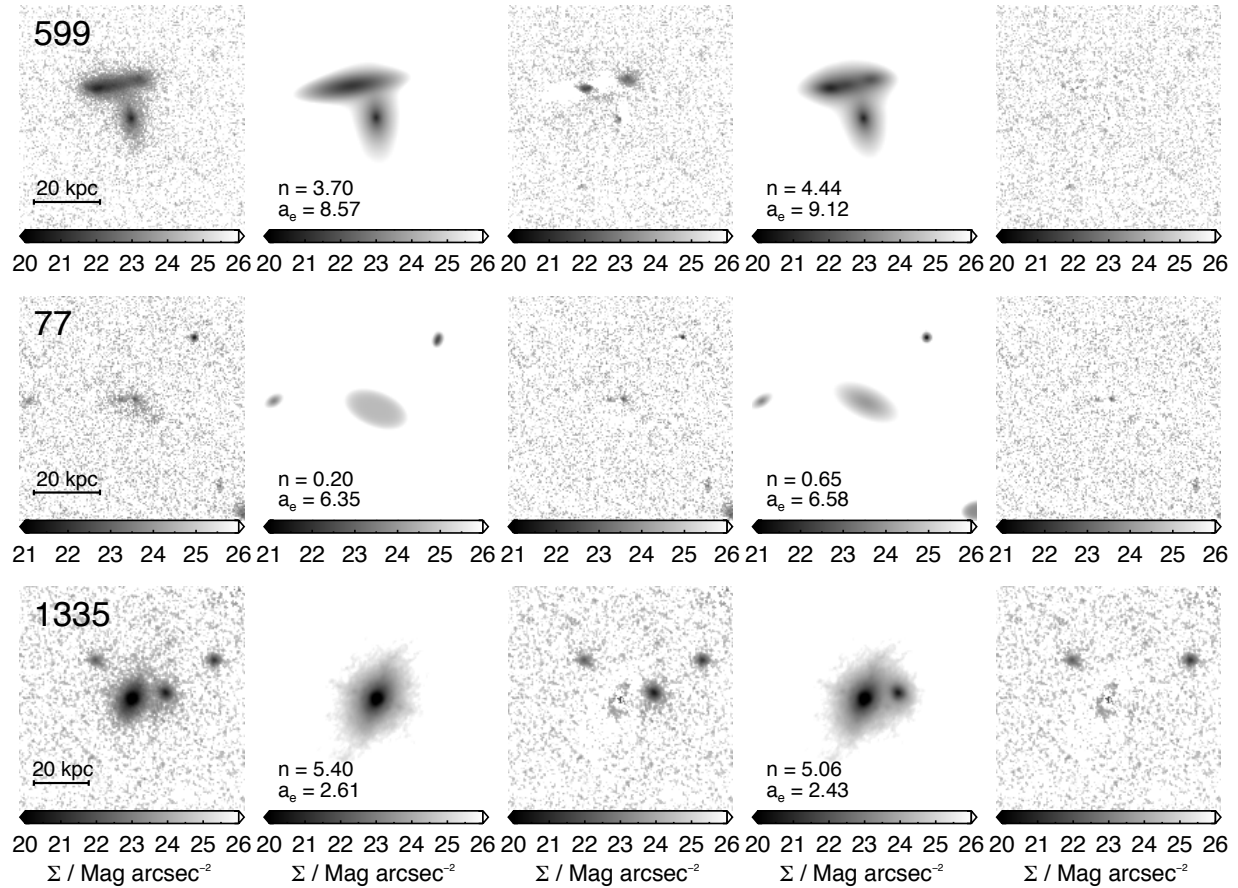


Figure 3.2: Examples of the additional checks on the fitted structural parameters. From left to right: H_{160} galaxy image cut-out centered on the primary object, GALFIT models and residuals before the checks, GALFIT best-fit models and residuals after the checks. The fitted Sérsic indices and effective semi-major axis (in kpc) are given in the model panels. From top to bottom: galaxy ID 599 illustrates the need of adding extra Sérsic component in an neighbouring object (Check 1). Galaxy ID 77 illustrates the need of replacing the Sérsic model with a PSF model for a neighbour (Check 2). Galaxy ID 1335 shows an example of masking and simultaneously fitting neighbouring objects (Check 3). See text for details. The colour scale is inverted to enhance contrast.

bands. While the removal of these objects might not be perfect (due to imperfect fits), we find that this extra correction can remove the majority of the flux of the neighbouring objects contributing to surface brightness profiles. For some galaxies the colour profiles show substantial change after we apply the correction.

We then obtain their $z_{850} - H_{160}$ colour profiles by subtracting the surface brightness profiles of the two bands, and measure the colour gradients of individual galaxies by fitting the logarithmic slope along the major axis, which are defined as follows:

$$z_{850} - H_{160} = \nabla_{z_{850}-H_{160}} \times \log(a/a_e) + Z.P. \quad (3.3)$$

where $\nabla_{z_{850}-H_{160}}$ is the (slope of) the colour gradient and $Z.P.$ is the colour of the profile at $a = a_e$.

At redshift $z \sim 1.5$ the $z_{850} - H_{160}$ colour gradient corresponds roughly to the rest-frame ($U - R$) colour gradient (∇_{U-R}).

The depth and angular resolution of our ACS and WFC3 data allow us to derive a 1D colour profile accurately to $\sim 3 - 4 a_e$, hence the colour gradient is fitted in the radial range of PSF half-width-half-maximum (HWHM) $< a < 3.5 a_e$. We note that the colour gradients of most galaxies, as well as the median colour gradient, do not strongly depend on the adopted fitting radial range. The colour profiles are in general well-described by logarithmic fits. Figure 3.3 shows the colour profiles and logarithmic gradient fits of four passive galaxies in XMMU J2235-2557 as an example.

We performed a test to investigate whether applying a S/N threshold before fitting the colour profiles would change the result, although in theory the error of the colour should have been taken into account in the fitting process. Figure 3.4 shows the slope of the colour gradient vs. applied S/N threshold of the objects in XMMU J2235-2557. For the majority of the sample, applying a S/N threshold does not have a large impact, and the median colour gradient of the sample is extremely stable over the S/N threshold. Only three galaxies show deviation more than 1σ after we apply a large S/N threshold. We find that this is mainly due to the lack of data points to quantify the radial change. Hence, we conclude that this is not a large issue and is unlikely to change any of our conclusions.

3.3 Stellar mass-to-light ratio – colour relation

We estimate the stellar mass-to-light ratios of the cluster galaxies using an empirical relation between the observed colour and the stellar mass-to-light ratio. As we explained in Section 1.5.1, this method has the advantage of obtaining M_*/L (and stellar masses M_*) for a large sample of galaxies with only the requirement of a suitable combination of imaging bracketing the 4000\AA break.

At $z \sim 1.5$, the $z_{850} - H_{160}$ colour is the perfect candidate for this purpose as it straddles the 4000\AA break and at the same time has a wide dynamic range. This colour is sensitive to variations in the properties of the stellar population (i.e. stellar age, dust and metallicity). In addition, the effects of these variations are relatively degenerate on the colour - M_*/L

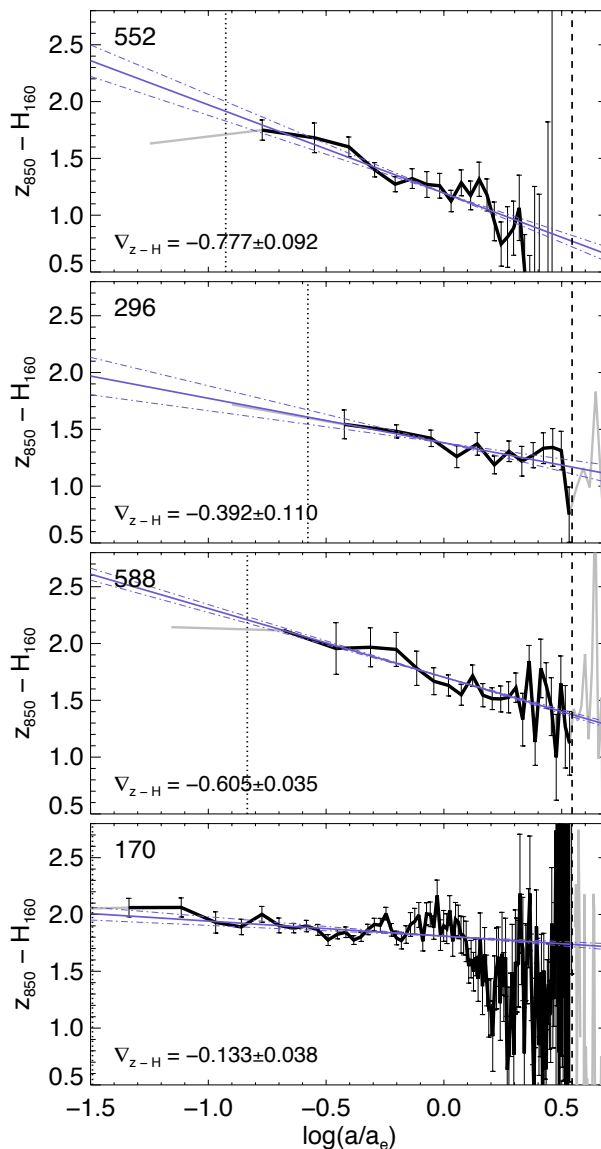


Figure 3.3: Examples of colour profile fitting of four passive galaxies in XMMU J2235-2557. From top to bottom: colour profiles for galaxies ID 552, 296, 588 and 170 along the logarithmic major axis ($\log(a/a_e)$). The gray line in each panel is the elliptical-averaged $z_{850} - H_{160}$ colour profile. Regions that are fitted (PSF HWHM $< a < 3.5 a_e$) are overplotted in black. The vertical black dotted and dashed line show the minimum (PSF HWHM) and maximum radial distance for fitting ($3.5 a_e$). The error bars show the error on the mean of the $z_{850} - H_{160}$ colour at each distance. The blue solid line is the best logarithmic gradient fits, and the blue dotted-dashed lines are the $\pm 1\sigma$ error of the slope.

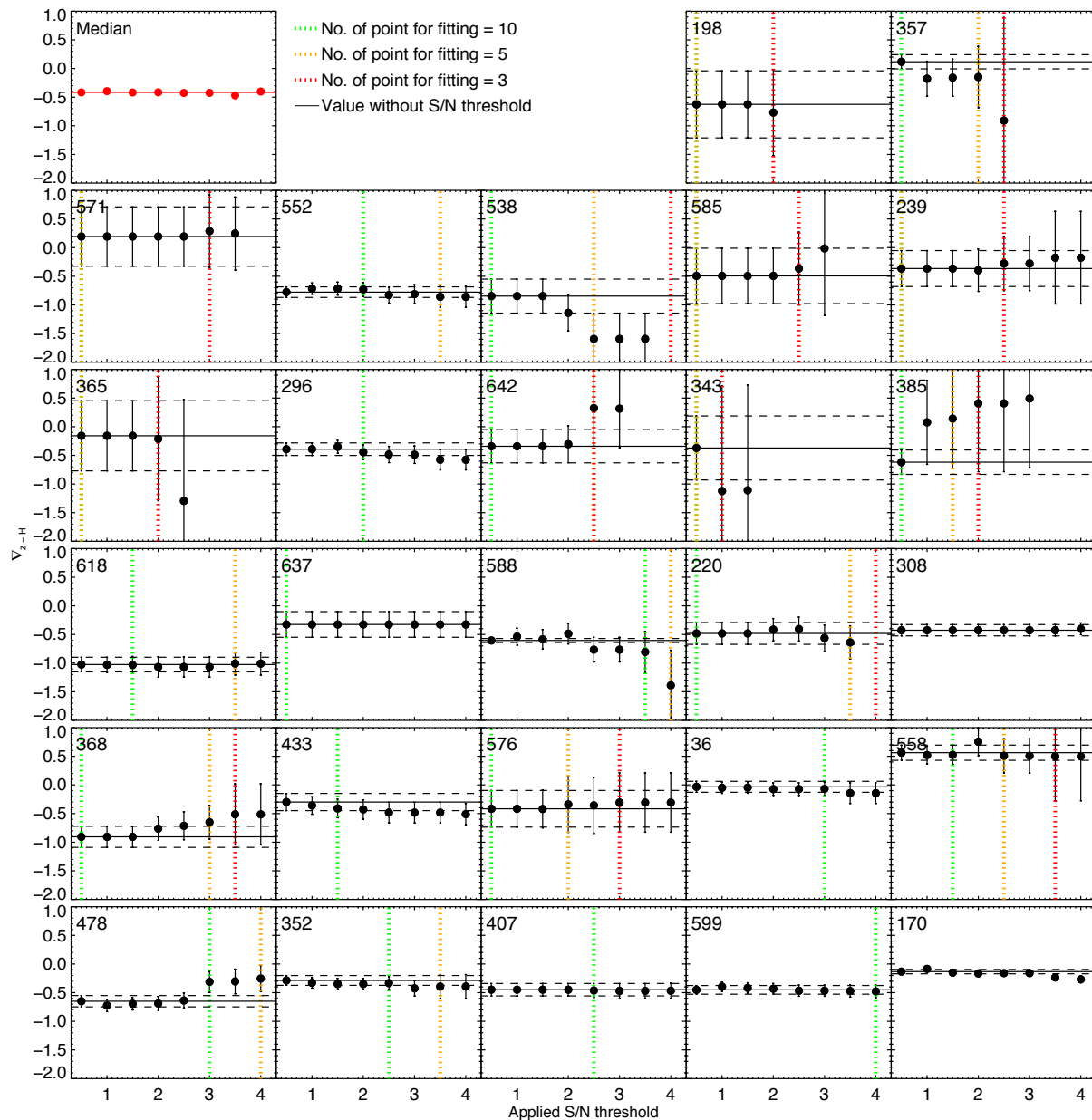


Figure 3.4: The effect of applying different S/N thresholds on colour profile fitting in XMMU J2235-2557. Top leftmost panel shows the median colour gradient of the red sequence galaxies in XMMU J2235-2557 vs. S/N thresholds. Each of the other panels corresponds to a galaxy with its ID on the top left corner. In each panel, the black solid and dashed line correspond to the value and 1σ error on the colour gradient without any S/N threshold (i.e. S/N threshold = 0). The green, orange and red dotted lines indicate the number of remaining data points for fitting (10,5,3) for a certain applied S/N threshold.

plane, as they are almost parallel to the relation (e.g Bell & de Jong, 2001; Bell et al., 2003; Szomoru et al., 2013), which makes this colour a useful proxy for the M_*/L .

3.3.1 The calibration sample

To calibrate a relation between $z_{850} - H_{160}$ colours and M_*/L , we need to rely on a separate reference population of galaxies that cover the properties and redshift range of our sample. We use the public catalogue from the NEWFIRM medium band survey (NMBS), which contains a large population of ~ 13000 galaxies at $z > 1.5$ (Whitaker et al., 2011). The survey employs a relatively new technique of observing with medium-bandwidth NIR filters (J_1, J_2, J_3, H_1, H_2) using the NOAO Extremely Wide-Field Infrared Imager (NEWFIRM) on the Mayall 4 m Telescope on Kitt Peak. These NIR filters (J_1, J_2, J_3, H_1, H_2) are finer in wavelength and enable them to sample the Balmer or 4000\AA break at a higher resolution than standard NIR filters, which improves the accuracy of the photometric redshifts.

The NMBS catalogue combines existing ground-based and space-based UV to mid-IR data, and new near-IR medium band NEWFIRM data in the AEGIS and COSMOS fields. It includes photometries in 37 bands in COSMOS (and 20 in AEGIS), spectroscopic redshifts for a subset of the sample, and high accuracy photometric redshifts (with $\sigma_z/(1+z) \sim 1 - 2\%$ compared to their spectroscopic subsample) derived with the code **EAZY** that fits linear combination of templates to SEDs (Brammer et al., 2008). Accurate photometric redshift estimation is crucial in this study as we will explain in the next section. Stellar masses and dust reddening estimates are also included in the NMBS catalogue, and are estimated by SED fitting using the **FAST** code (Kriek et al., 2009) with various stellar population synthesis models, star formation histories and stellar initial mass functions.

To derive the M_*/L -colour relation, we use the stellar masses from the NMBS catalogue in COSMOS estimated with stellar population synthesis models of Bruzual & Charlot (2003), an exponentially declining SFHs, solar metallicity and computed with a Chabrier IMF. We exclude the sample in AEGIS as it contains photometries with fewer bands and thus has a lower accuracy in photometric redshifts.

Note that in theory the 3D-HST catalogue from Momcheva et al. (2016) would also be suitable too, nevertheless our method was already developed and calibrated before the release of the public 3D-HST catalogue.

3.3.2 Methods

We derive the M_*/L -colour relation for each cluster in the observer frame, contrary to the typical approach which interpolates the data to obtain a rest-frame colour. For example, Szomoru et al. (2013) derive the M_*/L -colour relation in rest-frame $u - g$ colour and interpolate their photometry using InterRest (Taylor et al., 2009a). Instead, we compute the observed $z_{850} - H_{160}$ colour for all NMBS galaxies. This method has several advantages over the typical method. Firstly, the shape of the SED in the NMBS sample is well characterised by the plethora of photometries. On the other hand, we only have a few photometry bands in our data, it is therefore preferable to perform the interpolation on

the NMBS data instead of ours to avoid degeneracy in choices of templates. Secondly, deriving the relation in the observer frame reduces the number of interpolation required and allows for an easier redshift correction. As we consider clusters at different redshifts, using the typical approach would require us to interpolate also the photometries of the NMBS galaxies.

To derive the relations between M_*/L and colour, we first use the redshift measurements and photometries in the catalogue and rerun **EAZY** for all NMBS galaxies to obtain the best-fit SED templates. These SEDs are then integrated with the *HST*/ACS z_{850} and *HST*/WFC3 H_{160} filter response for the $z_{850} - H_{160}$ colour. Similarly we obtain the luminosity $L_{H_{160}}$ of each galaxy in the observed H_{160} band, from which we calculate the stellar mass-to-light ratio $M_*/L_{H_{160}}$. To ensure these best-fit SED templates are of good quality we apply a chi-square cut from template fitting in **EAZY** and select galaxies with $\chi^2 < 2.0$. For each cluster, we then select NMBS galaxies within a redshift window of 0.1 of the cluster redshift. Hence, for example for XMMU J2235-2557 we select galaxies in the redshift range of $1.29 < z < 1.49$. We then apply a similar magnitude cut as our red sequence selection (i.e. for XMMU J2235-2557 we choose those with $H_{160} < 22.5$) to better match the cluster sample.

With this criterion we select 718 objects for XMMU J2235-2557 ($1.29 < z < 1.49$), 919 objects for XMMXCS J2215-1738 ($1.36 < z < 1.46$) and 1325 objects for Cl 0332-2742 ($1.51 < z < 1.71$). A redshift correction is applied to these galaxies to redshift their spectra to the cluster redshift (i.e. similar to k-correction in observer frame). We then measure their $z_{850} - H_{160}$ colour and $L_{H_{160}}$ in the observer frame. This correction is only possible with accurate photometric redshifts, which makes the NMBS data an excellent choice for this study. We find that the redshift correction is effective in reducing the scatter of the relation, indicating that some of (but not all) the scatter is simply due to difference in redshifts. Figure 3.5 shows the fitted relations of the three clusters between $\log(M_*/L_{H_{160}})$ and $z_{850} - H_{160}$ colour. The black line in each panel is the best-fit relation:

For XMMU J2235-2557:

$$\log((M_*/L_{H_{160}})/(M_\odot/L_\odot)) = 0.625 (z_{850} - H_{160}) - 1.598 \quad (3.4)$$

For XMMXCS J2215-1738:

$$\log((M_*/L_{H_{160}})/(M_\odot/L_\odot)) = 0.635 (z_{850} - H_{160}) - 1.671 \quad (3.5)$$

For Cl 0332-2742:

if $(z_{850} - H_{160}) \leq 1.54$:

$$\log((M_*/L_{H_{160}})/(M_\odot/L_\odot)) = 0.716 (z_{850} - H_{160}) - 1.730 \quad (3.6)$$

if $(z_{850} - H_{160}) > 1.54$:

$$\log((M_*/L_{H_{160}})/(M_\odot/L_\odot)) = 0.320 (z_{850} - H_{160}) - 1.121 \quad (3.7)$$

The relation is almost perfectly linear in XMMU J2235-2557 and XMMXCS J2215-1738, while in Cl 0332-2742 a bilinear function is preferred as it significantly reduces the residuals. Using a two-component function is common in fitting M_*/L -colour relation (e.g. Mok et al., 2013), primarily due to the difference in M_*/L of the blue and red stellar population. We have also tried to use a bilinear fit for the other two clusters, but the results are completely consistent with single linear fits. The light gray line in the XMMXCS J2215-1738 panel illustrates the effect of using the bilinear fit.

Below the relation in each panel of Figure 3.5 we plot the residuals of the fit in colour bins of 0.1. The global scatter of the fits are ~ 0.06 dex for XMMU J2235-2557, ~ 0.06 dex for XMMXCS J2215-1738 and ~ 0.10 dex for Cl 0332-2742 respectively. The uncertainty in $\log(M_*/L)$ is generally ~ 0.1 in each bin and the bias is negligible. The remaining scatter results from a number of effects, including SED fitting uncertainties such as redshifts and stellar population models. There are also physical effects from the stellar population properties (age, dust and metallicity), as their effects are not exactly parallel to the relation. Note that this can lead to small systematics in measuring mass-to-light ratios and the mass-to-light ratio gradients. For example in metal-rich or old regions the mass-to-light ratio will likely be systematically slightly underestimated, and overestimated in metal-poor or young regions (Szomoru et al., 2013).

3.4 Integrated stellar masses

We estimate the integrated stellar masses (M_*) of the cluster galaxies using the empirical M_*/L -colour relations, $z_{850} - H_{160}$ aperture colours and total luminosities $L_{H_{160}}$ from their best-fit 2D GALFIT Sérsic models. The uncertainties in stellar mass hence comprise photometric uncertainties in the colour and H_{160} luminosity, as well as the scatter in the derived M_*/L -colour relation. Figure 3.6 shows the colour-mass relation of the three clusters. It is clear that the massive populations ($\log(M_*/M_\odot) > 11$) have a redder $z_{850} - H_{160}$ colour than the low-mass populations (see also Strazzullo et al., 2010, using *HST*/NICMOS data). The typical uncertainty of the mass estimates is $\sim 0.1 - 0.15$ dex. Note that the uncertainty of the absolute stellar masses is of course larger, as our M_*/L estimation depends on the details of NMBS SED fitting procedure, the stellar population model used and the choice of IMF.

Previous literature compute SED mass with multi-band `MAG_AUTO` photometry obtained with SExtractor (e.g. Strazzullo et al., 2010). It is known that `MAG_AUTO` can be systematically biased, due to the assumption in SExtractor that the sky background comprises only random noise without source confusion (White et al., 2007a). Hence, more recent studies use the total luminosity from best-fit Sérsic models to correct the masses to account for the missing flux in `MAG_AUTO` (e.g. Bernardi et al., 2013; Bezanson et al., 2013a). In our case, as we will demonstrate in Section 3.7.4, the total luminosity from the best-fit Sérsic models can recover the (input) galaxy magnitudes to a high accuracy. Hence, we scale our masses with the total luminosity $L_{H_{160}}$ from best-fit Sérsic models rather than H_{160} `MAG_AUTO` magnitudes. We also compute masses with H_{160} `MAG_AUTO` for the

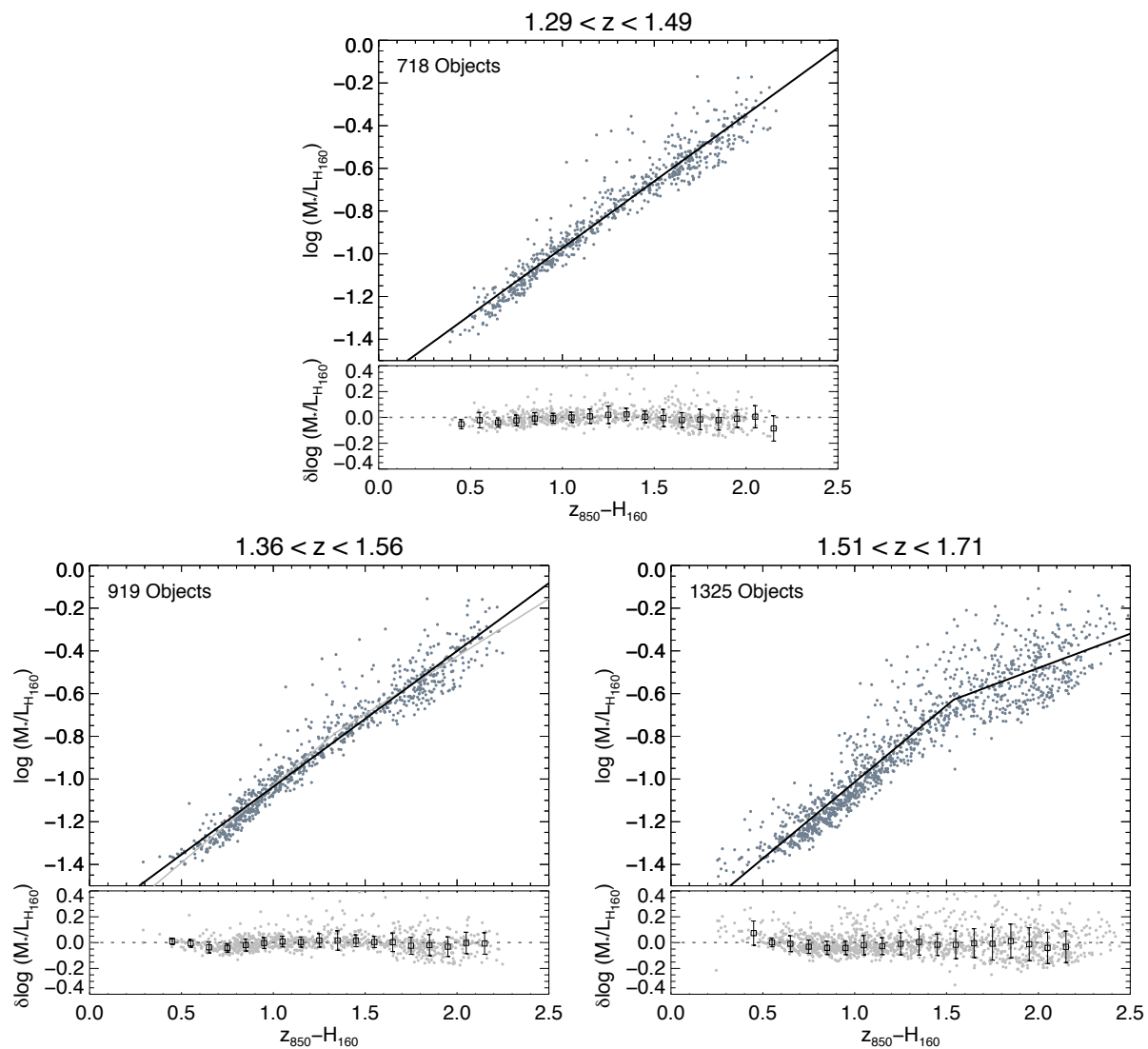


Figure 3.5: Relations between stellar mass-to-light ratio and $z_{850} - H_{160}$ colour at redshifts of the three KCS clusters. Gray points in each panel are galaxies from the NMBS catalogue that satisfy the selection criteria. Black line is the best-fit relation. Bottom part in each panel shows the residuals of the relation $\delta \log(M_*/L) = \text{data} - \text{linear fit}$ in colour bins of 0.1 dex.

XMMU J2235-2557 sample to estimate the difference. The difference between the two is small with $\langle M_{*,MAG-AUTO} - M_{*,Sersic} \rangle = -0.039$ dex.

3.4.1 Comparison of masses derived using M_*/L - colour relation with previous literature using SED fitting

In this section we compare our integrated stellar masses to values from previous literature where the samples overlap. Other studies usually estimate the stellar masses through spectral energy distribution fitting of multiple photometric bands (e.g. Strazzullo et al., 2010; Delaye et al., 2014). The advantage of using M_*/L - colour relation over SED fitting is that it does not require a large number of photometric bands, hence it is a relatively inexpensive mass indicator. The accuracy of the stellar mass estimates then depends on how well constrained the M_*/L - colour relation is, which in turn depends on the colour used (see discussion in e.g., Bell & de Jong, 2001; Bell et al., 2003). Hence we assess whether our mass estimates are biased.

For XMMU J2235-2557 and XMMXCS J2215-1738, Delaye et al. (2014) estimated stellar masses of our galaxies through SED fitting with four bands (*HST*/ACS i_{775} , z_{850} , HAWK-I, J , K_s). They used the LEPHARE code (Arnouts et al., 1999; Ilbert et al., 2006) with Bruzual & Charlot (2003) stellar population synthesis models with exponential declining SFHs, a Chabrier IMF and assuming solar metallicity. Their setting is almost identical to the stellar masses from the NMBS catalogue we chose to construct the M_*/L - colour relation, thus the derived masses can be compared directly.

The top panel of Figure 3.7 shows a direct comparison of the mass estimated using our M_*/L - colour relation and SED fitting from Delaye et al. (2014). Our sample covers 10 out of 13 early-type galaxies in their sample. The remaining 3 galaxies are out of the FOV of our WFC3 images (but are in the FOV of the ACS z_{850} image), thus are not included in our sample. The mass estimates from the two methods are consistent with each other, with a median difference and 1σ scatter of 0.03 ± 0.09 dex. Their SED fitting also gave an uncertainty of ~ 0.1 dex in mass, comparable to our uncertainties. The object that deviates from the one-to-one relation the most (at $\log(M_*/M_\odot) = 11.11$) is a galaxy close to the core of cluster with a very close neighbour (ID 368), which probably affect the mass estimates in both methods. Removing this object reduces the median difference to 0.01 ± 0.07 dex.

Similarly, the bottom left panel of Figure 3.7 shows the mass comparison of XMMXCS J2215-1738. Our sample covers 12 out of 20 early-type galaxies in their sample. The other galaxies are out of the FOV of the WFC3 images or are removed in our UVR selection. The mass estimates are generally within 1σ , with a median difference and 1σ scatter of -0.08 ± 0.14 dex.

Since Cl 0332-2742 is located in the GOODS-S field, the 3D-HST catalogue has all the red sequence galaxies in our sample. The 3D-HST program provides stellar population parameters determined with the optical-near-IR photometry using the FAST code (see, e.g. Skelton et al., 2014; Momcheva et al., 2016, for details). The stellar masses are estimated with Bruzual & Charlot (2003) stellar population synthesis models with exponential de-

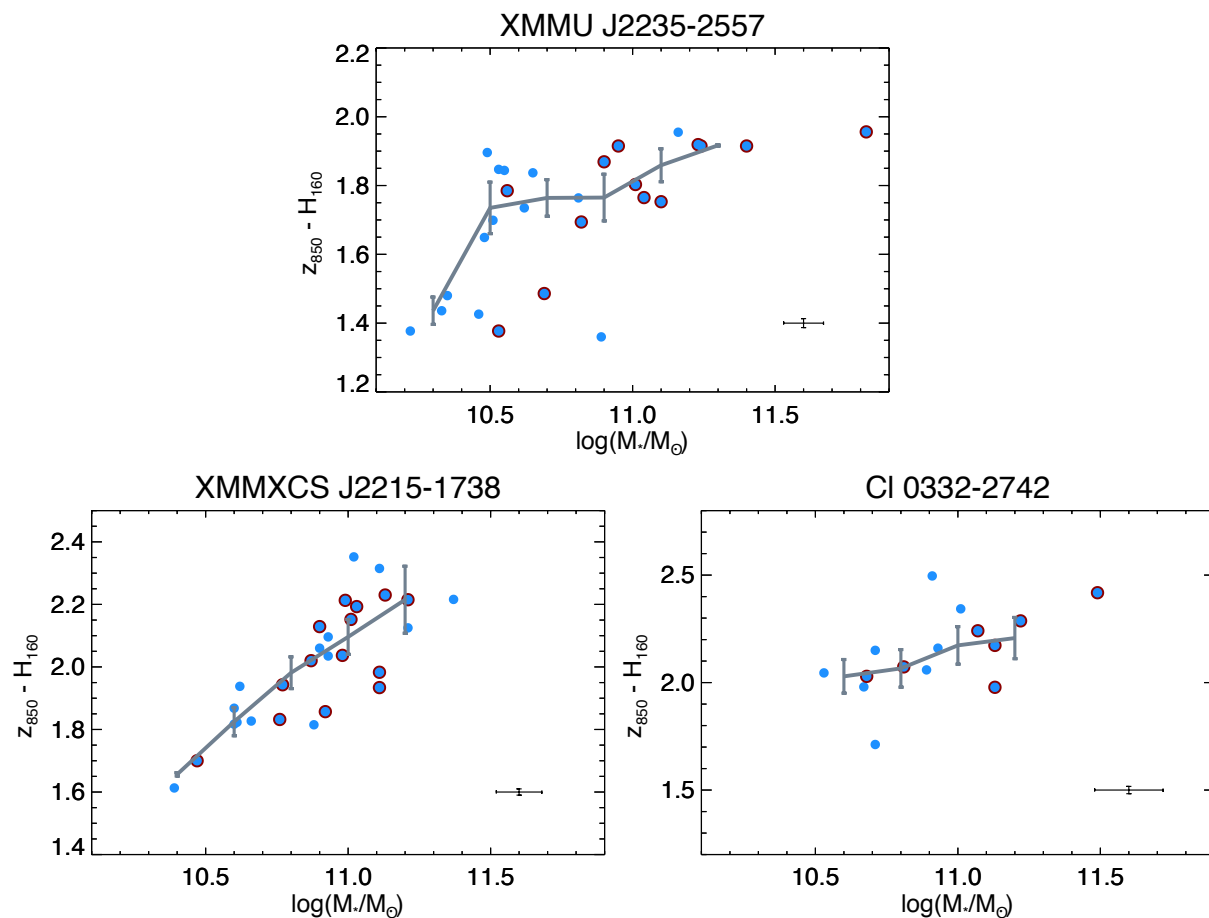


Figure 3.6: Colour-mass relations of the three KCS clusters. Objects that are spectroscopically confirmed cluster members (combining KCS observations and previous literature) are circled in dark red. The cross shows the median uncertainty of the $z_{850} - H_{160}$ colours and integrated stellar masses. The gray line in each panel shows the running median and the error bars show the uncertainty of the median in each bin. When there is only one point in the bin, the uncertainty of the quantity is plotted instead.

clining SFHs, a Chabrier IMF and solar metallicity. The right panel of Figure 3.7 shows a direct comparison of the mass estimated using our M_*/L - colour relation and SED fitting from Momcheva et al. (2016). The mass estimates from the two methods are consistent with each other, with a median difference and 1σ scatter of -0.06 ± 0.08 dex.

Therefore, we conclude that the masses derived using M_*/L - colour relation are not biased, and are consistent with masses derived with multiband SED fitting.

3.5 Resolved stellar mass surface density maps

We further exploit the M_*/L -colour relation to derive stellar mass surface density maps for the cluster galaxies. This allows us to study the mass distribution within each galaxy, at the same time eliminating the effect of internal colour gradient which influences the light-weighted size measurements. As we explained in Section 1.5.1, one can use either the M_*/L -colour relation (e.g. Szomoru et al., 2013; Fang et al., 2013) or resolved SED fitting to compute stellar mass surface density (e.g. Wuyts et al., 2012; Lang et al., 2014). Similar to the derivation of integrated stellar mass, since we only have a few photometric band, it is preferable to use the M_*/L -colour relation than resolved SED fitting. Below we describe the main steps involved in deriving stellar mass surface density maps with the M_*/L -colour relation.

3.5.1 From colour to stellar mass surface density

We first resample the PSF-matched z_{850} image to the same grid as the H_{160} image using the software SWarp (Bertin et al., 2002). Postage stamps of each galaxy are then generated in both H_{160} and PSF matched z_{850} images for deriving resolved stellar mass surface density maps. The next step is to convert the $z_{850} - H_{160}$ colour information into mass-to-light ratios with the M_*/L -colour relations described in Section 3.3. Nevertheless, a direct pixel-to-pixel conversion is not possible for our data. The conversion requires a certain minimum signal-to-noise (S/N) level because: a) significant biases or massive uncertainties may arise if colours are not well measured. b) our relation is only calibrated within a certain colour range. Low S/N colour that falls outside the calibrated range could be converted to an unphysical M_*/L .

Therefore, we adopt the Voronoi binning algorithm as described by Cappellari & Copin (2003), grouping pixels to a target S/N level of 10 per bin. For each galaxy in our sample, we run the Voronoi binning algorithm on the sky-subtracted PSF-matched z_{850} band postage stamps as a reference, as it has a lower S/N compared to the H_{160} image. The same binning scheme is then applied to the sky-subtracted H_{160} image. The subtracted sky levels are determined by GALAPAGOS (see Section 3.1). The two images are then converted into magnitudes. Binned $z_{850} - H_{160}$ colour maps are obtained by subtracting the two. We then construct a binned M_*/L map by converting the colour in each bin to a mass-to-light ratio with the derived colour - M_*/L relation.

An extrapolation scheme is implemented to determine the M_*/L in regions or bins with

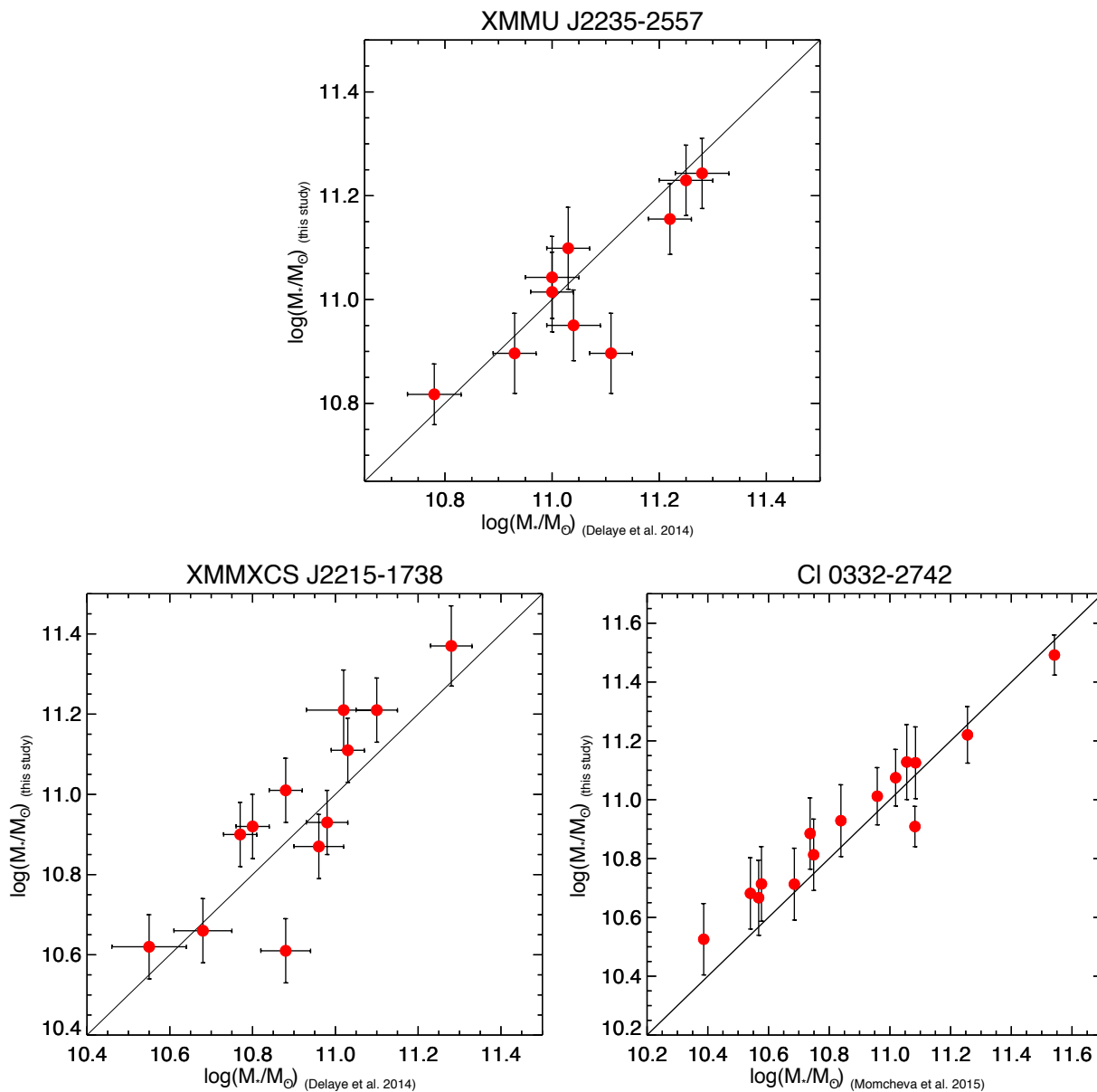


Figure 3.7: Comparison of masses derived using M_*/L - colour relation with SED fitting from previous literature. Top and bottom left: red circles are the stellar mass estimates of the galaxies that are common in our sample to Delaye et al. (2014). The stellar masses in Delaye et al. (2014) are derived from SED fitting using LEPHARE (Ilbert et al., 2006). Bottom right: Comparison of our masses with the 3D-HST masses derived using FAST (Momcheva et al., 2016). The solid black line is the one-to-one relation. The error bars are the 1σ uncertainties.

insufficient S/N, for example in the galaxy outskirts and the sky regions. We first run an annular average to derive a one-dimensional S/N profile in z_{850} for individual galaxies using the light-weighted galaxy centroid, axis ratio and position angle determined in Section 3.1. For the area outside the elliptical radius that has a S/N less than 1.5 times of our target S/N (i.e. $S/N \sim 6.6$), we fix the M_*/L to the annular median of M_*/L bins at the last radius with sufficient S/N. We find that this extrapolation is crucial for the following structural analysis as the sky noise is preserved. We illustrate the importance of this extrapolation using simulated galaxies in Section 3.7.5.

3.5.2 Construction of stellar mass surface density maps

We construct resolved stellar mass surface density maps (hereafter referred to as mass maps) by directly combining the extrapolated M_*/L map and the original (i.e. unbinned) H_{160} images. Figure 3.8 illustrates the procedure of deriving mass maps from the z_{850} and H_{160} images. Using the original H_{160} image instead of the binned one allows us to preserve the WFC3 spatial resolution in the mass maps. Note that in theory combining a binned (i.e. spatially discrete) M_*/L map with a smooth luminosity image would result in a discrete mass profile in low S/N region, in other words, induce a “discretization effect” in the mass maps.

This discretization effect is more severe in low S/N regions, i.e. the galaxy outskirts where the bins are larger (hence less smooth). For bright galaxies, since there are more bins with sufficient S/N and the dynamical range of the light distribution (surface brightness gradient) is much larger than the M_*/L gradient, this appears to have minimal effect and does not largely affect our result. For fainter galaxies this issue is non-negligible.

To tackle this, we employ a median-stacking technique to alleviate the discretization effect. For each galaxy we perform the abovementioned Voronoi binning procedure 10 times, each with a different randomised set of initial Voronoi nodes. After the binning, this ends up with a set of M_*/L maps with slightly different bins. We then median-stacked the M_*/L maps to create the final mass map. Similarly, we also generate mass RMS maps for each galaxy from the ERR weight maps output by Astrodrizzle.

3.6 Mass-weighted structural parameters

We measure mass-weighted structural parameters from the resolved stellar mass surface density maps. We follow a similar procedure as with the light-weighted structural parameters, using GALFIT to model the mass profiles with two-dimensional Sérsic profiles. All five parameters of the Sérsic profile ($M_{*,tot}$, n_{mass} , $a_{e,mass}$, q_{mass} and $P.A._{mass}$) and the centroid are left to be free parameters in the fit. We use the same GALFIT constraints as for the light-weighted structural parameters, except for allowing a larger range for the Sérsic indices: $0.2 < n < 15.0$. This is because the mass profiles are expected to be more centrally peaked compared to light profiles (Szomoru et al., 2013). As the H_{160} images are background subtracted before being converted into mass maps, the sky level (i.e. the

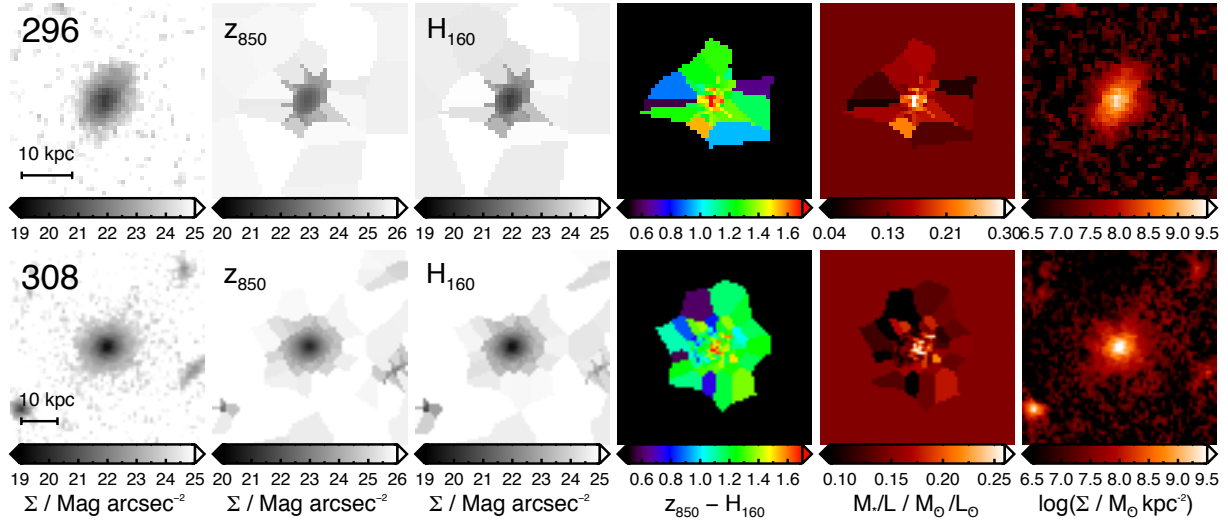


Figure 3.8: Examples of resolved stellar mass map derivation of two passive galaxies (ID 296, 308) in XMMU J2235-2557. From left to right: H_{160} galaxy image cut-outs centred on the primary object, Voronoi-binned z_{850} images, Voronoi-binned H_{160} images with binning scheme adopted from z_{850} images, $z_{850} - H_{160}$ colour maps, extrapolated M_*/L maps and the surface mass density maps Σ_{mass} . Bins that are extrapolated are masked out (shown in black) in the colour maps.

background mass level in mass maps) is fixed to zero in the fitting process.

While the fitting process is straightforward for most of the galaxies, we find that for a couple of objects the fits do not converge, or have resultant sizes smaller than the PSF size. To avoid biases and wrong conclusions we remove these objects that are not well-fitted from the mass parameter sample. 6 objects (out of 27) in XMMU J2235-2557 and 9 objects (out of 29) in XMMXCS J2215-1738 are hence discarded, among them two objects in XMMU J2235-2557 and four objects in XMMXCS J2215-1738 are spectroscopically confirmed. All of the objects in Cl 0332-2742 are well-fitted. Most of them initially have small light-weighted sizes and their fitted mass-weighted sizes become smaller than half of the PSF HWHM, which are unreliable (see the discussion in Section 3.7.4). The mass-weighted structural parameters of the three clusters are also provided in Table 3.1, Table 3.2 and Table 3.3, respectively.

3.6.1 Deviation of mass-weighted parameters - 1D vs. 2D

Szomoru et al. (2013) derived 1D mass profiles from 1D radial surface brightness profiles and measured mass-weighted structural parameters. We argue that deriving mass maps and fitting in 2D have certain advantages: a) It does not rely heavily on the Sérsic profile fitting in light. Deriving elliptical averaged profiles will require a predetermined axis ratio and position angle, which, in our case, come from the light Sérsic profile fitting (same for Szomoru et al. (2013)). This will of course fold in the uncertainties of these two

parameters into the 1D profiles, which complicates the propagation of uncertainties in the mass-weighted parameters. b) Similar to the argument in Section 3.1, the object density is high in the cluster region, and many galaxies have very close neighbours. Hence it will be more appropriate to fit all the sources simultaneously to take into account the contribution from the neighbouring objects, rather than deriving 1D profile without deblending the neighbouring contamination. A possible way to solve this is to first subtract the best-fit 2D models of the neighbours from the 2D images before generating the 1D profiles, similar to how we derive colour gradients (see Section 3.2), but of course this depends strongly on how well the neighbours can be subtracted, and still suffer from a). c) Using the same size measurement method allows us to better compare the light-weighted and mass-weighted sizes. Using mass-weighted structural parameters derived in 1D complicates the comparison and interpretation.

3.6.2 Comparison of our mass-weighted sizes with previous literature using resolved SED fitting

Lang et al. (2014) derived stellar mass maps for a mass-selected sample ($\log(M_*/M_\odot) > 10$) spanning a redshift range $0.5 < z < 2.5$ in all five CANDELS fields, including the GOODS-S field where Cl 0332-2742 resides. They fitted both two-dimensional Sérsic models and two-component (i.e., bulge + disk) decomposition to the mass maps. In this section we compare our mass-weighted sizes derived from our mass maps (from M_*/L -colour relation) to those derived from resolved SED fitting.

Figure 3.9 shows a direct comparison of our mass-weighted sizes to the mass-weighted sizes derived using resolved SED fitting of the 15 galaxies in Cl 0332-2742 (P. Lang, private communication). Overall, the sizes from the two methods are very consistent with each other. The entire sample have a median difference and 1σ scatter of 0.012 ± 0.081 dex ($\sim 20\%$). We have compared the mass maps of the two objects that largely deviates from the one-to-one relation, marked in red in Figure 3.9. Galaxy ID 25989 has a close neighbouring object, which we treated as a separate object and fitted simultaneously. On the other hand, the close neighbour is not deblended in the 3D-HST catalogue (and hence not fitted in Lang et al. (2014)). As a result, our size of this object appears to be much smaller. For galaxy ID 25338, there is a giant halo in the galaxy which makes the sky determination troublesome and probably results in the size difference. With our method we can recover measurements that are consistent with available literature, hence we conclude that our method is robust and unbiased.

3.7 Error analysis with simulated galaxies

Since the photometric uncertainties are folded directly into our mass estimates as well as the structural parameters measurements, a realistic estimate of the photometric uncertainties is required. In addition, Häussler et al. (2007) argued that the uncertainties output by GALFIT (and also GIM2D) are underestimated. The formal uncertainties derived from

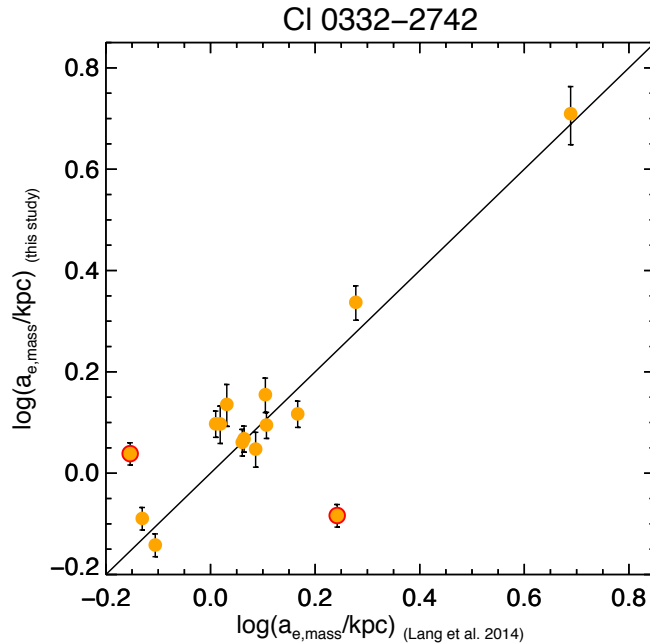


Figure 3.9: Comparison of mass-weighted sizes derived using M_*/L - colour relation with resolved SED fitting from Lang et al. (2014). The solid black line is the one-to-one relation. The error bars represent the 1σ uncertainties of our mass-weighted sizes (see Section 3.7.5 for a description). The two outliers (ID 25989, 25338) are marked in red. See text for details.

GALFIT χ^2 minimisation are not representative to the true uncertainties due to various reasons, such as contamination by neighbouring objects, correlations between different structural parameters and structure in the sky region. To give a more realistic estimate of the uncertainty of the photometry, light-weighted structural parameters and mass-weighted structural parameters, we perform extensive simulations with a set of simulated galaxies with surface brightness profiles described by a Sérsic profile on the *HST*/ACS and WFC3 images of the three clusters.

3.7.1 Outline of the simulations

We develop a suite of routines under a common framework in IDL¹ to automate the simulations. The program is implemented to perform most of the tasks for estimating uncertainties: it generates a set of simulated galaxies with randomised structural parameters with a user-input range and distribution, creates images with simulated objects in two bands in a single run, performs source detection with SExtractor in each band and recovers the photometry of the simulated objects, derives light-weighted structural parameters with GALAPAGOS and GALFIT, derives mass maps with a user-input M_*/L -colour relation

¹Interactive Data Language, Exelis Visual Information Solutions, Boulder, Colorado

and also mass-weighted structural parameters with GALFIT. A combined catalogue of the simulated and derived parameters is output for straightforward comparison.

The code is controlled through a single input parameter file, similar to the interface of the GALAPAGOS startup script. Figure 3.10 shows an example of the parameter file for the program. The parameter file is divided into five parts, the first block (I) defines the image locations and image related parameters. Parameter block (A) guides the construction of the simulation set and defines the distribution of the magnitudes and structural parameters of the simulated galaxies. Block (B) controls the creation of the images and (S) manages the SExtractor configuration. Block (G) controls the setup of GALAPAGOS and derivation of light-weighted structural parameters and (M) controls the derivation of the mass maps and mass-weighted structural parameters. The program is generalised to be used for most images and is flexible with different input structural parameter distributions (including uniform, Gaussian and log-normal distributions). The block structure of the code allows certain part of the code to be skipped or rerun easily. Below we will describe in detail the setup we used for our cluster sample and the procedure of the simulation.

3.7.2 Construction of the set of simulated galaxies

We perform simulations on most of the bands we derived structural parameters in the three KCS clusters. Below we describe in detail the simulations in the ACS z_{850} and WFC3 H_{160} bands, the two bands we used to derive mass-weighted structural parameters in each cluster, as examples.

The simulated galaxies (hereafter SGs) are uniformly distributed within a magnitude range of $17.0 < H_{160} < 26.0$ and a colour range of $0.4 < z_{850} - H_{160} < 2.4$ (hence a range of z_{850} magnitudes $17.4 < z_{850} < 28.4$). This selected magnitude range encompasses the entire range of our cluster sample, and is also the approximate range where our M_*/L - colour relations are calibrated (see Section 3.3). We generate on average a set of 20000 SGs for each simulation.

Each galaxy is described by a Sérsic profile with input structural parameters randomly drawn from distributions with means and dispersions taken from the real galaxies parameter distributions. For XMMU J2235-2557 we use Gaussian distributions with values taken from the distributions in the WFC3 H_{160} band, the means and dispersions of the Sérsic indices n , effective semi-major axis a_e and axis ratio q are $(\langle n \rangle, \sigma_n) = (3.19, 2.18)$, $(\langle a_e \rangle, \sigma_{a_e}) = (6.07, 5.16 \text{ (pixel)})$ and $(\langle q \rangle, \sigma_q) = (0.67, 0.20)$. For XMMXCS J2215-1738 and Cl 0332-2742, the distributions are taken from the 3D-HST structural parameter catalogue in the H_{160} band at the redshift range of the clusters (van der Wel et al., 2014). We assume Gaussian distributions for Sérsic index n and axis ratio q , but a log-normal distribution for the effective semi-major axis. The means and dispersions are $(\langle n \rangle, \sigma_n) = (3.18, 1.40)$, $(\langle \log(a_e) \rangle, \sigma_{\log(a_e)}) = (0.47, 0.29 \text{ log(pixel)})$ and $(\langle q \rangle, \sigma_q) = (0.71, 0.19)$. While a log-normal distribution can better reproduce the skewed tail towards large sizes in the observed semi-major axis distribution, on the other hand the size distribution in clusters may be different from the field (see, e.g. Delaye et al., 2014). The choice of Gaussian or log-normal dis-

```

-----
# Parameter file for full_light_mass_sim
#
# - Magnitude and Aperture color test with SExtractor (S)
# - Light-weighted structural parameter test with GALFIT (G)
# - Mass-weighted structural parameter test with mass map derivation routines (M)
#
-----
#
# I) Image parameters
#
I01) ./XMMXCS_images/f160w_aug04_0.8ivm_drz.image_wcs.fits          #img1
I02) ./XMMXCS_images/f160w_aug04_0.8err_drz.weight_wcs.fits       #err1
I03) ./psf_f160w_full_aug04_m1_fluxfix.fits                      #psf1
I04) ./XMMXCS_images/z850_aug04_0.8ivm_skysub_extracrr.image_wcs2.lresamp_psfmatch.fits          #img2
I05) ./XMMXCS_images/z850_aug04_0.8err_skysub_extracrr.image_wcs2.lresamp.weight_rms_psfmatch.fits #err2
I06) ./psf_f160w_full_aug04_m1_fluxfix.fits                      #psf2
I07) 33.740961          #magzpt1
I08) 35.429549          #magzpt2
I09) 0.0642            #platescale1
I10) 0.0642            #platescale2
I11) galb1_            #outprefix1
I12) galb2_            #outprefix2
I13) ./XMMXCS_images/f160w_aug04_0.8ivm_drz.weight_wcs_nan.fits  #ivmerr1
I14) ./XMMXCS_images/z850_aug04_0.8ivm_skysub_extracrr.image_wcs2.lresamp.weight_rms_psfmatch.fits #ivmerr2
I15) ./XMMXCS_images/f160w_aug04_0.8ivm_drz.mask.fits           #mask1
I16) ./XMMXCS_images/z850_aug04_0.8ivm_skysub_extracrr.mask.fits #mask2
#
#
# A) Build the galaxy parameter catalogue
#
A01) N                #make new catalogue?
A02) parameter_record #catalogue name.fits (read/output)
A03) 1                 #num of galaxies added in each image
A04) 20000             #num of image to make - total galaxy num =A03*A04
A05) 17,26,U          #Mag range (I7 - 26) (Always U)
A06) 3.1756,1.3978,G #n range (0.2) (G - med,sig, U - min,max, L -med,sig (med in pixel, sig_log))
A07) 2.9490,0.2874,L #re range (in image pixel) (0.3 - 500)
A08) 0.7064,0.1892,G #q range (0.001 - 1) > 0.001
A09) 0.4,2.4,U        #Color range (for mass test) (Always U)
A10) N                #use paramter below for band2? If yes the color
                        #is omitted, if no the mag range will depend on it
A11) 19,27,U          #Mag range2
A12) 0.2,14,G         #n range2
A13) 0.2,50,G         #re range2
A14) 0.0001,1,G       #q range2
#
# Create images with simulated galaxies
#
B01) N                #make new images?
B02) ./Image_storage/ #output directories of the images (bgimg/erring)
B03) ./Tmp/           #temporary working directories
B04) 1,20000          #ID range to create (consistent with catalog ID)
#
# S) SExtractor magnitude and aperture color test
#
S01) N                #run SExtractor to create new catalogues?
S02) N                #overwrite existing catalogues?
S03) /afs/ipp/home/k/koppenh/bin/sex #location of SExtractor
S04) ./Cat_storage/   #output directories of the catalogues (De_ID.txt)
S05) 1,20000          #ID range to run SExtractor
S06) ./testconfig_f160w_1.txt #input SExtractor configuration file 1
S07) ./testconfig_f160w_2.txt #input SExtractor configuration file 2
S08) 3.0              #detect threshold
S09) sex_color_record #output catalogue.fits (in the main directory)
                        #automatically overwritten the old one
#
# G) Galapagos parameter test
#
G01) N                #run Galapagos
G02) N                #overwrite existing v_gfs and galapagos files
G03) /data01/jchan/Raw_Gala_sim/Raw_Gala_sim/galfit #Location of Galfit
G04) 1,20000          #ID range to run Galapagos
G05) ./Galapagos_setup/ #setup directories of Galapagos
G06) ./Gal_cat_storage/ #output directories of Galapagos catalogues
G07) ./Gal_img_storage/ #output directories of Galapagos postage stamps#
G08) gap_galfit_record #output catalogue.fits (in the main directory)
                        #automatically overwritten the old one
#
# M) Mass parameter test
#
M01) Y                #run the massmap construction
M02) Y                #overwrite existing massmaps and mass galapagos files in the dir
M03) 1,11000          #ID range to run massmap construction
M04) ./Mass_cat_storage/ #output directories of Galapagos massmap obj and catalogues
M05) ./Mass_img_storage/ #output directories of massmaps and errmaps
M06) -0.573650, 12.259343 #median and sigma of background for img1
M07) 5.352901, 21.004308 #median and sigma of background for img2
M08) 10               #5/N used for binning
M09) 150              #Bin density (Pixel) (The maximum number of pixels a bin can have on average)
M10) L                #Type of the M/L-color relation (L - power law, B - 2component PL)
M11) 0.63545016, -1.6714819 #Slope, y-intercept of the M/L-color relation (L), slope1, xmidpt (B)
M12) 0.00, 0.00      #N/A (L), Slope2, ymidpt (B)
M13) 0.4, 2.2         #Color range to convert to M/L
M14) 1                #Color = img1-img2 (0) or img2-img1 (1)?
M15) 4.6466990        #Absmag of the sun in the band b1 or b2 - for computing Lsun_b1/b2 (1-b1), (0-b2)
M16) 1.46             #redshift of the system
M17) mass_galfit_record #output catalogue.fits (in the main directory)
                        #automatically overwritten the old one

```

Figure 3.10: Example of the parameter file for the simulation of XMMXCS J2215-1738. The file is divided in to five blocks (I, A, B, S, G), each defines a different part of the test.

tribution on a_e , however, have virtually no huge effect on the simulation results, as we generate a large enough number of galaxies to sufficiently populate the parameter space. The position angle $P.A.$ is uniformly distributed within $0^\circ < P.A. < 180^\circ$. To ensure the simulated profiles are physical, we further apply the following constraints: $n > 0.2$, $a_e > 0.3$, $0.001 < q \leq 1$. We use identical input structural parameters in the two bands.

The SGs were convolved with the adopted PSFs. Morishita et al. (2014) pointed out that there are differences in the central part of the Sérsic profiles produced by IRAF `gallist` and `mkobjects` compared to those produced by GALFIT. In our case, we produce our simulated galaxies using a custom-built routine that over-samples the central part of the Sérsic profiles before resampling it onto a 2D grid. To check whether the Sérsic profiles we generated are consistent with those used in GALFIT, we compare the Sérsic profiles by fitting the noise-free SGs with GALFIT and examine the residual maps. We notice there are residuals at the centre in the residuals map output by GALFIT, although the difference is negligible ($< 0.005\%$ of the flux). We also check that this effect is not due to PSF convolution. Excluding the PSF convolution does not noticeably increase this difference.

The SGs are then injected one by one uniformly to the sky regions of both the H_{160} images and the PSF-matched and resampled z_{850} images at the same location (i.e. a set of z_{850} and H_{160} images). For current simulations we do not add any Poisson noise into the profiles of the SGs. The only source of noise of the simulated galaxies is hence the sky background noise from the images. Hence, the uncertainties of the derived properties below are more likely to represent lower limits to the true uncertainties.

3.7.3 Quantifying the uncertainties on the photometry

We run SExtractor on the SG images using exactly the same setting as for the KCS sample. We then assess the detection rate of the SGs in different magnitudes, as well as investigate the uncertainties of the $z_{850} - H_{160}$ colour derived from $1''$ aperture and galaxy magnitude `MAG_AUTO`.

The detection rate above a certain magnitude reflects the completeness of the sample at that particular magnitude cut. We find that a magnitude cut of $H_{160} < 22.5$ corresponds to a completeness of $\sim 95\%$ for both XMMU J2235-2557 and XMMXCS J2215-1738. For Cl 0332-2742, the completeness is even higher as the 3D-HST H_{160} data is deeper than the other two clusters, for example a cut of $H_{160} < 22.7$ (roughly equivalent to our $J_{125} < 23.5$) corresponds to a completeness of $\sim 97\%$. Hence, we use these magnitude cuts for the KCS sample to ensure high completeness in detection.

We first assess the accuracy of the aperture colours. Having a uniform set of SGs allows us to select subsets to better understand the uncertainties in different quantities. Here we consider SGs within a magnitude range of $19 < H_{160} < 23.5$. Below we quote the results at 22.5 mag in H_{160} (or 23.5 mag in z_{850}) as a benchmark.

Figure 3.11 shows the result of the $1''$ $z_{850} - H_{160}$ aperture colour from simulated galaxies. We find no systematics between the input and recovered aperture colour for all three clusters. The bias is typically < 0.01 mag. The uncertainties on colour are generally small i.e. for XMMU J2235-2557 ~ 0.08 mag, for XMMXCS J2215-1738 ~ 0.06 mag, for

Cl 0332-2742 ~ 0.04 mag for a H_{160} magnitude of 22.5 mag. The uncertainty in colour tends to be larger for objects with redder $z_{850} - H_{160}$ colour, solely due to the fact that the z_{850} aperture magnitude has a larger uncertainty for a redder colour.

We then move to investigate the uncertainty of the recovered magnitude `MAG_AUTO` from SExtractor. Unlike aperture colour, the accuracy of `MAG_AUTO` depends strongly on how accurate SExtractor can estimate both magnitudes (mag_{in}) and sizes (a_e) of the SGs. Hence, we assess the accuracy in terms of input mean surface brightness ($\Sigma = mag_{in} + 2.5 \log(2\pi qa_e^2)$ in mag arcsec $^{-2}$) rather than input magnitudes. Below we quote the results at a mean surface brightness of 23.5 mag arcsec $^{-2}$ in H_{160} (or 24.5 mag arcsec $^{-2}$ in z_{850}) as a benchmark, as all objects we considered are brighter than 23.5 mag arcsec $^{-2}$. Figure 3.12 shows the result of `MAG_AUTO` from simulated galaxies for the three clusters.

For XMMU J2235-2557, the typical z_{850} 1σ uncertainty for the `MAG_AUTO` output at mean surface brightness of 24.5 mag arcsec $^{-2}$ is ~ 0.37 mag. For H_{160} , at a mean surface brightness of 23.5 mag arcsec $^{-2}$ the typical 1σ uncertainty is ~ 0.20 mag. Previous studies have shown that SExtractor `MAG_AUTO` misses a certain amount of flux especially for the faint objects (e.g. Bertin & Arnouts, 1996; Labbé et al., 2003; Taylor et al., 2009b). We find a systematic shift for both filters towards low surface brightness, the shifts are on average ~ 0.55 mag for a H_{160} mean surface brightness of 23.5 mag arcsec $^{-2}$ or ~ 0.62 mag for a z_{850} mean surface brightness of 24.5 mag arcsec $^{-2}$.

We find similar results for XMMXCS J2215-1738: the typical z_{850} 1σ uncertainty for the `MAG_AUTO` output at mean surface brightness of 24.5 mag arcsec $^{-2}$ is ~ 0.32 mag with an average shift of ~ 0.51 mag. For H_{160} , at a mean surface brightness of 23.5 mag arcsec $^{-2}$ the typical 1σ uncertainty is ~ 0.27 mag and the average shift of `MAG_AUTO` is ~ 0.69 mag. This is expected as the depth of the images are comparable to those of XMMU J2235-2557.

For Cl 0332-2742, the typical 1σ uncertainty for z_{850} at mean surface brightness of 24.5 mag arcsec $^{-2}$ is ~ 0.23 mag and the average shift is ~ 0.22 mag. For H_{160} , at a mean surface brightness of 23.5 mag arcsec $^{-2}$ the average shift of `MAG_AUTO` is ~ 0.28 mag and the typical 1σ uncertainty is ~ 0.13 mag.

3.7.4 Quantifying the uncertainties in light-weighted parameters

We assess the accuracy of our light-weighted structural parameter measurements by measuring the structural parameters of the SGs with the same GALAPAGOS setup as the KCS sample.

Figure 3.13, 3.14, 3.15 show the comparison between the input and recovered GALFIT magnitudes and structural parameters for the H_{160} band for the three clusters.

For XMMU J2235-2557, the magnitudes recovered by Sérsic profile fitting are accurate with almost no systematics and a 1σ dispersion less than 0.26 for objects having mean H_{160} surface brightness brighter than 23.5 mag arcsec $^{-2}$. The Sérsic index, effective radius and axis ratio measurements are generally robust for objects brighter than a mean H_{160} surface brightness of 23.5 mag arcsec $^{-2}$. The bias between the recovered and input Sérsic indices is less than 7% and the 1σ dispersion is lower than 28%. Effective radii have a bias

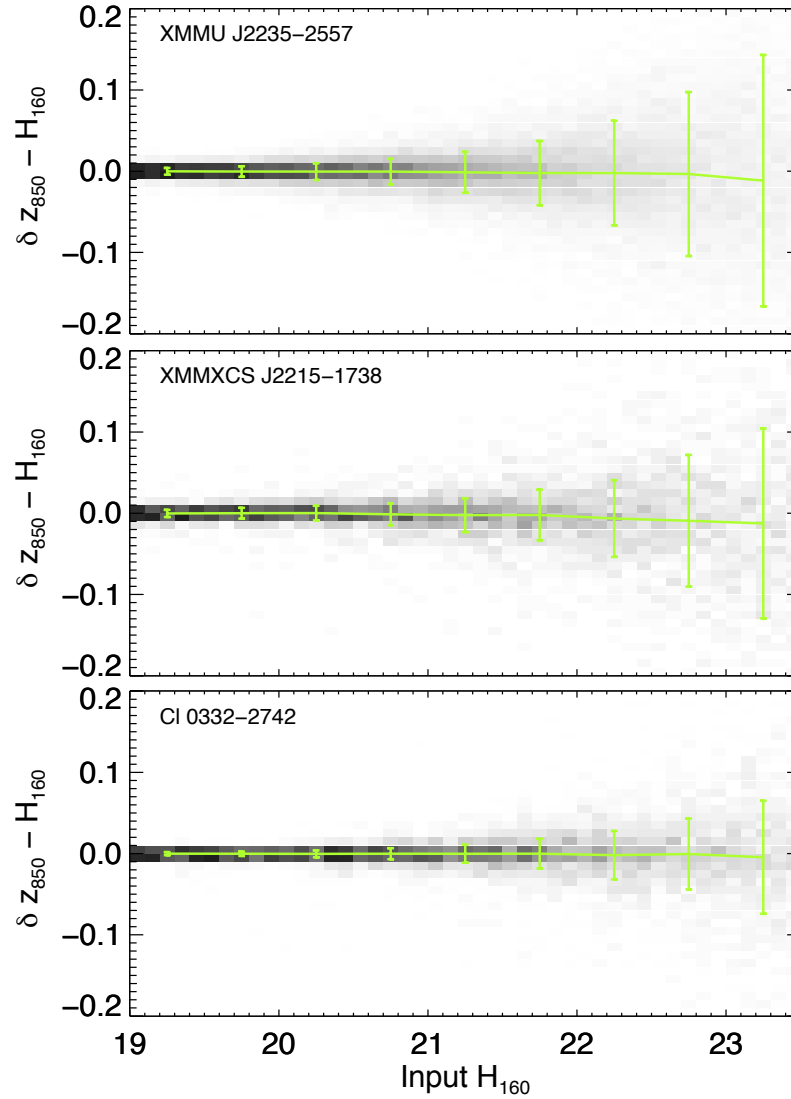


Figure 3.11: Differences between recovered and input aperture colour $\delta z_{850} - H_{160} = (z_{850} - H_{160})_{out} - (z_{850} - H_{160})_{in}$ as a function of input H_{160} magnitude. The green line indicates the median and 1σ dispersion in different bins (0.5 mag bin width). The gray-shaded 2D histograms show the number density distribution of the simulated galaxies.

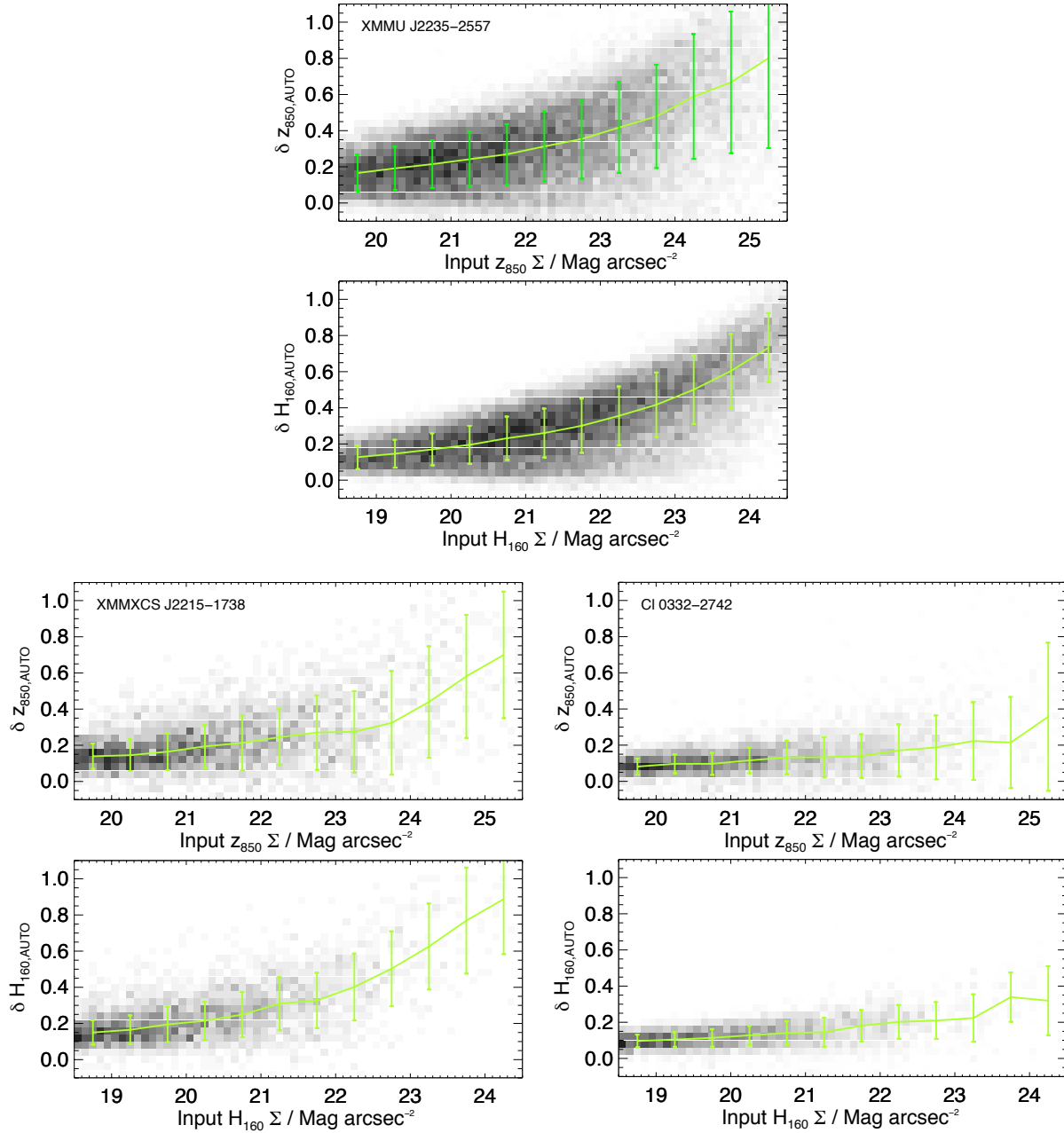


Figure 3.12: Differences between recovered MAG_AUTO and input magnitudes as a function of input mean surface brightness. The upper panel for each cluster shows the result of the z_{850} band $\delta z_{850,AUTO} = (z_{850,AUTO})_{out} - (z_{850,AUTO})_{in}$, while the bottom panel shows the result of the H_{160} band $\delta H_{160,AUTO} = (H_{160,AUTO})_{out} - (H_{160,AUTO})_{in}$. The green line indicates the median and 1σ dispersion in different bins ($0.5 \text{ mag arcsec}^{-2}$ bin width). The gray-shaded 2D histograms show the number density distribution of the simulated galaxies.

less than 4% and a 1σ dispersion lower than 35%. Axis ratios have a 1σ dispersion lower than 12% for objects brighter than H_{160} surface brightness of $23.5 \text{ mag arcsec}^{-2}$.

Similarly, for XMMXCS J2215-1738, the recovered magnitudes and structural parameters are also excellent with no systematics. The magnitudes recovered have a 1σ dispersion less than 0.32 for objects having mean H_{160} surface brightness brighter than $23.5 \text{ mag arcsec}^{-2}$. Sérsic indices have a bias less than 5% and a 1σ dispersion less than 39%. Effective radii have a bias less than 6% and a 1σ dispersion lower than 46%, while axis ratios have a 1σ dispersion less than 13% for objects brighter than H_{160} surface brightness of $23.5 \text{ mag arcsec}^{-2}$.

For Cl 0332-2742, the uncertainties are smaller than the other two clusters primarily due to the deeper H_{160} data. The magnitudes recovered has a 1σ dispersion less than 0.13 for objects having mean H_{160} surface brightness brighter than $23.5 \text{ mag arcsec}^{-2}$. Sérsic indices have a bias less than 2% and a 1σ dispersion lower than 18%, effective radii have a bias less than 3% and a 1σ dispersion lower than 21%. Axis ratios, similar to the other two clusters, have the highest accuracies among the structural parameters: the bias between the recovered and input axis ratio is less than 1% and the 1σ dispersion is lower than 5%.

We have also performed the same test on a simulated background similar to the actual images (where the main difference is that the simulated background has no issue of neighbour contamination), and find that the uncertainties on the effective radius are on average $\sim 15 - 20\%$ lower compared to those derived from real images.

To derive a more realistic uncertainty for the structural parameters, for each galaxy in the KCS sample we compute the mean H_{160} surface brightness and add the corresponding dispersion in quadrature to the error output by GALFIT (see Table 3.1, Table 3.2 and Table 3.3). Note that these uncertainties we derived represent the lower limits of the true uncertainties, as the simulated galaxies are also parametrised with a Sérsic profile.

The effect of unresolved objects to the uncertainties

In addition, from the simulations we find that for SGs with high mean surface brightness (i.e. $< 19 \text{ mag arcsec}^{-2}$), the effective radii are slightly overestimated and the Sérsic indices are underestimated by GALFIT. We find out that this bias is due to unresolved objects in our simulations. Figure 3.16 shows the difference between input and recovered structural parameters by GALFIT in XMMU J2235-2557 for three subpopulations of SGs with descending range of input a_e in terms of the size of PSF. We find that the bias between input and recovered effective radii increases sharply for SGs with input $a_e < \text{PSF HWHM}$. For SGs with input a_e in range of $1.0 \text{ PSF HWHM} < a_e < 2.0 \text{ PSF HWHM}$, the average bias is typically limited to $1 - 2\%$, while it increases to $\sim 10\%$ for SGs with $0.5 \text{ PSF HWHM} < a_e < 1.0 \text{ PSF HWHM}$. For those with $a_e < 0.5 \text{ PSF HWHM}$, the average bias rises sharply to $\sim 50\%$. Since the sizes of high-redshift galaxies can indeed be very small, we do not exclude this small-sized population from our set of simulated galaxies.

Hence, we conclude that our method is unable to measure sizes reliably from galaxies with $a_e < 0.5 \text{ PSF HWHM}$. Galaxies with such small sizes should not be included in the sample. For the KCS sample, this is not an issue as none of the galaxies have light-weighted

sizes smaller than 0.5 PSF HWHM.

3.7.5 Quantifying the uncertainties in mass-weighted parameters

We further assess the accuracy of our mass conversion procedures as well as the reliability of the mass-weighted structural parameter measurements. We convert the z_{850} and H_{160} images into mass maps using our pipeline with identical setting as the KCS sample. The resultant stacked mass maps are then fitted with GALFIT.

The galaxies that we injected have identical initial structural parameters in both z_{850} and H_{160} bands, hence there is no internal colour gradient within the set of simulated galaxies. This allows us to assess the accuracy of the output mass-weighted structural parameters, as the retrieved parameters should be in theory, exactly the same as the input (light) structural parameters. As the Voronoi binning and stacking take a certain amount of time, we can only perform the mass map derivation for a subsample of SGs. This sample is sufficient to provide an uncertainty estimates on the mass-weighted sizes in different bins of surface brightness.

Figure 3.17, 3.18 and 3.19 show the difference between input and recovered mass-structural parameters as a function of H_{160} surface brightness for the three clusters. The Sérsic index, effective radius and axis ratio measurements are generally robust for objects brighter than H_{160} surface brightness of $23.5 \text{ mag arcsec}^{-2}$. This is important, as it demonstrates that our mass conversion procedure does not significantly bias the result.

For XMMU J2235-2557, the bias between the recovered and input Sérsic indices is less than 6% and the 1σ dispersion is lower than 39% for objects having mean H_{160} surface brightness brighter than $23.5 \text{ mag arcsec}^{-2}$. Effective radii have a bias less than 11% and a 1σ dispersion lower than 48%. Again among the three parameters, axis ratios can be recovered most accurately. Axis ratios have almost no bias ($< 1\%$) and a 1σ dispersion lower than 14%.

For XMMXCS J2215-1738, Sérsic indices have a bias less than 10% and a 1σ dispersion lower than 44% for objects having mean H_{160} surface brightness brighter than $23.5 \text{ mag arcsec}^{-2}$. We notice the bias between the recovered and input Sérsic indices is larger for bright objects ($\sim 10\%$). Effective radii have a bias less than 21% and a 1σ dispersion lower than 35%. Axis ratios, on the other hand, have a bias less than 10% and a 1σ dispersion lower than 18%.

Similarly for Cl 0332-2742, Sérsic indices have a bias less than 7% and a 1σ dispersion lower than 20%, effective radii have a bias less than 7% and a 1σ dispersion lower than 28%. For axis ratio, the bias between the recovered and input axis ratio is less than 2% and the 1σ dispersion is lower than 7%. Compare with the light uncertainties (Figure 3.13, 3.14 and 3.15), for the three clusters the mass uncertainties in all parameters are ~ 1.5 times higher.

Similar to the uncertainties in the light-weighted parameters, for each galaxies we add the corresponding dispersion in quadrature to the error output by GALFIT (see Table 3.1, Table 3.2 and Table 3.3). Once again, the uncertainties quoted here are more likely to represent lower limits to the true uncertainties.

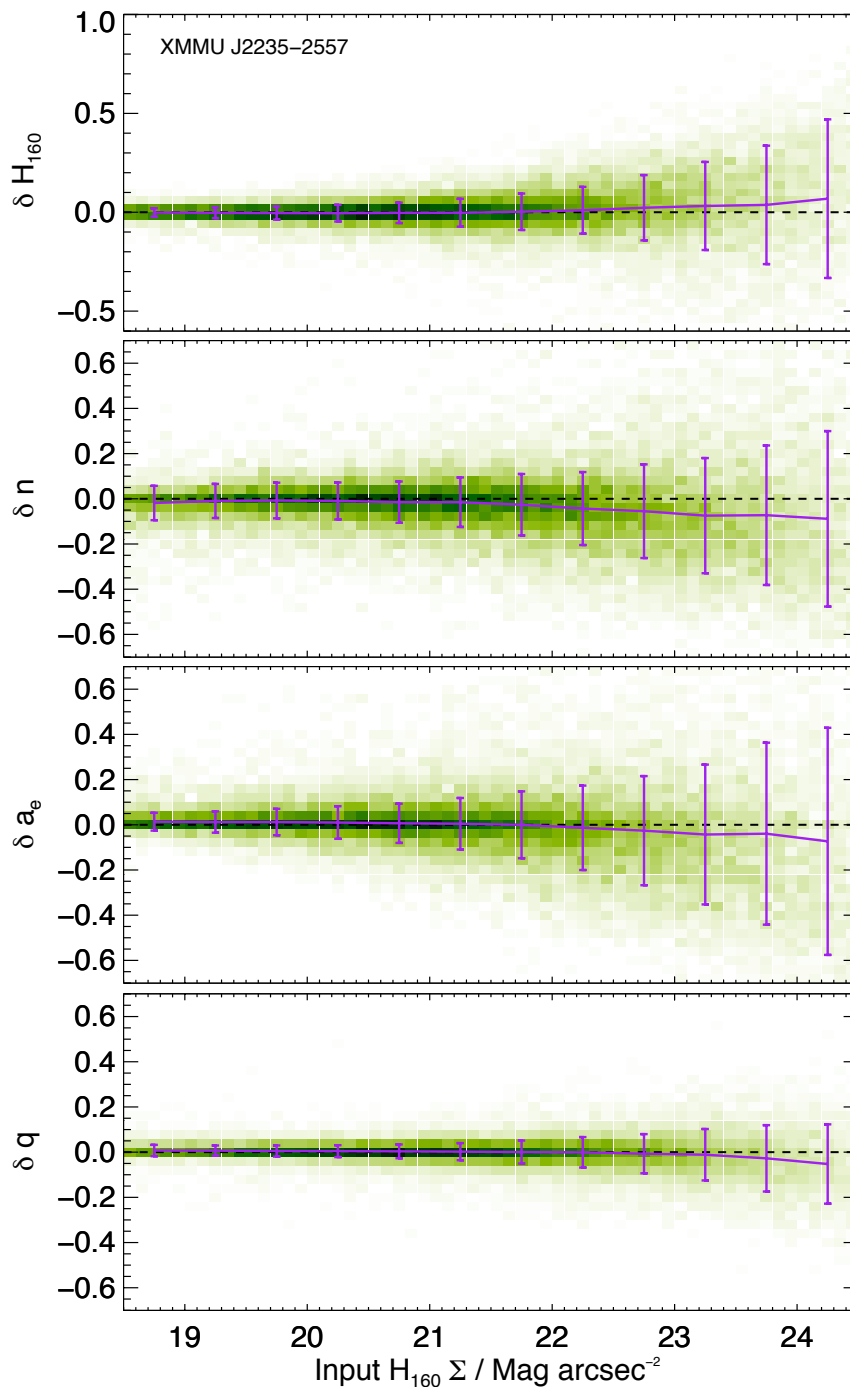


Figure 3.13: Differences between recovered and input structural parameters by GALFIT as a function of input mean H_{160} surface brightness in the simulation of XMMU J2235-2557. From top to bottom: magnitude $\delta H_{160} = (H_{160})_{out} - (H_{160})_{in}$, Sérsic indices $\delta n = (n_{out} - n_{in})/n_{in}$, effective semi-major axes $\delta a_e = (a_{e-out} - a_{e-in})/a_{e-in}$ and axis ratios $\delta q = (q_{out} - q_{in})/q_{in}$. Purple line indicates the median and 1σ dispersion in different bins ($0.5 \text{ mag arcsec}^{-2}$ bin width) and green-shaded 2D histogram shows the number density distribution of the simulated galaxies.

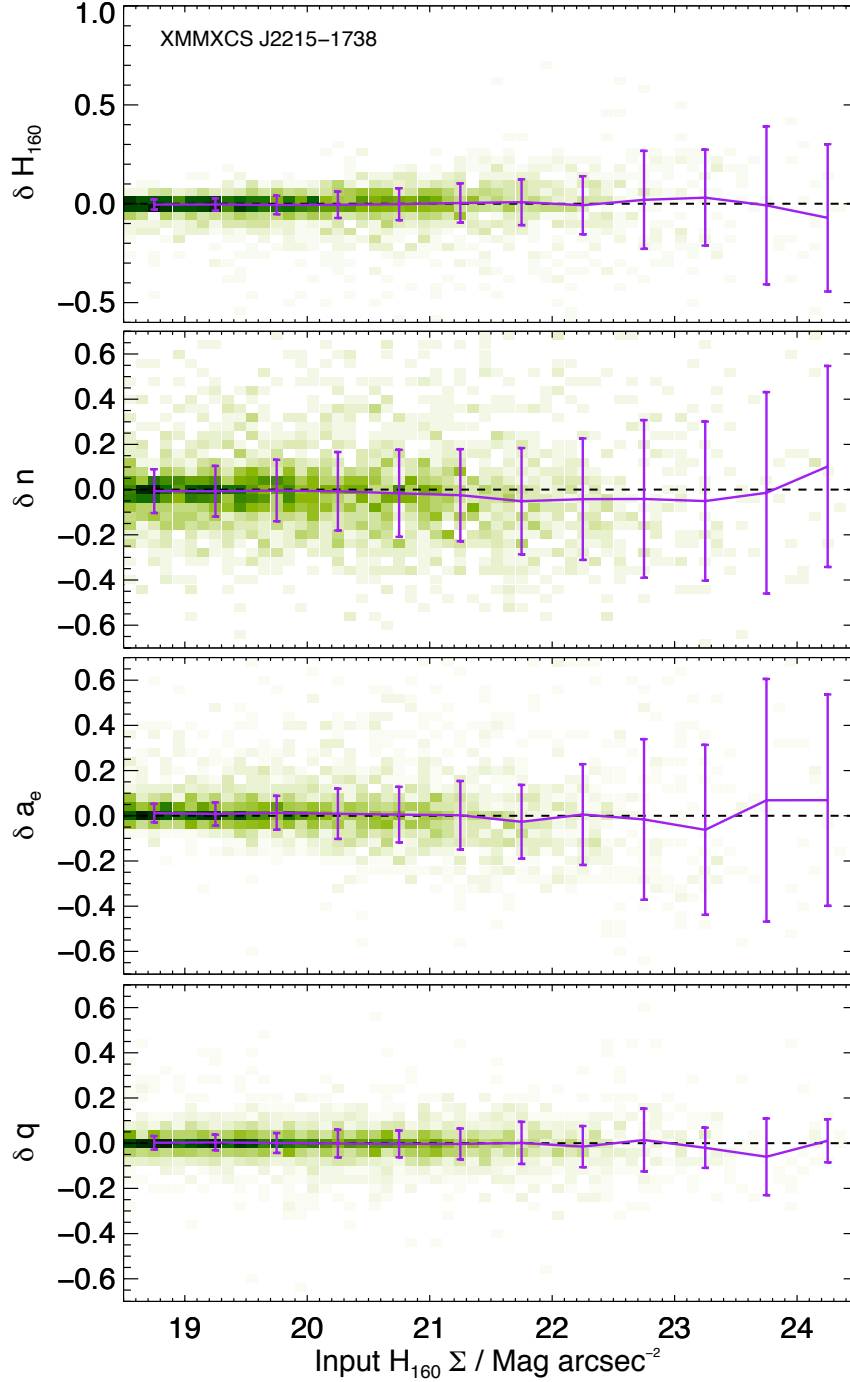


Figure 3.14: Differences between recovered and input structural parameters by GALFIT as a function of input mean H_{160} surface brightness in the simulation of XMMXCS J2215-1738. From top to bottom: magnitude $\delta H_{160} = (H_{160})_{out} - (H_{160})_{in}$, Sérsic indices $\delta n = (n_{out} - n_{in})/n_{in}$, effective semi-major axes $\delta a_e = (a_{e-out} - a_{e-in})/a_{e-in}$ and axis ratios $\delta q = (q_{out} - q_{in})/q_{in}$. Purple line indicates the median and 1σ dispersion in different bins ($0.5 \text{ mag arcsec}^{-2}$ bin width) and green-shaded 2D histogram shows the number density distribution of the simulated galaxies.

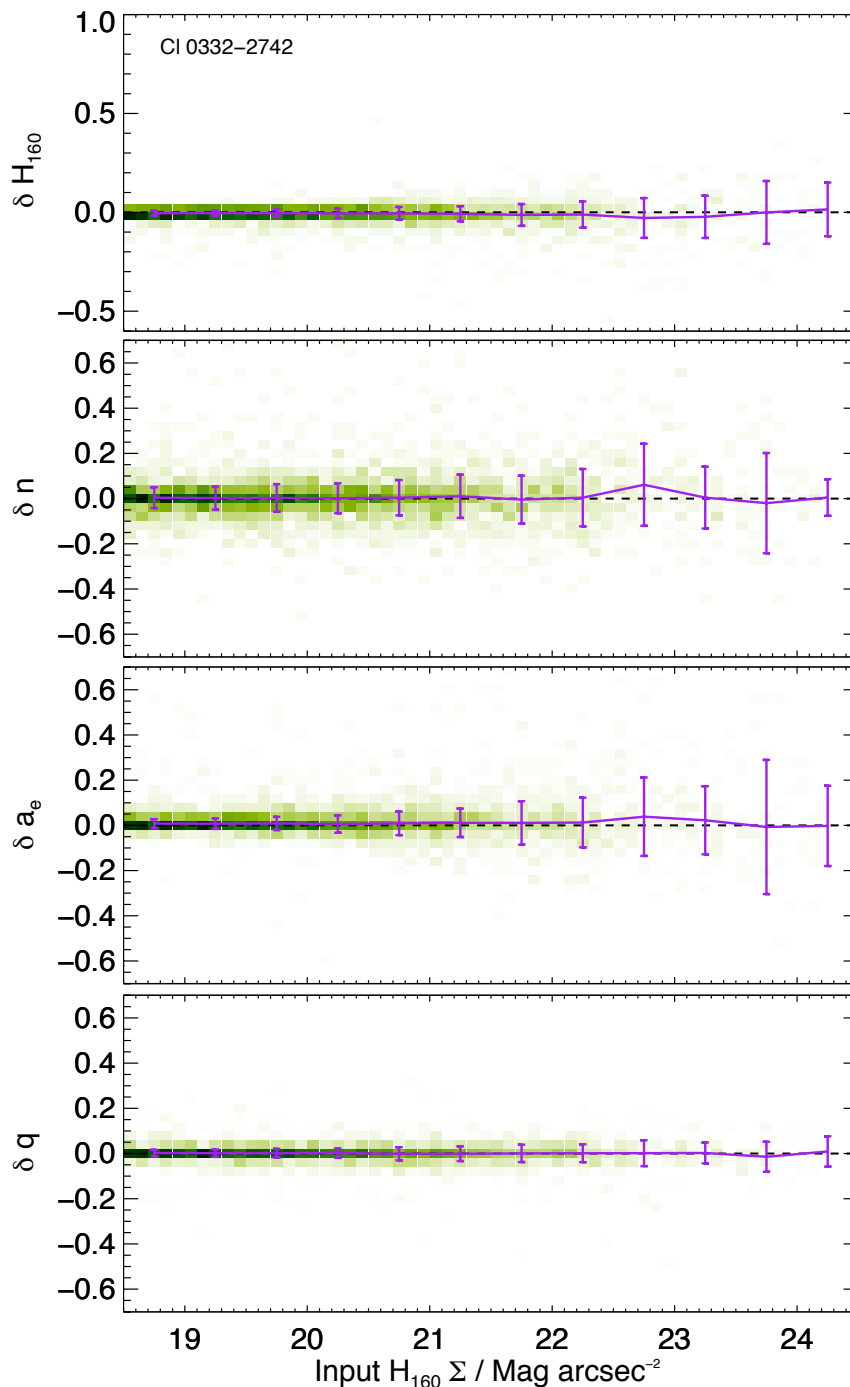


Figure 3.15: Differences between recovered and input structural parameters by GALFIT as a function of input mean H_{160} surface brightness in the simulation of CI 0332-2742. From top to bottom: magnitude $\delta H_{160} = (H_{160})_{out} - (H_{160})_{in}$, Sérsic indices $\delta n = (n_{out} - n_{in})/n_{in}$, effective semi-major axes $\delta a_e = (a_{e-out} - a_{e-in})/a_{e-in}$ and axis ratios $\delta q = (q_{out} - q_{in})/q_{in}$. Purple line indicates the median and 1σ dispersion in different bins ($0.5 \text{ mag arcsec}^{-2}$ bin width) and green-shaded 2D histogram shows the number density distribution of the simulated galaxies.

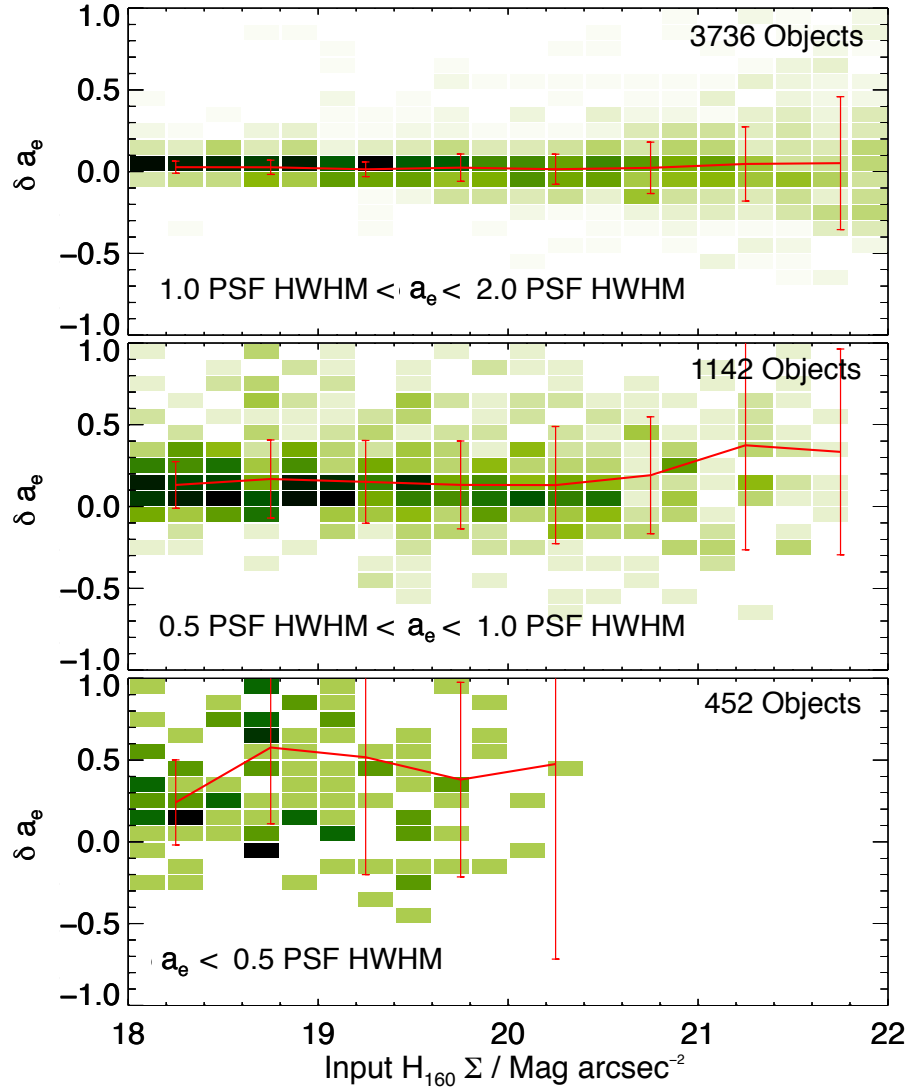


Figure 3.16: Differences between recovered and input effective semi-major axes by GALFIT $\delta a_e = (a_{e-out} - a_{e-in})/a_{e-in}$ of XMMU J2235-2557 as a function of input mean H_{160} surface brightness. From top to bottom: simulated galaxies with different ranges of input effective radius, $1.0 \text{ PSF HWHM} < a_e < 2.0 \text{ PSF HWHM}$, $0.5 \text{ PSF HWHM} < a_e < 1.0 \text{ PSF HWHM}$ and $a_e < 0.5 \text{ PSF HWHM}$. The red line indicates the median and 1σ dispersion in different bins ($0.5 \text{ mag arcsec}^{-2}$ bin width) and the green-shaded 2D histogram in each panel shows the number density distribution of the simulated galaxies.

As we explained in the previous section, our method is unable to measure sizes reliably from galaxies with $a_e < 0.5$ PSF HWHM. Several objects at the low-mass end have sizes < 0.5 PSF HWHM and are hence discarded in the analyses (see Section 3.6).

The necessity of the M_*/L extrapolation

In deriving the mass maps, we implement an extrapolation scheme to determine the M_*/L in regions with insufficient signal-to-noise (described in Section 3.5.1). The low S/N or sky regions are problematic as the colours (and hence M_*/L) are not well determined. Converting mass directly on these regions will induce a huge scatter of mass in the background, which in turn have serious effects on the structural parameter measurements. Our extrapolation scheme can preserve the sky noise and at the same time provide a reasonable M_*/L estimate to these regions. We illustrate this effect in Figure 3.20. The top panel shows the differences between input and recovered sizes by GALFIT with extrapolation, while the bottom panel shows the differences without applying the extrapolation. In the absence of extrapolation, a huge bias can be seen in all bins of surface brightness. Sizes are more underestimated in galaxies with low surface brightness.

Previous studies use a different method to solve this issue, for example in Lang et al. (2014) who derived mass maps for galaxies in CANDELS, these low S/N regions are assigned the average M_*/L of the three nearest Voronoi bins. We find that averaging the nearest three Voronoi bins does not work as well as our annular average extrapolation. For star-forming galaxies which have sub-structures such as star forming clumps and spiral arms (see, e.g. Wuyts et al., 2012), it might be more suitable to use the nearest neighbour extrapolation as in Lang et al. (2014). Our method, on the other hand, works well for early-type galaxies which usually have smooth(er) surface brightness profiles.

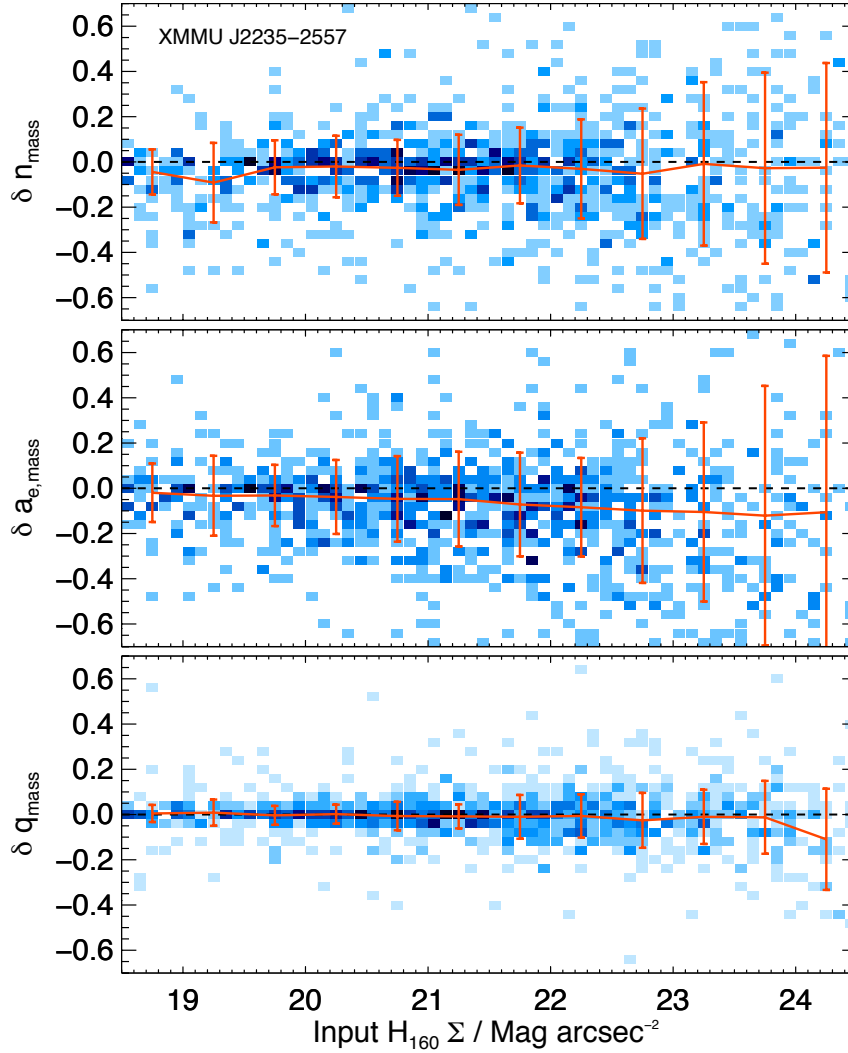


Figure 3.17: Differences between recovered and input mass-weighted structural parameters by GALFIT as a function of input mean H_{160} surface brightness in the simulation of XMMU J2235-2557. Similar to Figure 3.13, but for mass-weighted structural parameters. From top to bottom: Sérsic indices $\delta n = (n_{out} - n_{in})/n_{in}$, effective semi-major axes $\delta a_e = (a_{e-out} - a_{e-in})/a_{e-in}$ and axis ratios $\delta q = (q_{out} - q_{in})/q_{in}$. Red line indicates the median and 1σ dispersion in different bins ($0.5 \text{ mag arcsec}^{-2}$ bin width) and blue-shaded 2D histogram shows the number density distribution of the simulated galaxies.

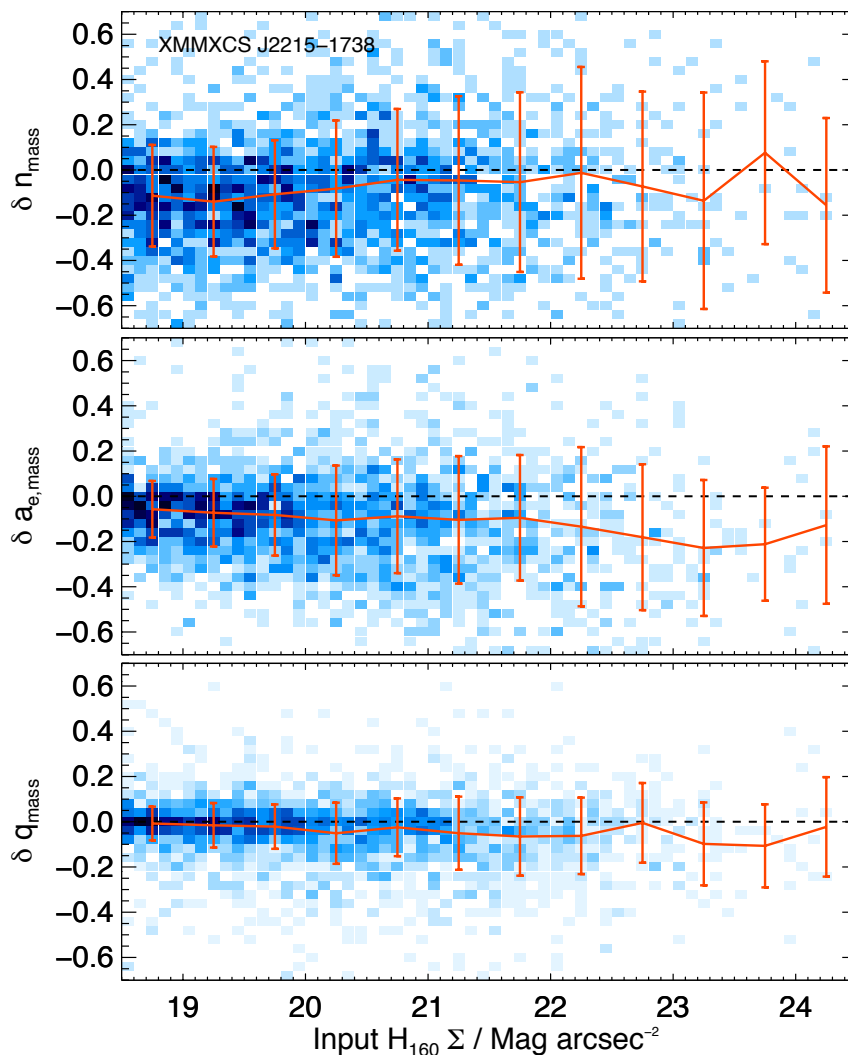


Figure 3.18: Differences between recovered and input mass-weighted structural parameters by GALFIT as a function of input mean H_{160} surface brightness in the simulation of XMMXCS J2215-1738. Similar to Figure 3.14, but for mass-weighted structural parameters. From top to bottom: Sérsic indices $\delta n = (n_{out} - n_{in})/n_{in}$, effective semi-major axes $\delta a_e = (a_{e-out} - a_{e-in})/a_{e-in}$ and axis ratios $\delta q = (q_{out} - q_{in})/q_{in}$. Red line indicates the median and 1σ dispersion in different bins ($0.5 \text{ mag arcsec}^{-2}$ bin width) and blue-shaded 2D histogram shows the number density distribution of the simulated galaxies.

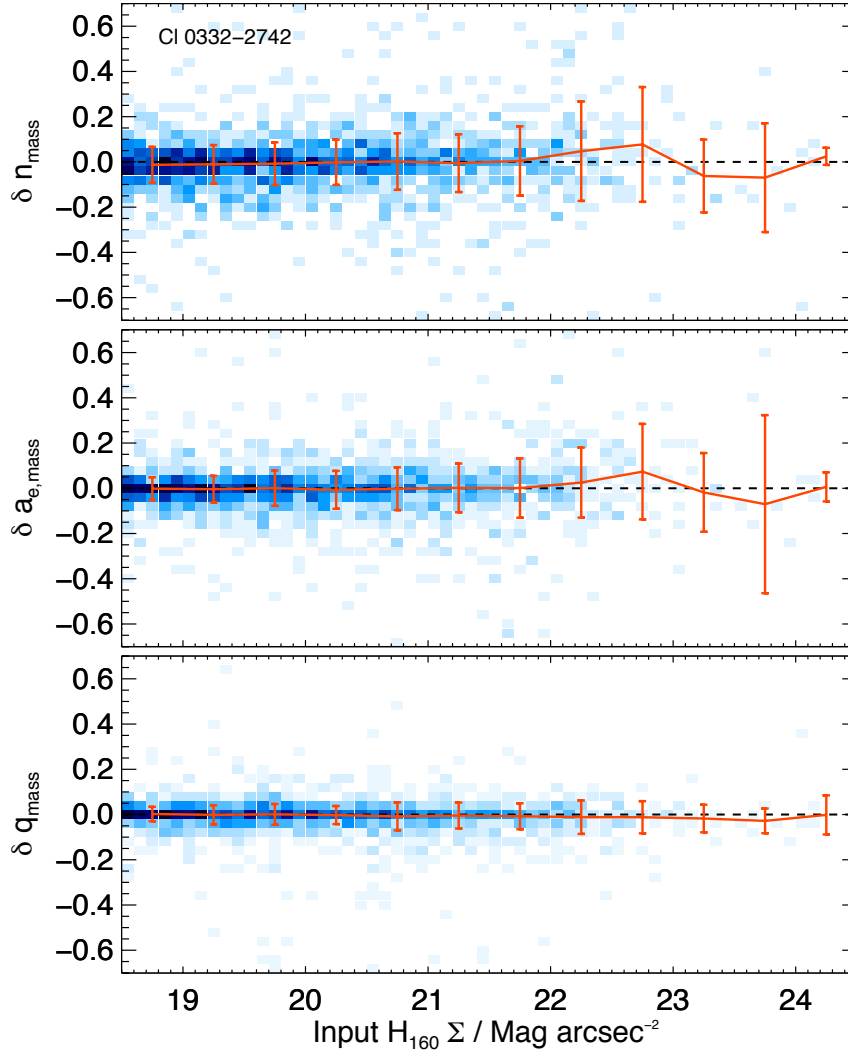


Figure 3.19: Differences between recovered and input mass-weighted structural parameters by GALFIT as a function of input mean H_{160} surface brightness in the simulation of Cl 0332-2742. Similar to Figure 3.15, but for mass-weighted structural parameters. From top to bottom: Sérsic indices $\delta n = (n_{out} - n_{in})/n_{in}$, effective semi-major axes $\delta a_e = (a_{e-out} - a_{e-in})/a_{e-in}$ and axis ratios $\delta q = (q_{out} - q_{in})/q_{in}$. Red line indicates the median and 1σ dispersion in different bins ($0.5 \text{ mag arcsec}^{-2}$ bin width) and blue-shaded 2D histogram shows the number density distribution of the simulated galaxies.

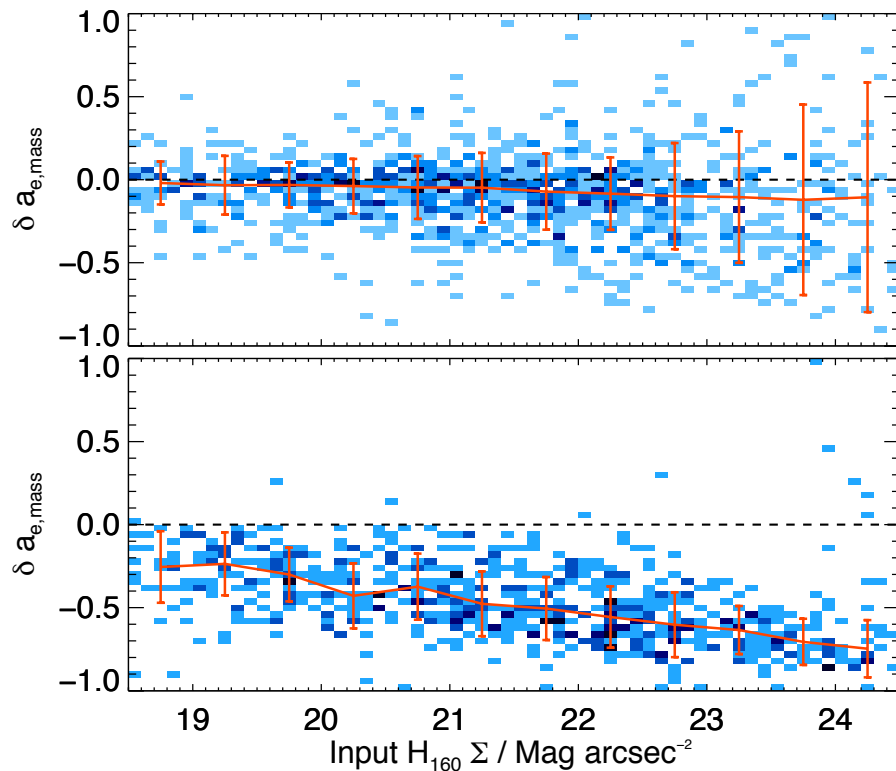


Figure 3.20: Differences between recovered and input mass-weighted effective semi-major axes by GALFIT $\delta a_e = (a_{e-out} - a_{e-in})/a_{e-in}$ of XMMU J2235-2557 as a function of input mean H_{160} surface brightness. Top: sizes derived from mass maps with the extrapolation applied, same as the middle panel in Figure 3.17 but with expanded y-axis for comparison. Bottom: sizes derived from mass maps without applying the extrapolation scheme. Red line indicates the median and 1σ dispersion in different bins ($0.5 \text{ mag arcsec}^{-2}$ bin width) and blue-shaded 2D histogram in each panel shows the number density distribution of the simulated galaxies.

Table 3.1: Structural parameters and colour gradients of the red sequence galaxies in XMMU J2235-2557

ID	$\log M_*$ ^a (M_\odot)	$\nabla_{z_{850}-H_{160}}$ ^b	$\nabla_{\log(M/L)}$ ^b	a_e (kpc)	n	q	R_{e-circ} (kpc)	$a_{e,mass}$ (kpc)	n_{mass}	q_{mass}	$R_{e-circ-mass}$ (kpc)	Σ^c (mag kpc ⁻²)	$\log(\Sigma_{mass})^c$ (M_\odot kpc ⁻²)	$\log(\Sigma_1)^d$ (M_\odot kpc ⁻²)
36	11.04 ± 0.08	-0.033 ± 0.096	-0.038 ± 0.220	4.12 ± 0.38	4.77 ± 0.46	0.79 ± 0.03	3.67 ± 0.35	3.66 ± 0.71	7.43 ± 0.97	0.79 ± 0.05	3.26 ± 0.65	25.62 ± 0.21	9.22 ± 0.19	9.74 ± 0.03
170	11.82 ± 0.07	-0.133 ± 0.038	-0.129 ± 0.095	24.62 ± 5.95	4.49 ± 0.93	0.62 ± 0.05	19.46 ± 4.77	8.39 ± 2.69	3.91 ± 1.13	0.64 ± 0.08	6.72 ± 2.19	27.60 ± 0.53	9.37 ± 0.29	10.00 ± 0.21
198	10.22 ± 0.05	-0.626 ± 0.585	-0.499 ± 0.995	1.02 ± 0.07	2.05 ± 0.28	0.86 ± 0.05	0.94 ± 0.07	0.71 ± 0.13	1.09 ± 0.19	0.34 ± 0.02	0.42 ± 0.08	24.11 ± 0.15	10.18 ± 0.16	9.58 ± 0.02
220	10.82 ± 0.06	-0.482 ± 0.190	-0.342 ± 0.348	2.34 ± 0.21	4.91 ± 0.49	0.71 ± 0.03	1.97 ± 0.18	1.53 ± 0.27	8.64 ± 1.59	0.37 ± 0.02	0.93 ± 0.17	24.72 ± 0.20	10.08 ± 0.17	9.98 ± 0.06
239	10.51 ± 0.06	-0.365 ± 0.314	-0.212 ± 0.588	1.37 ± 0.09	4.00 ± 0.42	0.84 ± 0.03	1.26 ± 0.09	0.90 ± 0.13	8.38 ± 1.54	0.55 ± 0.03	0.67 ± 0.10	24.52 ± 0.15	10.06 ± 0.14	9.81 ± 0.04
296	10.53 ± 0.05	-0.392 ± 0.110	-0.259 ± 0.220	3.00 ± 0.26	1.37 ± 0.13	0.59 ± 0.02	2.31 ± 0.21	2.20 ± 0.42	2.07 ± 0.27	0.48 ± 0.03	1.52 ± 0.29	25.26 ± 0.19	9.37 ± 0.17	9.53 ± 0.05
308	10.89 ± 0.05	-0.426 ± 0.099	-0.310 ± 0.204	2.99 ± 0.22	3.99 ± 0.34	0.79 ± 0.02	2.66 ± 0.20	1.50 ± 0.25	4.40 ± 0.61	0.72 ± 0.03	1.27 ± 0.21	24.68 ± 0.16	9.88 ± 0.15	9.92 ± 0.04
343	10.55 ± 0.08	-0.371 ± 0.558	-0.189 ± 0.887	1.18 ± 0.05	2.38 ± 0.24	0.39 ± 0.01	0.74 ± 0.04	1.23 ± 0.16	0.89 ± 0.12	0.13 ± 0.02	0.45 ± 0.07	23.48 ± 0.10	10.45 ± 0.16	9.85 ± 0.03
352	11.23 ± 0.07	-0.287 ± 0.086	-0.240 ± 0.158	4.58 ± 0.42	4.70 ± 0.44	0.57 ± 0.02	3.45 ± 0.32	3.42 ± 0.65	6.87 ± 0.89	0.37 ± 0.02	2.09 ± 0.41	25.23 ± 0.20	9.79 ± 0.18	10.23 ± 0.06
357	10.33 ± 0.05	0.117 ± 0.124	0.105 ± 0.254	2.38 ± 0.17	1.19 ± 0.11	0.40 ± 0.01	1.51 ± 0.11	1.92 ± 0.32	1.78 ± 0.26	0.26 ± 0.01	0.98 ± 0.16	24.97 ± 0.16	9.55 ± 0.15	9.47 ± 0.04
365	10.53 ± 0.08	-0.158 ± 0.612	-0.111 ± 0.964	1.38 ± 0.09	3.98 ± 0.46	0.53 ± 0.02	1.01 ± 0.07	-	-	-	-	24.23 ± 0.15	-	-
368	10.90 ± 0.08	-0.906 ± 0.184	-0.491 ± 0.401	2.41 ± 0.22	5.78 ± 0.56	0.89 ± 0.03	2.27 ± 0.21	-	-	-	-	25.12 ± 0.21	-	-
385	10.62 ± 0.08	-0.619 ± 0.213	-0.418 ± 0.355	1.73 ± 0.09	3.00 ± 0.26	0.35 ± 0.01	1.02 ± 0.05	1.65 ± 0.29	1.93 ± 0.36	0.29 ± 0.02	0.90 ± 0.16	23.85 ± 0.12	9.92 ± 0.18	9.73 ± 0.04
407	11.24 ± 0.07	-0.448 ± 0.108	-0.272 ± 0.206	3.03 ± 0.19	4.85 ± 0.40	0.69 ± 0.02	2.53 ± 0.16	1.53 ± 0.21	3.62 ± 0.45	0.60 ± 0.03	1.18 ± 0.16	24.53 ± 0.14	10.30 ± 0.14	10.25 ± 0.04
433	10.95 ± 0.07	-0.299 ± 0.150	-0.193 ± 0.266	2.76 ± 0.21	4.10 ± 0.36	0.70 ± 0.02	2.31 ± 0.18	1.72 ± 0.28	4.29 ± 0.61	0.55 ± 0.03	1.28 ± 0.21	25.08 ± 0.17	9.94 ± 0.16	10.00 ± 0.04
478	11.16 ± 0.07	-0.649 ± 0.099	-0.339 ± 0.225	5.14 ± 0.65	5.61 ± 0.65	0.78 ± 0.03	4.53 ± 0.58	2.41 ± 0.51	5.53 ± 0.88	0.73 ± 0.04	2.05 ± 0.43	26.09 ± 0.28	9.73 ± 0.20	10.06 ± 0.05
538	10.48 ± 0.06	-0.846 ± 0.296	-0.643 ± 0.566	1.65 ± 0.15	5.37 ± 0.62	0.82 ± 0.03	1.49 ± 0.14	-	-	-	-	24.88 ± 0.20	-	-
552	10.46 ± 0.05	-0.777 ± 0.092	-0.464 ± 0.217	6.69 ± 1.62	0.51 ± 0.11	0.80 ± 0.07	6.00 ± 1.48	5.21 ± 1.67	0.84 ± 0.24	0.69 ± 0.09	4.34 ± 1.41	27.61 ± 0.53	8.39 ± 0.29	8.52 ± 0.16
558	11.10 ± 0.08	0.562 ± 0.133	0.346 ± 0.306	4.93 ± 0.58	4.77 ± 0.54	0.73 ± 0.03	4.21 ± 0.51	-	-	-	-	25.77 ± 0.26	-	-
571	10.35 ± 0.05	0.194 ± 0.518	0.097 ± 0.689	1.16 ± 0.08	6.44 ± 0.84	0.68 ± 0.03	0.96 ± 0.07	-	-	-	-	24.00 ± 0.16	-	-
576	11.01 ± 0.08	-0.417 ± 0.320	-0.252 ± 0.447	2.18 ± 0.09	2.97 ± 0.24	0.36 ± 0.01	1.30 ± 0.06	1.47 ± 0.19	4.13 ± 0.44	0.21 ± 0.01	0.67 ± 0.09	23.51 ± 0.09	10.56 ± 0.14	10.20 ± 0.03
585	10.49 ± 0.08	-0.494 ± 0.483	-0.281 ± 0.762	1.05 ± 0.06	2.63 ± 0.28	0.58 ± 0.03	0.80 ± 0.05	-	-	-	-	23.91 ± 0.14	-	-
588	10.81 ± 0.08	-0.605 ± 0.035	-0.384 ± 0.084	5.42 ± 0.63	1.98 ± 0.22	0.35 ± 0.01	3.20 ± 0.38	3.65 ± 0.76	2.38 ± 0.38	0.27 ± 0.01	1.89 ± 0.40	25.89 ± 0.26	9.46 ± 0.20	9.65 ± 0.07
599	11.40 ± 0.07	-0.451 ± 0.076	-0.274 ± 0.148	7.05 ± 0.83	4.84 ± 0.54	0.52 ± 0.02	5.07 ± 0.60	3.50 ± 0.73	5.69 ± 0.88	0.45 ± 0.02	2.35 ± 0.50	25.67 ± 0.26	9.86 ± 0.20	10.27 ± 0.05
618	10.65 ± 0.08	-1.025 ± 0.128	-0.613 ± 0.278	3.37 ± 0.51	2.17 ± 0.31	0.79 ± 0.04	3.00 ± 0.46	1.54 ± 0.35	2.50 ± 0.43	0.64 ± 0.06	1.23 ± 0.29	26.27 ± 0.33	9.68 ± 0.22	9.63 ± 0.04
637	10.69 ± 0.05	-0.325 ± 0.224	-0.273 ± 0.403	1.46 ± 0.07	2.58 ± 0.21	0.82 ± 0.02	1.33 ± 0.07	0.70 ± 0.12	4.86 ± 0.88	0.80 ± 0.05	0.63 ± 0.11	23.86 ± 0.11	10.30 ± 0.16	9.97 ± 0.03
642	10.56 ± 0.08	-0.341 ± 0.289	-0.149 ± 0.445	1.71 ± 0.10	1.96 ± 0.18	0.39 ± 0.01	1.06 ± 0.07	1.24 ± 0.17	1.45 ± 0.19	0.34 ± 0.02	0.73 ± 0.10	24.18 ± 0.14	10.04 ± 0.14	9.74 ± 0.03

^a Total stellar masses are estimated using the M_*/L -colour relation, the $z_{850} - H_{160}$ aperture colours and the total luminosity $L_{H_{160}}$ from the best-fit Sérsic models.^b Colour gradients $\nabla_{z_{850}-H_{160}}$ and M_*/L gradients $\nabla_{\log(M/L)}$ are defined as $d(z_{850} - H_{160})/d\log(a)$ and $d(\log(M/L))/d\log(a)$ respectively. The gradient is fitted in the radial range of PSF HWHM $< a < 3.5 a_e$.^c Mean surface brightness Σ and mean surface mass density Σ_{mass} are defined as $\text{mag} + 2.5 \log(2\pi q a_e^2)$ and $\log(M_*/2\pi q_{mass} a_e^2)$.^d Mean surface mass density within a radius of 1 kpc Σ_1 is defined as $\log(M_*(< 1\text{kpc})/\pi(1\text{kpc})^2)$, derived from integrating the fitted 2D mass profiles.

Table 3.2: Structural parameters and colour gradients of the red sequence galaxies in XMMXCS J2215-1738

ID	$\log M_*$ ^a (M_\odot)	$\nabla_{z_{850}-H_{160}}$ ^b	$\nabla_{\log(M/L)}$ ^b	a_e (kpc)	n	q	R_{e-circ} (kpc)	$a_{e, mass}$ (kpc)	n_{mass}	q_{mass}	$R_{e-circ-mass}$ (kpc)	Σ^c (mag kpc ⁻²)	$\log(\Sigma_{mass})^c$ (M_\odot kpc ⁻²)	$\log(\Sigma_1)^d$ (M_\odot kpc ⁻²)
317	10.60 ± 0.08	-0.324 ± 0.118	-0.239 ± 0.237	1.85 ± 0.21	2.84 ± 0.51	0.84 ± 0.05	1.69 ± 0.20	1.16 ± 0.28	4.41 ± 1.34	0.73 ± 0.10	0.99 ± 0.25	24.96 ± 0.26	9.81 ± 0.23	9.86 ± 0.04
342	11.37 ± 0.10	-0.784 ± 0.068	-0.394 ± 0.180	8.49 ± 1.98	7.64 ± 2.07	0.69 ± 0.06	7.06 ± 1.68	1.46 ± 0.52	5.65 ± 2.65	0.50 ± 0.09	1.03 ± 0.37	26.94 ± 0.52	10.54 ± 0.33	10.19 ± 0.03
522	11.11 ± 0.10	-0.979 ± 0.084	-0.585 ± 0.225	8.11 ± 3.05	5.57 ± 1.96	0.75 ± 0.07	7.04 ± 2.67	1.03 ± 0.31	2.90 ± 1.39	0.83 ± 0.15	0.94 ± 0.29	27.74 ± 0.82	10.37 ± 0.29	9.89 ± 0.04
528	10.87 ± 0.08	-0.364 ± 0.148	-0.225 ± 0.248	2.14 ± 0.16	2.57 ± 0.36	0.36 ± 0.02	1.28 ± 0.10	1.41 ± 0.25	1.72 ± 0.41	0.16 ± 0.02	0.56 ± 0.10	24.18 ± 0.17	10.57 ± 0.18	10.04 ± 0.03
548	10.77 ± 0.08	-0.171 ± 0.349	-0.112 ± 0.520	1.12 ± 0.05	3.22 ± 0.33	0.29 ± 0.01	0.61 ± 0.03	—	—	—	—	22.68 ± 0.10	—	—
555	11.01 ± 0.08	-0.476 ± 0.097	-0.281 ± 0.208	3.49 ± 0.53	3.88 ± 0.79	0.67 ± 0.05	2.86 ± 0.45	1.56 ± 0.44	5.52 ± 2.07	0.77 ± 0.13	1.37 ± 0.40	25.80 ± 0.34	9.94 ± 0.27	10.04 ± 0.04
603	11.02 ± 0.10	-1.475 ± 0.115	-0.735 ± 0.299	4.28 ± 0.86	7.71 ± 1.90	0.76 ± 0.07	3.74 ± 0.77	—	—	—	—	26.63 ± 0.45	—	—
614	10.98 ± 0.08	-0.458 ± 0.071	-0.235 ± 0.117	3.33 ± 0.41	1.07 ± 0.21	0.46 ± 0.03	2.26 ± 0.29	2.69 ± 0.68	1.17 ± 0.37	0.29 ± 0.04	1.44 ± 0.37	25.15 ± 0.28	9.87 ± 0.24	9.88 ± 0.04
650	10.47 ± 0.07	-0.145 ± 0.376	-0.099 ± 0.741	0.75 ± 0.04	5.84 ± 0.66	0.93 ± 0.04	0.72 ± 0.04	—	—	—	—	23.40 ± 0.13	—	—
664	10.93 ± 0.08	-0.029 ± 0.139	-0.060 ± 0.254	2.00 ± 0.16	4.48 ± 0.63	0.58 ± 0.03	1.53 ± 0.12	0.92 ± 0.17	5.17 ± 1.26	0.52 ± 0.05	0.66 ± 0.12	24.42 ± 0.18	10.49 ± 0.18	10.18 ± 0.03
695	11.13 ± 0.10	-0.527 ± 0.104	-0.312 ± 0.199	2.77 ± 0.21	3.17 ± 0.44	0.39 ± 0.02	1.74 ± 0.14	1.62 ± 0.29	1.92 ± 0.46	0.20 ± 0.02	0.73 ± 0.14	24.48 ± 0.17	10.61 ± 0.19	10.27 ± 0.03
698	10.39 ± 0.07	-0.768 ± 0.059	-0.492 ± 0.129	3.09 ± 0.47	1.53 ± 0.31	0.88 ± 0.06	2.89 ± 0.45	1.38 ± 0.39	2.19 ± 0.82	0.90 ± 0.15	1.31 ± 0.38	26.12 ± 0.34	9.36 ± 0.27	9.50 ± 0.04
702	10.62 ± 0.08	-0.101 ± 0.224	0.008 ± 0.324	1.50 ± 0.06	2.39 ± 0.24	0.29 ± 0.01	0.81 ± 0.04	—	—	—	—	23.51 ± 0.10	—	—
727	10.88 ± 0.08	0.054 ± 0.158	0.001 ± 0.300	1.79 ± 0.08	3.47 ± 0.35	0.39 ± 0.01	1.11 ± 0.05	—	—	—	—	23.50 ± 0.10	—	—
728	11.11 ± 0.08	-0.445 ± 0.085	-0.265 ± 0.208	2.95 ± 0.33	4.00 ± 0.70	0.81 ± 0.05	2.66 ± 0.31	1.60 ± 0.39	3.57 ± 1.08	0.78 ± 0.11	1.41 ± 0.36	25.09 ± 0.25	10.01 ± 0.23	10.11 ± 0.03
764	10.92 ± 0.08	-0.639 ± 0.081	-0.486 ± 0.175	2.59 ± 0.29	4.38 ± 0.77	0.83 ± 0.05	2.36 ± 0.28	0.74 ± 0.18	2.98 ± 0.90	0.79 ± 0.11	0.66 ± 0.17	25.09 ± 0.26	10.48 ± 0.23	6.94 ± 0.03
774	10.76 ± 0.08	-0.160 ± 0.297	-0.086 ± 0.495	1.16 ± 0.05	4.19 ± 0.44	0.62 ± 0.02	0.91 ± 0.04	0.69 ± 0.09	5.17 ± 1.19	0.49 ± 0.04	0.48 ± 0.06	23.38 ± 0.10	10.60 ± 0.14	10.05 ± 0.03
889	10.90 ± 0.08	-0.260 ± 0.627	-0.166 ± 0.770	1.07 ± 0.05	2.16 ± 0.22	0.26 ± 0.01	0.54 ± 0.03	—	—	—	—	22.41 ± 0.10	—	—
1018	10.60 ± 0.08	-0.615 ± 0.057	-0.353 ± 0.139	2.42 ± 0.27	2.92 ± 0.52	0.36 ± 0.02	1.44 ± 0.17	—	—	—	—	24.85 ± 0.26	—	—
1046	10.66 ± 0.08	-0.330 ± 0.130	-0.238 ± 0.303	1.67 ± 0.19	2.92 ± 0.52	0.95 ± 0.06	1.63 ± 0.19	0.85 ± 0.21	4.64 ± 1.41	0.76 ± 0.10	0.74 ± 0.19	24.88 ± 0.25	10.13 ± 0.23	9.85 ± 0.03
1051	10.93 ± 0.08	-0.584 ± 0.132	-0.268 ± 0.299	2.34 ± 0.34	7.03 ± 1.30	0.81 ± 0.05	2.11 ± 0.32	0.71 ± 0.17	7.70 ± 2.32	0.71 ± 0.10	0.60 ± 0.15	25.14 ± 0.33	10.58 ± 0.23	10.06 ± 0.03
1058	10.90 ± 0.08	-0.999 ± 0.141	-0.440 ± 0.329	2.69 ± 0.94	8.00 ± 3.10	0.70 ± 0.05	2.26 ± 0.80	—	—	—	—	25.39 ± 0.77	—	—
1102	11.08 ± 0.10	-1.484 ± 0.088	-0.529 ± 0.189	3.05 ± 0.46	0.93 ± 0.19	0.80 ± 0.06	2.72 ± 0.42	2.05 ± 0.58	0.53 ± 0.20	0.65 ± 0.10	1.65 ± 0.48	26.04 ± 0.34	9.85 ± 0.27	6.56 ± 0.04
1129	11.03 ± 0.08	-1.107 ± 0.069	-0.605 ± 0.141	4.23 ± 0.65	3.99 ± 0.82	0.55 ± 0.04	3.14 ± 0.50	0.98 ± 0.28	2.32 ± 0.87	0.37 ± 0.06	0.60 ± 0.18	25.97 ± 0.34	10.68 ± 0.27	10.07 ± 0.03
1182	11.11 ± 0.08	-0.383 ± 0.184	-0.223 ± 0.268	1.79 ± 0.07	3.48 ± 0.34	0.31 ± 0.01	1.00 ± 0.04	0.96 ± 0.12	3.51 ± 0.79	0.21 ± 0.02	0.44 ± 0.06	22.87 ± 0.10	11.02 ± 0.14	10.36 ± 0.03
1189	10.99 ± 0.10	-0.519 ± 0.169	-0.312 ± 0.313	1.87 ± 0.15	5.89 ± 0.84	0.56 ± 0.03	1.41 ± 0.12	—	—	—	—	24.40 ± 0.18	—	—
1212	11.21 ± 0.10	-0.404 ± 0.088	-0.155 ± 0.173	2.90 ± 0.32	2.59 ± 0.45	0.76 ± 0.05	2.53 ± 0.29	1.57 ± 0.38	2.15 ± 0.65	0.78 ± 0.11	1.39 ± 0.35	25.11 ± 0.25	10.13 ± 0.24	10.15 ± 0.03
1217	10.61 ± 0.08	-0.602 ± 0.176	-0.310 ± 0.303	1.31 ± 0.07	1.99 ± 0.23	0.71 ± 0.03	1.11 ± 0.06	0.73 ± 0.11	2.50 ± 0.60	0.52 ± 0.05	0.53 ± 0.08	23.99 ± 0.12	10.37 ± 0.16	10.03 ± 0.03
1225	11.21 ± 0.08	-0.365 ± 0.075	-0.192 ± 0.222	3.92 ± 0.62	7.46 ± 1.54	0.96 ± 0.07	3.84 ± 0.62	2.14 ± 0.61	8.42 ± 3.16	0.91 ± 0.15	2.04 ± 0.60	25.88 ± 0.35	9.79 ± 0.27	10.16 ± 0.04

^a Total stellar masses are estimated using the M_*/L -colour relation, the $z_{850} - H_{160}$ aperture colours and the total luminosity $L_{H_{160}}$ from the best-fit Sérsic models.^b Colour gradients $\nabla_{z_{850}-H_{160}}$ and M_*/L gradients $\nabla_{\log(M/L)}$ are defined as $d(z_{850} - H_{160})/d\log(a)$ and $d(\log(M/L))/d\log(a)$ respectively. The gradient is fitted in the radial range of PSF HWHM $< a < 3.5 a_e$.^c Mean surface brightness Σ and mean surface mass density Σ_{mass} are defined as $\text{mag} + 2.5 \log(2\pi q a_e^2)$ and $\log(M_*/2\pi q_{mass} a_{e, mass}^2)$.^d Mean surface mass density within a radius of 1 kpc Σ_1 is defined as $\log(M_*(< 1\text{kpc}))/\pi(1\text{kpc})^2$, derived from integrating the fitted 2D mass profiles.

Table 3.3: Structural parameters and colour gradients of the red sequence galaxies in Cl 0332-2742

ID	$\log M_*^a$ (M_\odot)	$\nabla_{z_{850}-H_{160}}^b$	$\nabla_{\log(M/L)}^b$	a_e (kpc)	n	q	R_{e-circ} (kpc)	$a_{e,mass}$ (kpc)	n_{mass}	q_{mass}	$R_{e-circ-mass}$ (kpc)	Σ^c (mag kpc $^{-2}$)	$\log(\Sigma_{mass})^c$ (M_\odot kpc $^{-2}$)	$\log(\Sigma_1)^d$ (M_\odot kpc $^{-2}$)
11827	11.49 ± 0.07	-0.644 ± 0.034	-0.192 ± 0.047	7.97 ± 0.77	2.39 ± 0.25	0.60 ± 0.02	6.17 ± 0.61	5.12 ± 0.67	1.99 ± 0.30	0.60 ± 0.04	3.98 ± 0.53	26.38 ± 0.21	9.49 ± 0.14	9.90 ± 0.03
12177	11.13 ± 0.12	-0.422 ± 0.049	-0.138 ± 0.044	2.63 ± 0.08	1.84 ± 0.11	0.55 ± 0.01	1.95 ± 0.06	2.17 ± 0.17	1.79 ± 0.17	0.53 ± 0.02	1.58 ± 0.13	24.60 ± 0.07	9.93 ± 0.14	10.10 ± 0.03
12347	10.89 ± 0.12	-0.419 ± 0.114	-0.108 ± 0.113	1.52 ± 0.04	3.41 ± 0.18	0.62 ± 0.01	1.20 ± 0.03	1.24 ± 0.07	2.92 ± 0.25	0.56 ± 0.02	0.93 ± 0.06	24.05 ± 0.06	10.15 ± 0.13	10.07 ± 0.03
13096	10.53 ± 0.12	0.067 ± 0.165	0.001 ± 0.147	1.31 ± 0.05	2.86 ± 0.21	0.67 ± 0.02	1.07 ± 0.04	1.25 ± 0.11	2.94 ± 0.31	0.69 ± 0.03	1.04 ± 0.09	24.70 ± 0.09	9.69 ± 0.14	9.73 ± 0.03
19839	10.67 ± 0.13	-0.013 ± 0.273	-0.012 ± 0.223	1.31 ± 0.04	5.16 ± 0.32	0.48 ± 0.01	0.91 ± 0.03	1.15 ± 0.07	3.62 ± 0.33	0.40 ± 0.02	0.72 ± 0.05	23.90 ± 0.06	10.15 ± 0.14	9.90 ± 0.03
21613	10.91 ± 0.07	-0.776 ± 0.133	-0.172 ± 0.129	2.68 ± 0.15	5.76 ± 0.47	0.52 ± 0.02	1.94 ± 0.11	1.37 ± 0.13	3.28 ± 0.42	0.50 ± 0.03	0.97 ± 0.10	25.37 ± 0.13	10.14 ± 0.11	9.99 ± 0.03
21853	11.13 ± 0.13	-0.271 ± 0.055	-0.097 ± 0.061	1.61 ± 0.04	2.99 ± 0.16	0.95 ± 0.02	1.56 ± 0.04	1.31 ± 0.08	2.10 ± 0.18	0.92 ± 0.04	1.26 ± 0.08	23.96 ± 0.05	10.13 ± 0.14	10.20 ± 0.03
22281	10.68 ± 0.12	-0.029 ± 0.249	-0.014 ± 0.239	0.74 ± 0.02	2.62 ± 0.15	0.90 ± 0.02	0.71 ± 0.02	0.72 ± 0.04	1.71 ± 0.15	0.86 ± 0.03	0.67 ± 0.04	23.40 ± 0.05	10.23 ± 0.13	9.98 ± 0.03
22777	10.71 ± 0.12	-0.556 ± 0.134	-0.138 ± 0.128	1.30 ± 0.04	1.83 ± 0.12	0.64 ± 0.01	1.04 ± 0.03	1.12 ± 0.09	1.62 ± 0.16	0.70 ± 0.03	0.94 ± 0.08	24.27 ± 0.07	9.97 ± 0.14	9.91 ± 0.03
24147	10.93 ± 0.12	-0.411 ± 0.210	-0.128 ± 0.174	1.47 ± 0.03	2.28 ± 0.12	0.53 ± 0.01	1.06 ± 0.03	1.17 ± 0.07	2.49 ± 0.22	0.47 ± 0.02	0.81 ± 0.05	23.77 ± 0.06	10.32 ± 0.13	10.15 ± 0.03
24517	11.22 ± 0.10	-0.415 ± 0.109	-0.101 ± 0.112	1.84 ± 0.04	5.73 ± 0.30	0.77 ± 0.01	1.61 ± 0.04	1.25 ± 0.07	5.60 ± 0.48	0.76 ± 0.03	1.09 ± 0.07	24.02 ± 0.06	10.34 ± 0.11	10.38 ± 0.03
24882	10.81 ± 0.12	-0.160 ± 0.290	-0.051 ± 0.235	0.85 ± 0.02	3.47 ± 0.18	0.56 ± 0.01	0.63 ± 0.01	0.81 ± 0.04	3.86 ± 0.32	0.56 ± 0.02	0.61 ± 0.03	22.81 ± 0.05	10.45 ± 0.13	10.14 ± 0.03
25338	11.01 ± 0.10	-0.312 ± 0.248	-0.108 ± 0.199	1.36 ± 0.03	3.34 ± 0.17	0.38 ± 0.01	0.83 ± 0.02	1.09 ± 0.06	3.05 ± 0.25	0.40 ± 0.01	0.69 ± 0.04	23.18 ± 0.05	10.54 ± 0.11	10.26 ± 0.03
25972	11.07 ± 0.10	-0.499 ± 0.069	-0.141 ± 0.077	1.92 ± 0.06	2.73 ± 0.17	0.89 ± 0.02	1.81 ± 0.06	1.43 ± 0.11	1.61 ± 0.15	0.91 ± 0.04	1.36 ± 0.11	24.62 ± 0.07	10.01 ± 0.12	10.08 ± 0.03
25989	10.71 ± 0.13	-0.312 ± 0.284	-0.090 ± 0.239	0.93 ± 0.02	3.88 ± 0.22	0.63 ± 0.01	0.74 ± 0.02	0.82 ± 0.04	2.24 ± 0.19	0.57 ± 0.02	0.62 ± 0.03	23.17 ± 0.05	10.33 ± 0.14	9.97 ± 0.03

^a Total stellar masses are estimated using the M_*/L -colour relation, the $z_{850} - H_{160}$ aperture colours and the total luminosity $L_{H_{160}}$ from the best-fit Sérsic models.

^b Colour gradients $\nabla_{z_{850}-H_{160}}$ and M_*/L gradients $\nabla_{\log(M/L)}$ are defined as $d(z_{850} - H_{160})/d\log(a)$ and $d(\log(M/L))/d\log(a)$ respectively. The gradient is fitted in the radial range of PSF HWHM $< a < 3.5 a_e$.

^c Mean surface brightness Σ and mean surface mass density Σ_{mass} are defined as $\text{mag} + 2.5 \log(2\pi q a_e^2)$ and $\log(M_*/2\pi q_{mass} a_{e,mass}^2)$.

^d Mean surface mass density within a radius of 1 kpc Σ_1 is defined as $\log(M_*(< 1\text{kpc})/\pi(1\text{kpc})^2)$, derived from integrating the fitted 2D mass profiles.

Chapter 4

Structural parameters and Mass-size relations

In this chapter, we focus on the analysis of both light-weighted and mass-weighted structural parameters of the red sequence galaxies in the three KCS clusters described in Section 3.1 and 3.6. The structural parameters of galaxies are of particular interest since they reflect the structural evolutionary path and the underlying physical processes. We start with the distributions of the light-weighted parameters in Section 4.1 and the wavelength dependence of light-weighted galaxy sizes in Section 4.2. The stellar mass – light-weighted size relations of these clusters are studied in Section 4.3. We then move to the mass-weighted structural parameters and compare mass-weighted sizes to light-weighted sizes in Section 4.4. The stellar mass – mass-weighted size relations are studied in Section 4.5. We then focus on the ratio of mass-weighted to light-weighted size and discuss the dependence of this ratio on other galaxy properties in Section 4.6. We end the chapter with the evolution of the mass-weighted to light-weighted size ratio in Section 4.7 through a comparison with a sample of local passive galaxies at dense environments from the SPIDER sample described in Section 2.7. Parts of the results on XMMU J2235-2557 presented in this chapter are discussed in Chan et al. (2016).

4.1 Distribution of the light-weighted parameters

In this section we discuss the distribution of the light-weighted structural parameters of the three KCS clusters. The light-weighted structural properties of the passive galaxies in XMMU J2235-2557 have been investigated by Strazzullo et al. (2010), Delaye et al. (2014), De Propris et al. (2015) and De Propris et al. (2016), albeit in different bands or with different selection criteria. The cluster XMMXCS J2215-1738 was also included in the sample of Delaye et al. (2014), but the discussion was based on the ACS z_{850} band. Here we are able to study the light-weighted structural parameters at rest-frame r -band in all three clusters using our H_{160} images (see Section 2.3.1 for details).

Figure 4.1 shows the distribution of the H_{160} band light-weighted effective semi-major

axis a_e against the Sérsic index n of the red sequence galaxies in the three clusters. In each panel, the top and right histograms show the distribution of the Sérsic index and semi-major axis of the galaxies respectively. The size distribution in XMMU J2235-2557 is relatively flat, while XMMXCS J2215-1738 and Cl 0332-2742 show a clear peak. The distributions of the effective semi-major axis (i.e. sizes) follow roughly a log-normal distribution, with median values $\langle \log(a_e) \rangle = 0.38$ for XMMU J2235-2557, $\langle \log(a_e) \rangle = 0.38$ for XMMXCS J2215-1738 and $\langle \log(a_e) \rangle = 0.17$ for Cl 0332-2742.

This is qualitatively consistent with the size evolution in clusters found in other works (e.g. Lani et al., 2013; Delaye et al., 2014). Papovich et al. (2012) measured the sizes of passive galaxies in XMM-LSS J02182-05102 at $z = 1.62$ and found that ETG with masses $\log(M_*/M_\odot) > 10.48$ have a median circularised effective radius ($R_{e-circ} = a_e\sqrt{q}$) of 2.0 kpc with the interquartile percentile range (IQR) of 1.2 – 3.3 kpc. Considering the same range in mass, sizes in XMMU J2235-2557 are on average 15% larger ($\langle R_{e-circ} \rangle = 2.30$ kpc, IQR = 1.26–3.67 kpc) compared to the Papovich et al. (2012) cluster, those in XMMXCS J2215-1738 are on average 13% smaller ($\langle R_{e-circ} \rangle = 1.74$ kpc, IQR = 1.11 – 2.86 kpc) while sizes in Cl 0332-2742 are on average 46% smaller ($\langle R_{e-circ} \rangle = 1.07$ kpc, IQR = 0.83 – 1.94 kpc). Nevertheless, caution should be exercised when comparing sizes across clusters using IQR, as the red sequence populations can have very different mass distributions (even in the same considered mass range). In Section 4.3, we discuss the evolution of the sizes in our sample using the mass – size relation.

Contrary to the sizes, the distribution of Sérsic indices of XMMXCS J2215-1738 and Cl 0332-2742 is relatively flat, while XMMU J2235-2557 shows a double peak. 84.5% of the galaxies in the sample have $n > 2$; this suggests that they are dominated by spheroids, as expected for passive galaxies. The median Sérsic indices of the three clusters are: $\langle n \rangle = 3.99$ for XMMU J2235-2557, $\langle n \rangle = 3.48$ for XMMXCS J2215-1738 and $\langle n \rangle = 2.99$ for Cl 0332-2742.

The median Sérsic indices of our high-redshift passive populations are lower than those observed in local passive ellipticals ($n \sim 4 - 6$, e.g. Maller et al., 2009; La Barbera et al., 2010b), suggesting these galaxies are structurally distinct from local ellipticals. A substantial population (15.5%) of galaxies have low Sérsic index ($n < 2$), especially those in XMMU J2235-2557 (18.5%). The lower Sérsic indices suggest that the red sequence galaxies in our sample have more prominent disk-like components than local ellipticals (i.e. ‘disk-like’, see also van der Wel et al., 2011; Chevance et al., 2012; Buitrago et al., 2013). Similar results have been found in other high-redshift clusters (e.g. XMMU J1229+0151 at $z \sim 0.98$, XMM-LSS J02182-05102 at $z \sim 1.62$ and Cl J1449+0856 at $z \sim 2$, Papovich et al., 2012; Strazzullo et al., 2013; Cerulo et al., 2014). We also see an decrease of median Sérsic indices with redshift in our sample. This is consistent with De Propris et al. (2016) who studied the structural properties of passive galaxies in a sample of 29 clusters with a redshift range of 0.2 to 1.39 and found that the median Sérsic indices is higher at lower redshift (from $n \sim 2.2$ at $z \sim 1$ to $n \sim 3.3$ at $z < 0.6$).

Another angle to examine this is to look at the distribution of axis ratios. Figure 4.2 shows the distribution of the axis ratio q against the Sérsic index n . The lack of object with both low axis ratio ($q < 0.2$) and low sersic indices ($n < 2$) in our sample suggests

that our red sequence + colour-colour selection (see Section 2.5 for details) is effective in removing dusty star-forming galaxies, which are presumably thin disks. The blue line on the top histogram shows the distribution of low Sersic indices objects ($n < 2$), it is clear that these objects do not preferentially have low axis ratio. The median axis ratio of the three clusters are: $\langle q \rangle = 0.70$ for XMMU J2235-2557, $\langle q \rangle = 0.69$ for XMMXCS J2215-1738 and $\langle q \rangle = 0.62$ for Cl 0332-2742. It is also worth noting that the distribution of axis ratios in XMMU J2235-2557 and XMMXCS J2215-1738 shows very clear double peaks, at $q \sim 0.3$ and $q \sim 0.8$, while in Cl 0332-2742 the distribution is single peaked at $q \sim 0.6$ with three objects that have $q \sim 0.9$. Similar to our result, Papovich et al. (2012) pointed out that there are galaxies with very low axis ratio ($q \sim 0.2 - 0.3$) in the $z \sim 1.62$ cluster with the median q of the entire sample being $q \sim 0.6$.

In contrast, early-type galaxies in local to intermediate ($0 < z < 1$) redshift clusters have slightly higher axis ratio $q \sim 0.7 - 0.8$, with no indication of strong evolution with redshift up to $z = 1$ (Ryden et al., 2001; Holden et al., 2009; Vulcani et al., 2011; Holden et al., 2012). This indicates that the passive galaxy population in our cluster sample is on average more flattened, which is consistent with the picture of our sample being more disk-like than the local ellipticals. Similar result have also been found in the field, for example, Chang et al. (2013) modeled the axis ratio distribution of massive early-type galaxies in the CANDELS field and found an increased fraction of oblate galaxies at $z > 1$.

4.2 Wavelength dependence of light-weighted galaxy sizes

The measured size of a galaxy depends on the observed wavelength, as different stellar populations are being traced at different wavelength (e.g., the “morphological k-correction”, Papovich et al. 2003). With our multi-band measurements of light-weighted structural parameters of the cluster passive galaxies, in this section we investigate the wavelength dependence of galaxy sizes at $z \sim 1.5$.

This wavelength dependence of sizes (or the size-wavelength relation) has been quantified for local passive galaxies in a number of studies (e.g. Barden et al., 2005; Hyde & Bernardi, 2009; La Barbera et al., 2010b; Kelvin et al., 2012; Vulcani et al., 2014; Kennedy et al., 2015, 2016b). The dependence shown by the above mentioned studies is quite strong, in the sense that galaxy sizes can decrease up to $\sim 38\%$ from g through K band in the GAMA sample (Kelvin et al., 2012), or $\sim 32\%$ across the same range in SPIDER (La Barbera et al., 2010b). Nevertheless, different authors disagree on the extent of the reduction in sizes in various datasets. For example, in a recent study Lange et al. (2015) revisited the GAMA sample with deeper NIR imaging data and found a smaller size decrease, $\sim 13\%$ from g to K_s band.

At higher redshift, similar study of the wavelength dependence of sizes is scarce in clusters. The star formation history and age gradient may contribute significantly to the size-wavelength dependence at high redshift, for example the inside-out growth scenario

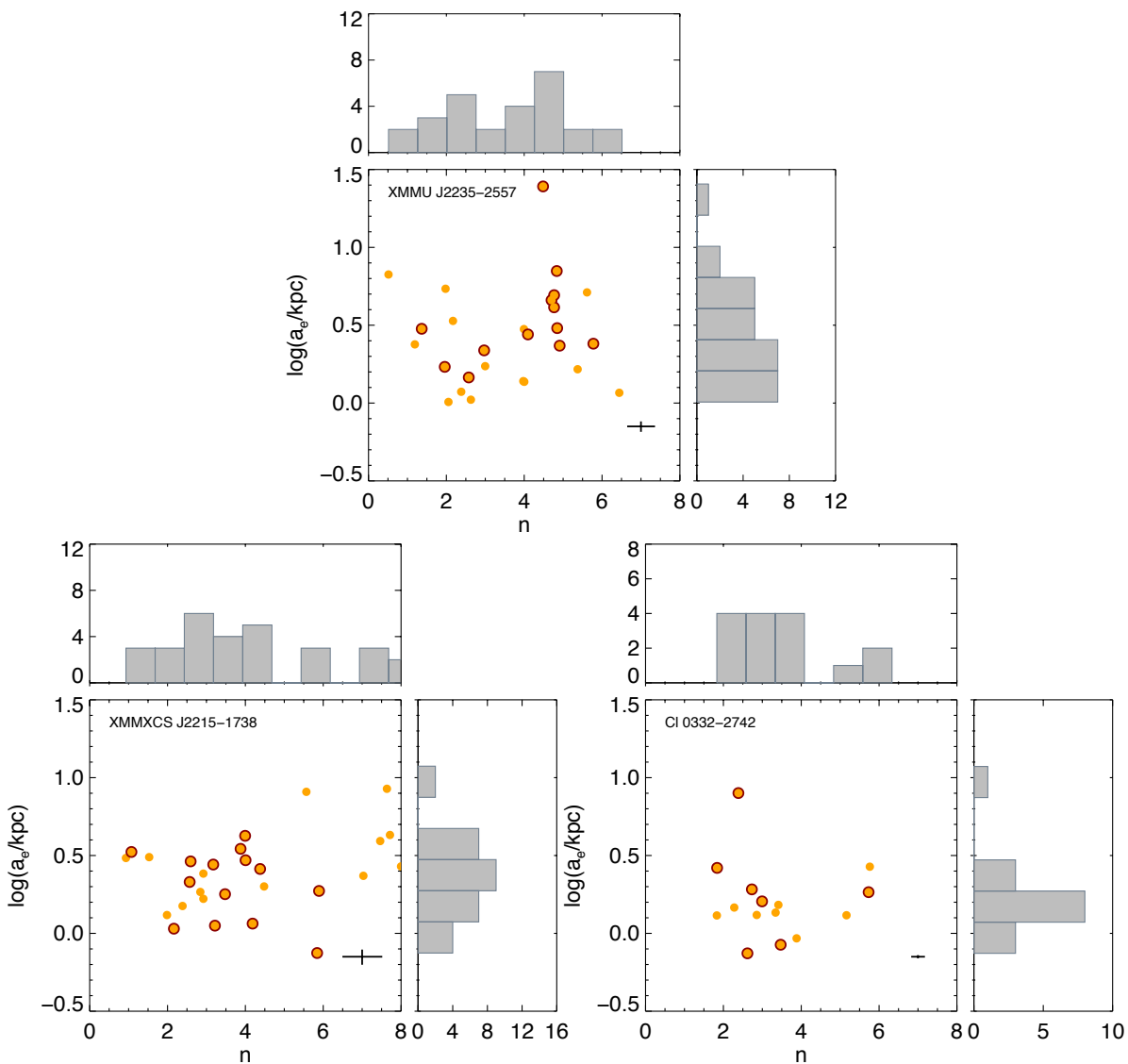


Figure 4.1: Distribution of the H_{160} light-weighted semi-major axis a_e against the Sérsic index n of the red sequence galaxies in the KCS clusters. On the top and right of each panel the histograms of the corresponding parameter are shown. Red circles correspond to spectroscopic confirmed cluster members. The cross shows the typical median uncertainty of the sizes and Sérsic indices.

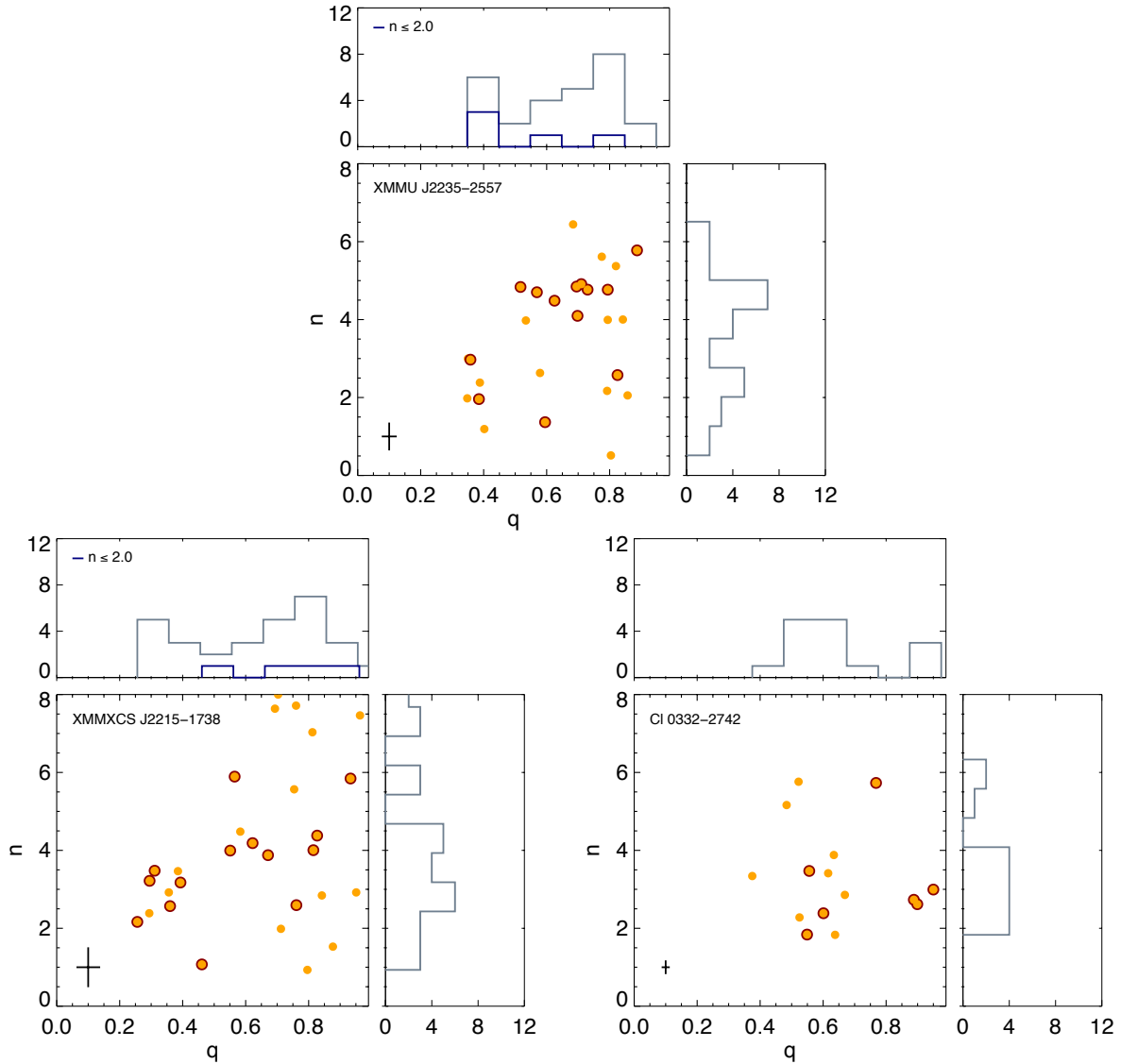


Figure 4.2: Distribution of the H_{160} light-weighted Sérsic index n against the axis ratio q of the red sequence galaxies in the KCS clusters. On the top and right of each panel the histograms of the corresponding parameter are shown. The blue histograms on the top panels show the distribution of low Sérsic indices objects ($n < 2$). Red circles correspond to spectroscopic confirmed cluster members. The cross shows the typical median uncertainty of the Sérsic indices and axis ratios.

suggests that younger stellar population are more spatially extended compared to the older population in the core of passive galaxies. Various authors have shown that measured sizes in the observed optical and NIR (i.e. rest-frame UV vs rest-frame optical for high-redshift galaxies) show a difference of $\sim 20\text{--}25\%$ (e.g. Trujillo et al., 2007; Cassata et al., 2010; Damjanov et al., 2011; Delaye et al., 2014), although some find no difference (Morishita et al., 2014). The comparisons are usually done with only two bands, hence it is unclear whether this dependence can change with redshift. Recent work from CANDELS studied the wavelength dependence of sizes for 122 early-type galaxies in the COSMOS field in three *HST* bands (F814W, F125W and F160W) at redshift $0 < z < 2$, and found an average gradient of $d \log(a_e)/d \log(\lambda) = -0.25$ independent of mass and redshift (van der Wel et al., 2014).

With our multi-band structural parameter measurements, we are able to study the wavelength dependence in a way similar to the local passive galaxies. As discussed in Section 3.1, we have derived light-weighted structural parameters of XMMU J2235-2557 for 5 bands, XMMXCS J2215-1738 for 4 bands and Cl 0332-2742 for 3 bands (see Table 2.1 for details of the available bands). Here again we use the light-weighted semi-major axis a_e as the galaxy size. We fit a power law to the galaxy sizes across wavelength, which can be written as

$$\log(a_{e,\lambda}) = \gamma \log(\lambda) + Z.P. \quad (4.1)$$

where γ is the exponent of the power law (i.e. the wavelength dependence) and the *Z.P.* is a normalisation factor. In the fitting we do not correct for the small variation in the observed wavelength due to redshift variations within the cluster, hence essentially we assume every galaxy in the cluster is at the cluster redshift. These small variations in redshift have a negligible effect on the measured sizes as the filters we used have a relatively broad coverage in wavelength.

Figure 4.3 shows the change in size with rest-frame wavelength for our KCS sample. We select galaxies with no problematic fits in all of the bands. 21 out of 27 in XMMU J2235-2557, 21 out of 29 in XMMXCS J2215-1738 and 14 out of 15 objects in Cl 0332-2742 are selected. The problematic fits are mainly from bands with shorter exposure time and lower filter throughput, such as i_{775} and Y_{105} for XMMU J2235-2557 and z_{850} for XMMXCS J2215-1738 and Cl 0332-2742, which result in lower S/N. These problematic fits will result in unreliable fits in the wavelength dependence and are discarded. To facilitate comparison with the literature, the sizes in Figure 4.3 are normalised with respect to the median H_{160} sizes of the sample, which is approximately equal to the rest-frame r -band size at $z \sim 1.5$. We plot the best-fitting relation for local spheroids by Kelvin et al. (2012) and the SPIDER cluster sample (see Section 2.7 for the selection), normalised in the same way, for comparison.

There is an additional caveat in deriving the wavelength dependence: one can fit the dependence with the median (or mean) sizes of the sample or for individual galaxies. For example, Kelvin et al. (2012) derived the fit of the wavelength dependence relation of the GAMA sample using 3σ clipped mean sizes in each band. While this is suitable for a large,

Table 4.1: Summary of the wavelength dependence parameter γ of the three KCS clusters.

Cluster	Values from median sizes	Median values from the sample [*]
XMMU J2235-2557	-0.489 ± 0.328	-0.289 ± 0.069
XMMXCS J2215-1738	-0.534 ± 0.295	-0.400 ± 0.139
Cl 0332-2742	-0.374 ± 0.334	-0.295 ± 0.034

^{*}The uncertainties quoted for the wavelength dependence derived from the median sizes are the formal error of the fits, while those for the median dependence derived from individual galaxies are the uncertainties of the median in each band, estimated as $1.253\sigma/\sqrt{N}$, where σ is the standard deviation of the γ distribution and N is the size of the sample.

complete sample, for our sample using median or mean sizes to derive the fit might be an issue given our small number of bands and galaxies (comparing to the abovementioned local studies).

Hence, besides using median sizes we also derive fits for individual galaxies and compute the median dependence of the sample (i.e. median value of γ) afterwards. The result is shown in the right panel of Figure 4.3. The sizes of individual galaxies in each band are normalised with respect to their H_{160} sizes. We notice there is a subtle difference in the dependence derived from the two methods, the dependence derived from median sizes (or similarly, 3σ clipped mean sizes) are larger compared to the median dependence of individual galaxies, presumably due to the uncertainty in the median sizes and the size distributions. The parameter γ of the three clusters derived from both methods are given in Table 4.1.

With either method we see a smooth variation of sizes decreasing from blue to red bands (rest-frame u to rest-frame r). The median dependence of individual galaxies shows a $\sim 16 - 21\%$ decrease across u to r band among the three clusters. The median reduction in the sizes is consistent (within 1σ) with the expected decrease across this wavelength range following the local relation of Kelvin et al. (2012) and the SPIDER cluster sample (La Barbera et al., 2010b). We notice that from both methods XMMXCS J2215-1738 has the steepest wavelength dependence, while the median dependences in XMMU J2235-2557 and Cl 0332-2742 are similar.

The ratio of sizes in different band is commonly used as an estimate of the colour gradient of a galaxy (e.g. La Barbera et al., 2002; De Propris et al., 2015), as the two quantities both probe the spatial distribution of different stellar population within the galaxy. The observed decrease in size from blue to red bands implies that the red sequence populations in the KCS clusters have a negative median colour gradient. In Section 5.1, we derive directly the $z_{850} - H_{160}$ colour gradients in the red sequence galaxies and study the origin and evolution of the colour gradient.

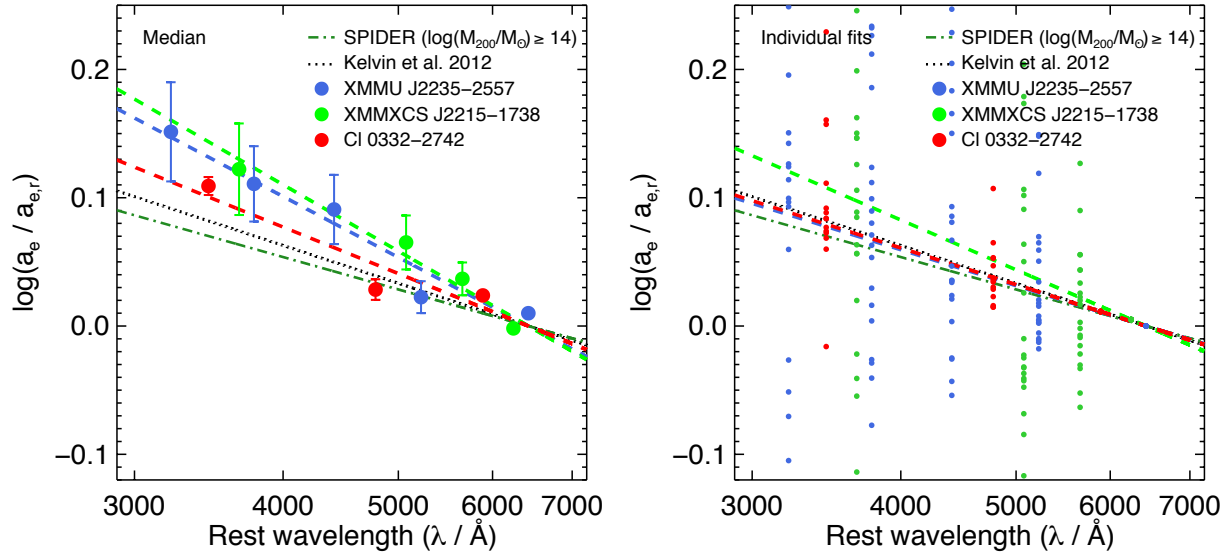


Figure 4.3: Size-wavelength relation of the red sequence galaxies in the KCS clusters. Left: Median sizes in each band at rest-frame wavelength. The circles show the median sizes of the sample in each band positioned at the rest-frame pivot wavelength, normalised with respect to the median H_{160} -band sizes (approximately rest-frame r -band, $a_{e,r}$). Sizes in XMMU J2235-2557 are shown in blue, those in XMMXCS J2215-1738 are shown in green and those in Cl 0332-2742 are shown in red respectively. Error bars show the uncertainty of the median in each band, estimated as $1.253\sigma/\sqrt{N}$, where σ is the standard deviation and N is the size of the sample. The best-fit power law to the median sizes of the clusters are shown as dashed lines. Right: Sizes of individual galaxies in each band at rest-frame wavelength (small circles). The dashed lines show the median exponent (γ) of the power law fit of individual galaxies. The green dot-dashed line in both panels is the best-fit relation for the SPIDER cluster sample (from g -band to K_s -band). The black dotted line is the best-fit relation for local galaxies from Kelvin et al. (2012).

4.3 Stellar mass – light-weighted size relations

In this section we study the stellar mass – H_{160} light-weighted size relation of the three KCS clusters. As we explain in Section 1.4, the stellar mass – size relations at different redshifts reflect the evolutionary path of passive galaxies. Studying the mass – size relation over cosmic time can hence pose constraints on existing models of galaxy evolution. Here we compare the mass – light-weighted size relation of the KCS clusters with other clusters at similar redshift as well as field galaxies from the literature. Similar to the structural parameters, the mass – size relations of XMMU J2235-2557 and XMMXCS J2215-1738 (in z_{850} band, rest-frame UV) have been studied in Strazzullo et al. (2010) and Delaye et al. (2014).

To compare with the literature, the size we use from this point onwards is the circularised effective radius (R_{e-circ}), defined as:

$$R_{e-circ} = a_e \times \sqrt{q} \quad (4.2)$$

where a_e is the elliptical semi-major axis and q is the axis ratio from the best-fit GALFIT Sérsic profile¹. The circularised effective radii of the galaxies are given in Table 3.1, Table 3.2 and Table 3.3.

Figure 4.4 shows the mass – light-weighted size relations of the red sequence galaxies in the three KCS clusters. The integrated stellar masses are derived from the M_*/L - colour relation and are scaled with the total GALFIT Sérsic magnitude (see Section 3.4 for details). We also plot the local mass – size relation of the SDSS passive sample by Bernardi et al. (2012) on Figure 4.4 for comparison. Note that although this relation was derived for galaxies regardless of their local density, a number of studies have established that there is no obvious environmental dependence on passive galaxy sizes in the local universe (Guo et al., 2009; Weinmann et al., 2009; Taylor et al., 2010; Huertas-Company et al., 2013; Cappellari, 2013) (see also Section 1.4.1). We pick the single Sérsic fit relation in Bernardi et al. (2012) for consistency, which is shown to have slightly larger sizes than the two-component exponential + Sérsic fit relation.

Hyde & Bernardi (2009) first demonstrated that the mass – size relation of passive galaxies shows curvature and Bernardi et al. (2012) fitted the curvature with a second order polynomial; their best-fit values were consistent with Simard et al. (2011). As we have shown in the last section, sizes show a wavelength-dependence, hence care has to be taken to ensure that the sizes being compared are at around the same rest-frame wavelength. The Bernardi et al. (2012) local relation is based on the Sloan r -band, while our sizes are measured in the H_{160} band at redshifts of 1.39, 1.46 and 1.61, which roughly corresponds to the same rest-frame band. As a result, no size-correction is required as the correction to r -band is negligible.

The H_{160} band sizes of the passive galaxies in XMMU J2235-2557 are on average $\sim 42\%$ smaller than expected from the local relation by Bernardi et al. (2012) with

¹The results would not change if we use the circularisation method proposed by Saglia et al. (2010): $R_{e-circ} = 0.5 \times (a + b)$, where b is the semi-minor axis.

$\langle \log(R_{e-circ}/R_{Bernardi}) \rangle = -0.24$ ($\sim 43\%$ smaller for the spectroscopic confirmed members, $\langle \log(R_{e-circ}/R_{Bernardi}) \rangle = -0.24$). There are also galaxies whose sizes are $\sim 70\%$ smaller than those of their local counterparts ($\log(R_{e-circ}/R_{Bernardi}) = -0.56$). As one can see from Figure 4.4, the most massive object in the cluster is the BCG, which also has the largest size (~ 24 kpc) and lies on the local relation. This is consistent with findings from Stott et al. (2010, 2011), who showed that as a population, BCGs have had very little evolution in mass or size since $z \sim 1$. Tirit et al. (2011) suggested that major mergers at $z \geq 1.5$ are required to explain the mass growth of these extremely massive passive galaxies.

For XMMXCS J2215-1738, the H_{160} band sizes of the passive galaxies are on average $\sim 55\%$ smaller than expected from the local relation with $\langle \log(R_{e-circ}/R_{Bernardi}) \rangle = -0.34$ ($\sim 65\%$ smaller for the spectroscopic confirmed members, $\langle \log(R_{e-circ}/R_{Bernardi}) \rangle = -0.46$), which is on average smaller compared to XMMU J2235-2557. The galaxy with the smallest size is $\sim 86\%$ smaller than those of their local counterparts ($\log(R_{e-circ}/R_{Bernardi}) = -0.86$). As we pointed out in Section 2.2.2, the BCG in XMMXCS J2215-1738 is not exceptionally bright compared to other galaxies in the cluster and is off-centered. From Figure 4.4 it is clear that the BCG is also not the most massive objects in the cluster and has a relatively small size (~ 1.0 kpc), probably related to the fact that XMMXCS J2215-1738 is not virialized (e.g. Hilton et al., 2010; Ma et al., 2015).

The average H_{160} band size of the passive galaxies in Cl 0332-2742 are the smallest among the three clusters. The galaxies are on average $\sim 69\%$ smaller than expected from the local relation, with $\langle \log(R_{e-circ}/R_{Bernardi}) \rangle = -0.51$ ($\sim 69\%$ smaller also for the spectroscopic confirmed members, $\langle \log(R_{e-circ}/R_{Bernardi}) \rangle = -0.51$). There are galaxies that are $\sim 82\%$ smaller than those of their local counterparts ($\log(R_{e-circ}/R_{Bernardi}) = -0.74$). The most massive object in the cluster also has the largest size among the passive galaxies (~ 6.2 kpc). This object (ID 11827) locates at the west part of the structure and is the brightest group galaxy (BGG) in the Tanaka et al. (2013) group.

We fit the mass – size relation with a Bayesian inference approach using Markov Chain Monte Carlo (MCMC; Kelly, 2007) with the following linear regression:

$$\log(R_{e-circ}/\text{kpc}) = \alpha + \beta (\log(M_*/M_\odot) - 10.5) + N(0, \epsilon) \quad (4.3)$$

where $N(0, \epsilon)$ is the normal distribution with mean 0 and dispersion ϵ . The ϵ represents the intrinsic random scatter of the regression. In fitting the relations, we do not consider the covariance between R_{e-circ} and M_\odot . Moreover, we exclude the BCGs (as well as the BGG in the Tanaka et al. (2013) group of Cl 0332-2742) in the fitting process as BCGs may have undergone a different evolutionary path (e.g. Stott et al., 2011).

The best-fit parameters (the intercept α , slope β and scatter ϵ) for both the entire red-sequence selected sample (case A) and the spectroscopically confirmed members only (case B) of the three clusters are summarised in Table 4.2. For comparison to previous literature, we also fit only massive objects with $\log(M_*/M_\odot) \geq 10.5$, the limiting mass adopted in Delaye et al. (2014) (case C & D). Note that since all objects in Cl 0332-2742 are with $\log(M_*/M_\odot) \geq 10.5$, we only give the result of case C & D. Although still consistent within

1σ , in some case we see a difference in the slope due to reduced number of objects. This suggests that while comparing the fitted slopes with literature values one needs to ensure the mass range of the fitted data is comparable.

The measured slopes β for the red-sequence selected samples (A & C) as well as the spectroscopic confirmed members (B & D) in the three clusters are consistent within 1σ respectively, suggesting the rest of the analysis is fairly representative of the population of passive cluster galaxies at $z \sim 1.5$. Among the three clusters, XMMXCS J2215-1738 has the steepest relations for the full sample fit (A & B) as well as the massive sample fit (C & D). We measure a typical slope of $\beta = 0.79 \pm 0.14$ if the entire massive red sequence sample (C) is fitted simultaneously.

Comparing the fits in different mass ranges (A & C), the fits with only massive objects always have a steeper slope, which probably suggests that the mass – size relation of passive galaxies are also curved similar to the local mass – size relation (Hyde & Bernardi, 2009).

Delaye et al. (2014) studied the mass – size relation in nine clusters at $0.89 < z < 1.5$ in the rest-frame B -band for $\log(M_*/M_\odot) > 10.5$. They reported a typical slope of $\beta = 0.49 \pm 0.08$ for the seven clusters up to $z \sim 1.2$, and a possible decrease in the slope of the two $z > 1.2$ clusters XMMU J2235-2557 and XMMXCS J2215-1738 in their sample ($\beta = 0.22 \pm 0.32$ for XMMU J2235-2557, $\beta = 0.31 \pm 0.32$ for XMMXCS J2215-1738). We notice that the relations in Delaye et al. (2014) for these two clusters are systematically flatter by more than 1σ compared to both our full sample fit (A) and massive sample fit (C). Our fitted relations also have smaller intrinsic scatter ϵ compared to the Delaye et al. (2014) relations ($\epsilon = 0.25$ for XMMU J2235-2557, $\epsilon = 0.26$ for XMMXCS J2215-1738).

These differences could be due to a combination of a) their mass – size relations are computed in the z -band while ours is in H_{160} , hence the comparison is complicated by the wavelength dependence of sizes discussed in the last section, b) the two red sequence samples are selected differently, since we perform an extra colour-colour selection to remove red dusty star forming galaxies, and c) the stellar masses used are computed differently. The masses in Delaye et al. (2014) are computed with SED fitting and scaled with `MAG_AUTO`, while our masses are scaled with total GALFIT Sérsic magnitude instead (see Section 3.4.1 for a comparison). We suggest that the discrepancy is primarily driven by the selection. We tested that with only the red sequence selection (i.e. without the colour-colour selection), the relation of XMMU J2235-2557 would have a much flatter slope and a larger scatter: $\beta = 0.50 \pm 0.20$ (instead of 0.72), $\epsilon = 0.23$, which is consistent at 1σ level with the value in Delaye et al. (2014). On the other hand, if we use masses scaled with `MAG_AUTO` but do not alter our selection, the relation of XMMU J2235-2557 is only slightly flatter: $\beta = 0.70 \pm 0.24$, suggesting that the difference is only partially related to the adopted photometry.

The abovementioned published relations are for passive galaxies in clusters. For galaxies in the field, the slopes of our massive sample fit (C) are in good agreement with previous works by Newman et al. (2012) ($\beta = 0.62 \pm 0.09$ for $\log(M_*/M_\odot) > 10.7$ galaxies with redshift range $1.0 < z < 1.5$ in the CANDELS field) and Cimatti et al. (2012) ($\beta = 0.50 \pm 0.04$ for $\log(M_*/M_\odot) > 10.5$ galaxies with $z > 0.9$). Our result is also consistent with the recent study by van der Wel et al. (2014), who found the slope of the mass –

Table 4.2: Best-fit parameters of the stellar mass – light-weighted size relations of the three KCS clusters

XMMU J2235-2557				
Stellar mass – light-weighted size relation				
Case	Mass range	$\alpha \pm \Delta\alpha$	$\beta \pm \Delta\beta$	ϵ
A	$10.0 \leq M_* \leq 11.5$	0.134 ± 1.436	0.584 ± 0.134	0.196
B	$10.0 \leq M_* \leq 11.5$ (spec)	0.094 ± 2.389	0.575 ± 0.218	0.174
C	$10.5 \leq M_* \leq 11.5$	0.067 ± 1.714	0.720 ± 0.158	0.169
D	$10.5 \leq M_* \leq 11.5$ (spec)	0.103 ± 2.483	0.573 ± 0.227	0.176

XMMXCS J2215-1738				
Case	Mass range	$\alpha \pm \Delta\alpha$	$\beta \pm \Delta\beta$	ϵ
A	$10.0 \leq M_* \leq 11.5$	-0.045 ± 2.439	0.766 ± 0.224	0.227
B	$10.0 \leq M_* \leq 11.5$ (spec)	-0.288 ± 4.884	1.125 ± 0.447	0.212
C	$10.5 \leq M_* \leq 11.5$	-0.182 ± 2.958	1.069 ± 0.271	0.187
D	$10.5 \leq M_* \leq 11.5$ (spec)	-0.732 ± 9.306	2.021 ± 0.849	0.171

Cl 0332-2742*				
Case	Mass range	$\alpha \pm \Delta\alpha$	$\beta \pm \Delta\beta$	ϵ
C	$10.5 \leq M_* \leq 11.5$	-0.211 ± 3.503	0.680 ± 0.322	0.138
D	$10.5 \leq M_* \leq 11.5$ (spec)	-0.396 ± 6.143	1.023 ± 0.558	0.160

* Since all the selected galaxies in Cl 0332-2742 have $\log(M_*/M_\odot) \geq 10.5$, only case C & D are applicable.

size relation at $z \sim 1.25$ and $z \sim 1.75$ to be $\beta = 0.76 \pm 0.04$ for UVJ passive galaxies ($\log(M_*/M_\odot) > 10.3$) in CANDELS. van der Wel et al. (2014) used semi-major axis a_e as sizes instead of R_{e-circ} . We check that using semi-major axis does not have a huge impact on our measured slopes, for example in XMMU J2235-2557 the slope is only slightly flatter ($\beta = 0.56 \pm 0.14$ (A) and $\beta = 0.65 \pm 0.20$ (C)) if a_e is used.

A caveat of the above comparison is that we have not considered the effect of progenitor bias (e.g. van Dokkum & Franx, 2001). Young galaxies get quenched and enter the red sequence at later epochs and “dilute” the existing sample, which makes a precise study of how pre-existing red sequence galaxies evolve difficult. Correcting the progenitor bias (in age and morphology) has been shown to reduce the magnitude of the observed size evolution (e.g. Saglia et al., 2010; Valentinuzzi et al., 2010b; Beifiori et al., 2014; Belli et al., 2015) since young galaxies have preferentially larger sizes. Recently, Jørgensen et al. (2014) corrected the progenitor bias by removing galaxies that are too young in the Coma cluster to be the descendants of a cluster at $z = 1.27$ and found no size evolution with redshift. Since we do not have information on the exact age of individual galaxy in our sample, at this moment it is not possible to apply a correction for the progenitor bias.

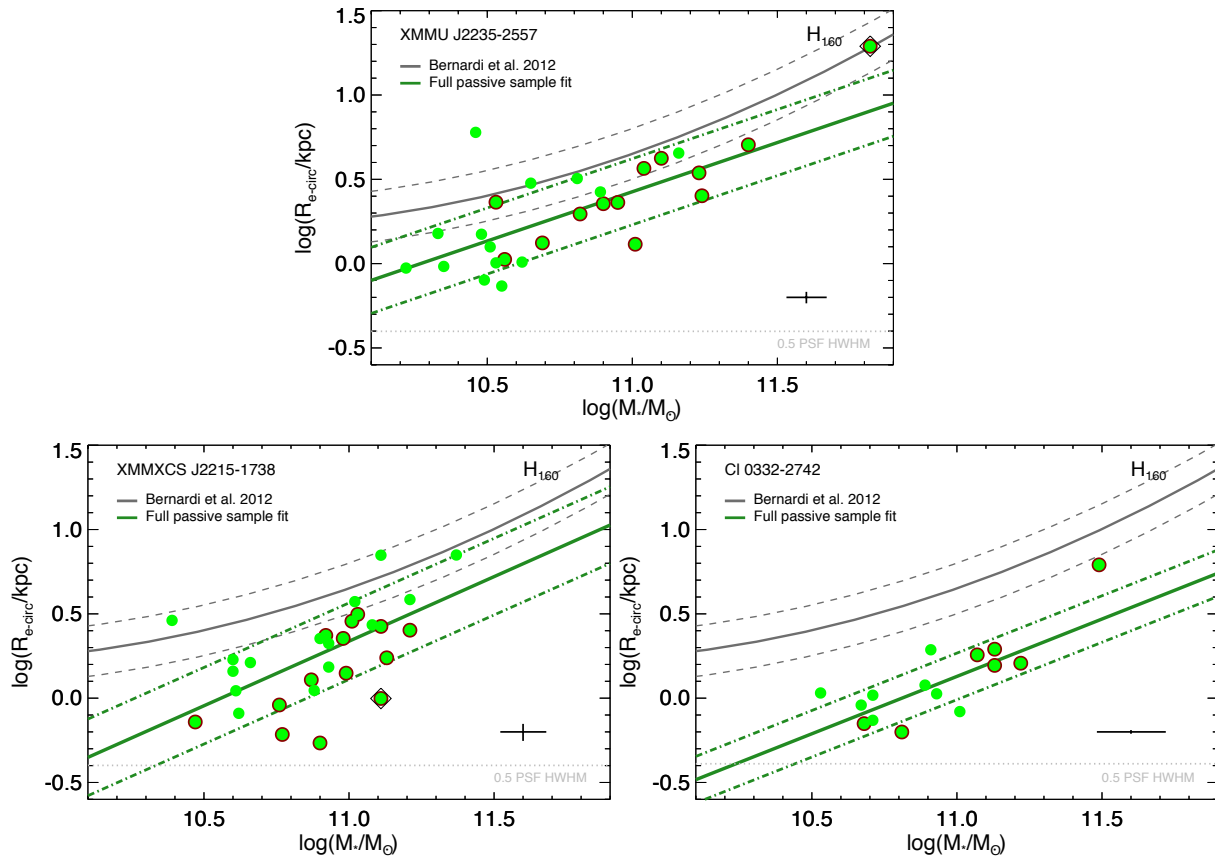


Figure 4.4: Stellar mass – light-weighted size relations of the red sequence galaxies in the KCS clusters. The green line in each panel is a linear fit to the full passive sample (Case A (C in Cl 0332-2742)), while the dot-dashed lines represent $\pm 1\sigma$. The dark grey line corresponds to the local r -band mass – size relation from Bernardi et al. (2012). Individual objects are shown in green and spectroscopically confirmed objects are circled with dark red. The BCGs in XMMU J2235-2557 and XMMXCS J2215-1738 are indicated with black diamonds. The cross shows the typical uncertainty of the sizes and the median uncertainty of the integrated mass in our sample.

4.4 Comparison of light-weighted to mass-weighted structural parameters

We move on to the mass-weighted structural parameters derived from the resolved stellar mass surface density maps of the red sequence galaxies (see Section 3.5 and 3.6 for details). In this section we compare the light-weighted sizes measured in H_{160} band to the mass-weighted sizes measured from the mass maps. Similar to the light-weighted sizes (R_{e-circ}), the mass-weighted sizes we use are circularised in the same way:

$$R_{e-circ,mass} = a_{e,mass} \times \sqrt{q_{mass}} \quad (4.4)$$

where $a_{e,mass}$ is the mass-weighted semi-major axis and q is the axis ratio from the best-fit Sérsic profile from the mass maps. The circularised mass-weighted sizes of the galaxies are also given in Table 3.1, Table 3.2 and Table 3.3.

Figure 4.5 shows a comparison of the light-weighted sizes (R_{e-circ}) to the mass-weighted sizes ($R_{e-circ,mass}$) for the three KCS clusters.

For XMMU J2235-2557, the mass-weighted sizes are $\sim 47\%$ smaller than the H_{160} light-weighted sizes, with a median difference of $\langle \log(R_{e-circ,mass}/R_{e-circ}) \rangle = -0.28$. The 1σ scatter $\sigma_{\log(R_{e-circ,mass}/R_{e-circ})}$ is ~ 0.11 . In the most extreme case the mass-weighted size can be up to $\sim 60\%$ smaller than its light counterpart (excluding the cluster BCG which is $\sim 65\%$ smaller).

For XMMXCS J2215-1738, the mass-weighted sizes are even smaller compared to XMMU J2235-2557, they are on average $\sim 55\%$ smaller than the H_{160} light-weighted sizes, with a median difference of $\langle \log(R_{e-circ,mass}/R_{e-circ}) \rangle = -0.34$. The scatter is also larger: $\sigma_{\log(R_{e-circ,mass}/R_{e-circ})} \sim 0.14$. For some galaxies the mass-weighted size can be $\sim 87\%$ smaller than its light counterpart.

For Cl 0332-2742, the mass-weighted sizes are similar to the H_{160} light-weighted sizes, with only an average $\sim 20\%$ decrease. The median difference is $\langle \log(R_{e-circ,mass}/R_{e-circ}) \rangle = -0.095$. Not only is the median difference lower compared to the other two clusters but also the scatter is much smaller, with $\sigma_{\log(R_{e-circ,mass}/R_{e-circ})} \sim 0.065$. For the galaxy with the lowest $\log(R_{e-circ,mass}/R_{e-circ})$, the mass-weighted size is $\sim 50\%$ smaller than its light-weighted size.

The general trend of mass-weighted sizes always being smaller than the light-weighted sizes shows that the mass distribution is more concentrated than the light distribution, which in turn suggests the M_*/L ratio at the inner part of the galaxy is higher compared to the outskirts. This implies the existence of a M_*/L gradient in these red sequence cluster galaxies. This trend of mass-weighted sizes being smaller is in qualitative agreement with the study at similar redshift by Szomoru et al. (2013), who computed the mass-weighted sizes using radially binned 1D surface brightness profiles for passive field galaxies in CANDELS.

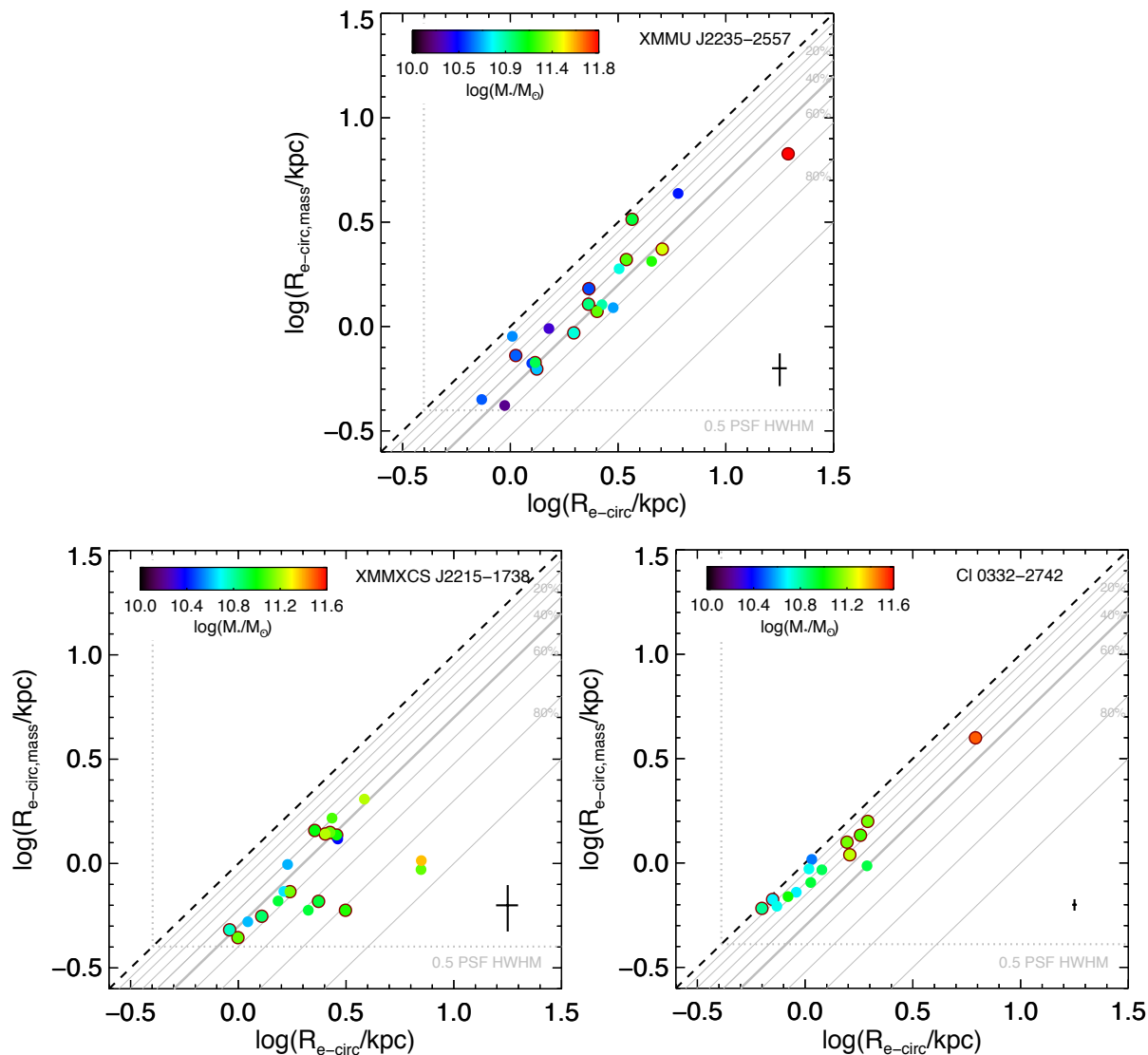


Figure 4.5: Comparison between mass-weighted size $R_{e-circ,mass}$ and light-weighted size R_{e-circ} of the red sequence galaxies in the KCS clusters. Spectroscopically confirmed objects are circled in dark red. The dashed line is the one-to-one relation. Each successive grey line represents a 10% decrement to the one-to-one relation. The 50% decrement is marked with a thick grey line. The galaxies are colour coded with their integrated mass. The dotted gray line on both axis indicates the 0.5 PSF HWHM limit, galaxies that are smaller than this limit are unreliable and hence are discarded (see Section 3.6 for details). The cross shows the median uncertainty of the light-weighted sizes and mass-weighted sizes. Note that the two uncertainties are correlated to some extent.

4.5 Stellar mass – mass-weighted size relations

In the above section we have demonstrated that the mass-weighted sizes in our sample are smaller than their corresponding light-weighted sizes. With the mass-weighted sizes we are able to derive the stellar mass – mass-weighted size relations of the three clusters similar to the light-weighted sizes. Here we investigate how using mass-weighted sizes can affect the mass – size relations.

Figure 4.6 shows the stellar mass – size relations of the clusters using mass-weighted sizes (hereafter mass-weighted relations). The relations are fitted in an identical way as the mass – light-weighted size relations (hereafter light-weighted relations) in Section 4.3 using equation 4.3. The best-fit parameters are summarised in Table 4.3. In Figure 4.6 we also over-plot the best-fit of the light-weighted relations in each panel for comparison.

The fact that the mass-weighted sizes are smaller can be seen from the intercept of the fits. Apart from the intercept, at first glance there seems to be a slight change in the slope of the relation if mass-weighted sizes are used. For example, for XMMU J2235-2557, the best-fitted relation for the full red sequence sample (A) has a value $\beta = 0.42 \pm 0.18$, 28% lower than the value of the corresponding light-weighted relation, though the two relations are consistent within 1σ . Similarly, Cl 0332-2742 has a flatter slope $\beta = 0.49 \pm 0.27$ with mass-weighted sizes, 28% lower than the light weighted relation. We notice that this is true for almost all cases of fitting, albeit they are still consistent within the relatively large 1σ error in β . We measure a typical slope of $\beta = 0.49 \pm 0.12$ if the entire massive red sequence sample (C) is fitted simultaneously.

One caveat we have to take into account before interpreting these results, is the effect of the discarded objects on the relations. Recall that we remove objects that have resultant sizes smaller than the PSF size or do not converge in the mass-fit. These small sizes are shown to be unreliable from the simulations (see Section 3.6 and 3.7.4 for details). Since galaxies with resultant mass-weighted sizes smaller than the PSF size predominately have small light-weighted sizes, removing those objects might have an effect on the mass – size relations.

To test this, we fit the light-weighted relations for the entire mass range using only the objects that have reliable mass-weighted sizes. This gives $\beta = 0.49 \pm 0.16$ (A) and $\beta = 0.54 \pm 0.24$ (B) for XMMU J2235-2557, $\beta = 0.56 \pm 0.22$ (A) and $\beta = 1.33 \pm 0.78$ (B) for XMMXCS J2215-1738, which results in a slightly smaller difference from the fitted slopes of the mass-weighted relations. The change in β suggests that the discarded objects do have an impact on the slope of the mass-weighted relations. Nevertheless, it does not rule out the fact that the slope of the mass-weighted relation is more flattened compared to the slope of the light-weighted relation. Although with reduced difference, the above quoted light-weighted slopes are still steeper compared to the ones of the mass-weighted relations. In addition, none of the objects is being discarded in Cl 0332-2742 and we see there is a change in the slope.

The possible change of the slope of the mass-weighted relation with respect to the light-weighted relation hints to a mass dependence for mass-weighted sizes to light-weighted sizes (i.e. ratio of the mass-weighted sizes to light-weighted sizes). Nevertheless, with the current

Table 4.3: Best-fit parameters of the stellar mass – mass-weighted size relations of the three KCS clusters

XMMU J2235-2557				
Stellar mass – mass-weighted size relation				
Case	Mass range	$\alpha \pm \Delta\alpha$	$\beta \pm \Delta\beta$	ϵ
A	$10.0 \leq M_* \leq 11.5$	-0.071 ± 1.989	0.419 ± 0.184	0.237
B	$10.0 \leq M_* \leq 11.5$ (spec)	-0.107 ± 3.837	0.444 ± 0.350	0.255
C	$10.5 \leq M_* \leq 11.5$	-0.146 ± 2.084	0.563 ± 0.192	0.191
D	$10.5 \leq M_* \leq 11.5$ (spec)	-0.114 ± 3.523	0.459 ± 0.322	0.251

XMMXCS J2215-1738				
Case	Mass range	$\alpha \pm \Delta\alpha$	$\beta \pm \Delta\beta$	ϵ
A	$10.0 \leq M_* \leq 11.5$	-0.210 ± 2.466	0.320 ± 0.225	0.163
B	$10.0 \leq M_* \leq 11.5$ (spec)	-0.641 ± 8.790	1.193 ± 0.800	0.155
C	$10.5 \leq M_* \leq 11.5$	-0.342 ± 2.804	0.617 ± 0.256	0.135
D	$10.5 \leq M_* \leq 11.5$ (spec)	-0.664 ± 8.590	1.299 ± 0.782	0.148

Cl 0332-2742*				
Case	Mass range	$\alpha \pm \Delta\alpha$	$\beta \pm \Delta\beta$	ϵ
C	$10.5 \leq M_* \leq 11.5$	-0.241 ± 2.937	0.493 ± 0.270	0.112
D	$10.5 \leq M_* \leq 11.5$ (spec)	-0.366 ± 5.978	0.759 ± 0.542	0.160

* Since all the selected galaxies in Cl 0332-2742 have $\log(M_*/M_\odot) \geq 10.5$, only case C & D are applicable.

uncertainties in the slopes, more statistics are required to confirm if the change of slope is genuine. A larger sample of passive galaxies in the same cluster (i.e. with a larger FOV) would help to reduce the measurement uncertainty in the slope, while a larger sample of clusters could help to quantify the dependence at different redshift and cluster properties.

4.6 Dependence of ratio of mass-weighted to light-weighted sizes on galaxy properties

In Section 4.4 we have shown that the mass-weighted sizes are smaller than the corresponding light-weighted sizes. Intuitively, one might expect some correlation between the ratio of mass-weighted sizes to light-weighted sizes ($\log(R_{e-circ,mass}/R_{e-circ})$, hereafter the size ratio) on the physical parameters that are related to the underlying stellar population, such as colour, stellar mass, and various structural parameters. In Section 4.5, we investigate the stellar mass dependence of the size ratio indirectly using the slope derived from the mass – size relations. Here we investigate the origin of the size ratio in our cluster sample

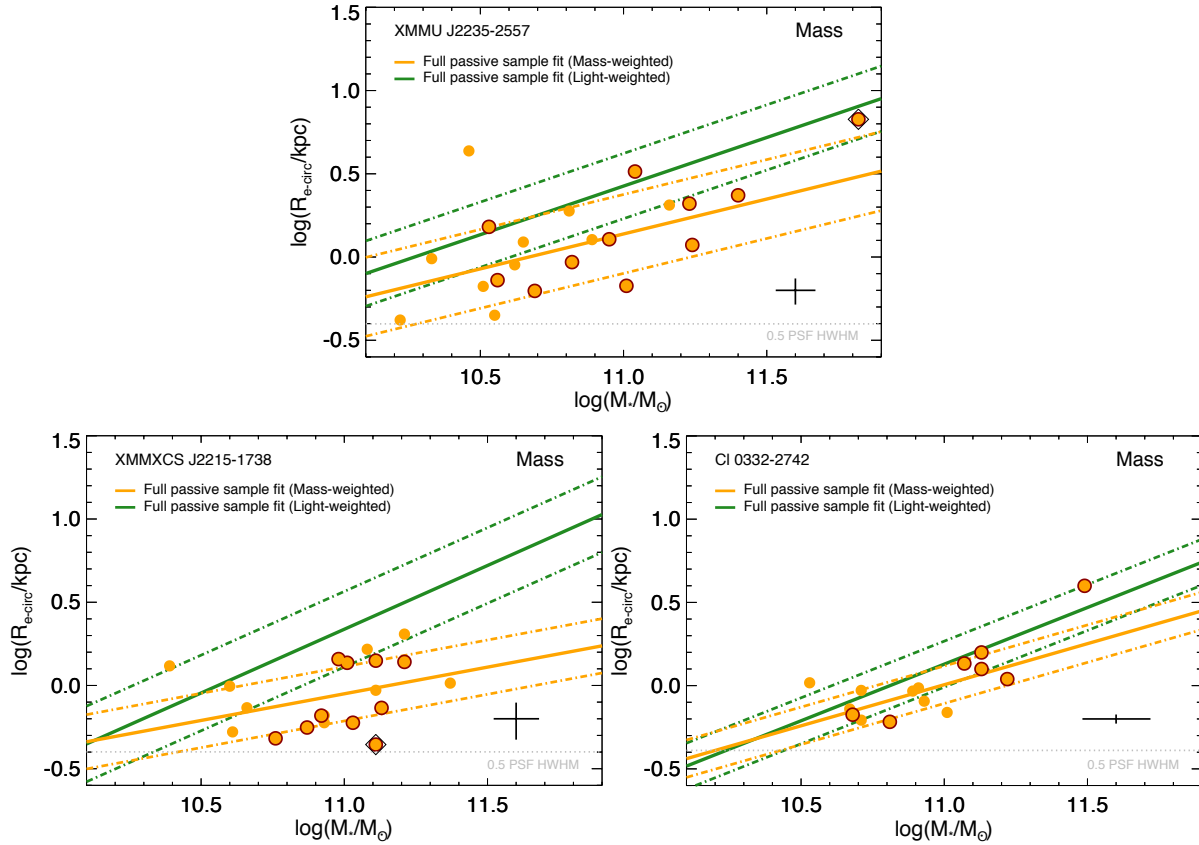


Figure 4.6: Stellar mass – mass-weighted size relations of the red sequence galaxies in the KCS clusters. The orange line in each panel is a linear fit to the full passive sample (Case A (C in Cl 0332-2742)), while the dot-dashed lines represent $\pm 1\sigma$. The green line is the same light-weighted mass – size relation fit in Figure 4.4 for comparison. Individual objects are shown in orange and spectroscopically confirmed objects are circled with dark red. The BCGs in XMMU J2235-2557 and XMMXCS J2215-1738 are indicated with black diamonds. The cross shows the typical uncertainty of the sizes and the median uncertainty of the integrated mass in our sample.

by examining the correlation with a number of integrated properties.

In Figure 4.7, 4.8 and 4.9 we show the correlations between the size ratio with the stellar mass, colour gradient $\nabla_{z_{850}-H_{160}}$, M_*/L gradient $\nabla_{\log(M/L)}$, $z_{850} - H_{160}$ colour, light-weighted / mass-weighted Sérsic indices, sizes, mean surface brightness Σ , mean surface mass density Σ_{mass} and the mean surface mass density within a radius of 1 kpc Σ_1 of the KCS clusters. Recent works have shown that Σ_1 is tightly correlated with stellar mass and is closely related to quenching of star formation (Fang et al., 2013; van Dokkum et al., 2014; Barro et al., 2015). We will discuss in detail the properties of the colour gradients and M_*/L gradients of the three clusters in Chapter 5. All parameters plotted for each cluster are given in Table 3.1, Table 3.2 and Table 3.3, respectively. The running median and the 1σ scatter are over-plotted in each panel.

We search for possible correlations with these physical parameters by computing the Spearman’s rank correlation coefficients (ρ) using a bootstrapping method. Similar to the mass – size relations we exclude the BCGs (and BGG in case of Cl 0332-2742) while computing the correlations. The ρ values quoted below are the median of the bootstrap distributions. Using the correlation coefficients ρ we then compute the p -value using the t -distribution. Although these are not formal definitions, in the following discussion we regard a correlation as strong if the p -value is < 0.01 , mild if $0.01 < p < 0.05$ and weak if $0.05 < p < 0.1$.

For XMMU J2235-2557, we see mild dependences with the colour and M_*/L gradient with ρ values of $-0.46, p \simeq 0.04$ and $0.49, p \simeq 0.03$ respectively. There are also weak dependences with the mean surface mass density Σ_{mass} and Σ_1 ($\rho = 0.39, p \simeq 0.09$ and $\rho = -0.42, p \simeq 0.06$). We see no obvious dependence with the light-weighted and mass-weighted structural parameters, with the light-weighted Sérsic indices having the highest ρ among them. There is no significant correlation between the size ratio and stellar mass. All other correlations have a $|\rho|$ value < 0.3 .

For XMMXCS J2215-1738, we find similar correlations as in XMMU J2235-2557. There is a strong dependence with the mass surface density ($\rho = -0.66, p \simeq 0.002$), as well as a mild dependence with the M_*/L gradient ($\rho = 0.48, p \simeq 0.04$). The colour gradient also shows a weak dependence with the size ratio. Among the structural parameters, the size ratio shows mild dependences with the light-weighted Sérsic index as well as mass-weighted size. Similarly, we find no correlation between the size ratio and stellar mass.

In Cl 0332-2742 we also see several mild correlations, for example with the M_*/L gradient ($\rho = 0.63, p \simeq 0.02$) and colour gradient ($\rho = 0.61, p \simeq 0.02$). There is also a mild dependence with light-weighted size. Intriguingly Cl 0332-2742 does not show obvious dependences with the mass surface densities (both Σ_{mass} and Σ_1) as in the other two clusters. On the other hand, the size ratio shows a mild dependence with the stellar mass, as well as a weak dependence with the $z_{850} - H_{160}$ colour.

In summary, combining the results of the three clusters, we conclude that the M_*/L gradient shows significant dependence with the size ratio. That our measured mass-weighted sizes tend to be significantly smaller than light-weighted sizes can only happen because there are gradients in mass-to-light ratio (and colours). Therefore it is encouraging to see that there are (mildly) significant positive correlations between the ratio of sizes and the

gradients in colour and M_*/L . The fact that the correlations are not perfect illustrates the contributions of both uncertainties in the data and the method, and the fact that our Sérsic fits are actually quite different from a straightforward linear 1D fit as used to derive the gradients.

The size ratio does not show significant dependence on the structural parameters in all three clusters. Szomoru et al. (2013) reported that in their sample there seems to be some evidence for a trend between the size ratio and the light-weighted Sérsic indices, albeit the correlations are very weak at $z > 1$. In our sample we see mild correlations with Sérsic indices only in XMMXCS J2215-1738, but there is no obvious correlation in XMMU J2235-2557 and Cl 0332-2742.

The correlation with stellar mass we see here is consistent with the slope difference we see in Section 4.5. While the size ratio in XMMU J2235-2557 and XMMXCS J2215-1738 shows almost no dependence with mass, Cl 0332-2742 indicates the contrary. A dependence with the mean surface mass density is also seen in only two out of the three clusters; the dependence may be concealed by the uncertainties in the size measurements and the other parameters or the presence of outliers, and in particular due to low number statistics. It is also possible that the strength of these correlations depends on the dynamical state or other properties of the clusters. A more sophisticated fit to these parameters, and better correlations, require higher S/N and / or a larger sample.

4.7 Evolution of the ratio of mass-weighted to light-weighted sizes to $z \sim 0$

In this section we investigate the evolution of the size ratio in our cluster sample by comparing with a sample of local passive galaxies in high-density environment. The local sample we used is selected from the SPIDER survey (La Barbera et al., 2010b) (the SPIDER cluster sample, see Section 2.7 for details on the selection).

4.7.1 Mass-weighted structural parameters at $z \sim 0$

The mass-weighted structural parameters of SPIDER are derived using a similar method as our KCS sample to facilitate comparison. We use the structural parameters in g -band and r -band from the publicly available multi-band structural catalogue from La Barbera et al. (2010b) to derive mass-weighted structural parameters. Firstly, 2D Sérsic model images in g -band and r -band are generated with fitted parameters from the structural catalogue. Given the large number and relatively low object density of local galaxies compared to our high redshift cluster sample, using fitted parameters from the structural catalogue is statistically reliable and the crowding issues mentioned in Section 3.1 do not contribute substantially here.

We construct mass maps for individual galaxies using the procedure described in Section 3.5 without Voronoi binning and stacking. A M_*/L -colour relation is again derived from the NMBS sample as in Section 3.3, but in g -band and r -band at $0 < z < 0.27$, a

4.7 Evolution of the ratio of mass-weighted to light-weighted sizes to $z \sim 0.131$

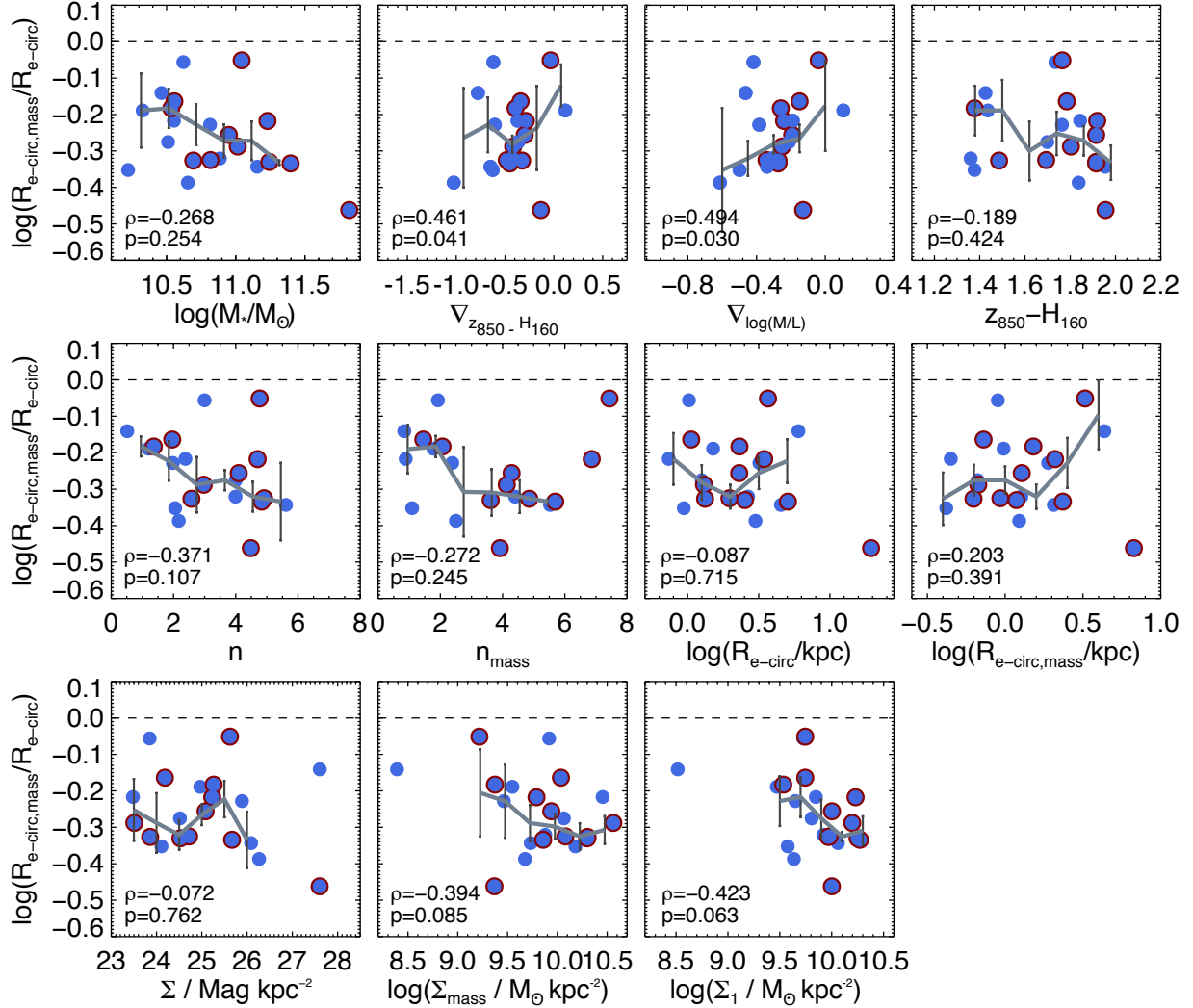


Figure 4.7: Dependence of ratio of mass-weighted to light-weighted sizes on different galaxy parameters of XMMU J2235-2557. H_{160} band sizes (rest-frame r -band) are used to compute the ratio of mass-weighted to light-weighted sizes ($R_{e-circ,mass}/R_{e-circ}$). From top left to bottom right: stellar mass, colour gradient $\nabla_{z_{850}-H_{160}}$, M_*/L gradient $\nabla_{\log(M/L)}$, $z_{850}-H_{160}$ colour, light-weighted Sérsic index n , mass-weighted Sérsic index n_{mass} , light-weighted size R_{e-circ} , mass-weighted size $R_{e-circ,mass}$, mean surface brightness Σ , mean surface mass density Σ_{mass} and mean surface mass density within 1 kpc Σ_1 . Spectroscopically confirmed objects are circled in dark red. The grey line in each panel shows the running median. The error bars show the uncertainty of the median in each bin. When there is only one point in the bin, the uncertainty of the ratio is plotted instead.

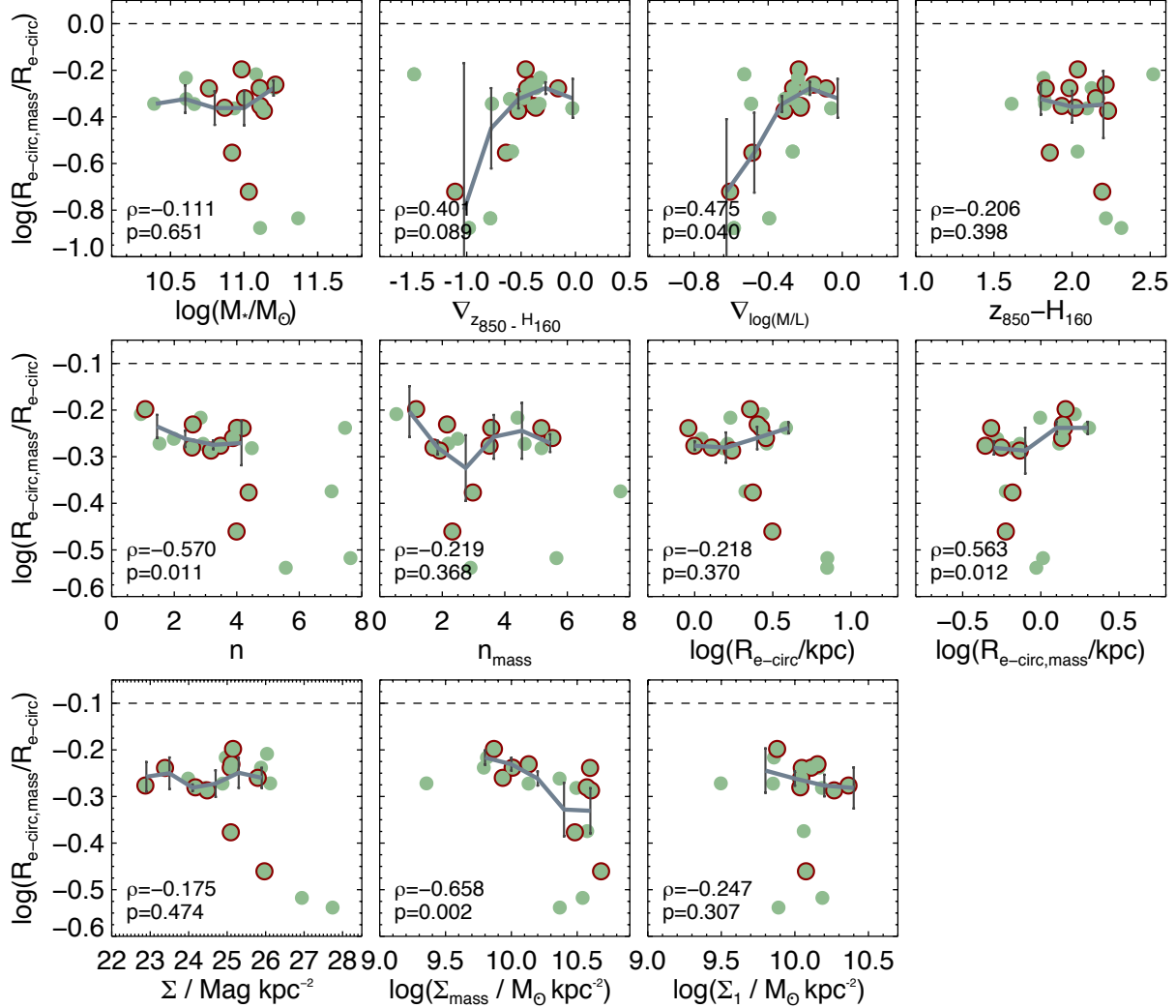


Figure 4.8: Dependence of ratio of mass-weighted to light-weighted sizes on different galaxy parameters of XMMXCS J2215-1738. H_{160} band sizes (rest-frame r -band) are used to compute the ratio of mass-weighted to light-weighted sizes ($R_{e-circ,mass}/R_{e-circ}$). From top left to bottom right: stellar mass, colour gradient $\nabla_{z_{850}-H_{160}}$, M_*/L gradient $\nabla_{\log(M/L)}$, $z_{850} - H_{160}$ colour, light-weighted Sérsic index n , mass-weighted Sérsic index n_{mass} , light-weighted size R_{e-circ} , mass-weighted size $R_{e-circ,mass}$, mean surface brightness Σ , mean surface mass density Σ_{mass} and mean surface mass density within 1 kpc Σ_1 . Spectroscopically confirmed objects are circled in dark red. The grey line in each panel shows the running median. The error bars show the uncertainty of the median in each bin. When there is only one point in the bin, the uncertainty of the ratio is plotted instead.

4.7 Evolution of the ratio of mass-weighted to light-weighted sizes to $z \sim 0.133$

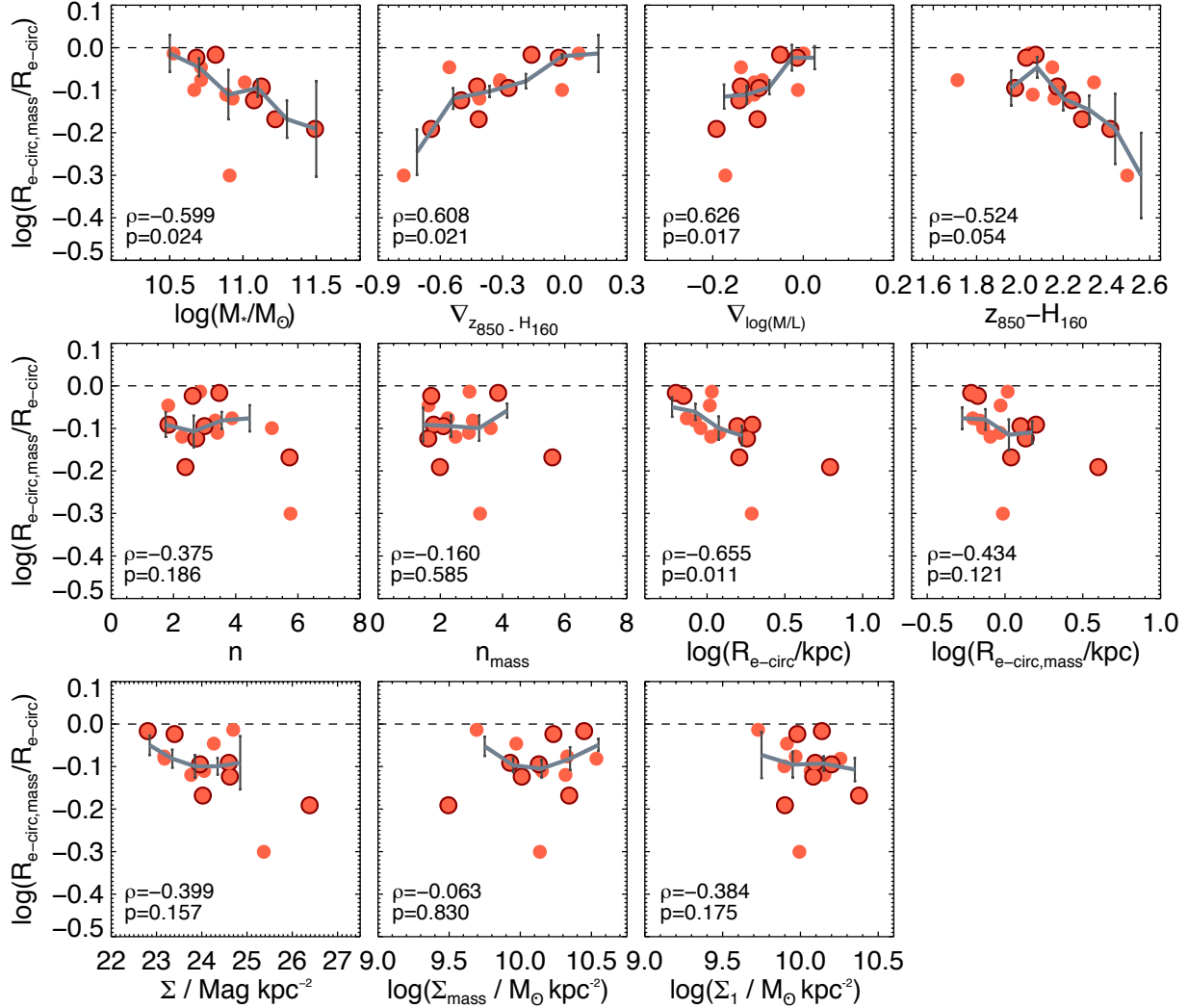


Figure 4.9: Dependence of ratio of mass-weighted to light-weighted sizes on different galaxy parameters of Cl 0332-2742. H_{160} band sizes (rest-frame r -band) are used to compute the ratio of mass-weighted to light-weighted sizes ($R_{e-circ,mass}/R_{e-circ}$). From top left to bottom right: stellar mass, colour gradient $\nabla_{z_{850}-H_{160}}$, M_*/L gradient $\nabla_{\log(M/L)}$, $z_{850} - H_{160}$ colour, light-weighted Sérsic index n , mass-weighted Sérsic index n_{mass} , light-weighted size R_{e-circ} , mass-weighted size $R_{e-circ,mass}$, mean surface brightness Σ , mean surface mass density Σ_{mass} and mean surface mass density within 1 kpc Σ_1 . Spectroscopically confirmed objects are circled in dark red. The grey line in each panel shows the running median. The error bars show the uncertainty of the median in each bin. When there is only one point in the bin, the uncertainty of the ratio is plotted instead.

window of 0.2 in redshift around the median redshift of the SPIDER sample. A total of 1315 NMBS objects are selected. The mass maps are then fitted with GALFIT to obtain mass-weighted structural parameters.

4.7.2 Comparison between KCS clusters and SPIDER

Figure 4.10 shows the comparison of the size ratio of the KCS clusters with SPIDER. We binned the size ratio of the SPIDER cluster sample (and the full SPIDER sample) in mass bins of 0.2, in the mass range $10.4 \leq \log(M_*/M_\odot) \leq 11.6$, to ensure there are sufficient numbers of local galaxies (> 50) in individual bins.

We find that the mass-weighted sizes in the SPIDER cluster sample are on average $\sim 12\%$ smaller than the r -band sizes with a median $\langle \log(R_{e-circ, mass}/R_{e-circ}) \rangle = -0.055 \pm 0.011$ ($\sim 13\%$ for the SPIDER sample, $\langle \log(R_{e-circ, mass}/R_{e-circ}) \rangle = -0.061 \pm 0.006$). Szomoru et al. (2013) reported the logarithmic ratio between mass-weighted sizes and rest-frame g -band light-weighted sizes at $z \sim 0$ to be -0.12 (for $\log(M_*/M_\odot) \geq 10.7$). The size ratio of our SPIDER sample is completely consistent with Szomoru et al. (2013) ($\langle \log(R_{e-circ, mass}/R_{e-circ, g}) \rangle = -0.127 \pm 0.008$, a decrease of $\sim 25\%$), if we restrict our sample to the same mass range and use g -band sizes from SPIDER. The larger difference in g -band compared to the r -band is simply an effect of the wavelength dependence, as the g -band sizes are larger compared to the r -band. We always use the r -band sizes below while comparing with the KCS sample for clarity.

Comparing the KCS size ratios with SPIDER, we find that there is an intriguing offset between the median size ratio of XMMU J2235-2557 and XMMXCS J2215-1738 and the SPIDER cluster sample, with a difference of ~ 0.2 dex.

A possible issue is the effect of recently quenched galaxies on the size evolution, i.e. the progenitor bias (e.g. Saglia et al., 2010; Valentinuzzi et al., 2010a; Carollo et al., 2013; Poggianti et al., 2013; Jørgensen et al., 2014; Belli et al., 2015; Keating et al., 2015). The effect on the evolution of the size ratio is however unclear, as the newly quenched galaxies may have a range of M_*/L gradients that depend on the quenching mechanism involved.

Using age measurements from La Barbera et al. (2010a), we try to correct the progenitor bias in the size ratio of the SPIDER cluster sample for the three clusters separately. An age cut is applied to the SPIDER cluster sample to remove galaxies that are younger than the cluster redshifts, which equals to the time difference between the lookback time at $z \sim 0$ and $z \sim 1.39, 1.46$ and 1.61 (8.98, 9.17 and 9.52 Gyr respectively).

The result is shown as a light brown line and wheat band in each panel of Figure 4.10 in the mass range $10.4 \leq \log(M_*/M_\odot) \leq 11.6$. Although some changes can be seen, the size ratios of the progenitor bias corrected sample are in general consistent with the SPIDER cluster sample, with median $\langle \log(R_{e-circ, mass}/R_{e-circ}) \rangle = -0.066 \pm 0.013$ for age > 8.98 Gyr. The median logarithmic size ratios in each bin between the SPIDER cluster sample and the progenitor bias corrected sample are all within ± 0.03 dex. The progenitor bias corrected SPIDER samples for the three clusters only show a slight difference mainly at the low-mass end, where we expect the progenitor bias to be stronger. Newly quenched galaxies are more likely to affect the passive population with $\log(M_*/M_\odot) < 11.0$ (see, e.g.

4.7 Evolution of the ratio of mass-weighted to light-weighted sizes to $z \sim 0.135$

Fagioli et al., 2016). We find that the offsets remain even after the correction. Hence, the progenitor bias alone cannot explain the observed offset.

The observed offset between the median size ratio of XMMU J2235-2557 and the progenitor bias corrected SPIDER cluster sample is $\langle \log(R_{e-circ, mass, 1.39}/R_{e-circ, 1.39}) - \log(R_{e-circ, mass, 0}/R_{e-circ, 0}) \rangle = -0.188$. This offset is larger in XMMXCS J2215-1738, with $\langle \log(R_{e-circ, mass, 1.46}/R_{e-circ, 1.46}) - \log(R_{e-circ, mass, 0}/R_{e-circ, 0}) \rangle = -0.259$. On the other hand, Cl 0332-2742, as indicated in Figure 4.10, shows almost no offset with the progenitor bias corrected SPIDER cluster sample, with $\langle \log(R_{e-circ, mass, 1.46}/R_{e-circ, 1.46}) - \log(R_{e-circ, mass, 0}/R_{e-circ, 0}) \rangle = -0.006$.

The smaller size ratios in the $z \sim 1.39$ and 1.46 cluster suggest that the median M_*/L gradient in these high redshift passive cluster galaxies is larger (i.e. steeper) compared to the local ones, which implies an evolution of M_*/L gradient with redshift. By contrast, the similarity between the local size ratio and those in Cl 0332-2742 argues against a monotonic evolution of M_*/L gradient with redshift. Nevertheless, since Cl 0332-2742 is a structure with several groups still in their assembly phase, it is hence plausible that the size ratio discrepancy is due to the difference in the environment and / or the state of the clusters. This implies the M_*/L gradients in high redshift cluster galaxies are closely related to cluster assembly, or at least are likely to originate in the same epoch. In Chapter 5, we discuss the colour gradient of the red sequence galaxies and explore the origin of the M_*/L gradients and the physical processes responsible for the evolution of these passive galaxies.

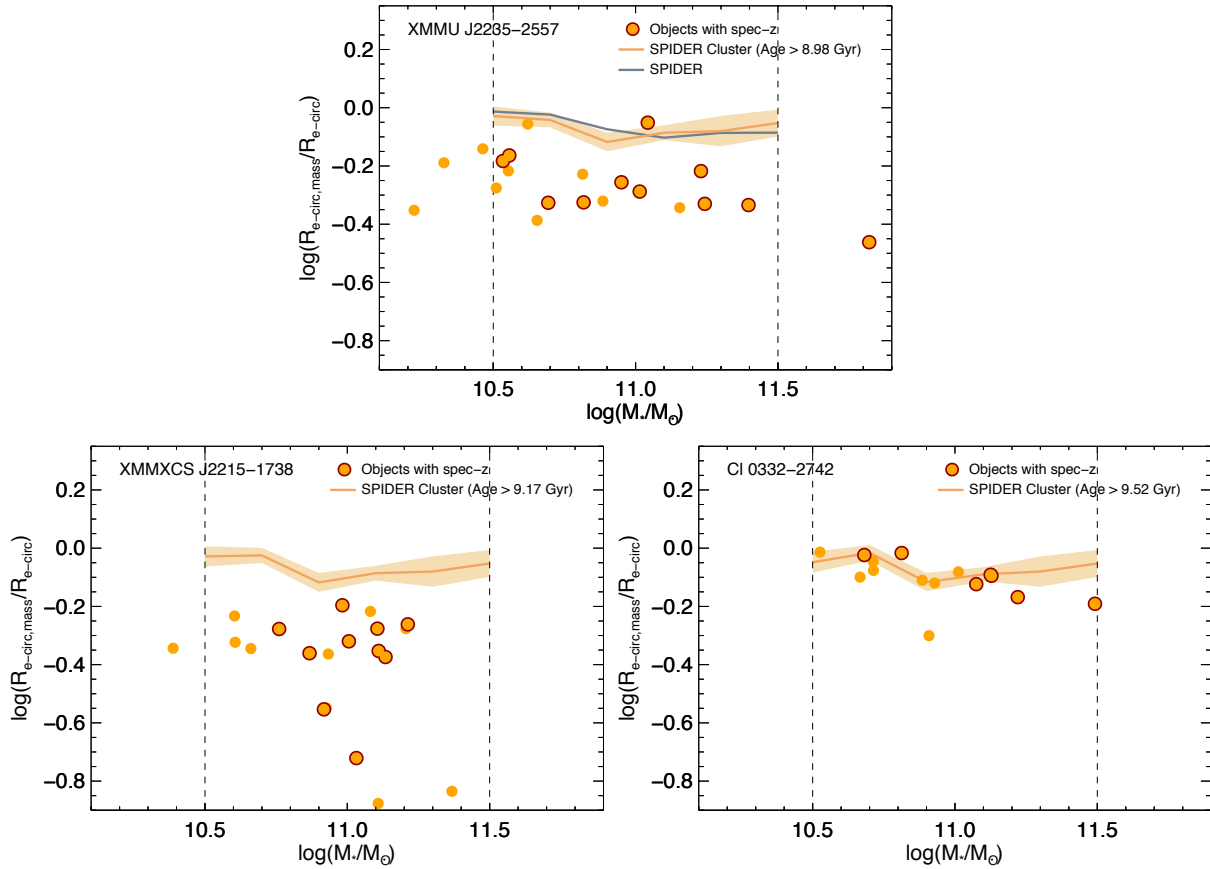


Figure 4.10: Comparison of the ratio of mass-weighted to light-weighted sizes vs. stellar mass at different redshift. Same as top leftmost panel of Figure 4.7 but includes the local size ratios from the SPIDER cluster sample. Spectroscopically confirmed objects are circled in dark red. The median size ratio of the SPIDER sample (from mass range $10.4 \leq \log(M_*/M_\odot) \leq 11.6$) is plotted as a slate grey line in mass bins of 0.2 in the top panel. The light brown line and wheat shaded region in each panel correspond to the median size ratio and $\pm 1\sigma$ error on the median for the progenitor bias corrected SPIDER cluster sample ($\log(M_{200}/M_\odot) \geq 14$ and age $> 8.98, 9.17$ and 9.52 Gyr for the three clusters respectively) from the mass range $10.4 \leq \log(M_*/M_\odot) \leq 11.6$.

Chapter 5

The origin and evolution of the colour gradients and the effect of environment

In this chapter, we focus on the analysis of the colour gradients in the three KCS clusters described in Section 3.2. Colour gradients are a probe of the spatial distribution of different stellar population in the galaxies, and their origin is directly related to how the stellar population in galaxies assembled and evolved. Understanding how colour gradient evolve over redshift provides insights on, and allows us to disentangle, different processes of mass assembly in galaxies. We begin with the distribution of colour gradients in the galaxies of the three KCS clusters and a comparison with various works in Section 5.1. We then investigate quantitatively the origin and evolution of the colour gradients in passive galaxies under different assumptions of the radial variation of stellar population properties (age and metallicity) in Section 5.2. We discuss the physical processes responsible for the evolution of the colour gradients and the formation histories of the galaxies in Section 5.3 and Section 5.4. At last, we end the chapter with a comparison of the properties in KCS clusters with the field and discuss the effect of environment in Section 5.5. Similar to the previous chapter, parts of the results on XMMU J2235-2557 presented in this chapter are discussed in Chan et al. (2016).

5.1 Colour gradients in the red sequence galaxies

In Figure 5.1 we show the colour gradients $\nabla_{z_{850}-H_{160}}$ and $\log(M_*/L)$ gradients $\nabla_{\log(M/L)}$ of the passive sample as a function of stellar mass. As described in Section 3.2, the colour gradients are derived with 1D $z_{850} - H_{160}$ profiles. Similarly, the $\log(M_*/L)$ gradients are derived from fitting 1D M_*/L profiles, which are in turn converted from 1D colour profiles using the M_*/L -colour relation.

The majority of the KCS galaxies (93%) have negative colour gradients. In XMMU J2235-2557, 24 out of 27 galaxies ($\sim 89\%$) show a negative gradient, and 8 out of 27 ($\sim 30\%$) have

very steep gradients with $\nabla_{z_{850}-H_{160}} < -0.5$. The median colour gradient and 1σ error is $\langle \nabla_{z_{850}-H_{160}} \rangle = -0.42 \pm 0.06$ and the median $\log(M_*/L)$ gradient $\nabla_{\log(M/L)}$ is -0.27 ± 0.05 .

In XMMXCS J2215-1738, the colour gradients are steeper: 28 out of 29 galaxies ($\sim 97\%$) show a negative gradient, and 13 out of 29 ($\sim 45\%$) have $\nabla_{z_{850}-H_{160}} < -0.5$. The median colour gradient is $\langle \nabla_{z_{850}-H_{160}} \rangle = -0.46 \pm 0.07$ and the median $\log(M_*/L)$ gradient $\nabla_{\log(M/L)}$ is -0.27 ± 0.04 .

The colour gradients in Cl 0332-2742 are also mostly negative (14 out of 15, $\sim 93\%$). There are 3 objects with $\nabla_{z_{850}-H_{160}} < -0.5$. The median colour gradient is $\langle \nabla_{z_{850}-H_{160}} \rangle = -0.41 \pm 0.07$ and the median $\log(M_*/L)$ gradient $\nabla_{\log(M/L)}$ is -0.11 ± 0.02 .

The observed gradients are consistent with previous findings at $1.3 < z < 2.5$ (Guo et al., 2011) which showed that the majority of passive galaxies have red cores and bluer stellar population at the outskirts. Gargiulo et al. (2012) measured $\nabla_{z_{850}-H_{160}}$ colour gradients for 11 early-type galaxies at $z \sim 1.5$ from the GOODS-S field. They found a median gradient of $\langle \nabla_{z_{850}-H_{160}} \rangle = -0.5$ which is in close agreement with our result.

We find no obvious dependence of colour gradients with stellar mass in XMMU J2235-2557 and XMMXCS J2215-1738. The median Spearman's rank correlation coefficient of the two clusters are $\rho = 0.37$ ($p \simeq 0.11$) for XMMU J2235-2557 and $\rho = -0.29$ ($p \simeq 0.23$) for XMMXCS J2215-1738, computed using the bootstrapping method. On the other hand, in Cl 0332-2742 we find a weak dependence: $\rho = -0.50$ ($p \simeq 0.07$).

At redshift ~ 1.5 , the observed $\nabla_{z_{850}-H_{160}}$ colour gradient roughly corresponds to rest-frame ∇_{U-R} . To ensure rest-frame ∇_{U-R} matches $\nabla_{z_{850}-H_{160}}$, we compute ∇_{U-R} from the observed $\nabla_{z_{850}-H_{160}}$ and $z_{850} - H_{160}$ colour using simple stellar population models (SSPs) of Bruzual & Charlot (2003) as a sanity check. The details of the methodology are described in Section 5.2.1. We confirm that the median $(U - R)$ gradient is comparable to $\nabla_{z_{850}-H_{160}}$.

We also plot the average local $(U - R)$ colour gradient from Wu et al. (2005) on each panel of Figure 5.1 ($\nabla_{U-R} = -0.21 \pm 0.04$) for comparison. Wu et al. (2005) studied the colour gradients for a sample of 36 local field early-type galaxies from SDSS and 2MASS. Due to a lack of deep U -band imaging, the $(U - R)$ colour gradient is not available in most local galaxy surveys. In order to take into account the average age difference between field and cluster passive galaxies (e.g. Thomas et al., 2005, 2010), we evolve the gradients of Wu et al. (2005) for an additional 2 Gyr with Bruzual & Charlot (2003) SSP models (assuming an age gradient of -0.05 and a metallicity gradient of -0.2 consistent with the literature, La Barbera et al., 2005; Wu et al., 2005). The extrapolated value ($\nabla_{U-R} = -0.20$) is very close to the one for local ETGs. The average $(U - R)$ colour gradient of our red sequence galaxies is found to be ~ 2 times steeper than colour gradients observed locally.

As a consistency check, we repeat the colour gradient measurements in $\nabla_{Y_{105}-H_{160}}$ (\sim rest-frame $g - r$) for XMMU J2235-2557, and compare them with the $g - r$ colour gradient in the SPIDER cluster sample. Note that this is a direct cluster - high-density environment comparison. We find consistent results with the $U - R$ gradients. The $g - r$ gradients at $z \sim 1.39$ (median and 1σ error $\langle \nabla_{g-r} \rangle = -0.15 \pm 0.09$) are steeper than the local $g - r$ gradients (-0.042 ± 0.008), although with a smaller dynamic range. Details are described in Section 5.2.7. Section 5.2.7 also explores the dependence of the local $g - r$ gradients on environment within the full SPIDER sample.

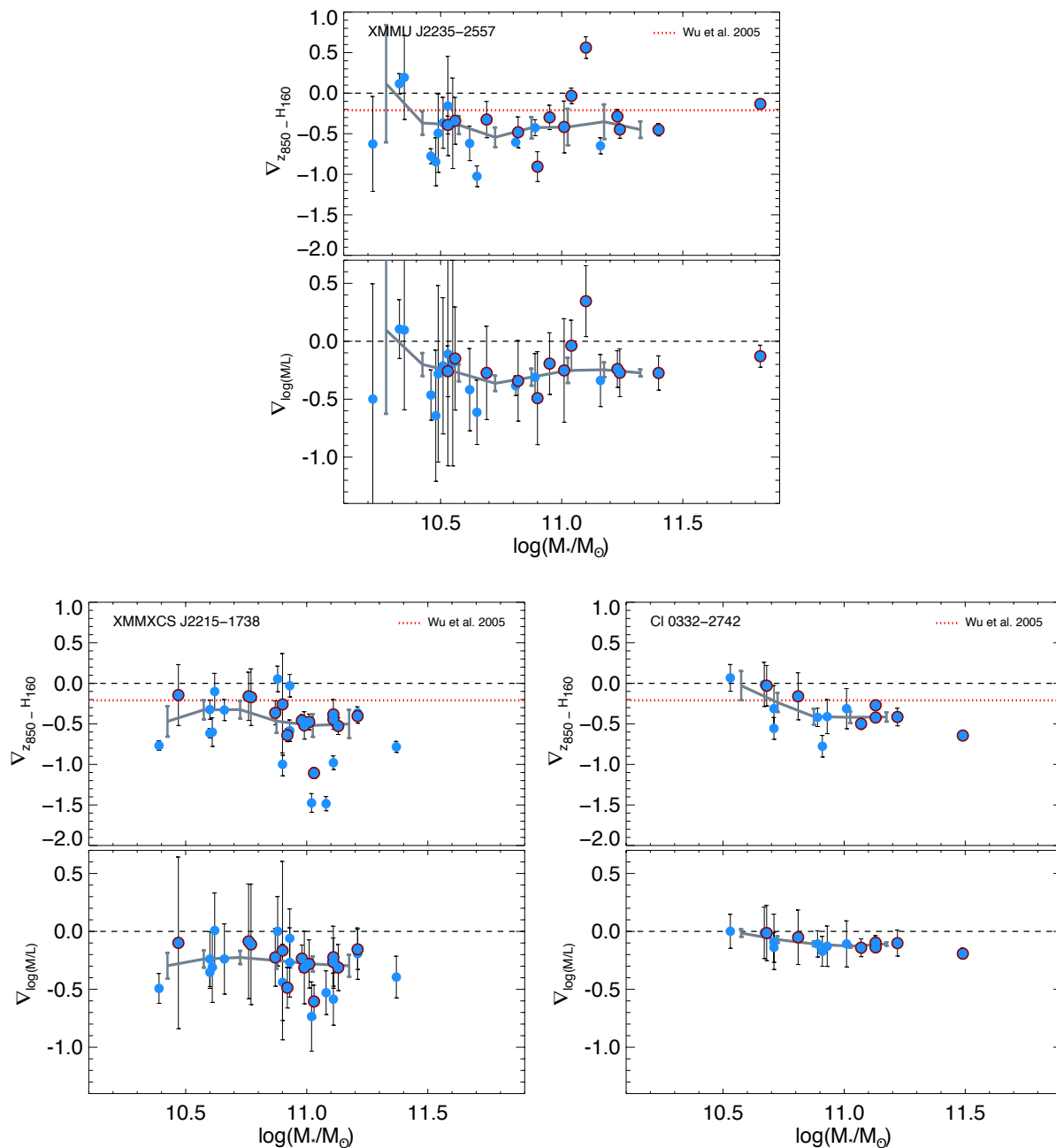


Figure 5.1: Colour and M_*/L gradients in the KCS clusters. Top: Colour gradient $\nabla_{z850-H160}$ as a function of stellar mass. Spectroscopically confirmed objects are circled in dark red. At redshift $z \sim 1.5$, this roughly corresponds to rest-frame $(U - R)$ colour gradient. The black dashed line in each panel shows the reference zero level. The red dotted line shows the average local $(U - R)$ gradient from Wu et al. (2005). Bottom: $\log(M_*/L)$ gradient $\nabla_{\log(M/L)}$ as a function of stellar mass. The grey line in each panel shows the running median and the error bars show the uncertainty of the median in each bin. When there is only one point in the bin, the uncertainty of the quantity is plotted instead.

5.2 The origin and evolution of colour gradients with redshift

In the previous section we have shown that the median colour gradient in our sample is ~ 2 times steeper than the measured local ($U - R$) gradient from Wu et al. (2005).

The origin of the colour gradients is directly related to how the stellar population in galaxies was assembled and evolved. It is however challenging to segregate the impact of age or metallicity using a small sample of galaxies due to the degeneracies in colour between age and metallicity (see Section 1.2.2).

In previous studies, colour gradients in passive galaxies are mostly interpreted as either age gradients ($\nabla_{age} = d \log(\text{age})/d \log(a)$) at fixed metallicity or metallicity gradients ($\nabla_Z = d \log(Z)/d \log(a)$) at fixed age. Some works in clusters at $z \sim 0.4$ (Saglia et al., 2000) and local clusters (e.g. Tamura & Ohta, 2003) showed however that the colour gradients may be preferentially produced by radial variation in metallicity rather than age. The age gradients in local passive galaxies are consistent with 0 (or slightly positive) while the average metallicity gradient is found to be of $\nabla_Z \approx -0.1$ to -0.3 (see also Mehlert et al., 2003; Wu et al., 2005; La Barbera & de Carvalho, 2009). This result is also supported by recent studies with integral field spectroscopy (e.g. Kuntschner et al., 2010; González Delgado et al., 2014; Oliva-Altamirano et al., 2015; Wilkinson et al., 2015).

Our ($U - R$) (and also ($g - r$) for XMMU J2235-2557) colour gradient measurements alone unfortunately do not allow us to break the age-metallicity degeneracy. Nevertheless, with additional colour information at $z \sim 0$, we can study the evolution of the colour gradient with redshift and shed light on the origin of the colour gradients in our sample of passive galaxies in clusters.

5.2.1 Methodology

We investigate quantitatively the evolution of colour gradients in our cluster sample by modeling them under different assumptions of the radial variation of stellar population properties. Simply put, we would like to evolve the observed $z_{850} - H_{160}$ colour gradients $\nabla_{z_{850}-H_{160}}$ in the cluster sample to see under which conditions in age and metallicity gradient will they match the observed ($U - R$) gradient at $z \sim 0$.

For simplicity, in this section we assume the stellar populations in the passive galaxies are coeval and chemically homogeneous in the regions we considered, hence they can be described by simple stellar populations (SSP) models. We use the models of Bruzual & Charlot (2003) (hereafter BC03) and adopt a Chabrier IMF. The BC03 distribution provides SSP models with metallicities $Z = [0.0001, 0.0004, 0.004, 0.008, 0.02, 0.05]$ from $t = 0$ to the age of the Universe in unequally spaced time steps. The results below do not strongly depend on the choice of IMF, since the $U - R$ broad band optical colours under different IMFs (e.g. Chabrier vs. Salpeter) are in reasonable agreement with each other. In Section 5.2.6 we also show that adopting exponentially declining τ -models for this analysis instead of SSPs does not change the main conclusions.

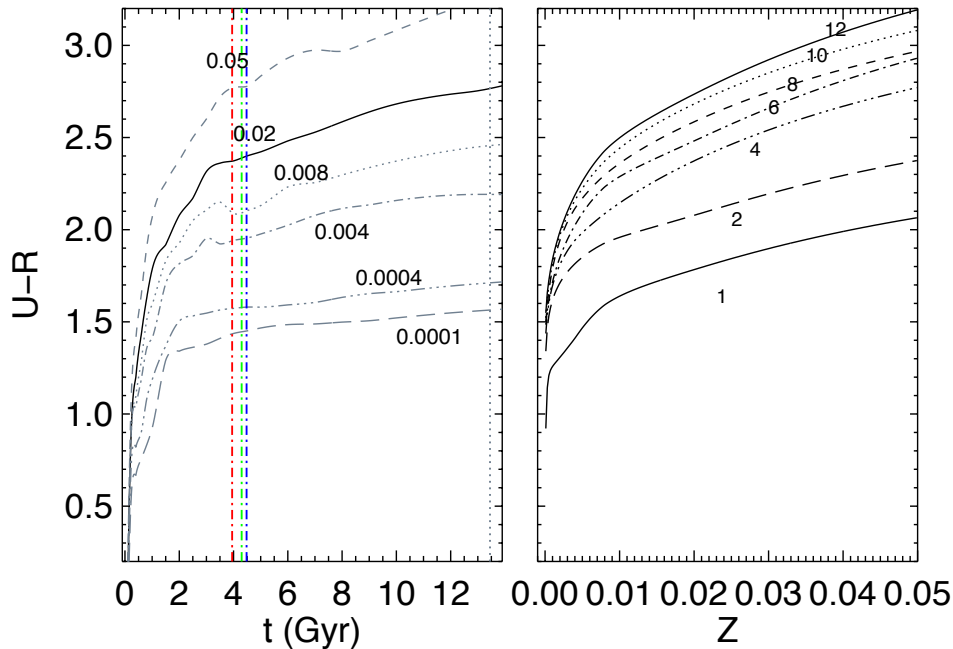


Figure 5.2: Rest-frame $U - R$ colour of stellar populations with different ages and metallicities. Left panel: $U - R$ colour-age relations. The black line shows the stellar populations with solar metallicity ($Z = 0.02$). The grey lines show populations with different metallicities ($Z = 0.0001, 0.0004, 0.004, 0.008, 0.05$) as indicated. The grey vertical dotted line shows the current age of the Universe (13.46 Gyr) with our choice of cosmology and the blue, green and red dotted dashed lines show the age of the Universe at redshift 1.39, 1.46 and 1.61 ($t = 4.48, 4.30, 3.95$ Gyr). Right panel: $U - R$ colour-metallicity relations. The black lines show populations with different ages (in Gyr) as indicated with the numbers.

We compute the rest-frame $U - R$ colour for individual SSP models with different ages and metallicities by convolving the model SEDs with the U and R filters. The colours are then interpolated with a cubic spline to obtain an equally spaced colour grid in age and metallicity. Figure 5.2 shows the rest-frame $U - R$ colour at several ages (left, i.e. the colour-age relations) and metallicities (right, i.e. the colour-metallicity relations) as an example. Using the same method, we compute a $z_{850} - H_{160}$ colour grid for each cluster by redshifting the SSP models to $z = 1.39, 1.46$ and 1.61 .

To simplify the modeling process, we analyse the evolution of colour at two radii, $0.5 a_e$ and $2.0 a_e$, representing the inner region and outer region of the galaxy, respectively. In similar studies (e.g. Saglia et al., 2000) more central regions are used instead ($0.1 - 0.2 R_e$), but this is not possible at this redshift due to limited resolution. Nevertheless, our choice of radial range is sufficient for the purpose as the colour gradients are well-fitted by a linear relation in logarithmic radius (see Figure 3.3).

Because of the age-metallicity degeneracy, we consider several scenarios with additional assumptions in the age or metallicity gradients. Here in this study we explore three possi-

bilities (hereafter cases) to interpret the colour gradient evolution:

- **Case I - Pure age-driven gradient evolution** – In this case we explore the possibility of using a single age gradient to interpret the evolution of colour gradients. The inner and outer regions are assumed to have identical metallicities (i.e. flat metallicity gradients $\nabla_Z = 0$). Assuming a certain metallicity for the inner regions (and equivalently the outer regions), we derive ages of the stellar population of the inner and outer regions in each galaxy (inner and outer ages) respectively, through matching the observed $z_{850} - H_{160}$ colours to the derived $z_{850} - H_{160}$ SSP colours.
- **Case II - Pure metallicity-driven gradient evolution** – In this case we assume that the stellar population in the inner and outer region are coeval (i.e. flat age gradients $\nabla_{age} = 0$). Assuming a certain metallicity for the inner regions, we derive the inner ages each galaxy using the same method as I. The same age is applied to the outer regions. With ages and $z_{850} - H_{160}$ colours, metallicities in the outer regions are then derived using the colour-metallicity relations.
- **Case III - Age-driven gradient evolution with an assumed metallicity gradient** – Same as case I, but assume a fixed metallicity gradient with $\nabla_Z = -0.2$, which is the mean value observed in local passive galaxies (e.g. Tamura & Ohta, 2003; Wu et al., 2005; Brough et al., 2007; Reda et al., 2007) as well as in recent simulations (e.g. Hirschmann et al., 2015). Again assuming a certain metallicity for the inner regions, we derive the age of the inner regions from the $z_{850} - H_{160}$ colour. The metallicity in the outer regions is then computed according to the assumed gradient; outer ages are then derived with this computed metallicity.

In summary, in each case we obtain the ages and metallicities in the inner and outer region of each cluster galaxy in a way according to the assumptions. We then evolve the corresponding SSPs in both regions to $z = 0$, and compute the corresponding local ($U - R$) colour gradients. We also compute the rest-frame ($U - R$) gradient for the high-redshift sample for comparison. For each of the three cases above, we test three scenarios with different assumed metallicity for the inner regions, sub-solar, solar and super-solar ($Z = 0.008, 0.02, 0.05 = 0.4Z_{\odot}, Z_{\odot}, 2.5Z_{\odot}$ or equivalently $[Fe/H] = -0.33, 0.09, 0.56$, Bruzual & Charlot, 2003). Hence we test for nine separate scenarios in total for each cluster. Assuming metallicities with $Z < 0.008$ or $Z > 0.05$ is unphysical for most galaxies in the cluster sample.

Under different assumed metallicity for the inner region, occasionally the age (or the metallicity for case II) determination for some galaxies results in an unphysical age (or metallicity). With our choice of cosmological parameters, the age of the Universe at $z = 1.39, 1.46, 1.61$ is 4.48, 4.30 and 3.95 Gyr respectively. Deduced ages that are too old for the cluster (e.g. > 4.48 Gyr for $z = 1.39$ or > 13.46 Gyr for $z = 0$ within 1σ uncertainty) are rejected to avoid drawing incorrect conclusions. Galaxies that are rejected may simply be unphysical to be modelled with particular metallicity (see, for example in Figure 5.2, a galaxy with $U - R > 2.15$ at $z = 1.39$ will result in an unphysical age if one assumes

$Z = 0.008$) or have a more complicated star formation history, which cannot be well-represented by SSPs.

5.2.2 Case I – Pure age-driven gradient evolution

In Figure 5.3, we show the evolution of the rest-frame ($U - R$) colour gradient from the cluster redshifts to $z = 0$ under the assumption of pure age gradient for the three KCS clusters.

We find that although the colour gradients evolve in the correct direction, the median gradients of the evolved sample at $z = 0$ are too shallow in all three clusters, independent of the assumed metallicity for the inner regions. The median gradients are very close to zero (i.e. flat colour profiles). For example, the median evolved colour gradients of the solar metallicity scenarios ($Z = 0.02$) are -0.038 ± 0.009 , -0.044 ± 0.009 and -0.036 ± 0.013 for XMMU J2235-2557, XMMXCS J2215-1738 and Cl 0332-2742, respectively.

Under the assumption of sub-solar metallicity, only 13 out of 27 galaxies in XMMU J2235-2557 have a physical age. On the other hand, most of the galaxies are retained if we assume a solar (24 out of 27) or super-solar metallicity (27 out of 27). Similarly, 8, 25 and 28 out of 29 galaxies in XMMXCS J2215-1738 are retained in each metallicity scenario ($Z = 0.008, 0.02, 0.05$). For Cl 0332-2742, 5, 11 and 15 out of 15 galaxies are retained. We conclude that in the reasonable range of metallicity that we covered, a pure age-driven gradient is not able to match the observed evolution of colour gradient.

The reason behind the rapid evolution is the flattening of the SSP colour-age relation over time. Since we assume identical metallicities for both inner and outer regions, the inner and outer region of an individual galaxy lie on the same colour-age relation in Figure 5.2. Take the solar metallicity $Z = 0.02$ case (black solid line) as an example, the $U - R$ colour increases sharply from 0 to 4 Gyr but flattens after, hence the ($U - R$) gradient evolves to almost zero at redshift 0.

5.2.3 Case II – Pure metallicity-driven gradient evolution

Instead of using a flat metallicity gradient as case I, Figure 5.4 shows the evolution of the ($U - R$) gradient under the assumption of pure metallicity-driven gradient, or in other words, a flat age gradient $\nabla_{age} = 0$.

Similar to case I, galaxies that have unphysical ages or metallicities are discarded. 14, 24 and 24 out of 27 galaxies in XMMU J2235-2557 are retained in each metallicity scenario respectively. For XMMXCS J2215-1738, 8, 25 and 27 out of 29 galaxies are retained. 5, 11 and 14 out of 15 galaxies are retained for Cl 0332-2742.

From Figure 5.4, we can see that the median gradients of the evolved sample are even steeper compared to the one at the cluster redshifts. This is true for all metallicity scenarios. Hence, it is clear that a pure metallicity-driven gradient fails to reproduce the observed gradient. As an example, the median gradients of the evolved sample of the solar metallicity scenarios are -0.88 ± 0.15 , -0.96 ± 0.16 and -0.54 ± 0.19 for XMMU J2235-2557, XMMXCS J2215-1738 and Cl 0332-2742, respectively.

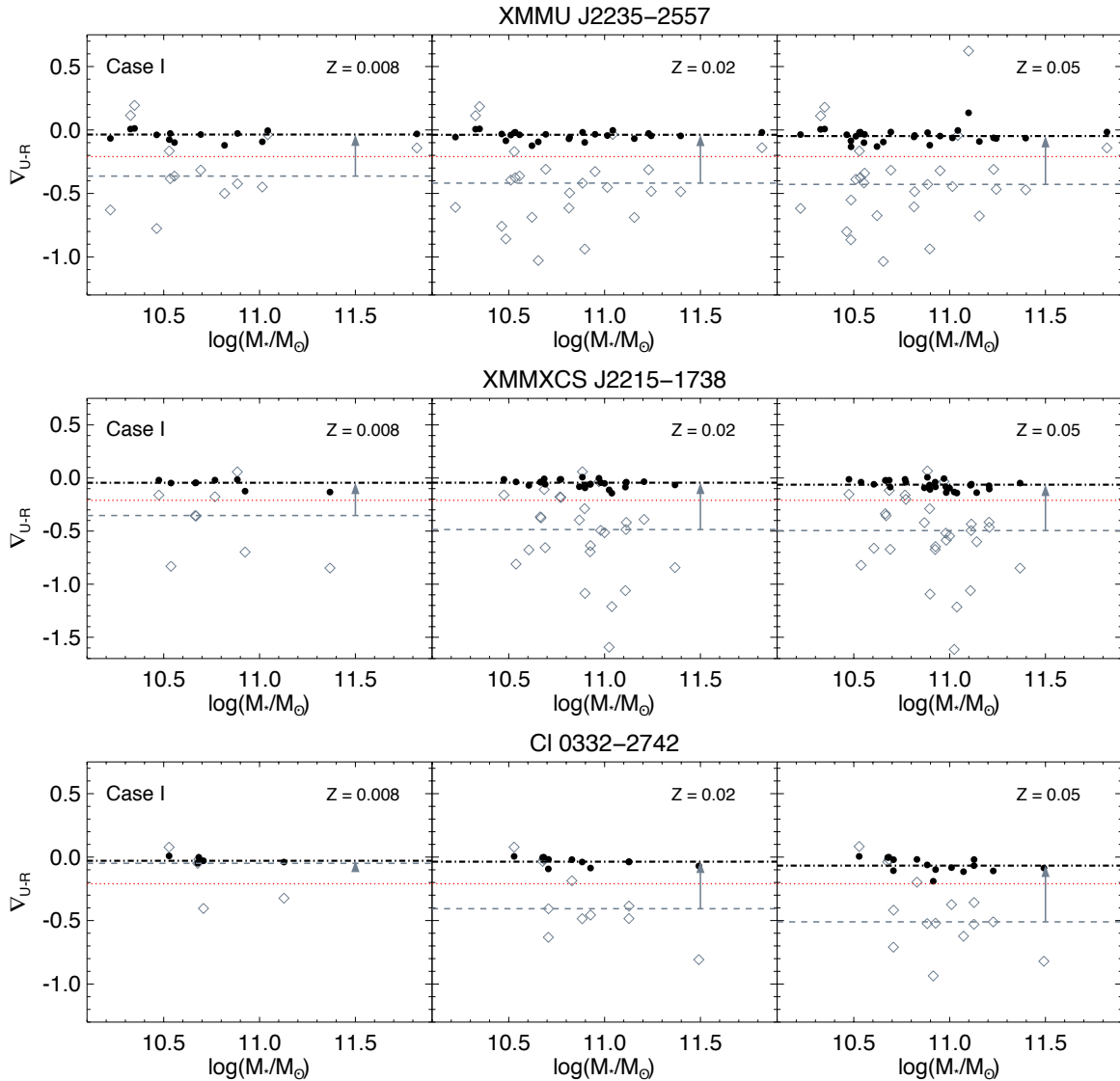


Figure 5.3: Evolution of colour gradient over redshift in case I (Pure age-driven gradient evolution) for the KCS clusters. From top row to bottom: The evolution of XMMU J2235-2557, XMMXCS J2215-1738 and Cl 0332-2742 respectively. Left to right: The sub-solar ($Z = 0.008$), solar ($Z = 0.02$) and super-solar ($Z = 0.05$) metallicity scenarios in each cluster. Grey diamonds correspond to the $(U - R)$ gradient at the cluster redshifts, with the median plotted as the grey dashed line. Black circles indicate the predicted $(U - R)$ gradient at redshift 0 of the same galaxy, and the black dot-dashed line indicate the median. Their masses remain unchanged as we do not consider any mass growth over the period. The grey arrow in each panel shows the direction of evolution of the median gradient. The red dotted line corresponds to the observed $(U - R)$ gradient at redshift 0 by Wu et al. (2005).

The evolution can be explained using the colour-metallicity relations in the right panel of Figure 5.2. As the population ages, the $U - R$ colour-metallicity relation steepens (for example, from 2 Gyr to 4 Gyr), which causes the colour gradient to become more negative. The steepening stops at around ~ 4 Gyr, thus the colour gradient after then remains unchanged. Of course in reality metallicity in individual galaxies differs, but mixing galaxies with different metallicity within our metallicity range would not change our conclusions.

5.2.4 Case III – Age-driven gradient evolution with assumed metallicity gradient

Figure 5.5 shows the evolution of the $(U - R)$ gradient with a metallicity gradient as observed in local passive galaxies: $\nabla_Z = -0.2$. Similar to case I, galaxies with unphysical ages in the inner or outer regions are rejected. For XMMU J2235-2557, 13, 24 and 27 out of 27 galaxies are retained in each metallicity scenario respectively. 7, 25 and 28 out of 29 galaxies in XMMXCS J2215-1738 are retained, and 5, 11 and 14 out of 15 galaxies are retained in Cl 0332-2742.

The solar metallicity scenario works reasonably well for the majority of the sample in all three clusters with evolved median gradients of $\nabla_{U-R} = -0.21 \pm 0.01$, -0.21 ± 0.01 and -0.20 ± 0.01 for XMMU J2235-2557, XMMXCS J2215-1738 and Cl 0332-2742, respectively, which is in close agreement with the observed value in the local universe by Wu et al. (2005).

Despite a number of objects have to be discarded due to unphysical ages (especially in XMMXCS J2215-1738), the median gradient as well as the individual gradients of the evolved samples in the sub-solar metallicity scenario are also close to but slightly smaller than the observed local value. Assuming super-solar metallicity for the inner regions, on the other hand, predicts gradients that are slightly too steep.

Besides the median values of the colour gradients, the 1σ scatter of the evolved colour gradients is also in excellent agreement to the local value by Wu et al. (2005) ($\sigma_{U-R} = 0.04$). For example, for the solar metallicity scenario the scatter reduces from $\sigma_{U-R} = 0.32, 0.36, 0.26$ at the cluster redshifts to $0.034, 0.035, 0.035$ at $z = 0$ for the three clusters respectively.

5.2.5 Implications and limitations

From the above case study, we find that the presence of an age gradient is a necessary condition for the evolution of the colour gradient, and with metallicity gradient it can sufficiently reproduce the magnitudes of the evolution of the colour gradient from the cluster redshifts to $z = 0$ for all three KCS clusters.

An age-driven gradient evolution with a metallicity gradient close to the local value is the most probable scenario, as it can well-reproduce the observed evolution of the colour gradients over redshift in both median and scatter. Among the three metallicity scenarios, the one with solar metallicity seems to best match the evolution of colour gradients for

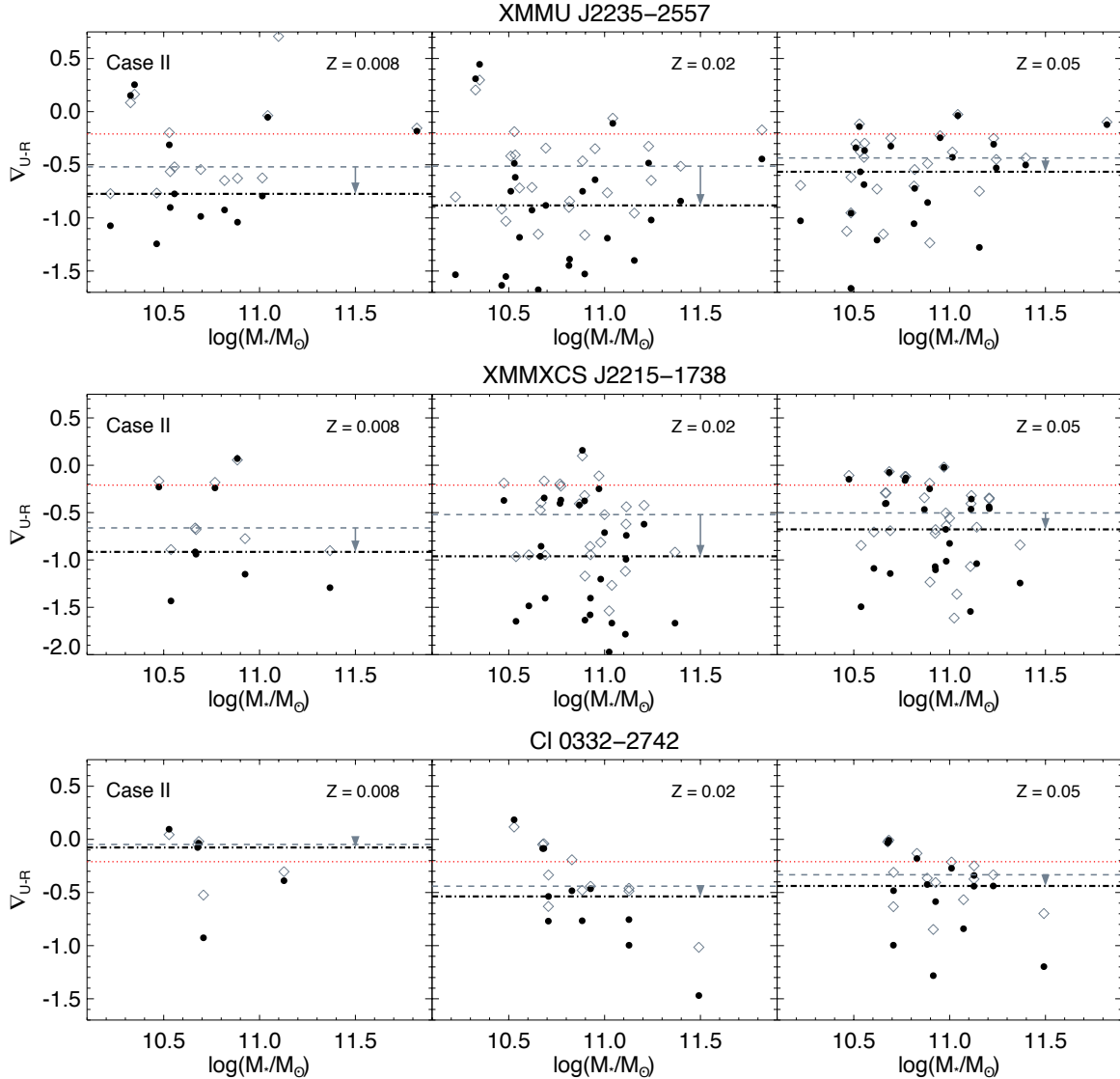


Figure 5.4: Evolution of colour gradient over redshift in case II (Pure metallicity-driven gradient evolution) for the KCS clusters. From top row to bottom: The evolution of XMMU J2235-2557, XMMXCS J2215-1738 and Cl 0332-2742 respectively. Left to right: The sub-solar ($Z = 0.008$), solar ($Z = 0.02$) and super-solar ($Z = 0.05$) metallicity scenarios in each cluster. Grey diamonds correspond to the $(U - R)$ gradient at the cluster redshifts, with the median plotted as the grey dashed line. Black circles indicate the predicted $(U - R)$ gradient at redshift 0 of the same galaxy, and the black dot-dashed line indicate the median. Their masses remain unchanged as we do not consider any mass growth over the period. The grey arrow in each panel shows the direction of evolution of the median gradient. The red dotted line corresponds to the observed $(U - R)$ gradient at redshift 0 by Wu et al. (2005).

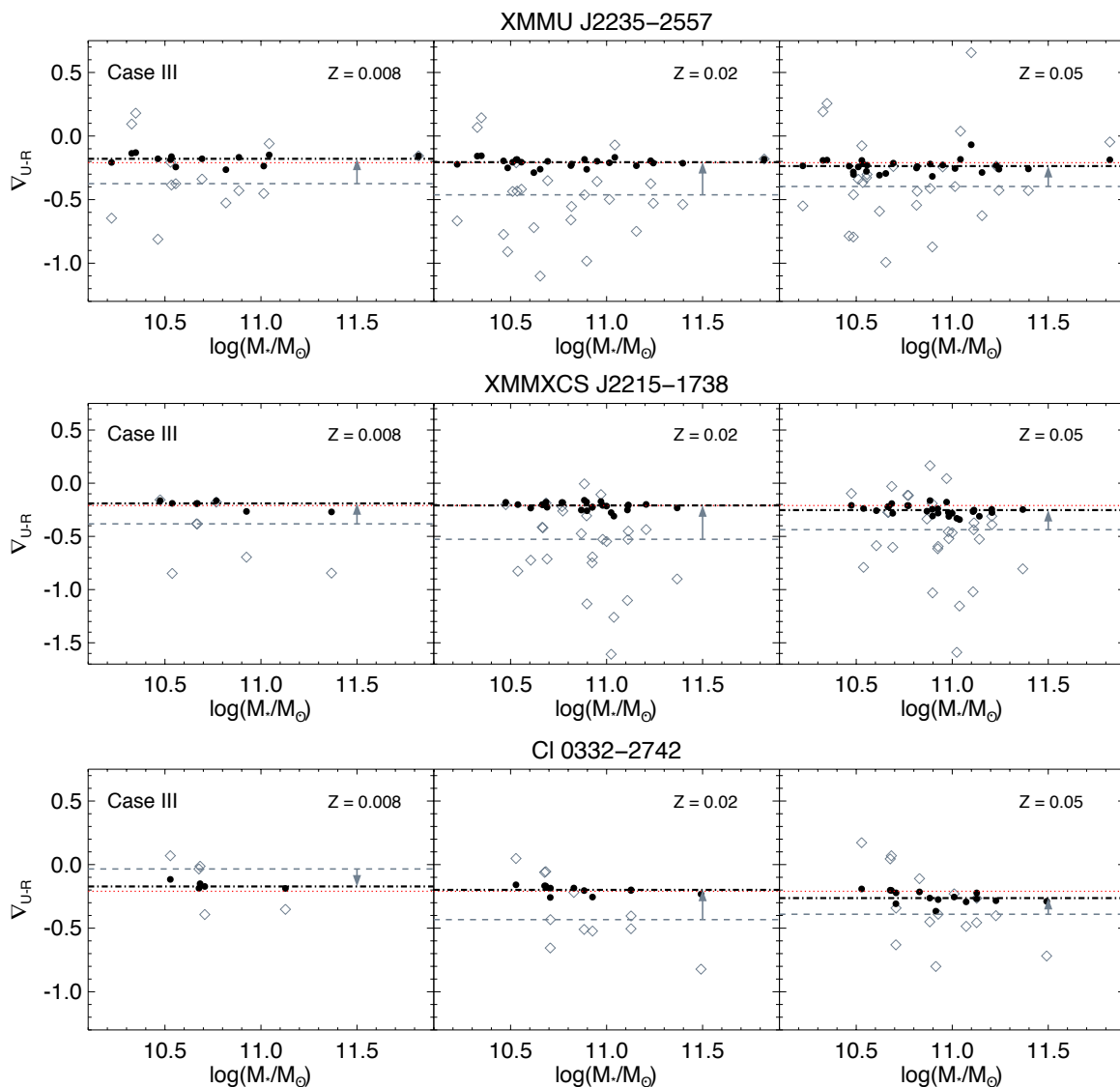


Figure 5.5: Evolution of colour gradient over redshift in case III (Age-driven gradient evolution with assumed metallicity gradient) for the KCS clusters. From top row to bottom: The evolution of XMMU J2235-2557, XMMXCS J2215-1738 and Cl 0332-2742, respectively. Left to right: The sub-solar ($Z = 0.008$), solar ($Z = 0.02$) and super-solar ($Z = 0.05$) metallicity scenarios in each cluster. Grey diamonds correspond to the $(U - R)$ gradient at the cluster redshifts, with the median plotted as the grey dashed line. Black circles indicate the predicted $(U - R)$ gradient at redshift 0 of the same galaxy, and the black dot-dashed line indicate the median. Their masses remain unchanged as we do not consider any mass growth over the period. The grey arrow in each panel shows the direction of evolution of the median gradient. The red dotted line corresponds to the observed $(U - R)$ gradient at redshift 0 by Wu et al. (2005).

most galaxies in the three clusters. In this scenario we find a median age gradient and 1σ error of $\langle \nabla_{age} \rangle = -0.32 \pm 0.08$ at $z = 1.39$ for XMMU J2235-2557, $\langle \nabla_{age} \rangle = -0.35 \pm 0.09$ at $z = 1.46$ for XMMXCS J2215-1738 and $\langle \nabla_{age} \rangle = -0.31 \pm 0.10$ at $z = 1.61$ for Cl 0332-2742. The median age gradients ($\langle \nabla_{age} \rangle$) and the median age difference ($\langle \delta_{age} \rangle$) of the galaxies in each cluster are given in Table 5.1.

Below we try to understand why this is the case. Figure 5.6 shows the evolution of the colour gradient in this case (case III) for XMMU J2235-2557 as an example, assuming a formation redshift of the inner regions of $z_{form} = 3.3$ and an age gradient of $\langle \nabla_{age} \rangle = -0.32$ at $z = 1.39$. The left panel shows the change in the evolution for different formation redshifts $z_{form} = 2.0, 4.0, 5.0$. The net evolution from $z \sim 1.39$ to $z \sim 0$ is clearly insensitive to the formation redshift. On the other hand, the path of evolution depends largely on the age gradient; from the right panel of Figure 5.6 we show that with different initial age gradient at $z = 1.39$, a large range of colour gradients at $z = 1.39$ can reach a similar value at $z \sim 0$. In other words, if the colour gradients in high redshift passive galaxies are mainly due to radial variation in age, this assumption would be able to match the evolution of colour gradient for most galaxies, which is why it works also for the passive galaxies in XMMXCS J2215-1738 and Cl 0332-2742.

The result we found is in agreement with Gargiulo et al. (2012), who investigated the origin of the colour gradient on a sample of early-type galaxies at $0 < z < 1.9$ with spatially resolved colour and global SED fitting. They found that the colour gradients of $\sim 50\%$ of their sample can be reproduced with pure age gradients, while invoking pure metallicity gradients can only explain a small subset of their sample. In addition, extremely steep metallicity gradients are required that are only marginally comparable with those observed in the local universe. Recent studies by De Propris et al. (2015, 2016) studied the ratio of galaxy sizes and colour gradients in rest-frame B & R bands in red sequence galaxies in a sample of 29 clusters with a redshift range of 0.2 to 1.39 (including XMMU J2235-2557) also found an indication of negative colour gradients, which they also attribute to due to the presence of age gradients.

Our result is also not inconsistent with studies on local and intermediate redshift passive galaxies which suggest colour gradients are mainly due to metallicity gradients (e.g. Saglia et al., 2000; Tamura & Ohta, 2003). For example, Kuntschner et al. (2010) found a mean $\nabla_Z = -0.25 \pm 0.11$ and mean $\nabla_{age} = 0.02 \pm 0.13$ for galaxies with age > 8 Gyr. Nevertheless, the age gradient (or its presence) is very difficult to constrain in local passive galaxies. As Gargiulo et al. (2012) pointed out, the effect of the age difference in the inner and outer regions is much more enhanced when the stellar population is young (i.e. at high redshift). Indeed, the age gradient flattens quickly over redshift (see right panel of Figure 5.6). For example, with a median age gradient of $\langle \nabla_{age} \rangle = -0.32 \pm 0.07$ at $z = 1.39$ for XMMU J2235-2557 (from our best scenario); assuming passive evolution this corresponds to a median age gradient of $\langle \nabla_{age} \rangle = -0.056 \pm 0.013$ at $z = 0$, which is consistent with a flat age gradient.

Given the assumption that the cluster passive galaxies at $z = 1.39$ have the same metallicity gradient as the local ones, it is implied that the evolution of colour gradients from the cluster redshifts to $z = 0$ can be explained simply through passive evolution. This conclusion is consistent with previous studies on the evolution of the characteristic

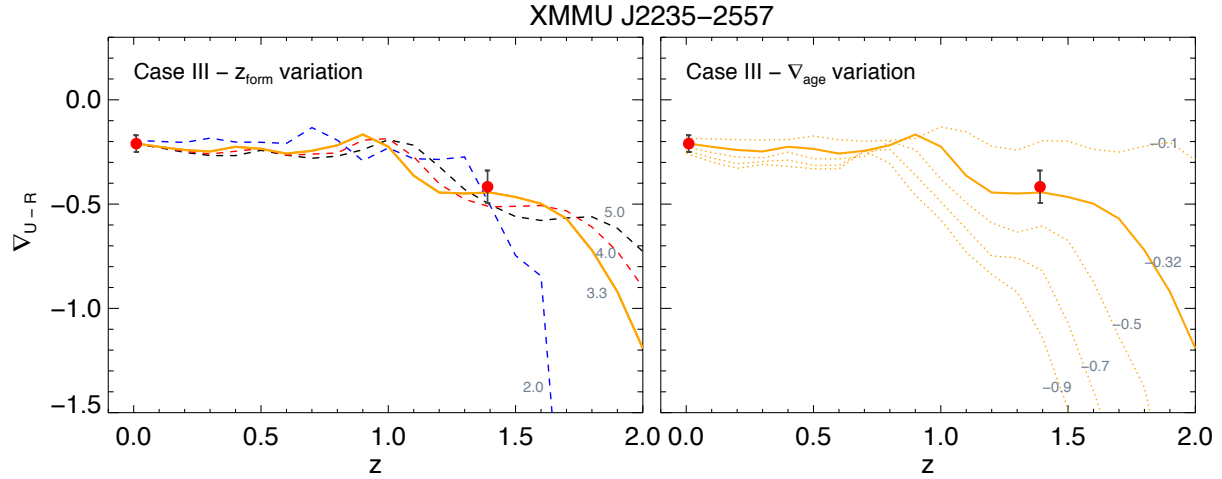


Figure 5.6: Evolution of colour gradient over redshift in case III (Age-driven gradient evolution with assumed metallicity gradient) for XMMU J2235-2557 with assumed solar metallicity $Z = 0.02$. The inner region is assumed to have a formation redshift $z_{form} = 3.3$. The initial age gradient at $z = 1.39$ is $\nabla_{age} = -0.32$, and the assumed metallicity gradient is $\nabla_Z = -0.2$. Left panel: variation in formation redshift $z_{form} = 2.0, 4.0, 5.0$ as indicated by blue, red and black dashed lines respectively. Right panel: variation in age gradients at $z = 1.39$. The dotted lines show the evolution with different initial age gradient as indicated ($\nabla_{age} = -0.1, -0.5, -0.7, -0.9$). Red circles correspond to the median $z_{850} - H_{160}$ gradient of our XMMU J2235-2557 sample at redshift 1.39, and the observed ($U - R$) gradient at redshift 0 by Wu et al. (2005). The error bars show the uncertainty of the median.

magnitude M^* of the luminosity functions of clusters (e.g. Andreon, 2008; De Propris et al., 2013).

One thing we did not test explicitly in the above three cases, is whether the observed colour gradients can be explained by an evolving metallicity gradient. In case II, we define the metallicity gradient for individual galaxy at the cluster redshift and assume it remains constant across redshift. In theory, the metallicity gradient can change with time, for example due to galaxy-galaxy interactions, and end up with $\nabla_Z \sim -0.2$ at $z \sim 0$ to match the local observations. Nevertheless, from case II we find that extremely steep metallicity gradients are required at the cluster redshifts to explain the colour gradients. For example, for the solar metallicity scenario, the median metallicity gradient we found is $\langle \nabla_Z \rangle \sim -1.09 \pm 0.24$ at $z = 1.39$ for XMMU J2235-2557. These steep metallicity gradients are unlikely to be physical and is almost never observed in local passive galaxies (see the range of ∇_Z in, e.g. Ogando et al., 2005; Wu et al., 2005; Spolaor et al., 2009; Kim & Im, 2013). Hence we suggest that an evolving metallicity gradient is unlikely to be able to explain the evolution of the colour gradients of the cluster population.

Table 5.1: The derived median age gradient (Case III) of the KCS clusters at the cluster redshift and $z = 0$

Cluster	$\langle \nabla_{age} \rangle$ at $z_{cluster}$	Median age at inner region(Gyr)	$\langle \delta_{age} \rangle$ (inner-outer)	Evolved ∇_{age} at $z = 0$
XMMU J2235-2557	-0.32 ± 0.08	2.57 ± 0.22	0.90 ± 0.20	-0.056 ± 0.013
XMMXCS J2215-1738	-0.35 ± 0.09	2.77 ± 0.18	1.10 ± 0.20	-0.068 ± 0.013
Cl 0332-2742	-0.31 ± 0.10	2.52 ± 0.44	0.70 ± 0.38	-0.046 ± 0.021

5.2.6 Effect of assuming exponentially declining SFRs

In the above analysis we assume that the stellar population in the inner and outer region of individual galaxies can be well described by simple stellar population models (SSPs). In reality the star formation history of passive galaxies can be much more complex. One of the commonly used parametrisations is the exponentially declining ‘tau’ models (Bruzual A., 1983), where the star formation history of a galaxy is described by an exponentially declining SFR with an e-folding time τ . In this section we use XMMU J2235-2557 as an example to discuss the effect of assuming tau models with different τ ($\tau = [0.2, 0.4, 0.6]$) instead of SSPs on our colour gradient analysis.

Figure 5.7 shows the $U - R$ colour at different ages (i.e. the colour-age relations) from models with various τ using BC03, similar to the left panel of Figure 5.2. The $U - R$ colour is computed using the same method as in Section 5.2.1. Due to the continual star formation, the $U - R$ colour of the τ models are bluer for a given age than the SSP. The difference is more pronounced when τ is larger. We stop at $\tau = 0.6$ as otherwise the $U - R$ colour would be too blue to account for the observations. Using τ models also has the effect of reducing the colour differences between different metallicities when the galaxy is young (see the trend before the colour dashed lines), while the evolution is very similar for later ages when the contribution of young stars falls off.

Using τ models instead of SSPs does not change our main conclusion. Since the evolution of the colour gradient at later times is very similar to SSPs, we find that an age-driven gradient evolution with a metallicity gradient close to the local value (case III) remains the best scenario to explain the colour gradients independent of the τ used. For example, Figure 5.8 shows the best-fit scenario of the evolution of the colour gradients of XMMU J2235-2557 with different τ (case III with solar metallicity). Within the range of τ the evolution can still be well modelled. Nevertheless, due to the change in $U - R$ colour over time (see Figure 5.7), the resulting age gradient, age difference of the inner and outer population and formation redshift for the best-fit scenario vary by a certain amount with τ . The values of the median age gradient, inner ages and the evolved age gradient at $z = 0$ for the best-fit scenario with different assumed τ can be found in Table 5.2. With an increasing τ , a flatter but still significant age gradient (e.g. $\langle \nabla_{age} \rangle = -0.16$ for $\tau = 0.4$) is needed to explain the colour gradient. This strengthens our result that an age gradient is a necessary component in the colour gradient at high-redshift.

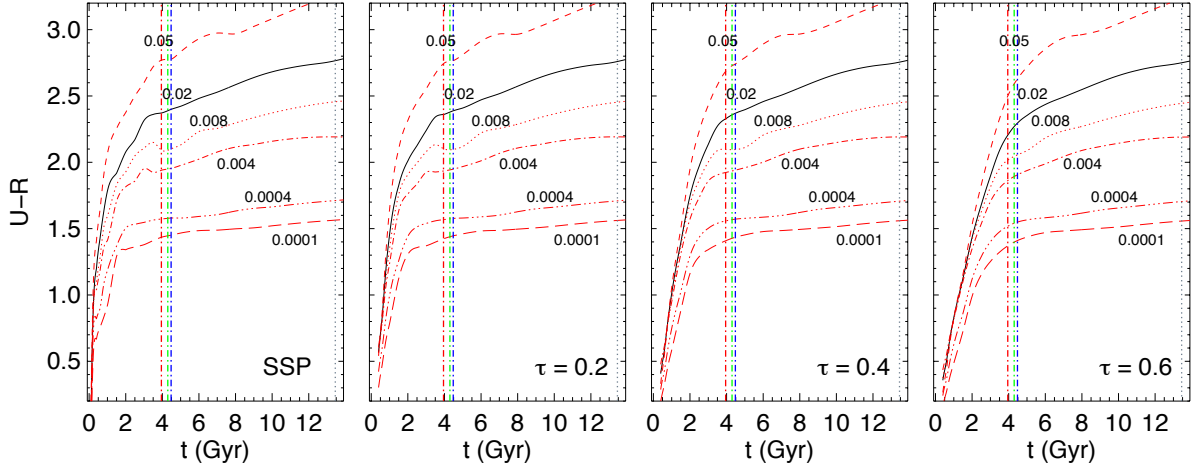


Figure 5.7: Rest-frame $U - R$ colour of stellar populations with different ages and metallicities with different values of τ (from left to right: SSP, $\tau = 0.2, 0.4, 0.6$). The black line shows the stellar populations with solar metallicity ($Z = 0.02$). The red lines show populations with different metallicities ($Z = 0.0001, 0.0004, 0.004, 0.008, 0.05$) as indicated. The grey vertical dotted line shows the current age of the Universe (13.46 Gyr) with our choice of cosmology and the blue, green and red dotted dashed lines show the age of the Universe at redshift 1.39, 1.46 and 1.61 ($t = 4.48, 4.30, 3.95$ Gyr). Note that age refers to the time passed when the populations start forming stars.

Table 5.2: The derived median age gradient (Case III) of XMMU J2235-2557 at $z = 1.39$ and $z = 0$ with exponentially declining τ -models

τ	∇_{age} at $z = 1.39$	Median age at inner region (Gyr)	Median δ_{age} (inner - outer)	Evolved ∇_{age} at $z = 0$
SSP	-0.32 ± 0.08	2.57 ± 0.22	0.90 ± 0.20	-0.056 ± 0.013
0.2	-0.26 ± 0.06	2.78 ± 0.23	0.87 ± 0.19	-0.049 ± 0.012
0.4	-0.16 ± 0.04	3.10 ± 0.19	0.65 ± 0.15	-0.039 ± 0.009
0.6	-0.18 ± 0.04	3.75 ± 0.21	0.79 ± 0.17	-0.043 ± 0.010

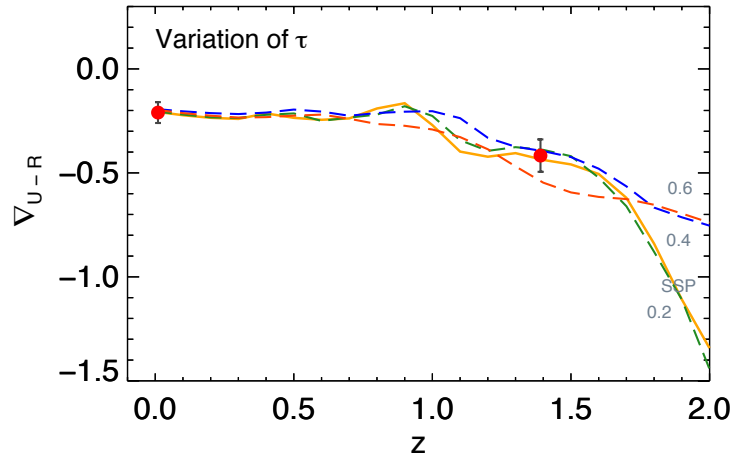


Figure 5.8: Evolution of colour gradient over redshift in case III (age and assumed metallicity gradient $\nabla_Z = -0.2$) for XMMU J2235-2557 using SSP and tau models with $\tau = 0.2, 0.4, 0.6$ with assumed solar metallicity $Z = 0.02$. The solid yellow line shows the result with SSP models and is identical to one on Figure 5.6. Green, blue and red lines show the result with tau models with $\tau = 0.2, 0.4, 0.6$ respectively. The derived initial age gradient at $z = 1.39$ for each τ can be found in Table 5.2. Red circles correspond to the median $z_{850} - H_{160}$ gradient of our sample at redshift 1.39 and the observed $(U - R)$ gradient at redshift 0 by Wu et al. (2005). The error bars show the uncertainty of the median.

5.2.7 Effect of using $(g - r)$ colour gradients and their evolution with redshift

Similar to the sizes, the colour gradient of a galaxy also depends on the considered band. In this section we investigate the effect of using a colour gradient in a different band, $g - r$ and their evolution with redshift, again using XMMU J2235-2557 as an example. The local SPIDER cluster sample (see Section 2.7 for the selection) allows us to derive the $(g - r)$ colour gradient at $z = 0$, hence we can perform a direct comparison between galaxies residing at high density environments at $z \sim 0$ and at the cluster redshift. At redshift ~ 1.39 , the observed $\nabla_{Y_{105}-H_{160}}$ colour gradient roughly corresponds to rest-frame ∇_{g-r} .

To compute the $(g - r)$ colour gradient from the SPIDER sample, we again make use of the structural parameters in g -band and r -band of the publicly available multiband structural catalogue from La Barbera et al. (2010b), described in Section 2.7. We generate 2D Sérsic model images in the two bands with fitted parameters from the structural catalogue, then convert the 2D image in both bands into 1D radial surface brightness profiles, similar to the procedure described in Section 3.2. This allows us to derive 1D $g - r$ colour profiles and measure the colour gradients of the galaxies in the SPIDER sample by fitting the logarithmic slope of their $g - r$ profiles along the major axis. The sample is split into low density and high density environment with a halo mass cut ($\log(M_{200}/M_{\odot}) < 14$ and $\log(M_{200}/M_{\odot}) \geq 14$) using the group catalogue from La Barbera et al. (2010c). The detail selection is described in Section 2.7. We also apply the same age cut (age > 8.98 Gyr for XMMU J2235-2557) using age measurements from La Barbera et al. (2010b) to correct for the progenitor bias in the SPIDER sample as in Section 4.7.

The median $(g - r)$ gradient and 1σ scatter in the local SPIDER cluster sample is $\nabla_{g-r} = -0.042 \pm 0.008$ while the median gradient in the low density sample is $\nabla_{g-r} = -0.060 \pm 0.008$. The values we derived are consistent with La Barbera et al. (2005); Kennedy et al. (2016a).

We derive the $Y_{105} - H_{160}$ colour gradient in XMMU J2235-2557 with structural parameters of the Y_{105} and H_{160} bands. This is because the above $(g - r)$ colour gradients are intrinsic gradients without PSF convolution, hence for better comparison and consistency we use the same method as above. Figure 5.9 shows the $Y_{105} - H_{160}$ colour gradients, roughly corresponds to rest-frame $g - r$. $\nabla_{Y_{105}-H_{160}}$ is less steep compared to $\nabla_{z_{850}-H_{160}}$, with a median of $\langle \nabla_{Y_{105}-H_{160}} \rangle = -0.15 \pm 0.09$. Hence, the $(g - r)$ colour gradient at $z = 1.39$ is also steeper than the local sample, consistent with the result of $(U - R)$ gradients.

After confirming that the $(g - r)$ gradient is steeper at high redshift, we repeat the analysis described in Section 5.2.1 to model the $g - r$ colour gradients under different assumptions in the radial variation of stellar population properties. The $g - r$ colour is less sensitive to age variation than $U - R$ colour, as the g -band is on the 4000\AA break. Hence, the evolution in the $(g - r)$ colour gradient is less pronounced than the $(U - R)$ gradients. Kennedy et al. (2016a) also demonstrated from the GAMA sample that the colour gradients are stronger for more widely spaced waveband pairs.

Figure 5.10 shows the evolution of the $g - r$ colour gradients from $z = 1.39$ to $z = 0$ (case III with solar metallicity). Despite the lack in dynamic range, the result with the

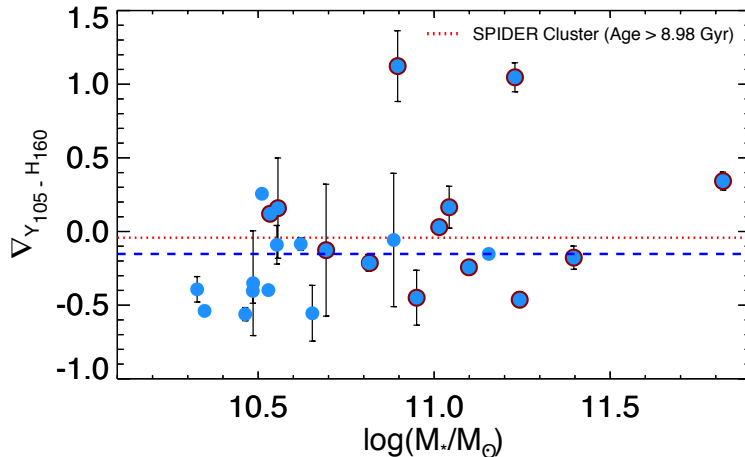


Figure 5.9: $Y_{105} - H_{160}$ colour gradients in XMMU J2235-2557. At redshift 1.39, this roughly corresponds to rest-frame $(g - r)$ colour gradient. The red dotted line shows the median local $(g - r)$ gradient from the progenitor bias corrected SPIDER cluster sample. The blue dashed line shows the median $Y_{105} - H_{160}$ colour gradients.

$(g - r)$ colour gradient is completely consistent with the $(U - R)$ colour gradients, in the sense that an age-driven gradient evolution with a metallicity gradient close to local value (case III) is the best scenario to explain its evolution. A pure age gradient would predict $(g - r)$ gradients that are too shallow at $z = 0$, while a pure metallicity gradient would predict gradients that are too steep. In addition, we find that the derived median age gradient is in good agreement with the one derived from $(U - R)$ gradients. The evolution can be well described with an age gradient of $\nabla_{age} = -0.32$, identical to the one we found from $(U - R)$ gradients. The consistent result from $(g - r)$ colour gradients reinforces our conclusion that an age gradient is necessary to explain the colour gradient at high-redshift.

5.2.8 Effect of dust obscuration

A complication that we have not considered in the above analysis is the effect of dust obscuration. The colour gradient can be affected by the radial variation of dust content. For local passive galaxies, Wise & Silva (1996) pointed out that their colour gradients can be reproduced by a dust gradient, albeit with much higher dust masses than observed (Saglia et al., 2000). Hence the colour gradient in these galaxies should be driven from the variation of the stellar population. Nevertheless, the amount of dust can vary with radius; it is not uncommon to find dust at the centre, for example in Lauer et al. (2005), central dust is visible in almost half of the local passive sample.

At high redshift, measuring the radial variation of dust content is even more difficult due to the compact nature of passive galaxies and limited angular resolution. Several studies suggest that although the effect of dust cannot be completely neglected, it plays

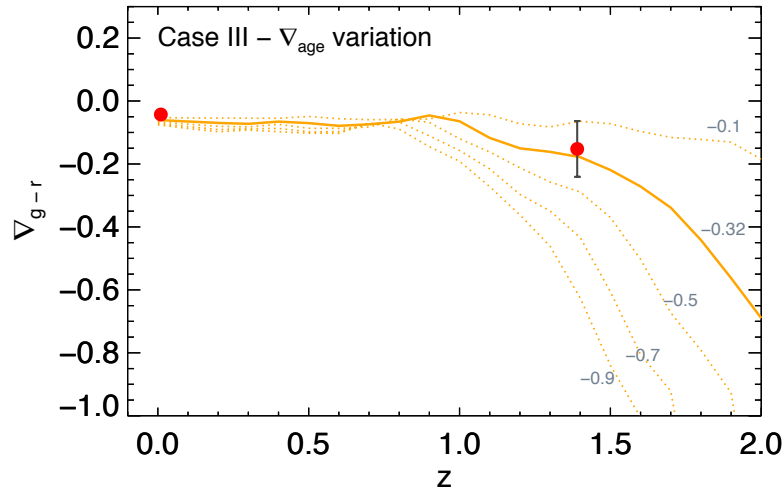


Figure 5.10: Evolution of $(g-r)$ colour gradient over redshift in case III (age and metallicity gradient) for XMMU J2235-2557 with assumed solar metallicity $Z = 0.02$. The inner region is assumed to have a formation redshift $z_{form} = 3.3$. The initial age gradient at $z = 1.39$ is $\nabla_{age} = -0.32$, and the assumed metallicity gradient is $\nabla_Z = -0.2$. The dotted lines show the evolution with different initial age gradient as indicated ($\nabla_{age} = -0.1, -0.5, -0.7, -0.9$). Red circles correspond to the median $Y_{105} - H_{160}$ gradient of our sample at redshift 1.39, and the observed local $(g-r)$ gradient from the SPIDER cluster sample. The error bars show the uncertainty of the median.

only a minor role in driving colour gradients. Belli et al. (2015) showed that their early-type sample at $1.0 < z < 1.6$ have little to no dust extinction (see also Mendel et al., 2015). For the radial variation of dust, Guo et al. (2011) demonstrated from spatially resolved annular SED fitting that, for their sample of six $z \sim 2$ galaxies dust partly contributes to the observed colour gradients, the inferred dust gradient and global extinction have a value of $dE(B - V)/d\log(R) \sim -0.07$ and $\langle E(B - V) \rangle \sim 0.1$. On the other hand, among the 11 early-type galaxies at $1.0 < z < 1.9$ in Gargiulo et al. (2012), half of the sample have no dust extinction (i.e. $A_V = 0$) from global SED fit and for most galaxies the main driver of the colour gradients is certainly not the radial variation of dust.

For the selection of the KCS sample, we applied a colour-colour selection on top of the red sequence selection and crossmatched with available $24 \mu\text{m}$ catalogue from the literature (Hilton et al., 2010) to remove objects that are presumably dusty star-forming objects on the red sequence (see Section 2.5). The colour-colour and $24 \mu\text{m}$ selections we used, however, are unable to separate the effect of dust in passive galaxies. As we described in Section 2.5, the mid-IR $24 \mu\text{m}$ emission is the re-radiation of UV photons from either star formation or AGN by dust, hence one can use the $24 \mu\text{m}$ to constrain the SFR (after confirm the emission is not from AGN). In case of passive galaxies with low SFR, the $24 \mu\text{m}$ observation is unable to provide any constraint on the dust content.

It is not possible to derive reliable dust gradients from our multi-band photometry data. Hence, for completeness we test whether the effect of dust would affect our conclusion. Assuming dust mainly affects the central region as in local passive galaxies, we deredden the $z_{850} - H_{160}$ colour in the inner region by a certain magnitude but leaving the outer part unchanged to reduce the observed gradient, then recompute all the evolution under different assumptions. We find that on average a decrease of 0.14 mag in the $z_{850} - H_{160}$ colour at the inner region ($\sim 0.30 \text{ mag}$ at $0.1a_e$) will remove the observed evolution for the KCS clusters, i.e. the differences of the observed median colour gradient at the cluster redshifts with local passive galaxies.

The most commonly used attenuation curve in studies of high redshift galaxies is the Calzetti law (Calzetti et al., 2000), calibrated using a sample of starburst galaxies at low redshift. The extinction curve of Calzetti et al. (2000) has the following form:

$$k(\lambda) = \begin{cases} 2.659 \left(-2.156 + \frac{1.509}{\lambda} - \frac{0.198}{\lambda^2} + \frac{0.011}{\lambda^3} \right) + R_V & \text{for } 0.12\mu\text{m} \leq \lambda \leq 0.63\mu\text{m} \\ 2.659 \left(-1.857 + \frac{1.040}{\lambda} \right) + R_V & \text{for } 0.63\mu\text{m} \leq \lambda \leq 2.20\mu\text{m} \end{cases} \quad (5.1)$$

where the extinction at a wavelength λ is given by

$$A_\lambda = \frac{k(\lambda)A_V}{R_V} \quad (5.2)$$

with the effective obscuration $R_V = A_V/E(B - V) = 4.05 \pm 0.80$ where $E(B - V)$ is the colour excess.

Table 5.3: The derived median age gradient (Case III) of Cl 0332-2742 at $z = 1.61$ and $z = 0$ with different values of $\langle A_V \rangle$

Dust extinction $\langle A_V \rangle$	$\langle \nabla_{age} \rangle$ at $z_{cluster}$	Median age at inner region(Gyr)	$\langle \delta_{age} \rangle$ (inner-outer)	Evolved ∇_{age} at $z = 0$
0*	-0.31 ± 0.10	2.52 ± 0.44	0.70 ± 0.38	-0.046 ± 0.021
0.6	-0.34 ± 0.09	1.18 ± 0.23	0.45 ± 0.18	-0.031 ± 0.012

* The $\langle A_V \rangle = 0$ case is identical to the result of Cl 0332-2742 quoted in Table 5.1.

Assuming this extinction curve, we convert the abovementioned required reddening to a dust gradient of $dA_V/d\log(a) \sim -0.40$ or $dE(B - V)/d\log(a) \sim -0.10$. Hence, our conclusion is robust if the dust gradient is less steep than this value. If the genuine colour gradient is shallower at the cluster redshift, the evolution will be best explained with a shallower age gradient (as seen from the right panel of Figure 5.6), and will not change any of our conclusions. Nevertheless, although unlikely, we cannot rule out the possibility that the observed colour gradients are driven by a large amount of dust located in the central region.

Although our conclusion is robust if there is no steep dust gradients, the values we derived, in particular the ages of the galaxies and the median age gradients ($\langle \nabla_{age} \rangle$) of the three clusters are affected by the global dust extinction (i.e. the values in Table 5.1). Not taking into account the effect of dust (if there is any) will result in an older age. Nevertheless as mentioned above we do not have dust information for all three KCS clusters, but since Cl 0332-2742 is in the GOODS-S field, we can take the global dust extinction A_V values from the public 3D-HST catalogue to estimate the effect on this particular cluster. The dust extinction of the 3D-HST catalogue comes from SED fitting of multiband photometries using the FAST code (Kriek et al., 2009). From the public 3D-HST catalogue, the median dust extinction of our Cl 0332-2742 sample has $\langle A_V \rangle = 0.6$, which is moderately high compared to the field passive galaxies at this redshift range (e.g. Belli et al., 2015).

We repeat the above analysis of Cl 0332-2742 with $\langle A_V \rangle = 0.6$ to investigate the effect of dust on the results. As expected, we find that Case III remains to be the best scenario among the three cases to explain the evolution of the colour gradients. The derived median age gradient, the median age difference between the inner and outer region and evolved age gradient of Case III are given in Table 5.3. Assuming an A_V of 0.6, however, has a large effect on the derived ages. For example, the median age at the inner region is drastically reduced from 2.52 Gyr ($A_V = 0$) to 1.18 Gyr ($A_V = 0.6$). The median age difference between the inner and outer region is also reduced. On the other hand, since the age gradient is related to the relative colour difference of the inner and outer population, it is relatively stable with various A_V . This suggests that without an accurate estimation of the dust extinction, one should not over-interpret the absolute ages and age differences derived with this method. Unfortunately, this also renders an age comparison between the three KCS clusters impossible.

5.3 Physical processes responsible for the evolution of size and colour gradient

Our colour gradient analysis suggests that the evolution of colour gradients from the cluster redshifts to $z = 0$ can be explained through passive evolution. While passive evolution is a very tempting conclusion, it alone cannot explain the observed size evolution in clusters over redshift. In Section 4.3 we have shown that the cluster passive galaxies in KCS are $\sim 50\%$ smaller than their local counterparts. Similarly, a large number of previous studies have confirmed that the sizes of passive galaxies in high redshift clusters are smaller than those in the local universe (e.g. Rettura et al., 2010; Strazzullo et al., 2010; Papovich et al., 2012; Strazzullo et al., 2013), although a part of this size evolution (e.g. Saglia et al., 2000; Jørgensen et al., 2014) may be due to progenitor bias. If we assume this observed size evolution is genuine, in the sense that it is not completely an effect of progenitor bias, additional physical processes must be in place over redshift to increase the size of the population but not significantly their stellar mass, and at the same time cannot severely disrupt the existing stellar population gradients.

The “puffing-up” scenario (or adiabatic expansion) is one of the candidates to explain the size evolution of passive galaxies (Fan et al., 2008, 2010) (see Section 1.4 for a description). While it may work for increasing the size, it is yet unclear whether it can sufficiently explain the observed colour gradients at the cluster redshifts or the evolution of colour gradients. It is also unclear how to reconcile this with the existence of age gradient at high redshift. Further detailed investigation with an accurate model is required to test this scenario, but current models (e.g. Fan et al., 2008) are much simplified.

Minor mergers, on the other hand, seem to be a viable scenario as the effects are primarily on the outer part of the galaxies (see Section 1.4 for a description). Hilz et al. (2013) showed from n-body/SPH simulations that for minor (with a mass ratio 1:10) or intermediate (1:5) dry mergers, the inner region of the galaxy remains almost unchanged and the accreted mass assembles predominately in the outer part of the galaxy. This is also seen in the Illustris simulation, where the accreted stars from mergers with lower mass ratio (i.e. merging with smaller galaxies) dominate at outer radius (Rodriguez-Gomez et al., 2016). Hence, the inner stellar populations of the galaxy can age through passive evolution without major disturbance. The negative age gradients we find here seem to be consistent with this picture given that the minor mergers are dry and the stars accreted are relatively young.

The minor merger scenario has been known to be a viable mechanism in the field. It is consistent with the observed inside-out growth as seen from the evolution of the stellar mass surface density profiles of passive field galaxies over redshift (e.g. van Dokkum et al., 2010; Patel et al., 2013). Nevertheless, traditionally this type of merger activity is believed to be suppressed in virialized clusters because of the high velocity dispersion, resulting in high relative velocities between cluster members (e.g. Conroy et al., 2007; Lotz et al., 2013). The exception being mergers of satellite galaxies onto the BCG due to dynamical friction (e.g. Burke & Collins, 2013; Burke et al., 2015), which contribute to the mass growth of

BCG and the intracluster light (ICL). On the other hand, merger events are thought to be very common in galaxy groups where the velocity dispersion is lower, or when the cluster is still assembling (see discussion in e.g. Lotz et al., 2013; Newman et al., 2014).

Despite the suppression of galaxy merging activity in clusters based on relative velocity arguments, it is clear that clusters themselves and their associated dark matter halos continue to grow by accreting galaxy groups. It is possible that some accretion can still happen to the cluster galaxy population during infall of these group-scale structures. Simulations of mergers with cluster mass halos have shown that the accreted mass resides mainly in the satellite galaxies and the ICL, but only mildly in the BCG (e.g. White et al., 2007b; Brown et al., 2008). Recent simulations also demonstrate that the size of clusters members can grow significantly via major and minor mergers and the frequency of mergers is sufficient to explain the observed size growth in clusters since $z \sim 2$ (Laporte et al., 2013). In addition, the observed merger rate in the cluster galaxy population, excluding the BCG, is poorly constrained. If this is possible, this kind of gradual mass growth is able to explain at the same time the evolution of both size and colour gradient in clusters.

If we take the size evolution into account and assume the mass growth takes place predominately at the outskirts, the stellar population we considered here in the colour gradient ($a < 3.5a_e$) will correspond to the central population at $R < 1.5 - 2R_{e-circ}$ in local cluster galaxies. If the evolution is primarily merger or accretion driven as we suggest above, one would expect that the outer stellar population depends on past merger activity.

Interestingly, there has been some evidence indicating changes in stellar population properties at the outer region of local massive passive cluster galaxies (e.g. NGC 4889 in Coma cluster Coccato et al., 2010) as well as in field ellipticals (e.g. Pu et al., 2010). More recent studies have extended the age and metallicity measurements to large radii ($\sim 8 - 10R_e$, for example in La Barbera et al. 2012) and revealed that the outer age or metallicity gradients at $\gtrsim 1 - 2R_e$ are distinct from those in the inner region (e.g. Greene et al., 2013; Pastorello et al., 2014; Raskutti et al., 2014). These changes in stellar population gradients are commonly interpreted to be result of mergers. Nevertheless, these changes can also come from recent quenched galaxies that underwent minor mergers before infalling to the cluster. One way to address this issue is to construct a local sample that can be descendants of galaxies at high redshift (i.e. a progenitor biased corrected sample) and look at the stellar population gradients at the outskirt.

5.4 Formation histories of passive galaxies in KCS

Does the existence of strong age gradients in high-redshift passive cluster galaxies give hints on their past formation histories, or how they are quenched in the first place? In this section we compare our findings with the results and predictions from various simulations in the literature.

Wellons et al. (2015) studied the formation of massive, compact galaxies at $z = 2$ in the Illustris simulation, a set of cosmological simulations which traces the formation and evolution of structure in the Universe from $z = 127$ to $z = 0$. The Illustris simulation

includes not only dark matter but also detailed treatment of gas, and includes various gas cooling, star formation and feedback mechanisms that are very important to galaxy formation. Combining the large volume (a box of comoving size of 106.5 Mpc^3) and high resolution (each baryonic resolution element with mass $\sim 10^6 M_\odot$), Illustris is able to provide a statistical sample of resolved galaxies to study the structural evolution of the galaxy population at high redshift.

By tracing the formation of a sample of 14 massive and compact galaxies at $z = 2$ ($\log(M_*/M_\odot) \geq 11.0$ and stellar half-mass radii $< 2 \text{ kpc}$), Wellons et al. (2015) proposed two primary mechanisms that these compact galaxies are produced, central starbursts and early formation. The ‘central starburst’ galaxies grow and gain their stellar mass rapidly during an episode of intense star formation at $z \sim 2.5$ after experiencing a gas-rich major merger. The size of the galaxies reduces by a large amount in the process, as the tidal torques from the merger drives cold gas to the centre of the galaxies, inducing star formation at their core (see also the simulations of merger remnants by, e.g. Wuyts et al., 2010). This results in a compact merger remnant that resembles in both the mass and compactness of the observed galaxies at $z = 2$. On the other hand, the ‘early formation’ galaxies did not experience a violent merger event. By contrast they are at the massive end of the galaxy population at very high redshift ($z \sim 4$), having nearly all the stellar mass formed already by then. These galaxies then fell off the star-forming main sequence because of gas depletion and stellar feedback and quenched by thermal quasar-mode feedback from the SMBH while the accretion rate was still high. Radio-mode AGN feedback then inhibits further gas accretion onto the galaxies and hence maintains their low SFR (Sijacki et al., 2007, 2015).

One way to distinguish observationally between whether a passive galaxy was a starburst major merger remnant or was formed and quenched early is to examine the age gradient of the galaxy, as suggested by Wellons et al. (2015). For the merger remnant galaxies, since it experiences a relatively recent central starburst event, the age of the core of the galaxy tend to be younger than the other part of the galaxy (i.e. positive age gradients). Those formed early, on the other hand, tends to have older stellar population at the core compared to the outer part (i.e. negative age gradients). Note that minor mergers that accrete mass predominately at the outer region can further steepen the age gradients.

The absence of strong positive age gradients in the galaxies in KCS favours the early formation mechanism over the central starbursts scenario. Among the 61 galaxies (in case III) that we can derive a physical age gradient, only 7 out of 61 ($\sim 11\%$) shows a positive age gradient ($\nabla_{age} \geq 0$). This might suggest the majority of KCS cluster galaxies are formed and quenched at very high redshift, and evolved passively since then.

One caveat of the above result from the Illustris simulation, as pointed out by Wellons et al. (2015), is the effect of the Plummer-equivalent gravitational softening employed in the simulation. This type of softening is usually employed in simulations to prevent the gravitational interactions between particles become arbitrarily large when they are at small spatial separations (see, e.g. Iannuzzi & Dolag, 2011). One drawback of the softening is that it will affect the mass profiles of these galaxies on small scales ($\sim 0.5 \text{ kpc}$, Wellons et al., 2015), which may have a subsequent effect on the gradients. As a result, the softening

renders a quantitative comparison between our observed values of the gradients to those from the simulation impossible.

5.4.1 Is Monolithic collapse still viable?

Traditional monolithic models predict very high metallicity gradients in passive galaxies, around $\nabla_Z \sim -0.5$, and a flat if not slightly positive age gradients (e.g. Larson, 1974; Carlberg, 1984). In local galaxies, only a small population of elliptical galaxies processes such a steep metallicity gradient (Spolaor et al., 2009; Kim & Im, 2013).

The fact that we find that on average a negative age gradient is necessary to explain the evolution of the colour gradient is inconsistent with the monolithic collapse scenario. This conclusion is independent of the metallicity gradient we assumed; in case III we assume the metallicity gradient to be $\nabla_Z = -0.2$ as observed in local passive galaxies, using a steeper metallicity gradient would not work. For example, if we assume the metallicity gradient to be $\nabla_Z = -0.5$, while the $(U - R)$ colour gradient at redshift 1.39 is still in reasonable agreement with the observed value, the evolved gradient is too steep (i.e. insufficient evolution) compared to the observed value at redshift 0.

Recently there has been attempts to revise the monolithic model by incorporating more physical processes and mechanisms into the simulations, such as mergers and stellar feedback, which successfully reproduce the observations (e.g. Kobayashi, 2004; Pipino et al., 2008). With semi-cosmological initial conditions, these revised monolithic models are able to match the age gradients and metallicity gradients observed in local passive galaxies.

We compare our observed $z_{850} - H_{160}$ colour gradients of the three KCS clusters with simulations based on one of the revised versions of the monolithic model by Pipino et al. (2008, 2010). Tortora et al. (2013) computed the colour gradients from the Pipino et al. (2010) simulations using BC03 SSP models, for which we can directly use for the comparison. The Pipino et al. (2010) simulation comprises four different models (E1, E2, E3, E4) with different initial conditions and parameters. For example, the models differ in the initial mass of the dark matter halo (with E4 having the largest mass) and the star formation efficiencies (E2 and E4 have high efficiencies, where E1 and E3 have low efficiencies). The interested reader can refer to Pipino et al. (2010) and Tortora et al. (2013) for details.

Among the four models presented in their work, we find that there is no single model that can match both the observed colour gradients at the cluster redshifts and $z = 0$. Our observed median colour gradient seems to be in reasonable agreement with models that predict steep metallicity gradient (E2, $\nabla_Z \sim -0.35$ and E4, $\nabla_Z \sim -0.45$) and nearly flat age gradient at $z = 0$. The comparison with the colour gradients in Gargiulo et al. (2011, 2012) at redshift $1 < z < 2$ also gives a similar result. However, the local colour gradient at $z \sim 0$, as well as the $F606W - F850LP$ gradients of high-redshift galaxies in Gargiulo et al. (2011) favours the other two models (E1, E3) instead, so there is not a single model that can explain the evolution of colour gradients. Hence, our result cannot be reproduced by the revised monolithic collapse model.

5.5 Environmental dependence of photometric properties of massive passive galaxies at high redshift

In this section, we focus on comparing the structural properties of the red sequence galaxies in the KCS clusters to a sample of field passive galaxies at similar redshifts. As we discussed in Section 1.4.1, recent works have found that the size distribution of massive passive galaxies in clusters differs from the field at high redshift, although the extent of this effect is still under debate (e.g. Cooper et al., 2012; Zirm et al., 2012; Papovich et al., 2012; Lani et al., 2013; Strazzullo et al., 2013; Jørgensen & Chiboucas, 2013; Delaye et al., 2014). On the other hand, no difference can be seen in different environment in the local universe (e.g. Huertas-Company et al., 2013).

Below we use the sample from Lang et al. (2014) as the field comparison sample. Lang et al. (2014) derived both H_{160} light-weighted sizes and mass-weighted sizes for a mass-selected sample ($\log(M_*/M_\odot) > 10$) spanning a redshift range $0.5 < z < 2.5$ in all the five CANDELS fields. In Section 3.6.2 we have shown that despite the mass-weighted sizes are derived with slightly different methods, our sizes are consistent with those of Lang et al. (2014). We select a subsample of massive passive galaxies from the Lang et al. (2014) sample following the UVJ passive criteria and a mass cut ($\log(M_*/M_\odot) \geq 10.5$) to match the KCS sample (hereafter L14 field sample). We further remove galaxies in Cl 0332-2742 from the L14 field sample to ensure the sample consists of field galaxies. A total of 1273 objects are selected, among them 266 objects are in the redshift range comparable to the three KCS clusters ($1.3 < z < 1.7$).

5.5.1 Size distributions in different environment

We first compare the observed size distributions of passive galaxies in clusters and the field. For the comparison, we use the mass-normalised circularised size ($R_{e-circ,MN}$) as defined by Newman et al. (2012) and Delaye et al. (2014), which is given by:

$$R_{e-circ,MN} = R_{e-circ}/(M_*/10^{11}M_\odot)^\beta \quad (5.3)$$

where β is the slope of the mass-size relation and $R_{e-circ,MN}$ is mass-normalised size at $\log(M_*/M_\odot) = 11.0$. Using $R_{e-circ,MN}$ removes the correlation between stellar mass and size, and hence allow us to compare the size distribution of two samples that do not share identical distribution in stellar mass.

Figure 5.11 shows the mass-normalised size distributions of the three KCS clusters for galaxies with $\log(M_*/M_\odot) \geq 10.5$. Having both light and mass-weighted size of each galaxy, we compute both the light-weighted and mass-weighted mass-normalised size distributions of each clusters using the best-fitted slope (case C) of the mass – size relations in Section 4.3 and 4.5 (see Table 4.2 for the light-weighted slopes and Table 4.3 for the mass-weighted slopes).

It is clear from Figure 5.11 that XMMU J2235-2557 and XMMXCS J2215-1738 have comparable light-weighted mass-normalised size distributions. On the other hand, the size

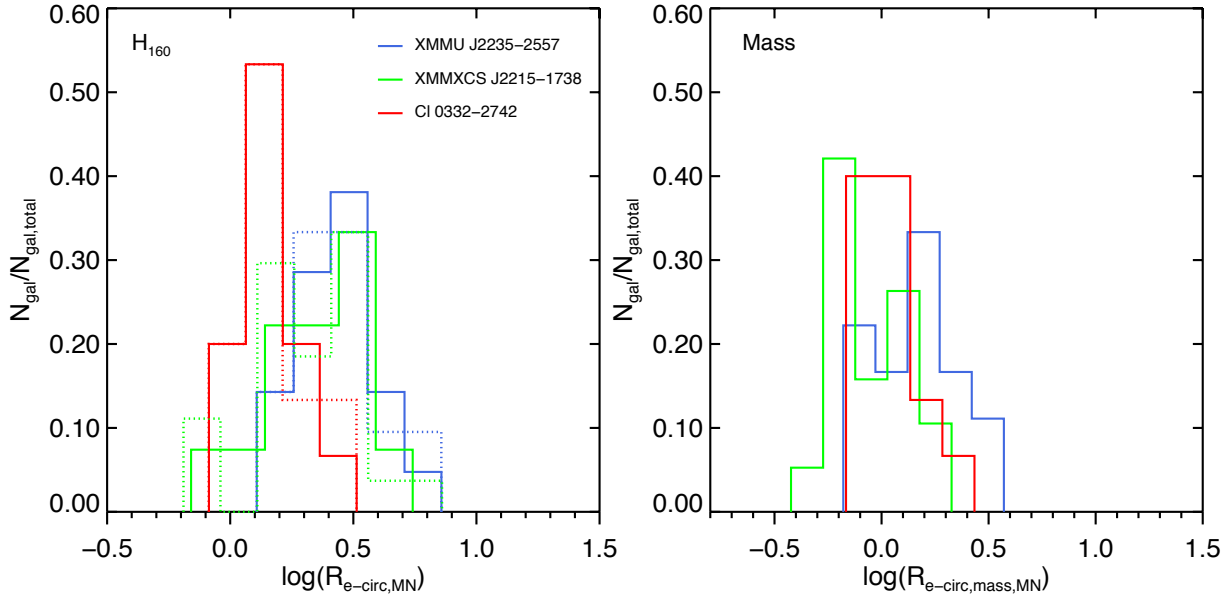


Figure 5.11: Mass-normalised size distributions of the KCS clusters. Left: The light-weighted mass-normalised size distributions. Distribution of XMMU J2235-2557 is shown in blue, the one of XMMXCS J2215-1738 is shown in green and the one of Cl 0332-2742 is shown in red, respectively. The solid histograms are computed with the slope (β) of the fitted light-weighted mass – size relation of each cluster, while the dotted histograms are computed with the slope adopted from van der Wel et al. (2014) for all three clusters ($\beta = 0.76$). Right: The mass-weighted mass-normalised size distributions. The histogram of each cluster is computed with the slope (β) of the fitted mass-weighted mass – size relation respectively.

distribution in Cl 0332-2742 is distinct from the other two clusters. The fact that sizes in Cl 0332-2742 are generally smaller is discussed in Section 4.3 with the mass – size relation at $z = 0$. It is also consistent with the size evolution picture, as Cl 0332-2742 has the highest redshift among the three clusters. We also checked that this difference in the distributions is not due to the different best-fit β that we applied to individual cluster. In the left panel of Figure 5.11 we show also the size distributions computed using the slope of the mass – size relations adopted from van der Wel et al. (2014) ($\beta = 0.76$) as the dotted histograms. The resultant histograms are very similar to the ones from the best-fitted slope. On the right panel of Figure 5.11 we show the mass-weighted mass-normalised size distributions of the three clusters. While we can still see subtle differences between the distributions of the three clusters, the differences between Cl 0332-2742 and XMMU J2235-2557/XMMXCS J2215-1738 seem to be reduced.

We then move to the comparison of the size distributions of the KCS clusters with the field sample. Nevertheless, the disparity between the size distribution of Cl 0332-

2742 and other two clusters can make a cluster - field comparison of the whole redshift range problematic. Hence to better understand both samples, we split the cluster - field comparison into two redshift ranges: XMMU J2235-2557+XMMXCS J2215-1738 with field galaxies at $1.3 < z < 1.5$, and Cl 0332-2742 alone with field galaxies at $1.5 < z < 1.7$. At the end of the section we also show, for completeness, the comparison of the three clusters combined with field galaxies at $1.3 < z < 1.7$.

In order to estimate the mean sizes of the distribution in clusters and the field, we follow Newman et al. (2012) to fit each size distribution with a skew normal distribution, which takes into account the asymmetry in the size distributions:

$$P(\log(R_{e-circ,MN})) = \frac{1}{\omega\pi} e^{-\frac{(\log(R_{e-circ,MN})-\phi)^2}{2\omega^2}} \int_{-\infty}^{s\left(\frac{\log(R_{e-circ,MN})-\phi}{\omega}\right)} e^{-\frac{t^2}{2}} dt \quad (5.4)$$

where the mean of the best-fit size distribution $\overline{\log(R_{e-circ,MN})}$ is given by $\overline{\log(R_{e-circ,MN})} = \phi + \omega(s/\sqrt{1+s^2})\sqrt{2/\pi}$, and s is the ‘shape’ parameter that governs the skewness. The mean of the best-fit skew normal distributions $\overline{\log(R_{e-circ,MN})}$ and the median of the original (not fitted) size distributions $\langle \log(R_{e-circ,MN}) \rangle$ discussed below are given in Table 5.4.

Figure 5.12 shows the comparison of the (combined) mass-normalised size distributions of XMMU J2235-2557 + XMMXCS J2215-1738 with the L14 field sample at $1.3 < z < 1.5$. The light-weighted distributions of the field sample are computed in the same way with the slope from van der Wel et al. (2014) ($\beta = 0.76$). Although this slope is computed with passive galaxies in a wider redshift bin of $1.0 < z < 1.5$, the slope of the light-weighted mass – size relations in the field is found to be an invariant with redshift (van der Wel et al., 2014). Similar to Figure 5.11, we also plot the the size distributions of the clusters computed using this slope in grey.

From Figure 5.12, we find that the peak of the light-weighted size distribution of the two clusters is offset to larger size compared to the field. The median of the clusters is larger than the field, as well as the mean of the best-fit size distribution $\overline{\log(R_{e-circ,MN})}$ (although less prominent). Assuming $\beta = 0.76$ gives a consistent $\overline{\log(R_{e-circ,MN})}$ to the field, although the median of the cluster size distribution is still larger. Contrary to Delaye et al. (2014), we do not see a tail of large-size cluster galaxies in the distribution with respect to the field. This may be due to the small sample that we have (a total of 48 galaxies in XMMU J2235-2557 and XMMXCS J2215-1738) or the fact that our colour-colour selections removes diskly star-forming galaxies, which will predominantly show up as large galaxies on this plot.

On the right panel of Figure 5.12 we show, for the first time, a comparison of the mass-weighted size distribution of clusters and field galaxies. Since there is no available estimate of the slope of the mass-weighted mass – size relations in the field, we assume two different slopes to compute the size distributions: a) the slope of the mass-weighted mass – size relations in the field is identical to the light-weighted one ($\beta = 0.76$) and b) the slope of the mass-weighted mass – size relations in the field is identical to the one in clusters ($\beta = 0.49$, see Section 4.5). The two cases are shown as blue and light green respectively.

It seems that when considering the mass-weighted sizes, the differences between the size distributions in clusters and the field decrease, independent of the β we assumed. While there may still be some offset in the two populations depends on the assumed β , the median of the mass-weighted size distribution of the two clusters is much closer to the one in the field compared to the abovementioned light-weighted comparison. The mean of the best-fit size distribution also suggests the same. As an additional check, we use the Kolmogorov-Smirnov (KS) test to evaluate whether the size distributions in clusters and field are different. The results are given in Table 5.5. While in some cases we see mild significance for the light-weighted size distributions, the p -values derived from the KS test are never low enough to show that the size distributions in clusters and the field are clearly distinct. The p -value for the light-weighted size distributions of the two clusters and the field is 0.07 ($p \simeq 0.04$ for $\beta = 0.76$), while the p -value for the mass-weighted size distributions is 0.54 ($p \simeq 0.51$ for $\beta = 0.49$).

We then turn to the comparison of the higher redshift cluster, Cl 0332-2742, with the L14 field sample $1.5 < z < 1.7$ in Figure 5.13. We do not fit a skew normal distribution for Cl 0332-2742 since the sample has only 15 galaxies in a relatively small range of size. From the histograms and the median of the size distributions, passive galaxies in Cl 0332-2742 have comparable (if not on average smaller) sizes compared to the field galaxies at a similar redshift. This is true for both light-weighted and mass-weighted sizes. The median of the mass-weighted size distribution of Cl 0332-2742 shows more resemblance to the field distribution than the light-weighted one. The Kolmogorov-Smirnov (KS) test presents small values for the light-weighted distributions of Cl 0332-2742 and the field ($p \simeq 0.03$), but not for the mass-weighted size distributions ($p \simeq 0.13$).

For completeness, in Figure 5.14 we show the comparison of the combined size distribution of the three clusters with the L14 field sample at $1.3 < z < 1.7$. The mean of the best-fit skew normal distributions and the median of the original (not fitted) combined size distributions are also given in Table 5.4.

5.5.2 Environmental dependence of the ratio of mass-weighted to light-weighted sizes

After comparing the light-weighted and mass-weighted size distributions separately, in this section we compare the ratio of the mass-weighted to light-weighted sizes in clusters (i.e. size ratio) with the field. As we have demonstrated and discussed in Section 4.6 and Section 4.7, the size ratio is an useful probe of the M_*/L gradient within the galaxies.

Figure 5.15 shows the comparison of the size ratio for galaxies with $\log(M_*/M_\odot) \geq 10.5$ in three KCS clusters with the L14 field sample at various redshift. To compare the size ratio at different redshift we have converted the H_{160} sizes of the L14 field sample at different redshift into rest-frame r -band sizes, assuming the wavelength dependence of Kelvin et al. (2012) derived from local passive galaxies. In Section 4.2, we have demonstrated that the wavelength dependence at high-redshift in clusters is consistent with Kelvin et al. (2012), hence this conversion should be reasonable for the average galaxy population. Note that

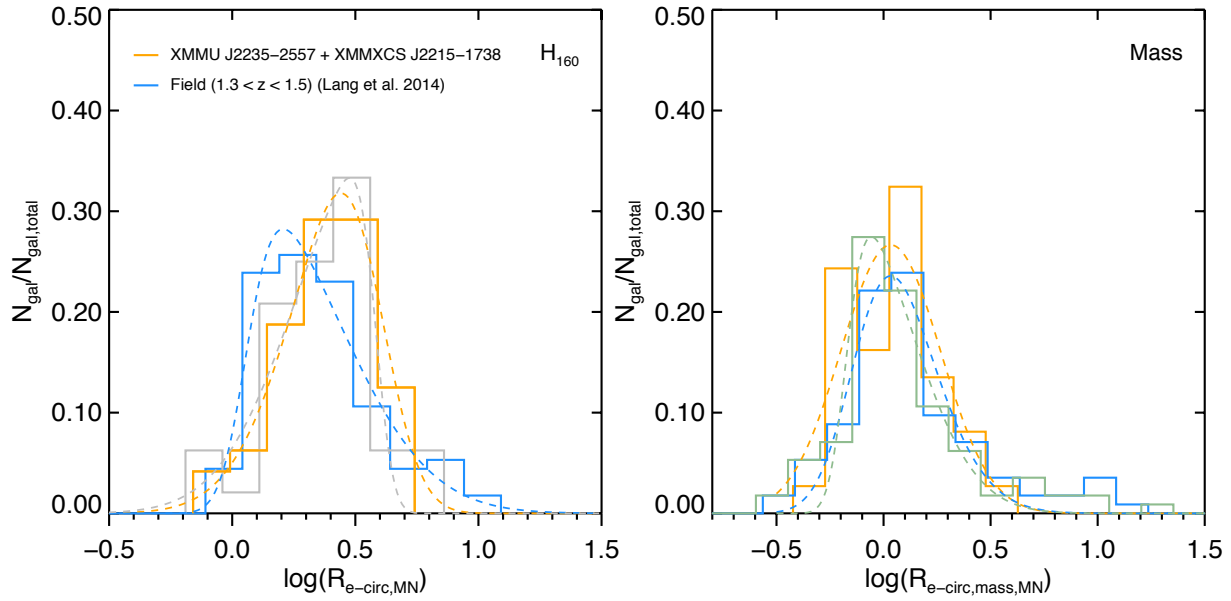


Figure 5.12: Comparison of the mass-normalised size distributions of XMMU J2235-2557 and XMMXCS J2215-1738 with the field. Left: The light-weighted mass-normalised size distributions. The combined size distribution of XMMU J2235-2557 + XMMXCS J2215-1738 is shown in orange. The size distribution of the L14 field sample with a redshift range of $1.3 < z < 1.5$ is shown in blue. The grey histogram is the size distribution of XMMU J2235-2557 + XMMXCS J2215-1738 computed with the slope adopted from van der Wel et al. (2014). Right: The mass-weighted mass-normalised size distributions. The blue histogram shows the size distribution of the L14 field sample computed with an assumed slope of $\beta = 0.76$, identical to the light-weighted mass – size relations. The light green histogram shows the size distribution with an assumed slope identical to the mass-weighted mass – size relations of the clusters ($\beta = 0.49$). The coloured dashed lines show the best-fit skew normal distributions for each size distribution respectively.

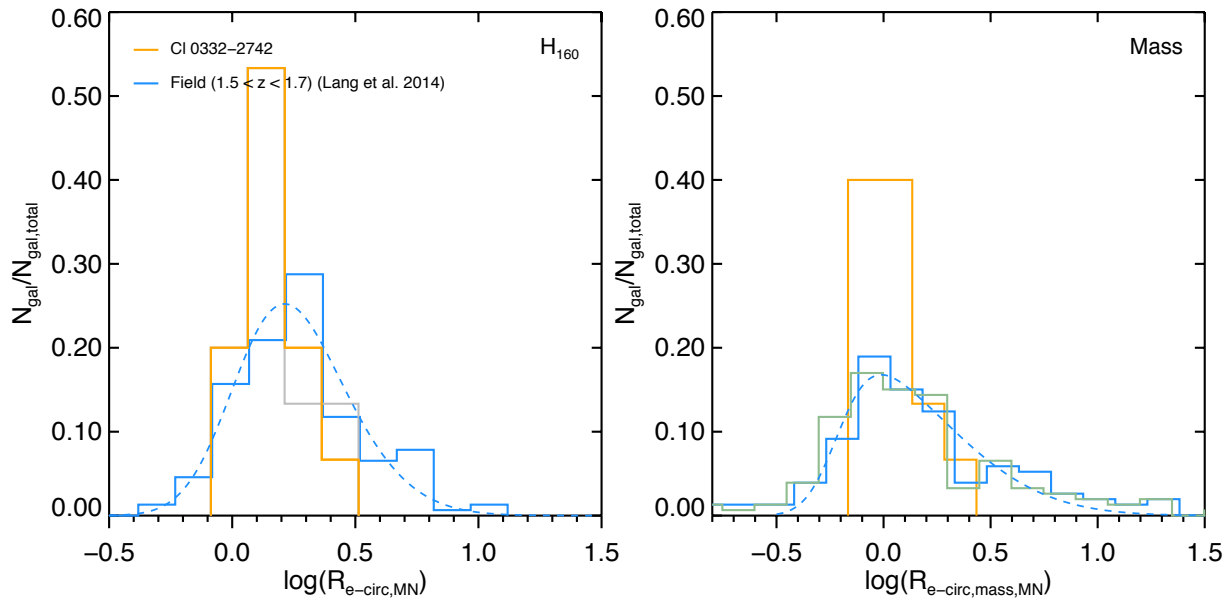


Figure 5.13: Comparison of the mass-normalised size distributions of Cl 0332-2742 with the field. Left: The light-weighted mass-normalised size distributions. The size distribution of Cl 0332-2742 is shown in orange. The size distribution of the L14 field sample with a redshift range of $1.5 < z < 1.7$ is shown in blue. The grey histogram is the size distribution of Cl 0332-2742 computed with the slope adopted from van der Wel et al. (2014). Right: The mass-weighted mass-normalised size distributions. The blue histogram shows the size distribution of the L14 field sample computed with an assumed slope of $\beta = 0.76$, identical to the light-weighted mass – size relations. The light green histogram shows the size distribution with an assumed slope identical to the mass-weighted mass – size relations of the clusters ($\beta = 0.49$). The coloured dashed lines show the best-fit skew normal distributions for each size distribution respectively.

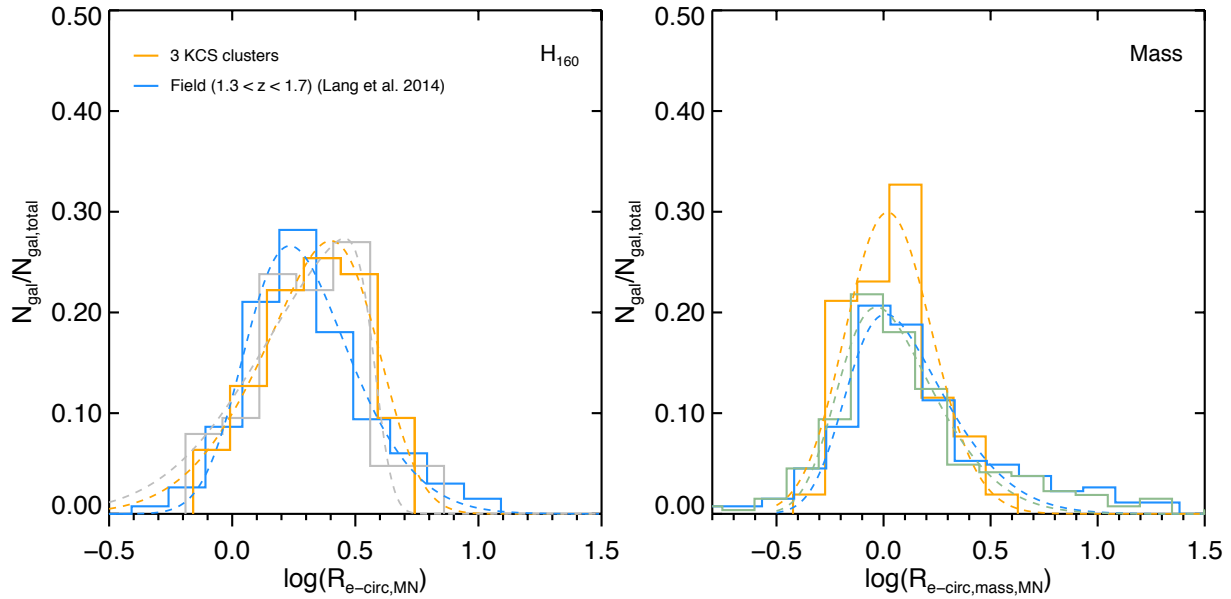


Figure 5.14: Comparison of the mass-normalised size distributions of the three KCS clusters with the field. Left: The light-weighted mass-normalised size distributions. The combined size distribution of the three KCS clusters is shown in orange. The size distribution of the L14 field sample with a redshift range of $1.3 < z < 1.5$ is shown in blue. The grey histogram is the size distribution of the clusters computed with the slope adopted from van der Wel et al. (2014). Right: The mass-weighted mass-normalised size distributions. The light green histogram is the size distribution of the L14 field sample computed with an assumed slope ($\beta = 0.49$), identical to the mass-weighted mass – size relations of the clusters. The coloured dashed lines show the best-fit skew normal distributions for each size distribution respectively.

Table 5.4: The mean (of the best-fit skew normal distributions) and the median of the mass-normalised size distributions of the KCS clusters and the L14 field sample

Light-weighted size distributions				
Sample	$\overline{\log(R_{e-circ,MN})}^*$	$\langle \log(R_{e-circ,MN}) \rangle$	$N_{gal,total}$	
XMMU J2235 + XCS J2215	0.388 ± 0.060	0.399 ± 0.036	48	
XMMU J2235 + XCS J2215 ($\beta = 0.76$)	0.336 ± 0.052	0.401 ± 0.036	48	
L14 field ($1.3 < z < 1.5$)	0.344 ± 0.035	0.305 ± 0.027	113	
Cl 0332-2742	-	0.152 ± 0.051	15	
Cl 0332-2742 ($\beta = 0.76$)	-	0.161 ± 0.052	15	
L14 field ($1.5 < z < 1.7$)	0.256 ± 0.023	0.236 ± 0.026	153	
3 KCS clusters	0.309 ± 0.064	0.348 ± 0.035	63	
3 KCS clusters ($\beta = 0.76$)	0.243 ± 0.087	0.359 ± 0.035	63	
L14 field ($1.3 < z < 1.7$)	0.299 ± 0.052	0.271 ± 0.019	266	

Mass-weighted size distributions				
Sample	$\overline{\log(R_{e-circ,MN})}$	$\langle \log(R_{e-circ,MN}) \rangle$	$N_{gal,total}$	
XMMU J2235 + XCS J2215	0.032 ± 0.069	0.081 ± 0.045	37	
L14 field ($1.3 < z < 1.5$) ($\beta = 0.76$)	0.077 ± 0.043	0.056 ± 0.036	113	
L14 field ($1.3 < z < 1.5$) ($\beta = 0.49$)	0.057 ± 0.030	0.007 ± 0.033	113	
Cl 0332-2742	-	0.023 ± 0.044	15	
L14 field ($1.5 < z < 1.7$) ($\beta = 0.76$)	0.155 ± 0.045	0.050 ± 0.051	153	
L14 field ($1.5 < z < 1.7$) ($\beta = 0.49$)	0.104 ± 0.031	0.019 ± 0.047	153	
3 KCS clusters	0.030 ± 0.052	0.071 ± 0.034	52	
L14 field ($1.3 < z < 1.7$) ($\beta = 0.76$)	0.108 ± 0.030	0.054 ± 0.030	266	
L14 field ($1.3 < z < 1.7$) ($\beta = 0.49$)	0.061 ± 0.034	0.012 ± 0.028	266	

*The uncertainties quoted for $\overline{\log(R_{e-circ,MN})}$ are computed by bootstrapping. We repeat the fitting procedure for 1000 times each with a randomly drawn subset of the sample, and the uncertainty is given by the standard deviation of these 1000 measurements. The uncertainties of the median are estimated as $1.253\sigma/\sqrt{N_{gal,total}}$, where σ is the standard deviation of the size distributions.

Table 5.5: The results of the Kolmogorov-Smirnov test on the mass-normalised size distributions of the KCS clusters and the L14 field sample

Light-weighted size distributions			
Sample		KS	p
XMMU J2235 + XCS J2215 vs. L14 field ($1.3 < z < 1.5$)		0.22	0.07
XMMU J2235 + XCS J2215 ($\beta = 0.76$) vs. L14 field ($1.3 < z < 1.5$)		0.24	0.04
Cl 0332-2742 vs. L14 field ($1.5 < z < 1.7$)		0.38	0.03
Cl 0332-2742 ($\beta = 0.76$) vs. L14 field ($1.5 < z < 1.7$)		0.32	0.09
3 KCS clusters vs. L14 field ($1.3 < z < 1.7$)		0.18	0.08
3 KCS clusters ($\beta = 0.76$) vs. L14 field ($1.3 < z < 1.7$)		0.20	0.03
Mass-weighted size distributions			
Sample		KS	p
XMMU J2235 + XCS J2215 vs. L14 field ($1.3 < z < 1.5$) ($\beta = 0.76$)		0.15	0.54
XMMU J2235 + XCS J2215 vs. L14 field ($1.3 < z < 1.5$) ($\beta = 0.49$)		0.15	0.51
Cl 0332-2742 vs. L14 field ($1.5 < z < 1.7$) ($\beta = 0.76$)		0.30	0.13
Cl 0332-2742 vs. L14 field ($1.5 < z < 1.7$) ($\beta = 0.49$)		0.30	0.14
3 KCS clusters vs. L14 field ($1.3 < z < 1.7$) ($\beta = 0.76$)		0.18	0.10
3 KCS clusters vs. L14 field ($1.3 < z < 1.7$) ($\beta = 0.49$)		0.19	0.08

the H_{160} size at $z \sim 1.5$ is at rest-frame r -band, hence this conversion only affects the galaxies at lower or higher redshifts. Assuming a slightly different wavelength dependence will not change the result of this comparison with KCS. Similar to Section 4.7, we apply a progenitor bias correction to the L14 field sample by removing galaxies with ages that are too young to be descendants of passive galaxies at $z = 1.39$. The ages of the L14 field sample are taken from the 3D-HST public catalog (Skelton et al., 2014) and are derived using the FAST code (Kriek et al., 2009). We then binned the galaxies with a redshift bin of 0.25.

We plot also the size ratio from Szomoru et al. (2013). We have converted their light-weighted size in rest-frame g -band into rest-frame r -band, again assuming the wavelength dependence of Kelvin et al. (2012). Besides the median size ratio of the three KCS clusters, we also plot the median size ratio of the progenitor bias SPIDER cluster sample (see Section 4.7 for details) at $z = 0$ for comparison. It is clear from Figure 5.15 that the size ratio in XMMU J2235-2557 and XMMXCS J2215-1738 is offset from the one from SPIDER sample (or from the redshift zero point of Szomoru et al. 2013), while Cl 0332-2742 shows a very small offset as already discussed in Section 4.7.

Before we compare the clusters to the field, we first address the discrepancy between the size ratio in Szomoru et al. (2013) and the L14 field sample. While the size ratios of the two sample are consistent with each other at high redshift ($z > 1.2$), they diverge at low redshift. Since the Szomoru et al. (2013) sample is selected in the GOODS-S field, it allows us to crossmatch the two catalogues and search for the same objects in the L14 field sample to better understand the differences. The results are shown in Figure 5.16. The consistent r -band sizes from both catalogue (top right panel) suggest our wavelength dependence conversion is generally correct, although slight bias can be seen at low redshift ($z < 0.8$) where the conversion factor is large (bottom left panel). The discrepancy of the size ratio originates from the mass-weighted sizes: the mass-weighted sizes in Szomoru et al. (2013) are on average $\sim 40\%$ larger than those derived by L14 for the same galaxies. The difference is smaller at high redshift ($z > 1.2$) compared to low redshift ($z < 1.2$). It is however unclear to us why this difference exists, one possible explanation is on the methodology they used. Szomoru et al. (2013) derived the mass-weighted size by integrating the 1D mass profiles derived from 1D colour profiles, while L14 derived the sizes with 2D GALFIT Sérsic fitting to the mass-maps. Different consideration of the ‘background’ mass’ (from background sky level) and the neighbouring galaxies may affect the derivation of the 1D mass-weighted sizes (see Section 3.6.1 for a discussion on derivation of mass-weighted sizes in 1D vs. 2D).

Despite the size discrepancy between the field samples, we find that the median size ratios in XMMU J2235-2557 and XMMXCS J2215-1738 are smaller than both field samples at similar redshifts. The offset of the two clusters from the L14 field sample is -0.074 ± 0.036 and $\sim -0.157 \pm 0.047$ dex respectively. The offset of the two clusters from the Szomoru et al. (2013) sample is larger. The median size ratio in Cl 0332-2742, on the other hand, is comparable to (if not larger than) the field galaxies (0.064 ± 0.037 dex to L14). This implies that M_*/L gradient in the two lower redshift clusters are steeper compared to the field, while galaxies in Cl 0332-2742 have more or less the same M_*/L gradient as the field

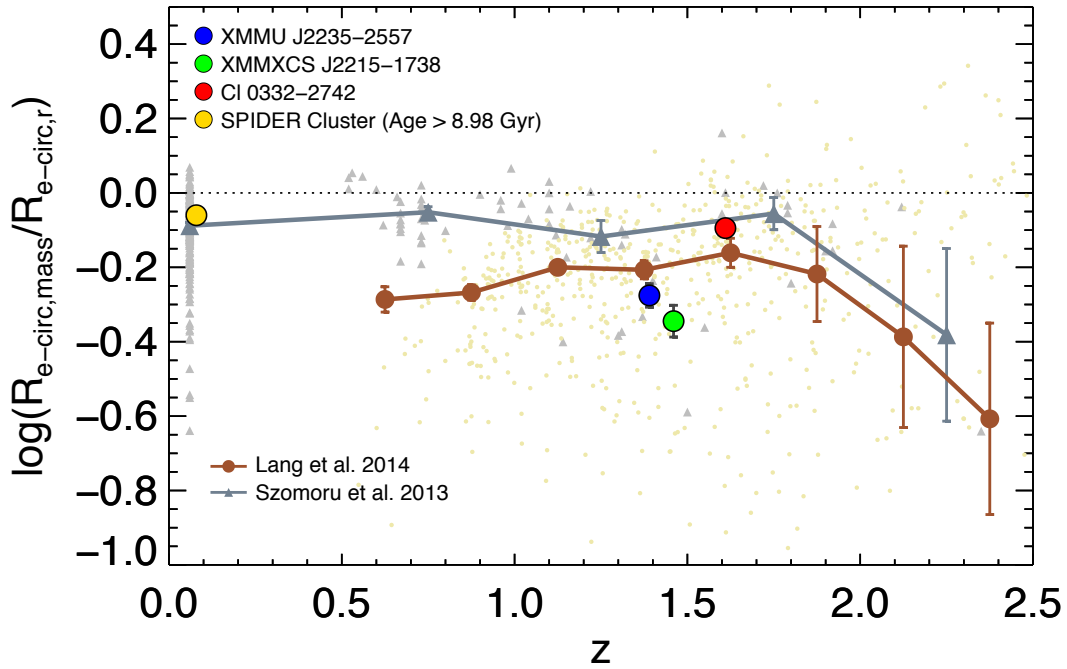


Figure 5.15: Comparison of the size ratio of the three KCS clusters with the field. The median size ratios of XMMU J2235-2557, XMMXCS J2215-1738 and Cl 0332-2742 are shown as red, blue and green circles respectively. The orange circle corresponds to the median size ratio of the progenitor bias corrected SPIDER cluster sample at $z \sim 0$. The brown circles and line show the binned median size ratio of the progenitor bias corrected L14 field sample across redshift in redshift bin of 0.2, while the light brown dots correspond to individual galaxies in the sample. The grey triangles and line show the binned median size ratio of the Szomoru et al. (2013) field sample across redshift in redshift bin of 0.5, while the light grey triangles represent individual galaxies in their sample. The error bars show the uncertainty of the median in each bin.

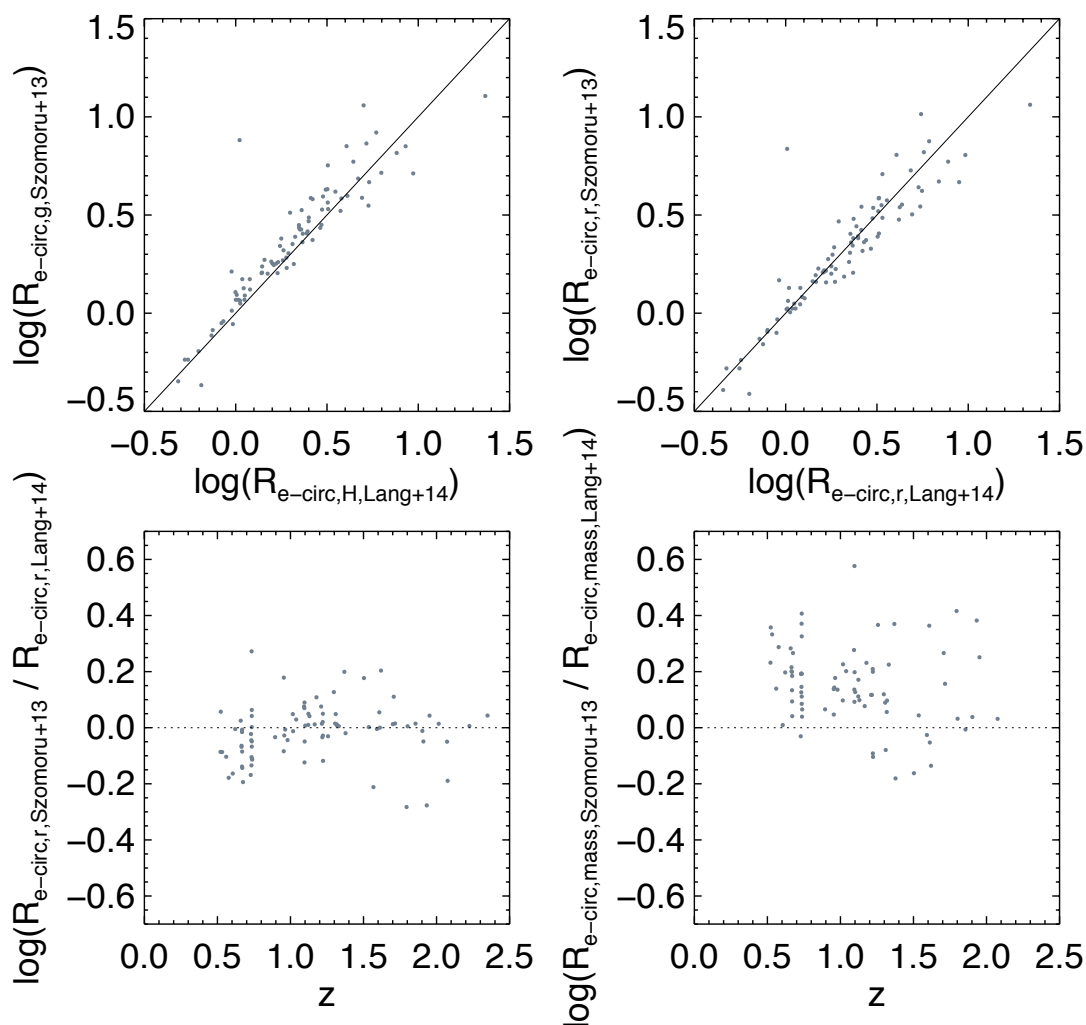


Figure 5.16: Comparison of the structural properties of the intersecting population of the Szomoru et al. (2013) and Lang et al. (2014) sample. Top left: Comparison of the light-weighted sizes (rest-frame g -band vs. H_{160}). Top right: Comparison of the light-weighted sizes in rest-frame r -band, converted using the wavelength dependence of Kelvin et al. (2012). Bottom left: The difference of light-weighted sizes between the two catalogues with redshift. Bottom right: The difference of mass-weighted sizes between the two catalogues with redshift.

galaxies.

Hence, from Figure 5.15 it seems that the effect of the environment is to steepen the M_*/L gradient in passive galaxies. If this is true, why does Cl 0332-2742 behave differently from the other two clusters? One plausible explanation stems from the dynamical state of the cluster, as we have first suggested in Section 4.7. Contrary to the other two relatively well-developed clusters, Cl 0332-2742 is a structure with several groups still in their assembly phase. The fact that Cl 0332-2742 is similar to the field indicates that it may still be too young (in the sense of cluster development) to reach the epoch of enhancement of the M_*/L gradient. If this is the reason, this phase of M_*/L gradient enhancement in cluster galaxies must happen during (or shortly after) cluster assembly.

5.5.3 Effect of environment on the evolution of passive galaxies

In the last section we showed that galaxies at high density environment have smaller size ratio, and hence steeper M_*/L gradient, than those in the field. The fact that Cl 0332-2742 shows stronger resemblance to the field plausibly suggests that the underlying environmental processes responsible is closely related to the state of the cluster.

Combined with our findings in Section 5.2 that the colour gradients (and hence M_*/L gradients) in high redshift cluster galaxies are due to age gradients, the most straightforward candidate that can explain the observed effect of environment is, again, mergers. Merger events are thought to be common among galaxy groups where the velocity dispersion is low, or when the cluster is still assembling. During the time period of cluster assembly, the cluster members experience an enhanced rate of mergers and galaxy-galaxy encounters. As the development of the cluster continues, the virialization results in a decreased merger rate (see, e.g. Lotz et al., 2013; Delaye et al., 2014; Newman et al., 2014). This coincides with the expected time period when the environmental process occurs.

The effect of this epoch of enhanced merger rate on galaxy sizes has been discussed in previous works comparing sizes between clusters and the field (e.g. Cooper et al., 2012; Zirm et al., 2012; Lani et al., 2013; Strazzullo et al., 2013; Jørgensen & Chiboucas, 2013; Delaye et al., 2014), which they referred to as an accelerated size evolution in high-density environments. In this picture, the size of the passive galaxies in clusters are ‘enhanced’ to larger sizes than those in the field due to mergers, resulting in an offset between the two populations at high redshift. As the clusters virialize the merger rate decreases, the sizes of the field galaxies evolve in a relatively faster pace than those in clusters. As a result, the field galaxies eventually catch up and match the cluster size distributions in the local universe, where there is no offset between the two (e.g. Huertas-Company et al., 2013; Cappellari, 2013).

The fact that we see a smaller difference between the mass-weighted size distributions of clusters and the field compare to the light-weighted ones, provides information about the type of mergers responsible at this epoch. Since the light-weighted size of the cluster galaxies is affected to a larger extent than the mass-weighted size, it suggests that major merger is not the dominant type of merger during cluster assembly. Minor dry merger is a more likely option as it can reproduce both the size distribution differences in clusters and

the field, as well as the age gradients in cluster galaxies (see the discussion in Section 5.3).

Since this epoch of enhanced merger rate occurs when the cluster is under assembly, the effect of environment on the size ratio will not translate directly to a monotonic trend in redshift. The environmental effect would be largest in clusters that just completed their assembly phase. Hence, to maximise the observed difference between clusters and field, the best approach would be to select a sample of clusters that are structurally bounded to be a single structure but yet not fully virialized, similar to XMMXCS J2215-1738. Young (proto-) clusters (like Cl 0332-2742) that have not yet undergone their assembly phase will behave similarly to the field galaxies. While in old virialized clusters, the difference with the field population will be less prominent than clusters that just assembled, due to continuous mergers in both environment, as well as the higher merger rate in the field. Although the two KCS clusters reside at roughly the same redshift $z \sim 1.4$, whether this type of cluster preferentially resides at a certain redshift is unclear, as there are clusters at even higher redshift that appear as evolved, virialized clusters with a large quiescent population (e.g. JKCS 041 in KCS, Newman et al., 2014; Andreon et al., 2014). The analysis of JKCS 041 will be part of the future work (see Section 6.2 for a description of the future work).

In summary, we suggest that minor dry merger during cluster assembly is the underlying physical process that drives the observed difference in size ratio between clusters and the field. The rate of mergers is known to be enhanced during the time period of cluster assembly. Hence, it can be a plausible candidate to explain the observed properties of the galaxies (i.e. M_*/L gradients and size distributions) and it also coincides with the time period when the environmental process is believed to occur.

Chapter 6

Conclusions and future work

Over the last decade, with the advent of new near-IR instrumentation, galaxy properties have been explored in increasing detail to redshift $z \sim 2$. This enabled studies on the progenitors of the local galaxy population, allowing us to constrain their formation and evolution, as well as to discern the relative importance of different physical processes. Despite the recent progress, a full characterisation of the galaxy properties yet remains to be performed. In particular, one of the essential questions that remains unresolved is the role of environment on the evolution of passive galaxies.

In this thesis we have analysed the structural properties and colour gradients of a sample of passive galaxies in three high redshift clusters, XMMU J2235-2557, XMMXCS J2215-1738 and Cl 0332-2742 at redshift $z \sim 1.39, 1.46, 1.61$, respectively. These three clusters are part of the selected sample of the KMOS Cluster survey (KCS, Davies et al., 2015, Davies, Bender et al., 2016 in prep). The goal is to study the properties of these high redshift cluster galaxies and compare them with the field population, to dissect the effect of environment and constrain the formation and evolution of this population.

In this work we have utilised a set of optical (ACS) and near infrared (WFC3) imaging data of the KCS clusters from the *Hubble Space Telescope*. The passive galaxy sample is selected using the red sequence of each cluster. We have applied an additional colour-colour selection to remove contamination from dusty star forming galaxies and interlopers, such as foreground or background galaxies.

We have derived structural parameters, resolved stellar mass distributions and colour gradients for this sample of passive galaxies. Light-weighted structural parameters are derived through two-dimensional single Sérsic fitting. The colour gradients are derived from fitting of their 1D $z_{850} - H_{160}$ colour profiles. In addition, improving on existing methods, we have also derived resolved stellar mass surface density maps for individual galaxies with an empirical M_*/L -colour relation and the z_{850} and H_{160} images. Mass-weighted structural parameters are then derived from the resolved stellar mass surface density map, which is a more accurate description of the underlying stellar mass distribution of a galaxy than the light-weighted structural parameters. We have carefully assessed the quality of the derived properties and quantified the uncertainties in our measurements using a large sample of simulated galaxies. This leads to a comprehensive catalogue of the photometric

and structural properties of passive galaxies in the three clusters (see Table 3.1, 3.2 and 3.3).

In Section 6.1, we summarise the results from Chapter 4 and Chapter 5 of this thesis. We then discuss ongoing and possible future work with the data provided by the KMOS Cluster survey and consider the future prospects in the field.

6.1 Summary of this thesis

6.1.1 Structural parameters and Mass-size relations

In Chapter 4, we have presented the analysis of both light-weighted and mass-weighted structural parameters of the passive galaxies and the relation between them and stellar mass. We then focus on the ratio of mass-weighted to light-weighted size and discuss the dependence of this ratio on galaxy properties and the evolution of this ratio with redshift. We find the following:

- From our multi-band light-weighted structural parameter measurements, the passive galaxies in the three KCS clusters show an average reduction of $\sim 20\%$ in size from rest-frame U to rest-frame R band, consistent with the wavelength dependence found in local passive galaxies.
- The H_{160} band sizes of the KCS clusters are on average smaller than that expected from the local mass-size relation by Bernardi et al. (2012) at the same rest-wavelength. The sizes are on average $\sim 42\%$, $\sim 55\%$ and $\sim 69\%$ smaller than local passive galaxies of the same mass for XMMU J2235-2557, XMMXCS J2215-1738 and Cl 0332-2742 respectively. In the extreme cases the galaxies can be $\sim 80\%$ smaller than their local counterparts.
- The slopes β of the stellar mass – light weighted size relation of the three KCS clusters are consistent with each other within the uncertainties. The derived slope for the full sample $\beta = 0.79 \pm 0.14$ as well as the values for individual clusters are consistent with the values derived from the field population at a similar redshift range (van der Wel et al., 2014).
- Comparing the mass-weighted sizes to the light-weighted sizes of the passive galaxies, we find that the mass-weighted sizes are smaller. However, the degree varies between clusters. For XMMU J2235-2557, the mass-weighted sizes are $\sim 47\%$ smaller than the light-weighted sizes, with a median $\langle \log(R_{e-circ,mass}/R_{e-circ}) \rangle = -0.28$. Galaxies in XMMXCS J2215-1738 show an even larger difference: the mass-weighted sizes are $\sim 55\%$ smaller, with a median $\langle \log(R_{e-circ,mass}/R_{e-circ}) \rangle = -0.34$. On the other hand, Cl 0332-2742 shows only $\sim 20\%$ decrease, with $\langle \log(R_{e-circ,mass}/R_{e-circ}) \rangle = -0.095$. The fact that the mass-weighted sizes are smaller suggests the stellar mass distribution is more concentrated than the light.

- Using the mass-weighted sizes of the galaxies, we study the stellar mass – mass-weighted size relation of the KCS clusters. From the intercept of the relations, we clearly see that the mass-weighted sizes are smaller compared to the light-weighted ones. The derived slope for the full sample is $\beta = 0.49 \pm 0.12$. There seems to be some indications that there is a flattening of slope of the mass – size relation if mass-weighted sizes are used instead of light-weighted sizes, although more statistics are required to confirm if the change of slope is genuine.
- The ratio of mass-weighted to light-weighted sizes does not show obvious dependence with galaxy properties, except with M_*/L gradient and colour gradients. The fact that they are correlated with colour (and M_*/L) gradient is expected as it is the primary driver of the size differences.
- By using a local reference sample from the SPIDER survey, we find that the mass-weighted sizes of local passive galaxies in high density environments are on average $\sim 12\%$ smaller than the rest-frame R -band light-weighted sizes, consistent with previous studies that based on different sample and methods. Comparing the KCS clusters to the local SPIDER cluster sample, we find an offset in the ratio of mass-weighted sizes to the light-weighted sizes for XMMU J2235-2557 and XMMXCS J2215-1738, with a median difference of $\langle \log(R_{e-circ,mass,1.39}/R_{e-circ,1.39}) - \log(R_{e-circ,mass,0}/R_{e-circ,0}) \rangle = -0.188$ and $\langle \log(R_{e-circ,mass,1.46}/R_{e-circ,1.46}) - \log(R_{e-circ,mass,0}/R_{e-circ,0}) \rangle = -0.259$, respectively. On the other hand, Cl 0332-2742 shows almost no offset with the SPIDER cluster sample, with $\langle \log(R_{e-circ,mass,1.61}/R_{e-circ,1.61}) - \log(R_{e-circ,mass,0}/R_{e-circ,0}) \rangle = -0.006$. We attribute the difference seen in XMMU J2235-2557 and XMMXCS J2215-1738 to an evolution of the M_*/L gradient over redshift. We also find that the progenitor bias alone cannot explain the observed offsets.

6.1.2 The origin and evolution of the colour gradients

In Chapter 5, we have presented the analysis on the colour gradients of the passive galaxies. We investigate quantitatively the origin and the evolution of the observed colour gradient by modeling the colour gradients with stellar population models under three different assumptions of the radial variation of stellar population properties. We find the following:

- The majority ($\sim 93\%$) of the KCS galaxies show a negative colour gradient $\nabla_{z_{850}-H_{160}}$, with redder colours at the core and bluer colour in the outskirts. $\sim 34\%$ of the sample have steep gradients with $\nabla_{z_{850}-H_{160}} < -0.5$. The median colour gradient for XMMU J2235-2557, XMMXCS J2215-1738 and Cl 0332-2742 are $\langle \nabla_{z_{850}-H_{160}} \rangle = -0.42 \pm 0.06$, $\langle \nabla_{z_{850}-H_{160}} \rangle = -0.46 \pm 0.07$ and $\langle \nabla_{z_{850}-H_{160}} \rangle = -0.41 \pm 0.07$, respectively. The observed colour gradients are two times steeper than the colour gradients found in local passive galaxies in previous studies.

We analyse the evolution of the rest-frame $(U - R)$ colour gradient at two radii, $0.5 a_e$ and $2.0 a_e$, representing the inner and outer region of the galaxy respectively.

We subdivide each of the assumptions summarised below into three different metallicity scenarios and fix the metallicity of the inner regions to sub-solar, solar and super-solar $Z = (0.008, 0.02, 0.05)$:

- **Case I - Pure age-driven gradient evolution** – the evolution of colour gradients is solely due to an age gradient. The inner and outer regions of the passive galaxies are assumed to have identical metallicities (i.e. flat metallicity gradients $\nabla_Z = 0$). We find that although an age gradient alone is sufficient to reproduce all the evolution in the colour gradient of the three clusters, it over-predicts the evolution over redshift, causing the evolved local gradients to be too shallow compared to the observation.
- **Case II - Pure metallicity-driven gradient evolution** – the evolution of colour gradients is solely due to a metallicity gradient. We assume the inner and outer regions have identical ages (i.e. flat age gradients $\nabla_{age} = 0$). A metallicity gradient alone cannot explain the observation as the evolution it predicts goes in the wrong direction.
- **Case III - Age-driven gradient evolution with an assumed metallicity gradient** – the evolution of colour gradients is due to a combination of age and metallicity gradients. The galaxies are assumed to have a fixed metallicity gradient identical to that observed in local passive galaxies, $\nabla_Z \simeq -0.2$. This model works reasonably well, the solar metallicity scenario can reproduce the observed evolution of the colour gradients in all three clusters well. In addition to the median values, the evolved 1σ scatters are also consistent with those seen in local passive galaxies.
- The above conclusions are robust if any central dust reddening at $0.5a_e$ is $\lesssim 0.14$ mag, or equivalently an extinction gradient $dA_V/d\log(a) \sim 0.40$ or $dE(B-V)/d\log(a) \sim -0.10$, assuming a Calzetti extinction law (Calzetti et al., 2000).
- Our case study indicates that the presence of an age gradient at high redshift is a necessary condition to explain the observed evolution of the colour gradients, while metallicity gradients probably dominate at $z \sim 0$. This conclusion is partially consistent with other studies (Saglia et al., 2000; Guo et al., 2011; Gargiulo et al., 2012). The study is repeated using the rest-frame $(g-r)$ colour gradient of XMMU J2235-2557 and completely consistent results are obtained. We also check that using exponentially declining τ -models with various τ will result in a shallower age gradients, but the conclusion remains unchanged. For the best-matching scenario (Case III with solar metallicity) with an assumed metallicity gradient of $\nabla_Z \simeq -0.2$, the derived median age gradient of XMMU J2235-2557, XMMXCS J2215-1738 and Cl 0332-2742 are negative, with $\langle \nabla_{age} \rangle \sim -0.32 \pm 0.08$, $\langle \nabla_{age} \rangle \sim -0.35 \pm 0.09$ and $\langle \nabla_{age} \rangle \sim -0.31 \pm 0.10$, respectively.
- Given the assumption that high redshift passive galaxies have the same metallicity gradient as the local ones, the evolution of colour gradients of the three clusters from the cluster redshifts to $z = 0$ can be explained by passive evolution.

We interpret our findings on the sizes and colour gradients as follows. We suggest that a gradual mass growth mechanism, such as minor mergers, is able to explain the evolution of both quantities at the same time. In the minor merger scenario, the accreted material from the merger primarily assembles in the other part of the galaxies, as demonstrated by simulations (e.g. Rodriguez-Gomez et al., 2016). This can explain the observed negative age gradients if the merger is dry and the accreted material is younger compared to the cluster galaxies. In this way the inner region of the galaxies remains undisturbed and can age through passive evolution. Minor mergers are likely to happen when group-scale structures are being accreted into the clusters, although the merger rate in clusters is still poorly constrained. It is hence probable that the cluster galaxies will undergo mergers with galaxies that have younger stellar populations. At the same time, the minor merger scenario can explain the size evolution of passive galaxies, as shown by various works on the field population (e.g. Patel et al., 2013; Newman et al., 2014).

Through a qualitative comparison with the Illustris cosmological simulations (Wellons et al., 2015), the negative age gradient we found in the KCS galaxies suggests that they are more likely to be galaxies that are formed and have their mass assembled early, than those which have experienced a violent major merger. The star formation rate of these galaxies gradually reduced through gas depletion, stellar feedback and finally got quenched completely by AGN activity. Furthermore, comparing with predictions by both traditional and revised monolithic models, we find that the monolithic collapse models cannot explain our colour gradient results.

6.1.3 The role of the environment in the evolution

In Chapter 5, we also investigate the effect of environment by comparing the structural properties of KCS galaxies to the field sample of Lang et al. (2014). We find the following:

- Comparing the light-weighted mass-normalised size distribution of the KCS galaxies to the field, we find that the peak of the combined light-weighted size distribution of XMMU J2235-2557 and XMMXCS J2215-1738 is offset to larger size. In contrast, the size distribution of Cl 0332-2742 have comparable, if not on average smaller, sizes compared to the field galaxies.
- The abovementioned offset in the combined light-weighted mass-normalised size distribution of XMMU J2235-2557 and XMMXCS J2215-1738 compared to the field is reduced if mass-weighted mass-normalised sizes are used instead.
- The median ratios of mass-weighted to light-weighted size in XMMU J2235-2557 and XMMXCS J2215-1738 are smaller than the field sample at similar redshifts. The offset of the two clusters from the field sample is -0.074 ± 0.036 and -0.157 ± 0.047 dex, respectively. On the other hand, the median size ratio in Cl 0332-2742 is comparable to, if not larger than, the field galaxies, with an offset of 0.064 ± 0.037 dex.

In summary, XMMU J2235-2557 and XMMXCS J2215-1738 show larger light-weighted size and smaller size ratio compared to the field, but Cl 0332-2742 shows none, if not the opposite, of these differences.

Given that Cl 0332-2742 is a structure with several groups still in their assembly phase, we suggest that the above result can be explained by an enhanced merger rate during cluster assembly. This idea is similar to the accelerated structural evolution picture proposed by previous works comparing the light-weighted sizes between clusters and the field (e.g. Lani et al., 2013; Delaye et al., 2014). Our measurements of size ratio and mass-weighted size provide further evidence to support this picture, and at the same time provide information about the type of mergers responsible at this epoch. We suggest that dry minor merger is a plausible candidate to also explain the environmental difference in structural properties between clusters and the field.

Combining all the findings, we propose the picture below. The majority of the passive galaxies in the clusters are formed and quenched early. While the passive galaxies are still in various group structures or in protoclusters, they have similar size and colour gradient as those in the field. The assembly of cluster via merging of these group structures enhances the merger rate for a certain period of time. Galaxies in the cluster experience on average a higher rate of minor mergers compared to the field population, and result in larger light-weighted sizes and stronger M_*/L gradients as the accreted materials predominantly reside on the outskirts. As the cluster virializes, merger activity is suppressed due to increased relative velocities between galaxies. The size evolution in cluster galaxies takes place through continual minor mergers, presumably during infall and accretion of galaxy groups by the cluster, albeit with slower rate compared to the field. The inner part of the passive galaxies in clusters remains undistributed in this evolution and ages through passive evolution. On the other hand, due to a relatively higher merger rate in the field, the average difference between the size of the field population and the clusters reduces over time. The field population eventually catches up and their size distribution matches the cluster size distribution in the local universe.

While this picture can sufficiently explain our results, an important factor that remains unclear is whether the rate of minor mergers can sufficiently explain the environmental differences in M_*/L gradient and the size evolution. Despite a few works attempting to quantify the minor merger rate in the field using pair fraction (e.g. Newman et al., 2012; Man et al., 2014), the merger rate in clusters remains poorly constrained. Besides in observations, the merger rate in clusters is also poorly constrained in simulations.

6.2 Future work

The properties of the KCS cluster galaxies we derived, together with the tools and the dataset we developed during this thesis work can potentially be used to address other unresolved questions. In this section we describe some of the ongoing and perspective work that can be done with our data and methods.

6.2.1 The stellar mass fundamental plane

As we describe in Section 1.3.3, passive galaxies lie on a tight relation connecting their surface brightness Σ , size R_e and velocity dispersion σ , known as the (luminosity) fundamental plane (e.g. Dressler et al., 1987; Djorgovski & Davis, 1987). The zero-point of the plane has been shown to evolve with redshift up to $z \sim 2$, which is the result of the evolving M/L with redshift as the galaxy population becomes younger (e.g van Dokkum & van der Marel, 2007; Toft et al., 2012; Bezanson et al., 2013a; van de Sande et al., 2014). A variation of the FP, known as the stellar mass fundamental plane, is derived by replacing the surface brightness in the FP with stellar mass surface density ($M_*/2\pi R_e^2$) (e.g. Bolton et al., 2008; Hyde & Bernardi, 2009). This drastically reduces the zero-point evolution as the effect of the stellar population M_*/L is removed (Bezanson et al., 2013b). The main difficulty of studying luminosity and mass-FP at high redshift lies in obtaining a large homogenous sample of velocity dispersion measurements of passive galaxies. The KCS survey has successfully obtained velocity dispersion measurements for cluster galaxies in the redshift range $1.39 < z < 1.6$ using the KMOS spectrograph. This allows us to study the luminosity FP of the KCS galaxies at this redshift (Beifiori et al., 2016, in prep).

In the current literature, the sizes used for the luminosity and mass-FP are always light-weighted sizes (commonly in rest-frame B -band). A further step can be taken to construct the stellar mass fundamental plane using the stellar masses and mass-weighted sizes derived in this thesis (see Table 3.1, 3.2 and 3.3), in combination with the stellar velocity dispersions derived in Beifiori et al 2016, in prep. Using mass-weighted sizes we can further include the effect of varying M_*/L gradient in passive galaxies in the mass-FP. For the local reference sample, we can use the stellar masses and mass-weighted sizes of the SPIDER sample derived in this thesis, together with the stellar velocity dispersions from SDSS.

For the local passive population, replacing the light-weighted sizes with mass-weighted sizes should make a minimal difference, perhaps only on the ‘tilt’ of the plane, as the colour gradients of the local passive population are not steep (see Section 5.1 and 5.2.7). At high redshift, given the steep and highly varied colour gradients we might expect some differences in the zero-point and ‘tilt’ of the mass-FP. Using mass-weighted sizes also allows us to directly compare with predictions from simulations. For example, Porter et al. (2014) studied the mass-FP in semi-analytic model and found that there is a slight decrease in the tilt of the mass-FP with redshift. They suggest that this is due to less dissipation in mergers at lower redshifts due to the lower gas content of the progenitors.

6.2.2 Colour gradients and mass distributions of RCS 2345-3632 and JKCS 041

The work of this thesis will be extended to the two remaining clusters in the KCS sample, RCS 2345-3632 at $z \sim 1.04$ and JKCS 041 at $z \sim 1.8$.

RCS 2345-3632 is an optically rich cluster that appears to be a virialized structure (see Section 2.2). The cluster has also both optical ACS and near-IR WFC3 data from archival

and our Cycle 22 WFC3 observation (see Table 2.1). Hence, we are able to study the colour gradients and derive mass-weighted sizes with the same method as we described in this thesis. Being at redshift $z \sim 1.04$, the colour gradients and mass-weighted sizes of this cluster will allow us to bridge our results of the three high-redshift KCS clusters to lower redshift studies.

JKCS 041 is a massive cluster at $z \sim 1.8$ with a large population of passive galaxies (see Section 2.2). This cluster is believed to be in a very evolved state, as suggested by its well populated red sequence and a mass of $M_{200} \sim 2 - 3 \times 10^{14} M_{\odot}$. With such a high cluster mass at this redshift, it is believed that this cluster will evolve into a Coma-like cluster by redshift $z \sim 0$ (Andreon et al., 2014). Both the range of the luminosity-weighted age (~ 1 Gyr) and light-weighted size distribution of this cluster are found to be comparable to the field population at this redshift (Newman et al., 2014). Being both young and in an evolved state, it is therefore very interesting to study the colour gradients in JKCS 041. For this cluster there is WFC3 imaging currently available in the Y_{105} and H_{160} band, which corresponds to roughly rest-frame U to B and g to r band. This allows us to derive colour gradients and compare with SSP models, in a way similar to the $Y_{105} - H_{160}$ colour gradient we derived for XMMU J2235-2557 (See Section 5.2.7). Furthermore, currently 16 passive galaxies in JKCS 041 are observed with KMOS. The KMOS data can potentially provide information on their kinematics and stellar population. Together with the colour gradients, these measurements can be used to study the evolution of various properties of these passive galaxies, as well as to test our proposed picture of the role of environment.

Besides RCS 2345-3632 and JKCS 041, in the future we can also extend the work of this thesis to other high-redshift clusters. There are already several high-redshift clusters and structures with enough ancillary data and suitable WFC3 (and ACS) data that can be used to study the colour gradients and size ratio of their passive population, for example XDCP J0044.0-2033 at $z \sim 1.58$ (Santos et al., 2011), SpARCSJ021524-034331 at $z \sim 1.63$ (Muzzin et al., 2013a), and SpARCS104922.6+564032.5 at $z \sim 1.71$ (Webb et al., 2015).

6.2.3 Size evolution in different environment with mass-weighted sizes

Another interesting question that can be explored with the tools developed in this thesis is the size evolution of passive (or even star-forming) galaxies. As we describe in Section 1.4.2, minor mergers are believed to be the main physical process responsible for the size evolution. One caveat is that the merger rate might be insufficient at high redshift; recent studies have demonstrated that minor mergers in the field can only account for the size evolution up to $z \lesssim 1$ (e.g. Newman et al., 2012), suggesting other mechanisms might be in place at higher redshift (see e.g. Ishibashi et al., 2013), while in clusters, the merger rate is still poorly constrained.

Currently, the size evolution of passive galaxies in different environments is characterised using light-weighted sizes. For passive galaxies, since their colour gradients are much steeper at high redshift (see Section 5.1), the size evolution derived using light-

weighted sizes, even taken at the same rest-frame wavelength, might be biased and not representative of the true evolutionary picture.

An improvement would be to use mass-weighted sizes instead of light-weighted sizes. In our work we have demonstrated that, although with a small range in redshift ($1.39 < z < 1.61$), the mass-weighted sizes of the KCS clusters show a much smaller difference to the field than the light-weighted sizes (see Section 5.5.1). Constructing the size evolution using mass-weighted size may provide extra insights on the role of environment.

While deriving mass-weighted sizes, we have discarded a fraction of objects in XMMU J2235-2557 and XMMXCS J2215-1738 due to their resultant sizes being smaller than 0.5 FWHM of the PSF of *HST*/WFC3 (see Section 3.6). This suggests that the type of analysis has started to reach the limit of the *HST* resolution. The coming *James Webb Space Telescope* (*JWST*) will be able to provide spatially resolved images of galaxies with a much higher spatial resolution. The primary imager on *JWST*, the Near Infrared Camera (NIRCam), has at least a factor of ~ 3 higher spatial resolution than *HST*/WFC3; it has a native pixel scale of $0.032'' \text{ pixel}^{-1}$ with an instrumental PSF that is $\sim 0.06''$ ($1.5 - 2$ pixels) for the wavelength range of 0.6 to $2.3 \mu\text{m}$ (Rieke et al., 2005), compared to the $\sim 0.128'' \text{ pixel}^{-1}$ pixel scale and $\sim 0.18''$ PSF FWHM of WFC3. With this type of data from *JWST*, we will be able to derive accurate mass-weighted sizes of the galaxies and extend the study of size evolution of passive galaxies using mass-weighted sizes to even higher redshift.

Bibliography

Abell, G. O. 1958, *ApJS*, 3, 211

—. 1965, *ARA&A*, 3, 1

Abraham, R. G. 1998, *ArXiv Astrophysics e-prints*, astro-ph/9809131

Allen, S. W., Evrard, A. E., & Mantz, A. B. 2011, *ARA&A*, 49, 409

Andreon, S. 2008, *MNRAS*, 386, 1045

Andreon, S., Maughan, B., Trinchieri, G., & Kurk, J. 2009, *A&A*, 507, 147

Andreon, S., Newman, A. B., Trinchieri, G., et al. 2014, *A&A*, 565, A120

Angulo, R. E., Springel, V., White, S. D. M., et al. 2012, *MNRAS*, 426, 2046

Arimoto, N., & Yoshii, Y. 1987, *A&A*, 173, 23

Arnouts, S., Cristiani, S., Moscardini, L., et al. 1999, *MNRAS*, 310, 540

Arnouts, S., Vandame, B., Benoist, C., et al. 2001, *A&A*, 379, 740

Baldry, I. K., Balogh, M. L., Bower, R. G., et al. 2006, *MNRAS*, 373, 469

Baldry, I. K., Glazebrook, K., Brinkmann, J., et al. 2004, *ApJ*, 600, 681

Balogh, M. L., Baldry, I. K., Nichol, R., et al. 2004, *ApJ*, 615, L101

Balogh, M. L., McGee, S. L., Mok, A., et al. 2016, *MNRAS*, 456, 4364

Barden, M., Häußler, B., Peng, C. Y., McIntosh, D. H., & Guo, Y. 2012, *MNRAS*, 422, 449

Barden, M., Rix, H.-W., Somerville, R. S., et al. 2005, *ApJ*, 635, 959

Barro, G., Faber, S. M., Pérez-González, P. G., et al. 2013, *ApJ*, 765, 104

Barro, G., Faber, S. M., Koo, D. C., et al. 2015, *ArXiv e-prints*, arXiv:1509.00469

- Bauer, A. E., Grützbauch, R., Jørgensen, I., Varela, J., & Bergmann, M. 2011, *MNRAS*, 411, 2009
- Bayliss, M. B., Ashby, M. L. N., Ruel, J., et al. 2014, *ApJ*, 794, 12
- Beifiori, A., Thomas, D., Maraston, C., et al. 2014, *ApJ*, 789, 92
- Bell, E. F., & de Jong, R. S. 2001, *ApJ*, 550, 212
- Bell, E. F., McIntosh, D. H., Katz, N., & Weinberg, M. D. 2003, *ApJS*, 149, 289
- Bell, E. F., Wolf, C., Meisenheimer, K., et al. 2004, *ApJ*, 608, 752
- Belli, S., Newman, A. B., & Ellis, R. S. 2014a, *ApJ*, 783, 117
- . 2015, *ApJ*, 799, 206
- Belli, S., Newman, A. B., Ellis, R. S., & Konidaris, N. P. 2014b, *ApJ*, 788, L29
- Bender, R., Doebereiner, S., & Moellenhoff, C. 1988, *A&AS*, 74, 385
- Bender, R., Saglia, R. P., & Gerhard, O. E. 1994, *MNRAS*, 269, 785
- Bennett, C. L., Halpern, M., Hinshaw, G., et al. 2003, *ApJS*, 148, 1
- Berlind, A. A., Frieman, J., Weinberg, D. H., et al. 2006, *ApJS*, 167, 1
- Bernardi, M., Meert, A., Sheth, R. K., et al. 2013, *MNRAS*, 436, 697
- Bernardi, M., Meert, A., Vikram, V., et al. 2012, *ArXiv e-prints*, arXiv:1211.6122
- Bernardi, M., Roche, N., Shankar, F., & Sheth, R. K. 2011, *MNRAS*, 412, L6
- Bernardi, M., Shankar, F., Hyde, J. B., et al. 2010, *MNRAS*, 404, 2087
- Bernardi, M., Sheth, R. K., Nichol, R. C., Schneider, D. P., & Brinkmann, J. 2005, *AJ*, 129, 61
- Bernardi, M., Sheth, R. K., Annis, J., et al. 2003, *AJ*, 125, 1817
- Berry, D., Currie, M., Jenness, T., et al. 2013, in *Astronomical Society of the Pacific Conference Series*, Vol. 475, *Astronomical Data Analysis Software and Systems XXII*, ed. D. N. Friedel, 247
- Bertin, E., & Arnouts, S. 1996, *A&AS*, 117, 393
- Bertin, E., Mellier, Y., Radovich, M., et al. 2002, in *Astronomical Society of the Pacific Conference Series*, Vol. 281, *Astronomical Data Analysis Software and Systems XI*, ed. D. A. Bohlender, D. Durand, & T. H. Handley, 228

- Bezanson, R., van Dokkum, P. G., Tal, T., et al. 2009, *ApJ*, 697, 1290
- Bezanson, R., van Dokkum, P. G., van de Sande, J., et al. 2013a, *ApJ*, 779, L21
- . 2013b, *ApJ*, 779, L21
- Bildfell, C., Hoekstra, H., Babul, A., et al. 2012, *MNRAS*, 425, 204
- Biviano, A., Murante, G., Borgani, S., et al. 2006, *A&A*, 456, 23
- Blanton, M. R., Hogg, D. W., Bahcall, N. A., et al. 2003, *ApJ*, 594, 186
- Blumenthal, G. R., Faber, S. M., Primack, J. R., & Rees, M. J. 1984, *Nature*, 311, 517
- Böhringer, H., Briel, U. G., Schwarz, R. A., et al. 1994, *Nature*, 368, 828
- Böhringer, H., Mullis, C., Rosati, P., et al. 2005, *The Messenger*, 120, 33
- Böhringer, H., Voges, W., Fabian, A. C., Edge, A. C., & Neumann, D. M. 1993, *MNRAS*, 264, L25
- Böhringer, H., & Werner, N. 2009, *ArXiv e-prints*, arXiv:0907.4277
- Bolton, A. S., Treu, T., Koopmans, L. V. E., et al. 2008, *ApJ*, 684, 248
- Borgani, S., Rosati, P., Tozzi, P., et al. 2001, *ApJ*, 561, 13
- Boselli, A., & Gavazzi, G. 2006, *PASP*, 118, 517
- . 2014, *A&A Rev.*, 22, 74
- Bower, R. G., Benson, A. J., Malbon, R., et al. 2006, *MNRAS*, 370, 645
- Bower, R. G., Kodama, T., & Terlevich, A. 1998, *MNRAS*, 299, 1193
- Bower, R. G., Lucey, J. R., & Ellis, R. S. 1992, *MNRAS*, 254, 589
- Boylan-Kolchin, M., Springel, V., White, S. D. M., Jenkins, A., & Lemson, G. 2009, *MNRAS*, 398, 1150
- Brammer, G. B., van Dokkum, P. G., & Coppi, P. 2008, *ApJ*, 686, 1503
- Brammer, G. B., Whitaker, K. E., van Dokkum, P. G., et al. 2009, *ApJ*, 706, L173
- . 2011, *ApJ*, 739, 24
- Brammer, G. B., van Dokkum, P. G., Franx, M., et al. 2012, *ApJS*, 200, 13
- Briel, U. G., Henry, J. P., & Böhringer, H. 1992, *A&A*, 259, L31
- Brodwin, M., McDonald, M., Gonzalez, A. H., et al. 2016, *ApJ*, 817, 122

- Brodwin, M., Brown, M. J. I., Ashby, M. L. N., et al. 2006, *ApJ*, 651, 791
- Brodwin, M., Stern, D., Vikhlinin, A., et al. 2011, *ApJ*, 732, 33
- Brough, S., Proctor, R., Forbes, D. A., et al. 2007, *MNRAS*, 378, 1507
- Brown, M. J. I., Dey, A., Jannuzi, B. T., et al. 2007, *ApJ*, 654, 858
- Brown, M. J. I., Zheng, Z., White, M., et al. 2008, *ApJ*, 682, 937
- Bruce, V. A., Dunlop, J. S., Cirasuolo, M., et al. 2012, *MNRAS*, 427, 1666
- Bruzual, G., & Charlot, S. 2003, *MNRAS*, 344, 1000
- Bruzual A., G. 1983, *ApJ*, 273, 105
- Buitrago, F., Trujillo, I., Conselice, C. J., et al. 2008, *ApJ*, 687, L61
- Buitrago, F., Trujillo, I., Conselice, C. J., & Häußler, B. 2013, *MNRAS*, 428, 1460
- Bullock, J. S., Kolatt, T. S., Sigad, Y., et al. 2001, *MNRAS*, 321, 559
- Bundy, K., Fukugita, M., Ellis, R. S., et al. 2009, *ApJ*, 697, 1369
- Bundy, K., Georgakakis, A., Nandra, K., et al. 2008, *ApJ*, 681, 931
- Burke, C., & Collins, C. A. 2013, *MNRAS*, 434, 2856
- Burke, C., Hilton, M., & Collins, C. 2015, *MNRAS*, 449, 2353
- Burstein, D., Faber, S. M., Gaskell, C. M., & Krumm, N. 1984, *ApJ*, 287, 586
- Byun, Y. I., & Freeman, K. C. 1995, *ApJ*, 448, 563
- Calzetti, D., Armus, L., Bohlin, R. C., et al. 2000, *ApJ*, 533, 682
- Caon, N., Capaccioli, M., & D’Onofrio, M. 1993, *MNRAS*, 265, 1013
- Capaccioli, M. 1989, in *World of Galaxies (Le Monde des Galaxies)*, ed. H. G. Corwin, Jr. & L. Bottinelli, 208–227
- Cappellari, M. 2013, *ApJ*, 778, L2
- . 2016, *ArXiv e-prints*, arXiv:1602.04267
- Cappellari, M., & Copin, Y. 2003, *MNRAS*, 342, 345
- Cappellari, M., & Emsellem, E. 2004, *PASP*, 116, 138
- Cappellari, M., di Serego Alighieri, S., Cimatti, A., et al. 2009, *ApJ*, 704, L34

- Cappellari, M., Emsellem, E., Krajnović, D., et al. 2011, MNRAS, 416, 1680
- Cappellari, M., Scott, N., Alatalo, K., et al. 2013, MNRAS, 432, 1709
- Carlberg, R. G. 1984, ApJ, 286, 403
- Carlstrom, J. E., Holder, G. P., & Reese, E. D. 2002, ARA&A, 40, 643
- Carlstrom, J. E., Ade, P. A. R., Aird, K. A., et al. 2011, PASP, 123, 568
- Carollo, C. M., Bschorr, T. J., Renzini, A., et al. 2013, ApJ, 773, 112
- Carroll, S. M., Press, W. H., & Turner, E. L. 1992, ARA&A, 30, 499
- Casertano, S., de Mello, D., Dickinson, M., et al. 2000, AJ, 120, 2747
- Cassata, P., Giavalisco, M., Guo, Y., et al. 2010, ApJ, 714, L79
- Castellano, M., Salimbeni, S., Trevese, D., et al. 2007, ApJ, 671, 1497
- Cen, R., & Ostriker, J. P. 1993, ApJ, 417, 415
- Cerulo, P., Couch, W. J., Lidman, C., et al. 2014, MNRAS, 439, 2790
- . 2016, MNRAS, 457, 2209
- Chabrier, G. 2003, PASP, 115, 763
- Chan, J. C. C., Beifiori, A., Mendel, J. T., et al. 2016, MNRAS, 458, 3181
- Chang, Y.-Y., van der Wel, A., Rix, H.-W., et al. 2013, ApJ, 773, 149
- Chary, R., & Elbaz, D. 2001, ApJ, 556, 562
- Chevance, M., Weijmans, A.-M., Damjanov, I., et al. 2012, ApJ, 754, L24
- Chiang, Y.-K., Overzier, R., & Gebhardt, K. 2013, ApJ, 779, 127
- . 2014, ApJ, 782, L3
- Cimatti, A., Daddi, E., & Renzini, A. 2006, A&A, 453, L29
- Cimatti, A., Nipoti, C., & Cassata, P. 2012, MNRAS, 422, L62
- Cimatti, A., Cassata, P., Pozzetti, L., et al. 2008, A&A, 482, 21
- Ciotti, L. 1991, A&A, 249, 99
- Ciotti, L., Lanzoni, B., & Renzini, A. 1996, MNRAS, 282, 1
- Clemens, M. S., Bressan, A., Nikolic, B., & Rampazzo, R. 2009, MNRAS, 392, L35

- Coccatto, L., Gerhard, O., & Arnaboldi, M. 2010, MNRAS, 407, L26
- Conroy, C., Gunn, J. E., & White, M. 2009, ApJ, 699, 486
- Conroy, C., Wechsler, R. H., & Kravtsov, A. V. 2007, ApJ, 668, 826
- Conselice, C. J. 2003, ApJS, 147, 1
- . 2006, MNRAS, 373, 1389
- . 2014, ARA&A, 52, 291
- Cooper, M. C., Gallazzi, A., Newman, J. A., & Yan, R. 2010, MNRAS, 402, 1942
- Cooper, M. C., Griffith, R. L., Newman, J. A., et al. 2012, MNRAS, 419, 3018
- Côté, P., Ferrarese, L., Jordán, A., et al. 2007, ApJ, 671, 1456
- Croton, D. J., Springel, V., White, S. D. M., et al. 2006, MNRAS, 365, 11
- Daddi, E., Renzini, A., Pirzkal, N., et al. 2005, ApJ, 626, 680
- Dale, D. A., & Helou, G. 2002, ApJ, 576, 159
- Damjanov, I., Abraham, R. G., Glazebrook, K., et al. 2011, ApJ, 739, L44
- Darvish, B., Mobasher, B., Sobral, D., Scoville, N., & Aragon-Calvo, M. 2015, ApJ, 805, 121
- Davies, R. I., Agudo Berbel, A., Wiezorrek, E., et al. 2013, A&A, 558, A56
- Davies, R. L., Beifiori, A., Bender, R., et al. 2015, in IAU Symposium, Vol. 311, Galaxy Masses as Constraints of Formation Models, ed. M. Cappellari & S. Courteau, 110–115
- Dawson, K. S., Aldering, G., Amanullah, R., et al. 2009, AJ, 138, 1271
- de Bernardis, P., Ade, P. A. R., Bock, J. J., et al. 2000, Nature, 404, 955
- De Grandi, S., Santos, J. S., Nonino, M., et al. 2014, A&A, 567, A102
- de Haan, T., Benson, B. A., Bleem, L. E., et al. 2016, ArXiv e-prints, arXiv:1603.06522
- De Lucia, G., Poggianti, B. M., Aragón-Salamanca, A., et al. 2007, MNRAS, 374, 809
- De Propriis, R., Bremer, M. N., & Phillipps, S. 2015, MNRAS, 450, 1268
- . 2016, MNRAS, 461, 4517
- De Propriis, R., Phillipps, S., & Bremer, M. N. 2013, MNRAS, 434, 3469
- de Vaucouleurs, G. 1948, Annales d’Astrophysique, 11, 247

- . 1961, *ApJS*, 6, 213
- Dekel, A., Sari, R., & Ceverino, D. 2009, *ApJ*, 703, 785
- Delaye, L., Huertas-Company, M., Mei, S., et al. 2014, *MNRAS*, 441, 203
- Demarco, R., Gobat, R., Rosati, P., et al. 2010, *ApJ*, 725, 1252
- Deustua, S. 2016, *WFC3 Data Handbook*
- Djorgovski, S., & Davis, M. 1987, *ApJ*, 313, 59
- Dressler, A. 1980, *ApJ*, 236, 351
- Dressler, A., Lynden-Bell, D., Burstein, D., et al. 1987, *ApJ*, 313, 42
- Dunn, R. J. H., Fabian, A. C., & Taylor, G. B. 2005, *MNRAS*, 364, 1343
- Dutton, A. A., & Macciò, A. V. 2014, *MNRAS*, 441, 3359
- Efstathiou, G., Frenk, C. S., White, S. D. M., & Davis, M. 1988, *MNRAS*, 235, 715
- Einasto, J. 1965, *Trudy Astrofizicheskogo Instituta Alma-Ata*, 5, 87
- Eisenhardt, P. R. M., Brodwin, M., Gonzalez, A. H., et al. 2008, *ApJ*, 684, 905
- Elmegreen, B. G., Bournaud, F., & Elmegreen, D. M. 2008, *ApJ*, 688, 67
- Faber, S. M., & Jackson, R. E. 1976, *ApJ*, 204, 668
- Faber, S. M., Tremaine, S., Ajhar, E. A., et al. 1997, *AJ*, 114, 1771
- Faber, S. M., Willmer, C. N. A., Wolf, C., et al. 2007, *ApJ*, 665, 265
- Fabian, A. C. 1994, *ARA&A*, 32, 277
- Fabian, A. C., Sanders, J. S., Ettori, S., et al. 2000, *MNRAS*, 318, L65
- Fabian, A. C., Sanders, J. S., Allen, S. W., et al. 2011, *MNRAS*, 418, 2154
- Fagioli, M., Carollo, C. M., Renzini, A., et al. 2016, *ArXiv e-prints*, arXiv:1607.03493
- Fan, L., Lapi, A., Bressan, A., et al. 2010, *ApJ*, 718, 1460
- Fan, L., Lapi, A., De Zotti, G., & Danese, L. 2008, *ApJ*, 689, L101
- Fang, J. J., Faber, S. M., Koo, D. C., & Dekel, A. 2013, *ApJ*, 776, 63
- Fassbender, R., Nastasi, A., Böhringer, H., et al. 2011, *A&A*, 527, L10
- Fassbender, R., Nastasi, A., Santos, J. S., et al. 2014, *A&A*, 568, A5

- Ferré-Mateu, A., Vazdekis, A., Trujillo, I., et al. 2012, MNRAS, 423, 632
- Forbes, D. A., Ponman, T. J., & Brown, R. J. N. 1998, ApJ, 508, L43
- Forman, W., Kellogg, E., Gursky, H., Tananbaum, H., & Giacconi, R. 1972, ApJ, 178, 309
- Fossati, M., Fumagalli, M., Boselli, A., et al. 2016, MNRAS, 455, 2028
- Franx, M., Illingworth, G., & Heckman, T. 1989, AJ, 98, 538
- Freeman, P. E., Izbicki, R., Lee, A. B., et al. 2013, MNRAS, 434, 282
- Fruchter, A. S., & Hook, R. N. 2002, PASP, 114, 144
- Fumagalli, M., Fossati, M., Hau, G. K. T., et al. 2014, MNRAS, 445, 4335
- Galametz, A., Vernet, J., De Breuck, C., et al. 2010, A&A, 522, A58
- Galametz, A., Stern, D., Pentericci, L., et al. 2013, A&A, 559, A2
- Gallazzi, A., Charlot, S., Brinchmann, J., & White, S. D. M. 2006, MNRAS, 370, 1106
- Gallazzi, A., Charlot, S., Brinchmann, J., White, S. D. M., & Tremonti, C. A. 2005, MNRAS, 362, 41
- Gao, L., Navarro, J. F., Cole, S., et al. 2008, MNRAS, 387, 536
- Gargiulo, A., Saracco, P., & Longhetti, M. 2011, MNRAS, 412, 1804
- Gargiulo, A., Saracco, P., Longhetti, M., La Barbera, F., & Tamburri, S. 2012, MNRAS, 425, 2698
- Giavalisco, M., Ferguson, H. C., Koekemoer, A. M., et al. 2004, ApJ, 600, L93
- Gilbank, D. G., Gladders, M. D., Yee, H. K. C., & Hsieh, B. C. 2011, AJ, 141, 94
- Gilbank, D. G., Yee, H. K. C., Ellingson, E., et al. 2007, AJ, 134, 282
- Gladders, M. D., & Yee, H. K. C. 2000, AJ, 120, 2148
- . 2005, ApJS, 157, 1
- Gobat, R., Daddi, E., Onodera, M., et al. 2011, A&A, 526, A133
- Gobat, R., Strazzullo, V., Daddi, E., et al. 2013, ApJ, 776, 9
- Gonzaga, S., et al., B, & C. 2012, The DrizzlePac Handbook
- Gonzalez, A. H., Zaritsky, D., Dalcanton, J. J., & Nelson, A. 2001, ApJS, 137, 117
- González Delgado, R. M., Pérez, E., Cid Fernandes, R., et al. 2014, A&A, 562, A47

- Graham, A. W., Erwin, P., Trujillo, I., & Asensio Ramos, A. 2003, *AJ*, 125, 2951
- Grazian, A., Fontana, A., Moscardini, L., et al. 2006, *A&A*, 453, 507
- Greene, J. E., Murphy, J. D., Graves, G. J., et al. 2013, *ApJ*, 776, 64
- Grogin, N. A., Kocevski, D. D., Faber, S. M., et al. 2011, *ApJS*, 197, 35
- Grützbauch, R., Bauer, A. E., Jørgensen, I., & Varela, J. 2012, *MNRAS*, 423, 3652
- Gunn, J. E., & Gott, III, J. R. 1972, *ApJ*, 176, 1
- Guo, Y., McIntosh, D. H., Mo, H. J., et al. 2009, *MNRAS*, 398, 1129
- Guo, Y., Giavalisco, M., Cassata, P., et al. 2011, *ApJ*, 735, 18
- Guth, A. H. 1981, *Phys. Rev. D*, 23, 347
- Hatch, N. A., Wylezalek, D., Kurk, J. D., et al. 2014, *MNRAS*, 445, 280
- Häussler, B., McIntosh, D. H., Barden, M., et al. 2007, *ApJS*, 172, 615
- Hawking, S. W. 1982, *Physics Letters B*, 115, 295
- Hayashi, M., Kodama, T., Koyama, Y., Tadaki, K.-I., & Tanaka, I. 2011, *MNRAS*, 415, 2670
- Hayashi, M., Kodama, T., Koyama, Y., et al. 2010, *MNRAS*, 402, 1980
- Hayes, M., Schaerer, D., & Östlin, G. 2010, *A&A*, 509, L5
- Henry, J. P., Salvato, M., Finoguenov, A., et al. 2010, *ApJ*, 725, 615
- Hilton, M., Collins, C. A., Stanford, S. A., et al. 2007, *ApJ*, 670, 1000
- Hilton, M., Stanford, S. A., Stott, J. P., et al. 2009, *ApJ*, 697, 436
- Hilton, M., Lloyd-Davies, E., Stanford, S. A., et al. 2010, *ApJ*, 718, 133
- Hilz, M., Naab, T., & Ostriker, J. P. 2013, *MNRAS*, 429, 2924
- Hirschmann, M., Naab, T., Ostriker, J. P., et al. 2015, *MNRAS*, 449, 528
- Hogg, D. W., Baldry, I. K., Blanton, M. R., & Eisenstein, D. J. 2002, *ArXiv Astrophysics e-prints*, astro-ph/0210394
- Hogg, D. W., Blanton, M. R., Brinchmann, J., et al. 2004, *ApJ*, 601, L29
- Holden, B. P., van der Wel, A., Kelson, D. D., Franx, M., & Illingworth, G. D. 2010, *ApJ*, 724, 714

- Holden, B. P., van der Wel, A., Rix, H.-W., & Franx, M. 2012, *ApJ*, 749, 96
- Holden, B. P., Franx, M., Illingworth, G. D., et al. 2009, *ApJ*, 693, 617
- Hopkins, P. F., Bundy, K., Hernquist, L., & Ellis, R. S. 2007, *ApJ*, 659, 976
- Horne, K. 1986, *PASP*, 98, 609
- Hubble, E. 1929, *Proceedings of the National Academy of Science*, 15, 168
- Hubble, E., & Humason, M. L. 1931, *ApJ*, 74, 43
- Hubble, E. P. 1925, *ApJ*, 62, doi:10.1086/142943
- . 1926, *ApJ*, 64, doi:10.1086/143018
- . 1930, *ApJ*, 71, doi:10.1086/143250
- . 1936, *Realm of the Nebulae*
- Hudson, D. S., Mittal, R., Reiprich, T. H., et al. 2010, *A&A*, 513, A37
- Huertas-Company, M., Shankar, F., Mei, S., et al. 2013, *ApJ*, 779, 29
- Husband, K., Bremer, M. N., Stott, J. P., & Murphy, D. N. A. 2016, *MNRAS*, 462, 421
- Hyde, J. B., & Bernardi, M. 2009, *MNRAS*, 394, 1978
- Iannuzzi, F., & Dolag, K. 2011, *MNRAS*, 417, 2846
- Idiart, T. P., Michard, R., & de Freitas Pacheco, J. A. 2002, *A&A*, 383, 30
- Ilbert, O., Arnouts, S., McCracken, H. J., et al. 2006, *A&A*, 457, 841
- Ilbert, O., Salvato, M., Le Floch, E., et al. 2010, *ApJ*, 709, 644
- Ilbert, O., McCracken, H. J., Le Fèvre, O., et al. 2013, *A&A*, 556, A55
- Ishibashi, W., Fabian, A. C., & Canning, R. E. A. 2013, *MNRAS*, 431, 2350
- Jee, M. J., Rosati, P., Ford, H. C., et al. 2009, *ApJ*, 704, 672
- Jee, M. J., Dawson, K. S., Hoekstra, H., et al. 2011, *ApJ*, 737, 59
- Jenkins, A., Frenk, C. S., White, S. D. M., et al. 2001, *MNRAS*, 321, 372
- Jørgensen, I., & Chiboucas, K. 2013, *AJ*, 145, 77
- Jørgensen, I., Chiboucas, K., Flint, K., et al. 2006, *ApJ*, 639, L9
- Jørgensen, I., Chiboucas, K., Toft, S., et al. 2014, *AJ*, 148, 117

- Jorgensen, I., Franx, M., & Kjaergaard, P. 1996, *MNRAS*, 280, 167
- Kauffmann, G., White, S. D. M., Heckman, T. M., et al. 2004, *MNRAS*, 353, 713
- Kauffmann, G., Heckman, T. M., White, S. D. M., et al. 2003a, *MNRAS*, 341, 33
- . 2003b, *MNRAS*, 341, 54
- Kaviraj, S., Peirani, S., Khochfar, S., Silk, J., & Kay, S. 2009, *MNRAS*, 394, 1713
- Keating, S. K., Abraham, R. G., Schiavon, R., et al. 2015, *ApJ*, 798, 26
- Kelly, B. C. 2007, *ApJ*, 665, 1489
- Kelvin, L. S., Driver, S. P., Robotham, A. S. G., et al. 2012, *MNRAS*, 421, 1007
- Kennedy, R., Bamford, S. P., Häußler, B., et al. 2016a, ArXiv e-prints, arXiv:1608.03495
- Kennedy, R., Bamford, S. P., Baldry, I., et al. 2015, *MNRAS*, 454, 806
- Kennedy, R., Bamford, S. P., Häußler, B., et al. 2016b, *MNRAS*, 460, 3458
- Kim, D., & Im, M. 2013, *ApJ*, 766, 109
- King, I. 1962, *AJ*, 67, 471
- King, I. R. 1966, *AJ*, 71, 64
- Kobayashi, C. 2004, *MNRAS*, 347, 740
- Kodama, T., & Arimoto, N. 1997, *A&A*, 320, 41
- Kodama, T., Arimoto, N., Barger, A. J., & Aragón-Salamanca, A. 1998, *A&A*, 334, 99
- Kodama, T., Tanaka, I., Kajisawa, M., et al. 2007, *MNRAS*, 377, 1717
- Kodama, T., Yamada, T., Akiyama, M., et al. 2004, *MNRAS*, 350, 1005
- Koekemoer, A. M., Faber, S. M., Ferguson, H. C., et al. 2011, *ApJS*, 197, 36
- Kogut, A., Banday, A. J., Bennett, C. L., et al. 1996, *ApJ*, 464, L5
- Komatsu, E., Kogut, A., Nolta, M. R., et al. 2003, *ApJS*, 148, 119
- Kormendy, J. 1977, *ApJ*, 218, 333
- Kormendy, J., & Bender, R. 1996, *ApJ*, 464, L119
- . 2009, *ApJ*, 691, L142
- . 2012, *ApJS*, 198, 2

- Kovač, K., Lilly, S. J., Knobel, C., et al. 2014, MNRAS, 438, 717
- Kriek, M., van der Wel, A., van Dokkum, P. G., Franx, M., & Illingworth, G. D. 2008, ApJ, 682, 896
- Kriek, M., van Dokkum, P. G., Labbé, I., et al. 2009, ApJ, 700, 221
- Krist, J. 1995, in *Astronomical Society of the Pacific Conference Series*, Vol. 77, *Astronomical Data Analysis Software and Systems IV*, ed. R. A. Shaw, H. E. Payne, & J. J. E. Hayes, 349
- Kuntschner, H., Emsellem, E., Bacon, R., et al. 2010, MNRAS, 408, 97
- Kurk, J., Cimatti, A., Zamorani, G., et al. 2009, A&A, 504, 331
- La Barbera, F., Busarello, G., Merluzzi, P., Massarotti, M., & Capaccioli, M. 2002, ApJ, 571, 790
- La Barbera, F., & de Carvalho, R. R. 2009, ApJ, 699, L76
- La Barbera, F., De Carvalho, R. R., De La Rosa, I. G., et al. 2010a, AJ, 140, 1528
- La Barbera, F., de Carvalho, R. R., de La Rosa, I. G., et al. 2010b, MNRAS, 408, 1313
- La Barbera, F., de Carvalho, R. R., Gal, R. R., et al. 2005, ApJ, 626, L19
- La Barbera, F., de Carvalho, R. R., Kohl-Moreira, J. L., et al. 2008, PASP, 120, 681
- La Barbera, F., Ferreras, I., de Carvalho, R. R., et al. 2012, MNRAS, 426, 2300
- La Barbera, F., Lopes, P. A. A., de Carvalho, R. R., de La Rosa, I. G., & Berlind, A. A. 2010c, MNRAS, 408, 1361
- Labbé, I., Franx, M., Rudnick, G., et al. 2003, AJ, 125, 1107
- Labbé, I., Huang, J., Franx, M., et al. 2005, ApJ, 624, L81
- Lang, P., Wuyts, S., Somerville, R. S., et al. 2014, ApJ, 788, 11
- Lange, R., Driver, S. P., Robotham, A. S. G., et al. 2015, MNRAS, 447, 2603
- Lani, C., Almaini, O., Hartley, W. G., et al. 2013, MNRAS, 435, 207
- Laporte, C. F. P., White, S. D. M., Naab, T., & Gao, L. 2013, MNRAS, 435, 901
- Larson, R. B. 1974, MNRAS, 166, 585
- Larson, R. B., Tinsley, B. M., & Caldwell, C. N. 1980, ApJ, 237, 692
- Lasker, B. M., Lattanzi, M. G., McLean, B. J., et al. 2008, AJ, 136, 735

- Lauer, T. R., Ajhar, E. A., Byun, Y.-I., et al. 1995, *AJ*, 110, 2622
- Lauer, T. R., Faber, S. M., Gebhardt, K., et al. 2005, *AJ*, 129, 2138
- Le Fevre, O., Deltorn, J. M., Crampton, D., & Dickinson, M. 1996, *ApJ*, 471, L11
- Lemaux, B. C., Gal, R. R., Lubin, L. M., et al. 2012, *ApJ*, 745, 106
- Lidman, C., Rosati, P., Tanaka, M., et al. 2008, *A&A*, 489, 981
- Lintott, C., Schawinski, K., Bamford, S., et al. 2011, *MNRAS*, 410, 166
- Lintott, C. J., Schawinski, K., Slosar, A., et al. 2008, *MNRAS*, 389, 1179
- Lloyd-Davies, E. J., Romer, A. K., Mehtens, N., et al. 2011, *MNRAS*, 418, 14
- Longhetti, M., Saracco, P., Severgnini, P., et al. 2007, *MNRAS*, 374, 614
- Lopes, P. A. A., de Carvalho, R. R., Kohl-Moreira, J. L., & Jones, C. 2009, *MNRAS*, 392, 135
- Lotz, J. M., Primack, J., & Madau, P. 2004, *AJ*, 128, 163
- Lotz, J. M., Papovich, C., Faber, S. M., et al. 2013, *ApJ*, 773, 154
- Lucas, R. A. 2016, *ACS Data Handbook*
- Ma, C.-J., Smail, I., Swinbank, A. M., et al. 2015, *ApJ*, 806, 257
- Maller, A. H., Berlind, A. A., Blanton, M. R., & Hogg, D. W. 2009, *ApJ*, 691, 394
- Maltby, D. T., Aragón-Salamanca, A., Gray, M. E., et al. 2010, *MNRAS*, 402, 282
- Man, A. W. S., Zirm, A. W., & Toft, S. 2014, *ArXiv e-prints*, arXiv:1410.3479
- Mancini, C., Daddi, E., Renzini, A., et al. 2010, *MNRAS*, 401, 933
- Mantz, A. B., Allen, S. W., Morris, R. G., et al. 2014, *MNRAS*, 440, 2077
- Maraston, C. 2005, *MNRAS*, 362, 799
- Maraston, C., & Strömbäck, G. 2011, *MNRAS*, 418, 2785
- Marchesini, D., Whitaker, K. E., Brammer, G., et al. 2010, *ApJ*, 725, 1277
- Marchesini, D., Muzzin, A., Stefanon, M., et al. 2014, *ApJ*, 794, 65
- Marriage, T. A., Acquaviva, V., Ade, P. A. R., et al. 2011, *ApJ*, 737, 61
- Martig, M., Bournaud, F., Teyssier, R., & Dekel, A. 2009, *ApJ*, 707, 250

- McGrath, E. J., Stockton, A., Canalizo, G., Iye, M., & Maihara, T. 2008, *ApJ*, 682, 303
- Meert, A., Vikram, V., & Bernardi, M. 2013, *MNRAS*, 433, 1344
- Mehlert, D., Thomas, D., Saglia, R. P., Bender, R., & Wegner, G. 2003, *A&A*, 407, 423
- Mei, S., Holden, B. P., Blakeslee, J. P., et al. 2009, *ApJ*, 690, 42
- Mendel, J. T., Saglia, R. P., Bender, R., et al. 2015, *ApJ*, 804, L4
- Méndez-Abreu, J., Aguerri, J. A. L., Corsini, E. M., & Simonneau, E. 2008, *A&A*, 478, 353
- Merritt, D. 1985, *ApJ*, 289, 18
- Messier, C. 1784, *Connaissance des Temps for 1787*, 238
- Meyers, J., Aldering, G., Amanullah, R., et al. 2010, in *Bulletin of the American Astronomical Society*, Vol. 42, American Astronomical Society Meeting Abstracts #215, 492
- Mo, H., van den Bosch, F. C., & White, S. 2010, *Galaxy Formation and Evolution*
- Mok, A., Balogh, M. L., McGee, S. L., et al. 2013, *MNRAS*, 431, 1090
- Momcheva, I. G., Brammer, G. B., van Dokkum, P. G., et al. 2016, *ApJS*, 225, 27
- Moore, B., Lake, G., & Katz, N. 1998, *ApJ*, 495, 139
- Moore, B., Lake, G., Quinn, T., & Stadel, J. 1999, *MNRAS*, 304, 465
- Moran, S. M., Ellis, R. S., Treu, T., et al. 2007, *ApJ*, 671, 1503
- Morishita, T., Ichikawa, T., & Kajisawa, M. 2014, *ApJ*, 785, 18
- Morishita, T., Ichikawa, T., Noguchi, M., et al. 2015, *ApJ*, 805, 34
- Muldrew, S. I., Hatch, N. A., & Cooke, E. A. 2015, *MNRAS*, 452, 2528
- Mullis, C. R., Rosati, P., Lamer, G., et al. 2005, *ApJ*, 623, L85
- Muzzin, A., Marchesini, D., van Dokkum, P. G., et al. 2009, *ApJ*, 701, 1839
- Muzzin, A., Wilson, G., Demarco, R., et al. 2013a, *ApJ*, 767, 39
- Muzzin, A., Marchesini, D., Stefanon, M., et al. 2013b, *ApJ*, 777, 18
- Naab, T., Johansson, P. H., & Ostriker, J. P. 2009, *ApJ*, 699, L178
- Nastasi, A., Fassbender, R., Böhringer, H., et al. 2011, *A&A*, 532, L6

- Navarro, J. F., Frenk, C. S., & White, S. D. M. 1996, *ApJ*, 462, 563
- . 1997, *ApJ*, 490, 493
- Navarro, J. F., Hayashi, E., Power, C., et al. 2004, *MNRAS*, 349, 1039
- Newman, A. B., Ellis, R. S., Andreon, S., et al. 2014, *ApJ*, 788, 51
- Newman, A. B., Ellis, R. S., Bundy, K., & Treu, T. 2012, *ApJ*, 746, 162
- Nipoti, C., Londrillo, P., & Ciotti, L. 2003, *MNRAS*, 342, 501
- Ogando, R. L. C., Maia, M. A. G., Chiappini, C., et al. 2005, *ApJ*, 632, L61
- Oke, J. B., & Gunn, J. E. 1983, *ApJ*, 266, 713
- Oliva-Altamirano, P., Brough, S., Jimmy, Kim-Vy, T., et al. 2015, *MNRAS*, 449, 3347
- Papovich, C., Giavalisco, M., Dickinson, M., Conselice, C. J., & Ferguson, H. C. 2003, *ApJ*, 598, 827
- Papovich, C., Momcheva, I., Willmer, C. N. A., et al. 2010, *ApJ*, 716, 1503
- Papovich, C., Bassett, R., Lotz, J. M., et al. 2012, *ApJ*, 750, 93
- Pastorello, N., Forbes, D. A., Foster, C., et al. 2014, *MNRAS*, 442, 1003
- Patel, S. G., van Dokkum, P. G., Franx, M., et al. 2013, *ApJ*, 766, 15
- Peletier, R. F. 2013, *Stellar Populations*, ed. J. Falcón-Barroso & J. H. Knapen, 353
- Peletier, R. F., Davies, R. L., Illingworth, G. D., Davis, L. E., & Cawson, M. 1990a, *AJ*, 100, 1091
- Peletier, R. F., Valentijn, E. A., & Jameson, R. F. 1990b, *A&A*, 233, 62
- Peng, C. Y. 2015, *TECHNICAL GALFIT FAQ*
- Peng, C. Y., Ho, L. C., Impey, C. D., & Rix, H.-W. 2002, *AJ*, 124, 266
- . 2010a, *AJ*, 139, 2097
- Peng, Y.-j., Lilly, S. J., Renzini, A., & Carollo, M. 2012, *ApJ*, 757, 4
- Peng, Y.-j., Lilly, S. J., Kovač, K., et al. 2010b, *ApJ*, 721, 193
- Penzias, A. A., & Wilson, R. W. 1965, *ApJ*, 142, 419
- Perlmutter, S., Aldering, G., Goldhaber, G., et al. 1999, *ApJ*, 517, 565
- Peterson, J. R., Kahn, S. M., Paerels, F. B. S., et al. 2003, *ApJ*, 590, 207

- Peterson, J. R., Paerels, F. B. S., Kaastra, J. S., et al. 2001, *A&A*, 365, L104
- Petrosian, V. 1976, *ApJ*, 209, L1
- Pipino, A., D’Ercole, A., Chiappini, C., & Matteucci, F. 2010, *MNRAS*, 407, 1347
- Pipino, A., D’Ercole, A., & Matteucci, F. 2008, *A&A*, 484, 679
- Planck Collaboration I. 2011, *A&A*, 536, A1
- Planck Collaboration XIII. 2015, *ArXiv e-prints*, arXiv:1502.01589
- Planck Collaboration XXIII. 2014, *A&A*, 571, A23
- Poggianti, B. M., Smail, I., Dressler, A., et al. 1999, *ApJ*, 518, 576
- Poggianti, B. M., Calvi, R., Bindoni, D., et al. 2013, *ApJ*, 762, 77
- Porter, L. A., Somerville, R. S., Primack, J. R., et al. 2014, *MNRAS*, 445, 3092
- Postman, M., Lauer, T. R., Szapudi, I., & Oegerle, W. 1998, *ApJ*, 506, 33
- Postman, M., Lubin, L. M., Gunn, J. E., et al. 1996, *AJ*, 111, 615
- Press, W. H., & Schechter, P. 1974, *ApJ*, 187, 425
- Prugniel, P., & Simien, F. 1997, *A&A*, 321, 111
- Prugniel, P., & Soubiran, C. 2001, *A&A*, 369, 1048
- Prugniel, P., Soubiran, C., Koleva, M., & Le Borgne, D. 2007, *VizieR Online Data Catalog*, 3251
- Pu, S. B., Saglia, R. P., Fabricius, M. H., et al. 2010, *A&A*, 516, A4
- Quadri, R. F., Williams, R. J., Franx, M., & Hildebrandt, H. 2012, *ApJ*, 744, 88
- Ragone-Figueroa, C., & Granato, G. L. 2011, *MNRAS*, 414, 3690
- Raichoor, A., Mei, S., Stanford, S. A., et al. 2012, *ApJ*, 745, 130
- Raskutti, S., Greene, J. E., & Murphy, J. D. 2014, *ApJ*, 786, 23
- Reda, F. M., Proctor, R. N., Forbes, D. A., Hau, G. K. T., & Larsen, S. S. 2007, *MNRAS*, 377, 1772
- Reed, D. S., Koushiappas, S. M., & Gao, L. 2011, *MNRAS*, 415, 3177
- Renzini, A. 2006a, *ARA&A*, 44, 141
- . 2006b, *ARA&A*, 44, 141

- Rettura, A., Rosati, P., Nonino, M., et al. 2010, *ApJ*, 709, 512
- Rettura, A., Martinez-Manso, J., Stern, D., et al. 2014, *ApJ*, 797, 109
- Reynolds, J. H. 1913, *MNRAS*, 74, 132
- Rieke, M. J., Kelly, D., & Horner, S. 2005, in *Proc. SPIE*, Vol. 5904, *Cryogenic Optical Systems and Instruments XI*, ed. J. B. Heaney & L. G. Burriesci, 1–8
- Riess, A. G., Filippenko, A. V., Challis, P., et al. 1998, *AJ*, 116, 1009
- Rodriguez-Gomez, V., Pillepich, A., Sales, L. V., et al. 2016, *MNRAS*, 458, 2371
- Rosati, P., Della Ceca, R., Norman, C., & Giacconi, R. 1998, *ApJ*, 492, L21
- Rosati, P., Tozzi, P., Ettori, S., et al. 2004, *AJ*, 127, 230
- Rosati, P., Tozzi, P., Gobat, R., et al. 2009, *A&A*, 508, 583
- Rudnick, G., von der Linden, A., Pelló, R., et al. 2009, *ApJ*, 700, 1559
- Rudnick, G. H., Tran, K.-V., Papovich, C., Momcheva, I., & Willmer, C. 2012, *ApJ*, 755, 14
- Ruel, J., Bazin, G., Bayliss, M., et al. 2014, *ApJ*, 792, 45
- Ryan, Jr., R. E., McCarthy, P. J., Cohen, S. H., et al. 2012, *ApJ*, 749, 53
- Ryden, B. S., Forbes, D. A., & Terlevich, A. I. 2001, *MNRAS*, 326, 1141
- Saglia, R. P., Maraston, C., Greggio, L., Bender, R., & Ziegler, B. 2000, *A&A*, 360, 911
- Saglia, R. P., Sánchez-Blázquez, P., Bender, R., et al. 2010, *A&A*, 524, A6
- Sandage, A., Freeman, K. C., & Stokes, N. R. 1970, *ApJ*, 160, 831
- Sanders, J. S., & Fabian, A. C. 2002, *MNRAS*, 331, 273
- Santos, J. S., Rosati, P., Tozzi, P., et al. 2008, *A&A*, 483, 35
- Santos, J. S., Fassbender, R., Nastasi, A., et al. 2011, *A&A*, 531, L15
- Sarazin, C. L. 1988, *X-ray emission from clusters of galaxies*
- Saro, A., Mohr, J. J., Bazin, G., & Dolag, K. 2013, *ApJ*, 772, 47
- Schawinski, K., Urry, C. M., Simmons, B. D., et al. 2014, *MNRAS*, 440, 889
- Schlafly, E. F., & Finkbeiner, D. P. 2011, *ApJ*, 737, 103
- Schlegel, D. J., Finkbeiner, D. P., & Davis, M. 1998, *ApJ*, 500, 525

- Scott, N., Fogarty, L. M. R., Owers, M. S., et al. 2015, MNRAS, 451, 2723
- Sersic, J. L. 1968, Atlas de galaxias australes
- Shankar, F., Marulli, F., Bernardi, M., et al. 2013, MNRAS, 428, 109
- Shankar, F., Buchan, S., Rettura, A., et al. 2015, ApJ, 802, 73
- Sharma, P., McCourt, M., Parrish, I. J., & Quataert, E. 2012, MNRAS, 427, 1219
- Shen, S., Mo, H. J., White, S. D. M., et al. 2003, MNRAS, 343, 978
- Sheth, R. K., & Tormen, G. 1999, MNRAS, 308, 119
- . 2004, MNRAS, 350, 1385
- Shetty, S., & Cappellari, M. 2014, ApJ, 786, L10
- Sifón, C., Battaglia, N., Hasselfield, M., et al. 2016, MNRAS, 461, 248
- Sijacki, D., Springel, V., Di Matteo, T., & Hernquist, L. 2007, MNRAS, 380, 877
- Sijacki, D., Vogelsberger, M., Genel, S., et al. 2015, MNRAS, 452, 575
- Silk, J. 1968, ApJ, 151, 459
- Simard, L., Mendel, J. T., Patton, D. R., Ellison, S. L., & McConnachie, A. W. 2011, ApJS, 196, 11
- Simard, L., Willmer, C. N. A., Vogt, N. P., et al. 2002, ApJS, 142, 1
- Skelton, R. E., Whitaker, K. E., Momcheva, I. G., et al. 2014, ApJS, 214, 24
- Smith, R. J., Lucey, J. R., Price, J., Hudson, M. J., & Phillipps, S. 2012, MNRAS, 419, 3167
- Smith, S. 1936, ApJ, 83, 23
- Smoot, G. F., Gorenstein, M. V., & Muller, R. A. 1977, Physical Review Letters, 39, 898
- Smoot, G. F., Bennett, C. L., Kogut, A., et al. 1992, ApJ, 396, L1
- Snyder, G. F., Brodwin, M., Mancone, C. M., et al. 2012, ApJ, 756, 114
- Spolaor, M., Proctor, R. N., Forbes, D. A., & Couch, W. J. 2009, ApJ, 691, L138
- Springel, V., White, S. D. M., Jenkins, A., et al. 2005, Nature, 435, 629
- Stanford, S. A., Eisenhardt, P. R., & Dickinson, M. 1998, ApJ, 492, 461
- Stanford, S. A., Holden, B., Rosati, P., et al. 2001, ApJ, 552, 504

- Stanford, S. A., Eisenhardt, P. R., Brodwin, M., et al. 2005, *ApJ*, 634, L129
- Stanford, S. A., Romer, A. K., Sabirli, K., et al. 2006, *ApJ*, 646, L13
- Stanford, S. A., Brodwin, M., Gonzalez, A. H., et al. 2012, *ApJ*, 753, 164
- Starobinsky, A. A. 1982, *Physics Letters B*, 117, 175
- Stott, J. P., Collins, C. A., Burke, C., Hamilton-Morris, V., & Smith, G. P. 2011, *MNRAS*, 414, 445
- Stott, J. P., Pimblet, K. A., Edge, A. C., Smith, G. P., & Wardlow, J. L. 2009, *MNRAS*, 394, 2098
- Stott, J. P., Smail, I., Edge, A. C., et al. 2007, *ApJ*, 661, 95
- Stott, J. P., Collins, C. A., Sahlén, M., et al. 2010, *ApJ*, 718, 23
- Strateva, I., Ivezić, Ž., Knapp, G. R., et al. 2001, *AJ*, 122, 1861
- Strazzullo, V., Rosati, P., Pannella, M., et al. 2010, *A&A*, 524, A17
- Strazzullo, V., Gobat, R., Daddi, E., et al. 2013, *ApJ*, 772, 118
- Sunyaev, R. A., & Zeldovich, Y. B. 1972, *Comments on Astrophysics and Space Physics*, 4, 173
- Szomoru, D., Franx, M., Bouwens, R. J., et al. 2011, *ApJ*, 735, L22
- Szomoru, D., Franx, M., & van Dokkum, P. G. 2012, *ApJ*, 749, 121
- Szomoru, D., Franx, M., van Dokkum, P. G., et al. 2013, *ApJ*, 763, 73
- . 2010, *ApJ*, 714, L244
- Tamura, N., & Ohta, K. 2003, *AJ*, 126, 596
- Tanaka, M., Finoguenov, A., & Ueda, Y. 2010, *ApJ*, 716, L152
- Tanaka, M., Kodama, T., Arimoto, N., et al. 2005, *MNRAS*, 362, 268
- Tanaka, M., Toft, S., Marchesini, D., et al. 2013, *ApJ*, 772, 113
- Taylor, E. N., Franx, M., Glazebrook, K., et al. 2010, *ApJ*, 720, 723
- Taylor, E. N., Franx, M., van Dokkum, P. G., et al. 2009a, *ApJS*, 183, 295
- . 2009b, *ApJ*, 694, 1171
- Thomas, D., Maraston, C., Bender, R., & Mendes de Oliveira, C. 2005, *ApJ*, 621, 673

- Thomas, D., Maraston, C., Schawinski, K., Sarzi, M., & Silk, J. 2010, MNRAS, 404, 1775
- Tinker, J., Kravtsov, A. V., Klypin, A., et al. 2008, ApJ, 688, 709
- Tinsley, B. M. 1978, ApJ, 222, 14
- Tiret, O., Salucci, P., Bernardi, M., Maraston, C., & Pforr, J. 2011, MNRAS, 411, 1435
- Toft, S., Gallazzi, A., Zirm, A., et al. 2012, ApJ, 754, 3
- Toft, S., van Dokkum, P., Franx, M., et al. 2007, ApJ, 671, 285
- Tortora, C., Napolitano, N. R., Cardone, V. F., et al. 2010, MNRAS, 407, 144
- Tortora, C., Pipino, A., D'Ercole, A., Napolitano, N. R., & Matteucci, F. 2013, MNRAS, 435, 786
- Trager, S. C., Faber, S. M., & Dressler, A. 2008, MNRAS, 386, 715
- Treu, T., Ellis, R. S., Kneib, J.-P., et al. 2003, ApJ, 591, 53
- Trujillo, I., Carrasco, E. R., & Ferré-Mateu, A. 2012, ApJ, 751, 45
- Trujillo, I., Cenarro, A. J., de Lorenzo-Cáceres, A., et al. 2009, ApJ, 692, L118
- Trujillo, I., Conselice, C. J., Bundy, K., et al. 2007, MNRAS, 382, 109
- Trujillo, I., Erwin, P., Asensio Ramos, A., & Graham, A. W. 2004, AJ, 127, 1917
- Trujillo, I., Ferreras, I., & de La Rosa, I. G. 2011, MNRAS, 415, 3903
- Trujillo, I., Feulner, G., Goranova, Y., et al. 2006a, MNRAS, 373, L36
- Trujillo, I., Förster Schreiber, N. M., Rudnick, G., et al. 2006b, ApJ, 650, 18
- Valentinuzzi, T., Poggianti, B. M., Saglia, R. P., et al. 2010a, ApJ, 721, L19
- Valentinuzzi, T., Fritz, J., Poggianti, B. M., et al. 2010b, ApJ, 712, 226
- Valtchanov, I., Pierre, M., Willis, J., et al. 2004, A&A, 423, 75
- van de Sande, J., Kriek, M., Franx, M., Bezanson, R., & van Dokkum, P. G. 2014, ApJ, 793, L31
- van de Sande, J., Kriek, M., Franx, M., et al. 2013, ApJ, 771, 85
- van den Bergh, S. 1976, ApJ, 206, 883
- van der Wel, A., Holden, B. P., Zirm, A. W., et al. 2008, ApJ, 688, 48
- van der Wel, A., Rix, H.-W., Wuyts, S., et al. 2011, ApJ, 730, 38

- van der Wel, A., Bell, E. F., Häussler, B., et al. 2012, *ApJS*, 203, 24
- van der Wel, A., Franx, M., van Dokkum, P. G., et al. 2014, *ApJ*, 788, 28
- van Dokkum, P. G., & Franx, M. 2001, *ApJ*, 553, 90
- van Dokkum, P. G., & van der Marel, R. P. 2007, *ApJ*, 655, 30
- van Dokkum, P. G., Franx, M., Kriek, M., et al. 2008, *ApJ*, 677, L5
- van Dokkum, P. G., Whitaker, K. E., Brammer, G., et al. 2010, *ApJ*, 709, 1018
- van Dokkum, P. G., Bezanson, R., van der Wel, A., et al. 2014, *ApJ*, 791, 45
- Vazdekis, A., Ricciardelli, E., Cenarro, A. J., et al. 2012, *MNRAS*, 424, 157
- Vázquez, G. A., & Leitherer, C. 2005, *ApJ*, 621, 695
- Vikhlinin, A., Kravtsov, A. V., Burenin, R. A., et al. 2009, *ApJ*, 692, 1060
- Visvanathan, N., & Sandage, A. 1977, *ApJ*, 216, 214
- Voigt, L. M., & Fabian, A. C. 2006, *MNRAS*, 368, 518
- Vulcani, B., Poggianti, B. M., Dressler, A., et al. 2011, *MNRAS*, 413, 921
- Vulcani, B., Bamford, S. P., Häußler, B., et al. 2014, *MNRAS*, 441, 1340
- Webb, T., Noble, A., DeGroot, A., et al. 2015, *ApJ*, 809, 173
- Weinmann, S. M., Kauffmann, G., van den Bosch, F. C., et al. 2009, *MNRAS*, 394, 1213
- Weinmann, S. M., van den Bosch, F. C., Yang, X., & Mo, H. J. 2006, *MNRAS*, 366, 2
- Wellons, S., Torrey, P., Ma, C.-P., et al. 2015, *MNRAS*, 449, 361
- Whitaker, K. E., Labbé, I., van Dokkum, P. G., et al. 2011, *ApJ*, 735, 86
- Whitaker, K. E., van Dokkum, P. G., Brammer, G., et al. 2013, *ApJ*, 770, L39
- Whitaker, K. E., Franx, M., Leja, J., et al. 2014, *ApJ*, 795, 104
- White, M., Zheng, Z., Brown, M. J. I., Dey, A., & Jannuzi, B. T. 2007a, *ApJ*, 655, L69
- . 2007b, *ApJ*, 655, L69
- Wilkinson, D. M., Maraston, C., Thomas, D., et al. 2015, *MNRAS*, 449, 328
- Williams, R. J., Quadri, R. F., Franx, M., van Dokkum, P., & Labbé, I. 2009, *ApJ*, 691, 1879

- Williams, R. J., Quadri, R. F., Franx, M., et al. 2010, *ApJ*, 713, 738
- Willis, J. P., Clerc, N., Bremer, M. N., et al. 2013, *MNRAS*, 430, 134
- Wilson, G., Muzzin, A., Yee, H. K. C., et al. 2009, *ApJ*, 698, 1943
- Wilson, G. W., Hughes, D. H., Aretxaga, I., et al. 2008, *MNRAS*, 390, 1061
- Windhorst, R. A., Cohen, S. H., Hathi, N. P., et al. 2011, *ApJS*, 193, 27
- Wise, M. W., & Silva, D. R. 1996, *ApJ*, 461, 155
- Worthey, G., Faber, S. M., Gonzalez, J. J., & Burstein, D. 1994, *ApJS*, 94, 687
- Wu, H., Shao, Z., Mo, H. J., Xia, X., & Deng, Z. 2005, *ApJ*, 622, 244
- Wuyts, S., Cox, T. J., Hayward, C. C., et al. 2010, *ApJ*, 722, 1666
- Wuyts, S., Labbé, I., Franx, M., et al. 2007, *ApJ*, 655, 51
- Wuyts, S., Förster Schreiber, N. M., van der Wel, A., et al. 2011, *ApJ*, 742, 96
- Wuyts, S., Förster Schreiber, N. M., Genzel, R., et al. 2012, *ApJ*, 753, 114
- Yee, H. K. C., Gladders, M. D., Gilbank, D. G., et al. 2007, in *Astronomical Society of the Pacific Conference Series*, Vol. 379, *Cosmic Frontiers*, ed. N. Metcalfe & T. Shanks, 103
- York, D. G., Adelman, J., Anderson, Jr., J. E., et al. 2000, *AJ*, 120, 1579
- Zeimann, G. R., Stanford, S. A., Brodwin, M., et al. 2012, *ApJ*, 756, 115
- Zhuravleva, I., Churazov, E., Schekochihin, A. A., et al. 2014, *Nature*, 515, 85
- Zhuravleva, I., Churazov, E., Arévalo, P., et al. 2016, *MNRAS*, 458, 2902
- Zibetti, S., Charlot, S., & Rix, H.-W. 2009, *MNRAS*, 400, 1181
- Zirm, A. W., Toft, S., & Tanaka, M. 2012, *ApJ*, 744, 181
- Zirm, A. W., van der Wel, A., Franx, M., et al. 2007, *ApJ*, 656, 66
- Zwicky, F. 1933, *Helvetica Physica Acta*, 6, 110
- . 1937, *ApJ*, 86, 217

Acknowledgements

First of all, I would like to express my sincere gratitude to my supervisors, PD. Dr. Roberto Saglia and Dr. Alessandra Beifiori, for their continuous scientific and personal support over the last years. I am also grateful to Prof. Dr. Ralf Bender for his oversight of this project. This work would not have been possible without their guidance and encouragement.

My sincere thanks also goes to Dr. John Trevor Mendel, Dr. David Wilman, Matteo Fossati and Dr. Audrey Galametz for their lively discussions, insightful comments and helpful advice on this project. Furthermore, I would also like to thank all members of the KMOS Cluster Survey team, who have also given many useful suggestions and ideas.

I would also like to thank Dr. Francesco La Barbera and Dr. Philipp Lang for providing various catalogues and data for the comparison with our sample. This work has also benefitted from financial support of the Deutsche Zentrum für Luft- und Raumfahrt (DLR) via Project ID 50OR1513.

In addition, there are many people at MPE and MPA who had made my time enjoyable and have contributed to a good working environment here. I would like to thank my fellow officemates and neighbours: Dr. Alessia Longobardi, Dr. Anna Brucalassi, Claudia Pulsoni, Surangkha Rukdee, Michael Opitsch, Fabrizio Finozzi and Dr. Sandesh Kulkarni. Thanks also to my great friends, Haakon Andresen, Dijana Vrbanec and Suryashree Aniyani, who make my day-to-day life more entertaining. Special thanks to Isabella Söldner-Rembold, who takes care of me all the time, without your support everything would have been so much harder.

Last, but by no means least, I would like to thank my parents Ms. Becky Chung and Mr. Andrew Chan, for their love, care and support.